



Compression behavior of loose wet granular materials : experiment and discrete numerical simulation

Vinh-Du Than

► To cite this version:

Vinh-Du Than. Compression behavior of loose wet granular materials : experiment and discrete numerical simulation. Other. Université Paris-Est, 2017. English. NNT : 2017PESC1204 . tel-01621813

HAL Id: tel-01621813

<https://pastel.hal.science/tel-01621813>

Submitted on 23 Oct 2017

HAL is a multi-disciplinary open access archive for the deposit and dissemination of scientific research documents, whether they are published or not. The documents may come from teaching and research institutions in France or abroad, or from public or private research centers.

L'archive ouverte pluridisciplinaire **HAL**, est destinée au dépôt et à la diffusion de documents scientifiques de niveau recherche, publiés ou non, émanant des établissements d'enseignement et de recherche français ou étrangers, des laboratoires publics ou privés.



UNIVERSITÉ PARIS-EST
ÉCOLE DOCTORALE SCIENCE INGÉNIERIE ET ENVIRONNEMENT

THÈSE

présentée pour l'obtention du diplôme docteur de

L'UNIVERSITÉ PARIS-EST

Spécialité: *Géotechnique*

par

Vinh Du THAN

Sujet de la thèse :

**Compression behavior of loose wet granular materials:
experiment and discrete numerical simulation**

Thèse soutenue le 26 avril 2017 devant le jury composé de :

Gaël COMBE	Professeur, Université Grenoble Alpes	Président
Jean-Yves DELENNE	Directeur de recherche, INRA	Rapporteur
Bertrand FRANÇOIS	Professeur, Université Libre de Bruxelles	Rapporteur
Jean-Noël ROUX	Chercheur, IFSTTAR	Examineur
Jean-Michel PEREIRA	Chercheur, École des Ponts ParisTech	Examineur
Anh Minh TANG	Chercheur, École des Ponts ParisTech	Directeur de thèse

Acknowledgment

Ce travail de thèse n'aurait être possible sans appui de beaucoup de gens. Je tiens à remercier dans cette page un certain nombre de personnes qui m'ont aidé à mener à bien ce travail.

Je tiens tout d'abord à remercier Monsieur Gaël Combe, qui m'a fait l'honneur de présider le jury de ma soutenance de thèse ainsi qu'a examiné mon travail. Ses remarques et questions sont très intéressantes et constructives.

Je voudrais remercier vivement Messieurs Jean-Yves Delenne et Bertrand François qui ont accepté la longue et lourde tâche d'être rapporteurs de ma thèse. Leurs remarques fructueuses et précieuses m'ont aidé à améliorer le niveau scientifique de ce travail.

Je souhaite exprimer ma profonde gratitude à mes trois directeurs de thèse Anh Minh Tang, Jean-Noël Roux et Jean-Michel Pereira pour leur confiance, leur suivi et leur gentillesse. Merci à Jean-Michel pour tes conseils précieux et ton aide. Merci sincèrement à Jean-Noël pour ton modèle de la simulation, tes conseils précieux, tes encouragements ainsi que ta patience dans les moments que je n'ai pas pu bien comprendre ton modèle. Si ce travail est une réussite, c'est une très grande partie grâce à toi. Un grand merci à Minh pour avoir accepté ma demande à faire ma thèse à l'École des Ponts ParisTech. C'est un grand honneur pour moi. Tu m'as beaucoup aidé, tu m'as guidé et accompagné tout le long de l'élaboration de ce travail. Tes soutiens et encouragements m'ont permis mener à bien ce travail.

Je voudrais également adresser mes remerciements aux Messieurs Michel Bornert et Patrick Aimedieu de l'équipe multi-échelles, qui m'ont aidé de faire des essais de microtomographie aux rayons X. Leurs conseils sont très utiles pour la partie du traitement d'imagerie.

Je tiens aussi à remercier l'équipe technique du CERMES: Emmanuel, Hocine, Xavier, Baptiste, Marine pour leurs aides à faire des essais en laboratoire.

Je n'oublie pas, non plus, de remercier le Ministère de l'Éducation et la Formation du Vietnam pour avoir financé cette thèse ainsi que les soutiens de mes collègues dans le département de génie civile de l'Institut Universitaire de Technologie de l'Université de Danang.

J'aimerais remercier tous les chercheurs et les amis dans l'équipe CERMES pour

l'ambiance de travail et les très bons moments qu'on a eu ensemble. Mes remerciements vont ensuite à mes amis vietnamiens avec qui j'ai partagé des moments inoubliables dans la vie quotidienne.

J'aurais une grande reconnaissance à mes parents, mes grands frères, ma grande sœur et ma petite sœur pour leurs soutiens et encouragements.

Enfin, j'aimerais remercier infiniment mon épouse Phuong Thao et mon fils Vinh Khoa qui ont fait tant de sacrifices pour moi avec l'amour et un soutien sans limites. À eux, je dédie cette thèse.

Champs-sur-Marne, le 10 mai 2017

THÂN Vinh Du

The present work was carried out in the Laboratoire Navier at the Ecole des Ponts ParisTech, Paris-Est University. The scholarship was financed by the Ministry of Education and Training of Vietnam (project 911).

Ce travail a été réalisé au Laboratoire Navier de l'Ecole des Ponts ParisTech, Université Paris-Est. La bourse de thèse est financée par le Ministère de l'Education et la Formation du Vietnam (projet 911).

Abstract

The behavior under compression, either oedometric or isotropic, of model granular materials (glass beads) wet by a small quantity of liquid forming capillary bridges is studied both by discrete element numerical simulation (DEM) and by laboratory experiments, which combine oedometric tests and X-ray microtomography (XRCT). Special attention is paid to very loose initial states (solid fraction below 30 %) stabilized by capillary cohesion. XRCT observations involve suitable spherical particle detection adapted to relatively low resolution images. It enables heterogeneities to be visualized and microstructural information to be collected. DEM simulations lead to the identification of parameters that influence the plastic compression behavior of the material. Important factors include in particular the initial coordination number of the loose contact network, which varies to a large extent as a consequence of the ability of the assembling procedure to restructure cohesive clusters in their aggregation stage; and some possible slight resistance to rolling and pivoting in the contacts. The macroscopic compression curve (the void ratio dependence on stress) is controlled by a dimensionless reduced pressure comparing confining stress to capillary forces. In the stress interval corresponding to irreversible collapse, it assumes the classical logarithmic form of soil mechanics. For this compression law as well as for various microscopic observations, experiments and simulations are found to agree semi-quantitatively.

Keywords: DEM, wet granular materials, one-dimensional compression, isotropic compression, X-ray computed tomography, grain-scale analysis, plastic behavior, microstructure

Résumé

Le comportement en compression, oedométrique ou isotrope, de matériaux granulaires (billes de verre) en présence d'une faible quantité d'eau formant des ponts capillaires est étudié par la simulation numérique aux éléments discrets (DEM) et par des expériences en laboratoire, combinant essais oedométriques et microtomographie aux rayons X (XRCT). On porte une attention particulière aux états initiaux très lâches (compacité inférieure à 30 %) stabilisés par la cohésion capillaire. L'observation par XRCT, fondée sur une méthode de détection des grains sphériques adaptée aux images relativement peu résolues, permet de visualiser les hétérogénéités et d'accéder à des informations microstructurelles. L'approche numérique par DEM permet de dégager les paramètres influençant le comportement de compression plastique du matériau. Parmi ceux-ci la coordinence initiale du réseau des contacts, plus ou moins élevée selon que le procédé d'assemblage permet ou non aux amas connectés par la cohésion capillaire de se restructurer, ainsi qu'une éventuelle légère résistance au roulement ou au pivotement dans les contacts, jouent un rôle déterminant. La courbe de compression macroscopique (variation de l'indice des vides avec la pression) est régie par une pression réduite qui compare les effets du confinement à l'attraction capillaire, et prend la forme, dans l'intervalle de contraintes correspondant à un effondrement irréversible, de la loi logarithmique familière dans les sols cohésifs. Pour cette loi comme pour différentes observations microscopiques, un accord semi-quantitatif est obtenu entre expériences et simulations numériques.

Mots-clés: Modélisation des éléments discrets, matériaux granulaires mouillés, compression oedométrique, compression isotrope, microtomographie aux rayons X, analyse à l'échelle du grain, comportement plastique, microstructure

Contents

Acknowledgment	i
Abstract	v
Résumé	vii
Contents	xi
List of Figures	xviii
List of Tables	xix
Overview	1
1 Literature review	5
1.1 Mechanical behavior of granular materials	7
1.1.1 General considerations	7
1.1.2 Bonded granular materials	10
1.1.3 Wet granular materials	12
1.2 Experimental investigations	15
1.2.1 Techniques	20
1.2.2 Typical observations	22
1.3 Numerical investigations	28
1.3.1 Numerical methods	28
1.3.2 Typical observations	30
1.3.3 Some characteristics of wet granular material in DEM simulation	34
1.4 Experimental investigation versus numerical investigation	39
1.4.1 Existing studies combining experimental and numerical methods .	39
1.4.2 Combination between the XRCT and the DEM	43
1.5 Conclusion	49

2	Experimental investigations	51
2.1	Introduction	53
2.2	Material and methods	53
2.2.1	Material	53
2.2.2	Specimen preparation	54
2.2.3	Oedometric compression tests	57
2.2.4	X-ray computed tomography tests	59
2.3	Mechanical behavior under increasing vertical stress	62
2.4	Global scan observations	63
2.4.1	3D reconstruction from the image stack	63
2.4.2	Segmentation process	65
2.4.3	Heterogeneity	66
2.4.4	Pore scale deformation	71
2.5	Local scan observations	74
2.5.1	General principles	74
2.5.2	Algorithm to detect spherical structures	76
2.5.3	3D reconstruction after detection process	80
2.5.4	Grain size distribution after the detection process	82
2.5.5	General description of the structure at grain-scale	82
2.5.6	Heterogeneity	85
2.5.7	Geometrical structure analysis	86
2.5.8	Contact networks	92
2.6	Links between macro and microscopic behaviors	94
2.7	Conclusion	95
3	Isotropic compression: DEM study	97
3.1	Introduction	99
3.2	Model material and interaction laws	99
3.2.1	Particle shape and size distribution	99
3.2.2	Interaction law: normal forces	100
3.2.3	Tangential forces	104
3.2.4	Resistance to rolling and pivoting (RPR)	105
3.3	Basic definitions and properties	106
3.3.1	DEM equations, boundary conditions and stress control	106
3.3.2	Equilibrium condition	108
3.3.3	Coordination numbers	109
3.3.4	Liquid content and limit of pendular state	110
3.3.5	Average normal force	111
3.3.6	Dimensionless control parameters	112
3.4	Simulation procedures for the compression test	113

3.4.1	Specimen preparation	113
3.4.2	Simulation parameters	115
3.4.3	Compression cycle	118
3.5	Material behavior in isotropic compression	118
3.5.1	A reference case	118
3.5.2	Influence of drying or of saturating	130
3.5.3	Influence of initial state	131
3.5.4	Effects of polydispersity	138
3.6	The case of wet beads with RPR	143
3.6.1	Influence of initial solid fraction	143
3.6.2	Influence of initial agitation intensity	145
3.6.3	Influence of rolling and pivoting friction coefficients	149
3.6.4	Comparison of bead assemblies with and without RPR	151
3.7	Conclusion	153
4	Oedometric compression: DEM study and experimental confrontation	155
4.1	Introduction	156
4.2	Simulation of oedometric compression tests	156
4.2.1	Compression of different initial states: initial V_0 and coordination.	157
4.2.2	Influence of initial solid fraction	162
4.3	Oedometric versus isotropic compression	166
4.4	Experiment versus simulation	168
4.4.1	Compaction behavior	168
4.4.2	Geometrical structure change	170
4.5	Conclusion	171
	Conclusions and Perspectives	173
	Bibliography	175

List of Figures

1.1	Particles displacement during triaxial compression	9
1.2	Photoelastic image of a small assembly of disks	9
1.3	Skeletal versus contact-level capillary and electrical forces	12
1.4	Schematic view of a XRCT	21
1.5	One-dimensional compression plots for carbonate and silica sands	23
1.6	Capillary bridges in glass beads	23
1.7	Water menisci form at contacts of sand grains: (a) concave menisci; (b) convex menisci.	24
1.8	The differences of water content for different regions 1, 2, 3, and 4 as a function of time	25
1.9	An example of XRCT scans of Hostun sand, with D is the diameter of cell and r is the resolution of image	25
1.10	Examples of partitioning and subsequent ball-and-stick network construction, applied to an unconsolidated sand imaged at $2.8 \mu\text{m}$	26
1.11	Four different domains (fully saturated, funicular, pendular and hygroscopic) shown in slices from trinarised 3D images of Hostun sand	27
1.12	Effect of soil compaction on interpores (a) and intrapores (b) volumes from soil aggregates with varying levels of soil moisture and compaction	28
1.13	The cycle of the DEM calculation	30
1.14	The packing fraction of different sized glass beads as a function of the effective gravitational acceleration	31
1.15	Ballistic deposit before and after compaction by a constant external force on the piston	32
1.16	Compression and decompression curves: effect of initial agitation level in aggregation stage and influence of rolling resistance parameter.	32
1.17	A map of tensile (green) and compressive (red) forces in a thin layer cut out in the packing	33
1.18	Schematic view of liquid bridge between two smooth (a) polydisperse spheres and (b) monodisperse spheres.	34

1.19	Capillary force and capillary pressure as a function of the gorge's radius for different values of contact angle θ	35
1.20	Evolution of the capillary force F_{cap} as a function of the interparticle distance h for a given capillary pressure Δu	37
1.21	Loose cohesive assembly of disk	38
1.22	An example of compression curve of loose systems obtained with 2D and 3D models.	39
1.23	Illustration of the clumping of spheres method with no overlapping particles.	44
1.24	Pore size distributions of granules produced under high shear	45
1.25	Comparison of coordination measurements on numerical sphere packings produced by DEM and by analysis of XRCT images.	46
1.26	Comparison of the RDFs of (a) the monodisperse glass packing structure, and (b) polydisperse glass packing structure	47
1.27	(a) Cemented numerical sample and (b) laboratory sample.	48
2.1	Cumulative grain size distribution of glass beads	54
2.2	Specimen preparation for cell $\phi 50$	54
2.3	Specimen preparation for cell $\phi 20$	55
2.4	Schematic view of the system for preparing the specimen	56
2.5	Initial void ratio e_0 and initial porosity n versus height of free fall h_f	57
2.6	Schematic view of oedometric compression system	58
2.7	Applied force versus time during compression process. The inset shows the signal noise during the initial stage when the specimen approached and touched the piston	58
2.8	Global view of in-situ compression test combined with XRCT at Laboratoire Navier	59
2.9	(a) The PMMA cell with several gaskets and pistons (heights δ given in mm, see Fig. 2.10 for definition of δ). (b) Several wedges with different values of thickness	60
2.10	Illustration of the compressed heights of in-situ compaction test that were scanned for XRCT	61
2.11	Void ratio versus vertical stress during oedometric compression tests for cells $\phi 50$ and $\phi 20$	62
2.12	3D reconstructed images of the specimen at different stages of compaction	64
2.13	Illustration of grey level histograms for all global scans	65
2.14	Images at different steps of segmentation: (a) original image, (b) segmented image	66
2.15	Illustration of grey level as a function of the height of specimen	66
2.16	Schematic view of several types of diagram for calculating the heterogeneity	68

2.17	Void ratio distribution according to the compressed height of sample for different compaction steps (diagram 1)	69
2.18	Void ratio distribution according to the average radii of the selected cylinders for different compaction steps (diagram 2)	69
2.19	Void ratio distribution according to eight equal sectors for different compaction steps (diagram 3)	70
2.20	Void ratio distribution according to five equal volumes for different compaction steps (diagram 4)	70
2.21	Void ratio distribution according to the x (a) and y (b) directions for different compaction steps (diagram 5)	71
2.22	Total volume and total pore volume of volume V2 for different steps of compaction	72
2.23	An example of the local thickness for volume V2 (a) at step S01G and a slice (b) extracted from (a)	72
2.24	Distribution of pore volume of the volume V2 for different levels of compaction	73
2.25	Position of the local scan (b) from the global scan (a) and an example of investigated cube (c)	74
2.26	3D reconstructed image of four local scans	75
2.27	The algorithm to detect the spherical structures	76
2.28	Construction of the accumulation array from the gradient field	77
2.29	Definition of the signature curve	78
2.30	An example of a signature curve computed from the 3D image	79
2.31	A slice in a 3D detected image	79
2.32	Method to find the lost contacts, inside cube is the standard volume; outside cube is the extended volume	80
2.33	Example of 3D reconstructed cubes of four local scans. Left-hand side: before detection, right-hand side: after detection	81
2.34	Grain size distribution of the 3D reconstructed specimens	82
2.35	Example of 3D reconstructed specimen	84
2.36	Number of particles of the ten SVs for four local scans after detection process	85
2.37	Macroscopic solid fraction (triangle) and the average solid fraction of 4 local scans before and after the detection process	86
2.38	Average total coordination numbers of 4 local scan with three values of tolerance (0, 1 and 2 voxels)	87
2.39	Coordination numbers of close neighbors for four local scans	88
2.40	Number of contacts per grain for three tolerances of 0, 1 and 2 voxels	89
2.41	An example of a sphere with one contact	90
2.42	Radial distribution functions for particle centers of four local scans	91

2.43	Contact network of a typical SV under growing of compaction	93
2.44	3d-slices of the typical SV under growing of compaction	94
3.1	Grain size distribution of the polydisperse system	100
3.2	Static normal force, $F_N = F_N^e + F_{cap}$, as a function of the interparticle distance h	102
3.3	Coulomb cone limiting the value of the tangential force	104
3.4	Motion of two spheres	107
3.5	Three spheres connected with liquid bridges	110
3.6	Capillary force law $F_{cap}(h)$, for two different meniscus values, according to the Maugis approximation and the Soulié formula	112
3.7	Monodisperse system on FCC lattice	114
3.8	Typical specimens of (a) the monodisperse ($\Phi_0 = 0.30$) and (b) the polydisperse ($\Phi_0 = 0.24$) systems.	115
3.9	((a) e versus $\log P^*$ for reference system in compression cycle; (b) comparison of reference case and typical non-cohesive behavior	119
3.10	Effect of different (isotropic) unloading and reloading histories on void ratio	120
3.11	a) Coordination numbers z , z_c and z_d ; and (b) coordination numbers z_c , z_+ , and z_- versus P^* in compression and decompression cycles	121
3.12	Contact networks in loading (a, b, and c) and unloading (d, e, and f) cycle	122
3.13	Networks of compressive contacts (red lines), tensile ones (green lines), and contacts with $F_N = 0$ (magenta)	123
3.14	Distribution of normal forces for different values of P^* from the compression path, (a) normalized by the maximum tensile force F_0 , and (b) normalized by the average normal force $\langle F_N \rangle$	124
3.15	Distribution of normal forces for different values of P^* in non-cohesive case, normalized by the average normal force $\langle F_N \rangle$	125
3.16	Void ratio (a), coordination numbers z_c and z_d (b) versus P^* of the reference case for different values of meniscus V_m/d^3	126
3.17	Coordination numbers of z_+ and z_- versus reduced pressure P^* for different values of V_m/d^3	127
3.18	Distribution of the number of contacts per grain of the reference case for different values of V_m/d^3 at three typical states of P^*	128
3.19	Evolution of coordination number of close neighbors $z(h)$ versus dimensionless interparticle distance h/d for different values of P^* in loading path	129
3.20	Void ratio versus pressure P , as cohesive forces are suppressed at the beginning of unloading	130
3.21	(a) Void ratio e , and (b) coordination numbers z_c and z_d versus P^* for different values of initial solid fraction Φ_0	132
3.22	Coordination numbers z_+ and z_- versus P^* for different values of Φ_0 . .	133

3.23	Distribution of the number of contacts per grain for different values of Φ_0 at three typical states of P^*	134
3.24	Distribution of normal forces for different values of Φ_0 under low pressure $P^* = 10^{-2}$, is normalized by the maximum tensile force F_0	134
3.25	(a) Compression and decompression curves, and (b) coordination numbers z_c and z_d for different values of V_0/V^*	135
3.26	Coordination numbers z_+ and z_- versus P^* for different values of V_0/V^*	136
3.27	A 3D slice of specimen for different values of V_0/V^* at the beginning of loading path ($P^* = 10^{-3}$)	137
3.28	Number of contacts per grain for different values of V_0/V^* at three typical states of P^*	138
3.29	Distribution of normal forces for different values of V_0/V^* under $P^* = 10^{-3}$, normalized by F_0	138
3.30	(a) Void ratio e and (b) coordination numbers z_c and z_d versus P^* for different values of V_0/V^*	139
3.31	Contacts (red lines) and distant interactions (blue lines) for different values of V_0/V^* at $P^* = 10^{-3}$	140
3.32	Grains contained in a slice (thickness $3d_{\min}$), at low P^* , for different values of V_0/V^*	141
3.33	(a) Void ratio e and (b) coordination numbers z_c and z_d versus P^* for MDS and PDS.	142
3.34	(a) Void ratio e and (b) coordination numbers z_c and z_d versus P^* in compression cycle for different values of Φ_0	143
3.35	Coordination numbers z_+ and z_- versus reduced pressure P^* for different values of Φ_0	144
3.36	(a) Void ratio e and (b) coordination numbers z_c and z_d versus P^* in compression cycle for different values of V_0/V^*	145
3.37	Coordination numbers z_+ and z_- versus P^* for different values of V_0/V^*	146
3.38	$3d$ -slices of specimens assembled with RPR for different values of V_0/V^* , under $P^* = 10^{-3}$	147
3.39	Number of contacts per grain for six values of V_0/V^* at three typical states $P^* = 10^{-3}$, $P^* = 10^{-1}$, and $P^* = 10^1$	148
3.40	Distribution of normal forces at low pressure $P^* = 10^{-3}$ for different V_0/V^* . P.D.F normalized by F_0	149
3.41	(a) Void ratio e and (b) coordination numbers z_c and z_d versus P^* for different values of $\mu_R = \mu_P$	150
3.42	Distribution of normal forces for different values of μ_R/d at $P^* = 10^{-2}$	151
3.43	(a) Void ratio e and (b) coordination numbers z_c and z_d versus P^* in compression cycle for systems both without RPR and with RPR	152

4.1	(a) Void ratio e , and (b) coordination numbers z_c and z_d versus σ_1^* for different values of V_0/V^*	157
4.2	Coordination numbers z_+ (compressive contacts) and z_- (tensile contacts) versus reduced axial stress σ_1^* for different values of V_0/V^*	158
4.3	Coefficient of lateral pressure K_0 versus reduced vertical stress σ_1^* for different values of V_0/V^*	159
4.4	Contribution of distant interactions to normal stress σ_{22} . Red arrow denotes the increasing of values	160
4.5	a) Contributions of tangential (a) and capillary (b) interactions to normal stress σ_{22}	161
4.6	(a) Void ratio e , and (b) coordination numbers z_c and z_d versus σ_1^* for different values of initial solid fraction Φ_0	162
4.7	Coordination numbers of z_+ and z_- versus reduced vertical stress σ_1^* for different values of Φ_0	163
4.8	K_0 versus reduced axial stress σ_1^* for different values of Φ_0	164
4.9	Contribution of distant interactions to normal stress σ_{22} for different values of Φ_0	164
4.10	(a) Contributions of tangential (a) and capillary (b) interactions to normal stress σ_{22} for different values of Φ_0	165
4.11	(a) Void ratio e , and (b) coordination numbers z_c and z_d versus reduced mean stress σ_m^* for the minimum and maximum V_0/V^* in both simulations of oedometric and isotropic tests	166
4.12	Distribution of normal forces for both oedometric and isotropic models	167
4.13	Oedometric compression curves in experiments and simulations (no RPR) for different values of Φ_0	169
4.14	Coordination numbers of neighbors $z(h)$ versus vertical stress σ_1 and the total coordination number z versus positions of scans	171

List of Tables

1.1	Schematic diagrams for classification of wet granular materials with various amount of liquid	13
1.2	Examples of imaging techniques to porous media systems	17
1.3	Combining experimental observations with computer simulations	42
2.1	Initial parameters of selected specimens after preparation. The sample CT03 was prepared for the XRCT tests	57
2.2	Details of the scanning program. G: global scan, L: local scan	61
3.1	Initial parameters of the monodisperse system without RPR	116
3.2	Initial parameters of the polydisperse system without RPR	116
3.3	Initial parameters of the monodisperse system with RPR	117
3.4	Probability of meniscus formation between close neighbors versus P^* . .	130
4.1	Initial parameters of the oedometric simulations (without RPR)	156

Overview

Granular materials appear in various natural and industrial processes. They are composed of individual grains that vary in shape, size, composition, surface texture, etc. These granular characteristics can remarkably affect the packing and the contact distribution properties of granular assemblies. Therefore, granular materials may exhibit quite different behaviors depending on the applied external forces, the size and geometry of the grains, the density and composition of particles, the type of interactions at the grain scale and many other material properties. Because of these complexities, it is generally difficult to relate in a straightforward manner the macroscopic properties of granular materials to the microscopic properties of their constituents. In the case of wet granular materials, the existence of liquid menisci between particles plays a key role in the overall behavior of the assembly. Capillary cohesion bestows to these materials specific mechanical features that do not exist with dry grains, such as the ability to form stable structures with very low density, and a strong sensitivity to stress intensity as well as to stress direction. So far, many experimental and numerical studies of bonded granular materials in general and wet granular materials in particular have been carried out to tackle the difficulties exposed here above.

Published studies cover a wide range of applications. For instance, some investigate the mechanical properties of cohesive soils (clays and silts) [1, 2, 3, 4, 5], metallic powder processing [6] or modeling and treatment of ceramic powders [7, 8, 9]. Assemblies of wet beads were observed [10, 11, 12], and descriptions of such materials at microscopic scale were made possible by using numerical and experimental tests [11, 12]. A 2D numerical investigation into the microstructure and mechanical properties of cohesive powders is reported in [13, 14]. In addition, some numerical studies of cohesive materials have shown that the stability of loose structures formed by particles packed under gravity rely on adhesive forces (see for instance Dong *et al.* [15]). Other numerical works studied loose packings stabilized by cohesion and their collapse when subjected to increasing loads during oedometric compression [16, 17, 18, 19]. Some studies focused on the failure of bounded particle assemblies in static [20, 21] or dynamic conditions [22]. Other works on wet bead packs in which cohesion stems from liquid bridges joining neighbouring particles investigated the structure of poured samples [23], or their shear strength [24].

Shear flow of cohesive granular materials has also been simulated [25, 26, 27, 28, 29]. Besides, the collapsible behavior of loessic soils [30, 31, 32], as well as wet sand with capillary bridges [33, 34, 35] has been investigated experimentally. The contribution of artificial solid bridges to the micro-macroscopic behavior of soils, especially in the case of cemented sands, has been studied using both numerical simulations and experimental observations [36, 37, 38, 39, 40, 41, 42]. These works evidenced the link between the macroscopic mechanical behavior and changes in the microstructure. However, most studies on wet granular materials have focused on dense states, and few works have focused on the grain-scale behavior.

Currently, the grain-scale behavior of wet granular materials is usually investigated using numerical simulations, such as the discrete element method [43], in 2D and/or 3D [44, 45, 17, 29, 24, 46, 27, 47]. These studies characterized precisely the microstructure in terms of coordination number of contacts, coordination number of distant interactions, coordination number of compressive and tensile bonds, radial distribution function, force chains, distribution of forces between particles, etc. The evolution of these microstructural descriptors with the externally applied pressure was also investigated. However, few works have quantitatively compared simulations (e.g. with the discrete element method) with experimental results (e.g. with microstructural observations using the X-ray computed tomography) in order to validate the numerical method [48, 49, 50, 36, 37].

Following the two-dimensional model for cohesive powders which is based on the discrete element method and developed by Gilabert *et al.* [13, 14], we propose a three-dimensional model to investigate the mechanical behavior of a wet granular material at very loose states of density. On the same material, we also perform one-dimensional compression tests combined with microstructural observations using X-ray computed tomography. Thereby, we provide a comprehensive view of the mechanical behavior, as well as a further insight into microstructure changes of wet granular materials at very loose states under growing applied external forces. In the present study, we only focus on the properties of wet granular materials in the pendular state.

This thesis is organized in four chapters, as follows:

In Chapter 1, the mechanical behavior of granular materials is briefly described. Several typical experimental and numerical observations of wet granular materials are then presented in details. The combinations of experiments and simulations which have been studied in literature are also presented in order to provide a comprehensive view of wet granular materials.

In Chapter 2, we present two experimental tests on wet spherical beads at very loose states. The behavior is characterized at the macroscopic scale as well as at the grain (and pore) scale, by combining one-dimensional compression tests and X-ray computed tomography.

In Chapter 3, following the 2D model from Gilabert *et al.* [13, 14], we propose a 3D model to investigate the mechanical behavior of wet spherical glass beads at very loose

states under isotropic compression. Three systems, including monodisperse systems without and with rolling and pivoting resistances and a polydisperse system without rolling and pivoting resistances, are simulated. The plastic response of the material, as well as the evolution of microstructure and force transmission, along compression and decompression paths are then characterized. The influence of various micromechanical parameters have also been investigated.

In Chapter 4, we first propose a 3D observation of wet spherical glass beads in an oedometrically compressed model. We then validate the compaction behavior and microstructural changes by comparing the results of experiments and simulations.

Finally, some conclusions and perspectives are drawn.

Literature review

In this chapter, the mechanical behavior of granular materials is briefly described, with a particular focus on wet granular materials. Several non-destructive techniques to observe the micro-macroscopic behavior of such materials are then presented. Numerical investigations, which provide a detailed access to the microstructure of these materials, are then described. A comparison of experimental and numerical results are finally presented.

Contents

1.1	Mechanical behavior of granular materials	7
1.1.1	General considerations	7
1.1.2	Bonded granular materials	10
1.1.3	Wet granular materials	12
1.2	Experimental investigations	15
1.2.1	Techniques	20
1.2.2	Typical observations	22
1.3	Numerical investigations	28
1.3.1	Numerical methods	28
1.3.2	Typical observations	30
1.3.3	Some characteristics of wet granular material in DEM simulation	34
1.4	Experimental investigation versus numerical investigation .	39
1.4.1	Existing studies combining experimental and numerical methods	39
1.4.2	Combination between the XRCT and the DEM	43

1.5 Conclusion	49
---------------------------------	-----------

1.1 Mechanical behavior of granular materials

1.1.1 General considerations

Granular materials are ubiquitous in various fields, and natural or industrial processes including soft matter physics, soil mechanics, powder technology, agronomic transformations, and geological processes. They are composed of individual grains that vary in shape, size, and surface texture. Because of the wide variety of physicochemical and morphological grain properties, the fundamental behavior of granular materials should be investigated under different working environments. The analysis of physical systems involving granular materials requires a clear understanding of their behavior not only at the single particle level, but should also consider multi-physics problems involving multi-scale phenomena from molecular to macroscopic scales. A brief description of granular materials in general is now given.

Satake and Tobita [51] defined granular materials as grains in contact and the surrounding voids. The micromechanical behavior of granular materials is therefore inherently discontinuous and heterogeneous. The macroscopic (overall or averaged) behavior of granular materials is determined not only by how discrete grains are arranged in space, but also by what kinds of interactions are operating among them. In order to understand the mechanical behavior of granular materials from a microscopic point of view, the spatial distribution and orientation of grains and their contact conditions should be first specified.

Lanier [52] described granular materials as an intermediate class of materials between fluids and solids, that not only flow like fluids (snow avalanches, emptying silos, etc.) but also resist to deviatoric stresses (like solids). This type of materials is in the category of complex structured materials, anisotropic, and strongly heterogeneous. Their mechanical behavior depends on the interactions occurring at the particle level. Noteworthy is the fact that this behavior is partially reversible only within a very restricted domain and that it is non-linear.

After Radjaï and Lanier (in Cambou *et al.* [53]), granular materials consist of densely packed solid particles and a pore-filling material which can be a fluid or a solid matrix. The particles interact via elastic repulsion, friction, adhesion and other surface forces. By nature, the length scales involved in these contact interactions are much smaller than the particle size. External loading leads to particle deformations as well as cooperative particle rearrangements. For instance, the particle deformations are of particular importance in powder metallurgy but the particles may be considered as quasi-rigid beyond the elastic deformation.

From a macroscopic scale point of view, the phenomena that make granular materials interesting are pattern formation, mixing or segregation, clustering (granular gases), avalanches, rotating flows, granular convection, and jamming/ unjamming. For example,

if a granular material is heaped on an inclined plane, then the large scale state of the system depends on the angle of the plane. For large angles of this plane, the granular material flows like a non-Newtonian liquid. For small angles of this plane, the granular material will behave like a solid and remain stationary. The critical value of the plane angle delimiting the two regimes (or phases) depends on the preparation history, and on the transition between the phases. The fundamental behavior of granular materials has been widely studied in the literature [54]. The following features have been investigated: (i) quasi-static deformation characteristics of granular materials at both small and large strains, with discrete particles considered in the analysis; (ii) effects of mechanical periodic excitation on a granular medium; (iii) advances in the constitutive modeling of granular materials using a continuum approach; (iv) interactions of particles at elevated temperatures, including adhesion forces and sintering; (v) critical state starting from distinct initial conditions using experiments and computer simulations. In summary, there is a lot of interesting and complex physics to be understood by studying just the large scale properties of granular assemblies. As the composition of the assembly becomes more complicated, its behavior becomes even richer.

From a meso-microscopic scale point of view, Radjaï and Lanier (in Cambou *et al.* [53]) noted that the geometrical changes of granular texture were at the origin of the complex rheology of granular materials. These changes were highly nonlinear, involving creation and loss of contacts, rotation frustration and frictional sliding. They depended on the dissipative nature of contact interactions and steric exclusions among particles. In quasi-static deformation, various features of the plastic behavior such as shear strength and dilatancy could be traced back to the evolution of the granular texture. Therefore, these authors proposed to analyze and distinguish the variables as follows: granular texture, kinematics, and force transmission in granular materials.

The granular texture is disordered with many different variants depending on the composition (particle shapes and sizes), interactions and assembling procedure. The granular texture evolves with loading. The inhomogeneous distribution of contact forces reflects granular disorder in static equilibrium. At the lowest order, the relevant scalar parameters concern the connectivity of this network. At higher orders, the anisotropy of the texture is described by fabric tensors. The granular texture evolves mainly due to contact losses and gains. The fraction of lost and gained contacts depends on the contact orientation. During the deformation process, the gained contacts tend to move in the direction of the major principal stress, conversely, the lost contacts are generally observed in the direction of the minor principal stress [55, 54].

The kinematics are directly linked to the deformation of granular media. In other words, the kinematics are the displacement of particles. Each grain has six degrees of freedom (three components of translation and three components of rotation). As an example, the analysis of the displacement field is shown in Fig. 1.1 [56]. A triaxial compression test was carried out and combined with the X-ray microtomography to get

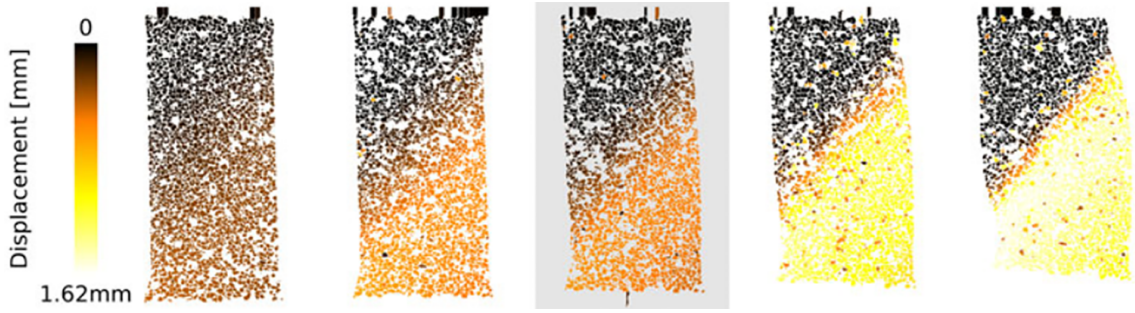


Figure 1.1: Particles displacement (color shows the displacement magnitude) during triaxial compression. Results are shown as vertical slices. Subfigures from left to right correspond to increasing vertical stresses (from Andò *et al.* [56]).

the displacement field within the sample.

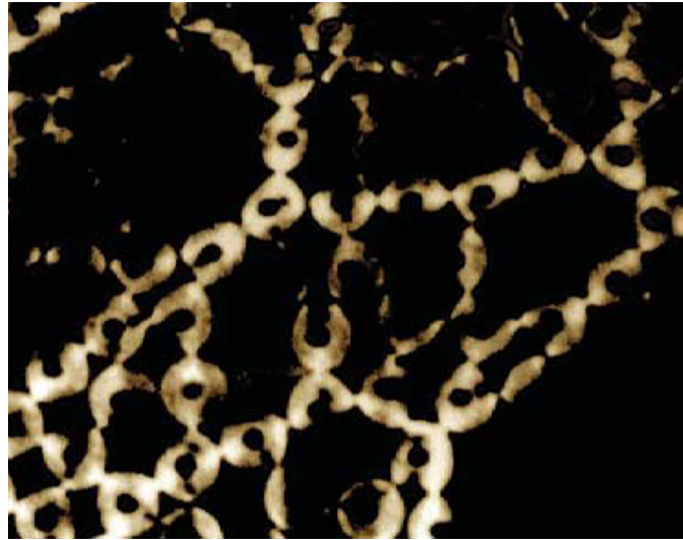


Figure 1.2: Photoelastic image of a small assembly of disks (from Dantu [57]).

The contact forces are considered like the static variable of granular assemblies. These forces appear when the granular materials are subjected to an external load. The contact network and the corresponding contact forces result from the reaction of the granular material to the applied load and the transmission of internal forces. The inhomogeneity of these forces in granular assemblies were first observed optically in assemblies of photoelastic particles, which have the property to develop birefringence upon the application of stresses [57], as shown in Fig. 1.2. This precursory experimental study allowed to observe the load bearing contacts and the establishment of force chains within a granular material. Since then, other studies have tried to use this technique to measure forces in such granular assemblies [58]. However, it is difficult to measure accurately tangential forces experimentally.

Later, numerical simulations enabled to analyze and provide detailed evidence of force chains, the classification of force networks in strong and weak networks, and the exponential distribution of strong forces [59, 60]. Moreover, the force probability density

function from simulation showed that the weak forces (below the average force) in a sheared granular system have a nearly uniform or decreasing power-law shape which is in agreement with experiments [61, 62].

1.1.2 Bonded granular materials

In general, two types of bonding are distinguished in the literature: solid bonding and liquid bonding. While liquid bonding arises from the presence of capillary menisci at the grain contacts, solid bonds between grains may originate from different sources, such as the process of sedimentation in natural soil and rock deposits or the precipitation of a solid, having either a natural or an artificial origin. During sedimentation, cementation is often observed during the early diagenesis process [63]. In the case of solid precipitation, on the one hand, natural cementation takes various forms such as calcite, silica, iron oxides, or even clays [1, 2, 3, 4, 64, 5]. On the other hand, artificial bonded materials are often encountered in applications involving materials improved by mixing with Portland cement or lime.

Despite the complicatedness of the formation of the bonds, the effects of general features of solid bonding on the properties of granular materials were widely observed based on experimental findings: (i) the strength (dynamic and static) and small-strain stiffness are enhanced [65, 66, 67, 68, 69]; (ii) the stress-strain and volumetric response become relatively brittle and more dilative, respectively [67, 70, 71]; and (iii) quasi-preconsolidation pressure or yield stress can be observed in loading path [72, 73]. Furthermore, the mechanical responses of cemented soils are found to depend on the amount and nature of the cementing agent [74]. At the macroscopic scale, cementation induces a strength enhancement and the occurrence of volumetric dilation [36, 37]. In addition, at the grain scale, the contact behavior of bonded materials was also observed by several studies using the idealized granules bonded [75, 76], and the artificially structured bonds [77].

Furthermore, liquid bonds were also observed in several experimental investigations. The effect of capillary bonding on the mechanical behavior of granular materials is of primary importance in powder technology [78, 79, 80] and transformations of geomaterials [81, 82, 83]. The effects of inter-grain cohesion were also observed in order to present a general observation of the mechanical properties of wet granular materials [12, 34]. Finally, the dynamics of wet granular matter were clearly reported in the study by Herminghaus [84].

Besides, bonded granular materials have been extensively investigated using numerical simulations in various contexts, such as: metallic powder processing [6, 85], modeling and treatment of ceramic powders [7, 8, 9]. Assemblies of wet beads were observed [10, 11, 12], in which some microscopic observations are possible by combining numerical and experimental tests [11, 12]. A 2D numerical investigation into the microstruc-

ture and mechanical properties of cohesive powders was carried out [13, 14]. Furthermore, the micro-macroscopic behavior of granular materials containing artificial solid bridges, especially cemented sands, was extensively investigated [36, 37, 40, 41, 86, 42, 87, 88].

In addition, the effects of liquid bonds on the mechanical behavior of granular matter have been extensively studied in the past, and several models of capillary cohesion have been proposed [89, 90, 91]. The contribution of capillary bridges to the micro-macroscopic mechanical behavior has been investigated by means of numerical simulations [92, 24, 46, 93, 94, 95, 29, 47].

The most relevant known features of bonded granular materials at the macroscale are the yield criterion, the stress-strain response, the critical state, the influence of cohesion, etc. Here, we present the influence of intergranular cohesion on the overall behavior.

Macroscopic influence of cohesion

A non-null cohesion in the Mohr-Coulomb failure criterion has an important consequence since it introduces a stress scale in the behavior of the material. While non-cohesive materials are essentially sensitive to ratios of stress components, cohesive ones respond differently according to the absolute magnitude of stresses. This is quite remarkable when dealing with compression tests in which all stress ratios remain constant. During an oedometric compression test, the vertical stress σ_1 increases, while the radial strain is maintained null. Hence, the stresses are also observed to correspond to coefficient of lateral stress ratio σ_3/σ_1 . In addition, it is well recognized that the density of non-cohesive materials is slightly evolve with growing stresses, while cohesive ones undergo some irreversible compression under growing average pressure \mathcal{P} . In soil mechanics [2], the irreversible compression curves are usually described using a linear relationship between the void ratio e (i.e. $e = -1 + 1/\Phi$ with $\Phi = 1 - n$, Φ is the solid fraction and n is the porosity) and the logarithm of \mathcal{P} :

$$e = e_0 - C_c \log \left(\frac{\mathcal{P}}{\mathcal{P}_0} \right), \quad (1.1)$$

in which, e_0 and \mathcal{P}_0 are the initial void ratio and initial pressure, respectively. This relation applies to cohesive materials such as clays and silts [1, 5] and also to cohesive powders with rather wide intervals of void ratio (e varying normally by a factor of 2). It was also applied to critical states, characterized by a specific value of the stress ratio σ_3/σ_1 , and the compaction curve is often modeled with the same slope C_c (called the compression index). Relation (1.1) only applies for the monotonically growing pressures. The irreversibility of the plastic compression phenomenon implies that it does not apply to pressure values lower than the highest pressure reached in the past, namely the *pre-consolidation pressure*. The reports on bonded materials are similar but the change of density is considerably lower.

1.1.3 Wet granular materials

The mechanical properties of granular materials are remarkably affected when a small amount of water is added. For instance, a wet sand can be sculptured into quite stable structures, for instance a sand castle, while this is impossible when it is dry. However, this phenomenon significantly depends on the size of particles, as shown in Fig. 1.3 (van der Waals attraction is computed for an inter-particle separation of 30 Å, the skeletal force is shown for $\sigma' = 10$ kPa and $\sigma' = 1$ MPa) [96]. These compressive forces mobilize the electrical repulsion forces and bring particles together until compression and repulsion are balanced. Changing the pore fluid can alter the inter-particle distance at equilibrium; the upper part of the figure shows the strain caused by changing the pore fluid from fresh-water to seawater concentrations.

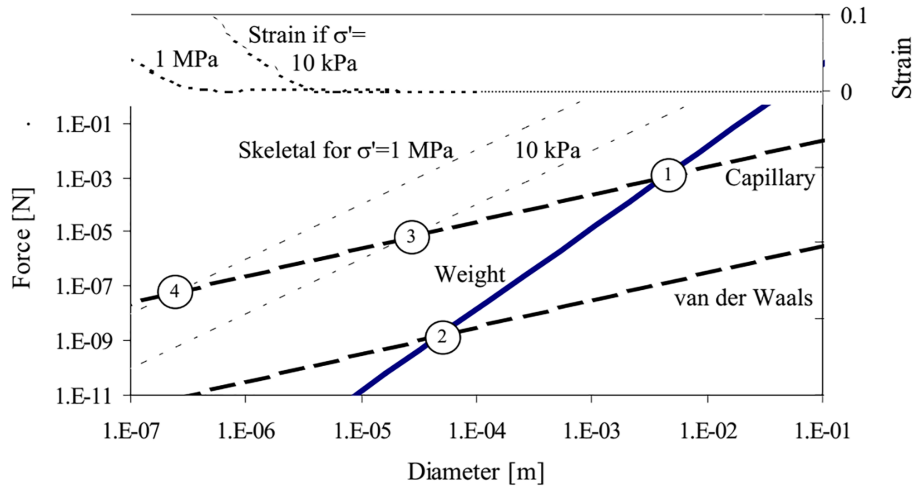


Figure 1.3: Skeletal versus contact-level capillary and electrical forces. The upper part of the figure shows the strain (axis on right) caused by changing the pore fluid ionic concentration from fresh-water to seawater conditions. Note slopes: skeletal 2:1, weight 3:1, capillary and van der Waals 1:1 (from Santamarina [96]).

Here, several observations can be made as follows (from Santamarina [96]):

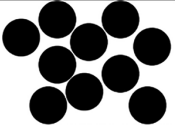
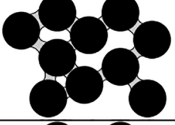
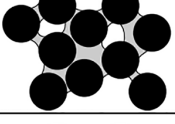
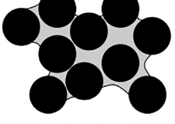
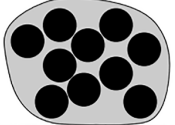
- Particle weight loses relevance with respect to capillary forces for particles smaller than $d \approx 3$ mm (point 1), and with respect to van der Waals attraction for particles smaller than $d \approx 30$ μm (point 2).
- Capillary forces can exceed the contribution of $\sigma' = 10$ kPa confinement for particles smaller than $d \approx 20$ μm (point 3) and the contribution of $\sigma' = 1$ MPa for $d < 0.2$ μm (point 4).
- Particles are considered “coarse” when skeletal forces due to boundary loads prevail. This is the case for particles larger than $d \approx 20$ μm (point 3).

- Particles are “fine” when contact-level capillary and electrical forces gain relevance. This is the case when particles are smaller than $d \approx 1 - 10 \mu\text{m}$.

Therefore, we can see that the smaller the particle size, the stronger the capillary forces. Even the moisture in the atmosphere may create tiny liquid bridges at the contact point between particles. The presence of these liquid bridges induces capillary forces that attract the particles to each other. In reality, because of the asperities on the particles surfaces, molecular interactions scale down to small adhesive forces, and capillary forces can be large and dominant.

Unlike in the nanoscale range of adhesive forces, they can apply from an interparticle distance of the order of the particle size. Such unique properties of capillary interactions lead to remarkable changes in mechanical properties of granular materials in the appearance of the liquid in their interstitial spaces. Therefore, the presence of liquid menisci plays a key role in the overall mechanical properties of wet granular materials. Based on the liquid content, wet granular materials can be classified in different regimes [97, 79, 34], as given in Table. 1.1.

Table 1.1: Schematic diagrams for classification of wet granular materials with various amount of liquid. In the third column, the black circles represent the grains and the grey regions represent the interstitial liquid (from Mitarai and Nori [34]).

Liquid content	State	Schematic diagram	Physical description
No	Dry		Cohesion between grains is negligible.
Small	Pendular		Liquid bridges are formed at the contact points of grains. Cohesive forces act through the liquid bridges.
Middle	Funicular		Liquid bridges around the contact points and liquid-filled pores coexist. Both give rise to cohesion between particles.
Almost saturated	Capillary		Almost all the pores are filled with the liquid, but the liquid surface forms menisci and the liquid pressure is lower than the air pressure. This suction results in a cohesive interaction between particles.
More	Slurry		The liquid pressure is equal to, or higher than, the air pressure. No cohesive interaction appears between particles.

- **Pendular state:** When a small amount of liquid is added to the granular material, the liquid initially collect near the contact point of particles. In this regime, the

liquid content is limited to the domain where menisci can form without coalescence; in this domain, the capillary forces are limited to pair-wise interactions.

- **Funicular state:** As the liquid content is increased further, the neighbor liquid bridges start to coalesce. The liquid fills some pores and multiple grains can be in contact with a given volume of liquid.
- **Capillary state:** At higher values of liquid content most of the pores fills with liquid and large contiguous wet clusters forms.
- **Slurry state:** In this regime all the pore space are fully saturated and the particles are completely immersed in the liquid.

In the first three regimes, the role of capillary force is very important while it is negligible in the slurry state.

Many numerical and experimental studies reported that the presence of a small amount of interstitial liquid strongly affects the yield stress of the materials. The effects of the presence of water on the apparent Coulomb cohesion was widely studied in the literature. Richefeu *et al.* [24] studied the Coulomb cohesion in pendular state for different values of liquid content by using both numerical and experimental observations. They observed that the Coulomb cohesion increases nonlinearly with liquid content and saturates to a maximum value, $c_m \simeq 600$ Pa at $w_m \simeq 0.03$. They found a constant value of friction angle φ ($=\tan^{-1}\mu$), regardless the level of liquid content.

In soil mechanics, Terzaghi [98] proposed the concept of *effective stress* to describe the mechanical properties of water-saturated soils. Terzaghi's principle states that “*all measurable effects of a change of stress of the soil, that is compression, distortion and change of shearing resistance, are exclusively due to changes in effective stress*” [99]. Effective stress σ'_{ij} is defined as

$$\sigma'_{ij} = \sigma_{ij} - u_w \delta_{ij}, \quad (1.2)$$

with u_w is the pore water pressure and the Kronecker's delta δ_{ij} : $\delta_{ii} = 1$, $\delta_{i \neq j} = 0$.

In the early works of Bishop [100], this principle was extended to unsaturated soils, as:

$$\sigma'_{ij} = (\sigma_{ij} - u_a \delta_{ij}) + \chi(u_a - u_w) \delta_{ij}, \quad (1.3)$$

where χ is called the effective stress parameter or Bishop's parameter, vary from 0 for dry soils to 1 for saturated soils, and u_a is the pore air pressure. The terms $\sigma_{ij} - u_a \delta_{ij} = \sigma_{net-ij}$ and $u_a - u_w = s$, define the net stress and the matric suction, respectively. Independently of the stress state, the capillary forces are assumed to react in an isotropic way, generating the same pressure in all directions. However, Scholtès *et al.* reported on their recent studies [93, 94] that this assumption is not valid. These authors performed numerical simulations of the triaxial compression of unsaturated granular materials. They assumed

that the components of the stress tensor includes two terms: the contributions of contact forces σ_{ij}^c (effective stress), and an isotropic stress due to capillary interactions σ_{ij}^{cap} , assuming an isotropic distribution of liquid bridges in the material. The additive effect of capillary forces in stress tensor is verified for an initial isotropic configuration, although deformation creates a slight anisotropy in liquid bridge distribution. Therefore, the contribution of capillary forces to the total stress is not an isotropic pressure, which is not consistent with the Bishop form of the effective stress, or any expression ignoring the deviatoric effect of the forces in liquid bridges.

Moreover, at the microscopic level, the influence of liquid bridges on the tensile strength of unsaturated granular materials was observed in the pendular state by Kim & Hwang [92] and Gröger *et al.* [11]. They numerically studied the tensile strength under isotropic pressure. Kim and Hwang [92] measured the actual magnitude of tensile strength induced by water in moist granular soils with low water contents ($w < 4\%$). They found that the magnitudes of the measured tensile strength are significantly different from zero. The tensile strength generally increases with increasing water content and relative density. They also proposed a model to estimate approximately the tensile strength of an unsaturated granular material. Gröger *et al.* [11] reported that there was a large influence of the surface roughness on the tensile stresses in wet particle systems. By means of simulated tensile tests, they have shown that even when the tensile strength is reached, elastic body contacts supporting the external tensile load still exist. They also simulated shear tests to compare with tensile test simulations and concluded that for a small tensile load, the yield locus appeared to be the straight extension of the graphs for positive loads [11].

In addition, Gilabert *et al.* [13] reported the influences of assembling procedure of model cohesive powders under low pressure. They also studied the plastic compression, structural changes of this materials under isotropic loads with the same value of tensile strength between grains [14]. Under low pressure, the tensile strength plays a key role to stabilize the loose structures. Moreover, in recent study of Delenne *et al.* [45], they numerically investigated the process of growth and coalescence of liquid clusters in a granular material as the amount of liquid increases under the isotropic compaction. The most important finding of their work is that a peak grain pressure induced by capillary forces in a granular packing occurs inside the funicular state. It presents the transition from a primary coalescence process, where the volume of the largest cluster remains small, to a secondary coalescence process governed by the increase of liquid cluster volumes carrying a larger capillary stress [45].

1.2 Experimental investigations

Aside from the conventional destructive techniques (e.g. shear box, one-dimensional compression test, biaxial compression test, triaxial compression test, etc.), more and

more non-destructive methods have been widely applied to observe effectively the properties of granular materials, from macro- to microscopic level. In order to have a general view of non-destructive techniques, we present here a sketchy history of some recent advanced techniques (type of imaging techniques) and its applications to granular materials research, as given in Table 1.2 (following from Al-Raoush & Willson [101]). These typical studies were carried out over the last thirty years (from 1982 to 2016). The techniques are briefly presented and their application will be clearly illustrated in the following sections.

Table 1.2: Examples of imaging techniques to porous media systems

Measured properties	Material	System	Resolution	Reference
Soil bulk density	Soil, glass beads	X-ray scanner	*	Petrovic <i>et al.</i> [102]
Water content variations	Sandy and fine sandy loam	X-ray computed tomography	*	Crestana <i>et al.</i> [103]
Water content and soil bulk /density	Fine sandy loam	X-ray miniscanner	*	Crestana <i>et al.</i> [104]
Volume fractions	Bera sandstone	X-ray computed tomography	*	Vinegar and Wellington [105]
Fractures, mud invasion, and lithologic characterization	Natural soil	X-ray computed tomography	*	Hunt <i>et al.</i> [106]
Air-filled porosity and pore size distribution	Natural soil	X-ray computed tomography	*	Warner <i>et al.</i> [107]
Variation in water content	Natural soil	X-ray computed tomography	*	Cassel <i>et al.</i> [108]
Topology and connectivity	Fontainebleau sandstone	Synchrotron computed tomography	10 μm	Spanne <i>et al.</i> [109]
Porosity, volume fractions, and specific surface area	Random soil samples	Photoluminescence volumetric imaging	1 μm	Montemagno and Gray [110]
Porosity, volume fractions, permeability and connectivity	Fontainebleau sandstone	X-ray computed tomography	7.5 μm	Auzerais <i>et al.</i> [111]
Porosity, specific surface area and pore size distribution	Fontainebleau sandstone	Synchrotron tomography	7.5 μm	Coker <i>et al.</i> [112]

Porosity, tortuosity, connectivity and specific surface area	Bera sandstone, glass bead	X-ray computed tomography	5 μm	Lindquist <i>et al.</i> [113]
Pore size distribution, coordination, and specific surface area	Uniform glass beads	Magnetic Resonance Imaging	*	Baldwin <i>et al.</i> [114]
Pore size distribution	Glass filter system	Magnetic Resonance Imaging	*	Pauli <i>et al.</i> [115]
Porosity	Rock samples	X-ray computed tomography with mercury porosimetry	400 μm	Klobes <i>et al.</i> [116]
Visualization of fluid transport through the sample	Sandy sediment soil	Positron emission tomography	*	Khalili <i>et al.</i> [117]
Porosity and water content	Sandstone	Synchrotron tomography	30 μm	Coles <i>et al.</i> [118]
Porosity and volume fractions	Dolomite	Gamma-ray computed tomography	*	Hsieh <i>et al.</i> [119]
Volume fractions	Glass beads	X-ray computed tomography	*	Clausnitzer and Hopmans [120]
Geometrical analysis	Fontainebleau sandstone	Synchrotron tomography	6 μm	Lindquist and Venkatarangan [121]
Porosity, permeability, and specific surface area	Silty and clayey quartz	Scanning electron microscopy	1.6 μm	Solymer and Fabricius [122]
Critical angle of sandpiles	Spherical glass beads	Electron and fluorescence microscopy	*	Mason <i>et al.</i> [33]
Soil structure	FEBEX bentonite	ESEM and mercury porosimetry	50 μm	Musso <i>et al.</i> [123]
Microstructural change during sintering	Metal powder	X-ray microtomography	2.5 μm	Lame <i>et al.</i> [124]

Liquid bridge coordination numbers and liquid bridge volumes	Glass beads	Fluorescence microscopy	*	Kohonen <i>et al.</i> [125]
Localized deformation	Sedimentary soil	X-ray microtomography	14 μm	Viggiani <i>et al.</i> [126]
Agglomerate breakage	PVA, NaCl and Silica glass	X-ray microtomography	4.555 & 3.904 μm	Golchert <i>et al.</i> [49]
3D particle shape characterization	Various	X-ray microtomography	Various	Lin and Miller [127]
Microstructure characterization	Acrylic beads	X-ray computed tomography	0.03 mm	Aste <i>et al.</i> [128]
Network of capillary forces	Glass beads	Fluorescence microscopy	*	Fournier <i>et al.</i> [12]
Localized deformation	Hostun sand	X-ray microtomography and V-DIC	14 μm	Hall <i>et al.</i> [129]
Localized deformation at grain-scale	Hostun and Caicos Ooid sands	X-ray microtomography, ID-Track** and DIC	15 μm	Andò <i>et al.</i> [56]
Water menisci at different relative humidities	Spherical spheres, sand, clay	ESEM	*	Lourenço <i>et al.</i> [130]
Capillary collapse	Hostun sand	X-ray computed tomography	50 & 25 μm	Bruchon <i>et al.</i> [35]
Strain localisation and grain breakage	Hostun and Ottawa sands	X-ray tomography	15.6 μm	Alikarami <i>et al.</i> [131]
Particle breakage	Sand and granite	X-ray microtomography	3.3 μm	Zhao <i>et al.</i> [132]
Grain-scale behavior	Caicos Ooid sand	X-ray computed tomography	15.56 μm	Lim <i>et al.</i> [133]

* Resolution is of the order of mm or not provided by the author. Abbreviation: PVA, polyvinyl alcohol; ESEM, Environmental Scanning Electron Microscopy; DIC, Digital Image Correlation; V-DIC, Volumetric Digital Image Correlation; ** Method named by the author.

1.2.1 Techniques

Among the techniques listed in Table 1.2, three techniques have been extensively applied to observe the wet granular materials, such as the Fluorescence Microscopy (FM), the Environmental Scanning Electron Microscopy (ESEM), and the X-ray Computed Tomography (XRCT).

A Fluorescence Microscopy is an optical microscope that uses fluorescence and phosphorescence instead of, or in addition to, reflection and absorption to study properties of organic or inorganic substances. The FM refers to any microscope that uses fluorescence to generate an image, whether it is a simpler set up like an epifluorescence microscope, or a more complicated design such as a confocal microscope, which uses optical sectioning to get better resolution of the fluorescent image. However, in the FM, fluorophores lose their ability to fluoresce as they are illuminated in a process called photobleaching. Photobleaching occurs as the fluorescent molecules accumulate chemical damage from the electrons excited during fluorescence. Photobleaching can severely limit the time over which a sample can be observed by fluorescent microscopy. Besides, the specimen must be fluorescent to be suitable for fluorescence microscopy and FM is also limited to 2D observations.

One of the newer and most promising qualitative methods for studying, and, where possible, quantifying the arrangements of aggregations/particles and voids in unsaturated soils is the ESEM. ESEM is a special type of scanning electron microscope that works under controlled environmental conditions and requires no conductive coating on the specimen. This makes it possible to examine wet samples and to preserve their natural characteristics for further testing, which is an obvious advantage of ESEM compared to the conventional SEM. This method enables to observe the surface of moist materials without pre-treatment, at dimensions from millimeters to micrometers. Nevertheless, when saturated samples are observed, the presence of a water film covering the solid grains makes image analysis difficult to carry out, so that little information about the sample can be collected.

Getting more and more success over recent years, XRCT is a nondestructive technique for visualizing interior features within solid objects, and for obtaining digital information on their three-dimensional geometries and properties. A XRCT image is typically called a slice, as it corresponds to what the object being scanned would look like if it were sliced open along a plane. An even better analogy is a slice from a loaf of bread, because just as a slice of bread has a thickness, a XRCT slice corresponds to a certain thickness of the object being scanned. So, while a typical digital image is composed of pixels (picture elements), a XRCT slice image is composed of voxels (volume elements). Taking the analogy one step further, just as a loaf of bread can be reconstituted by stacking all of its slices, a complete volumetric representation of an object is obtained by acquiring a contiguous set of XRCT slices.

The gray levels in a XRCT slice image correspond to X-ray attenuation, which reflects the proportion of X-rays scattered or absorbed as they pass through each voxel. X-ray attenuation is primarily a function of X-ray energy and the density and composition of the material being imaged.

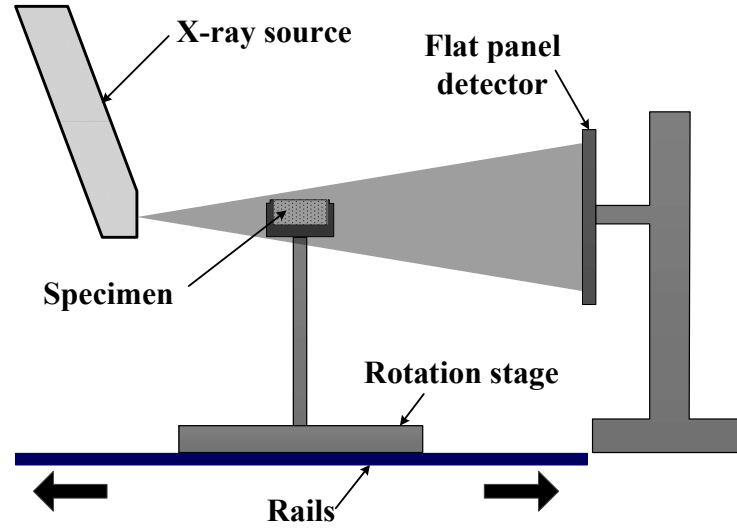


Figure 1.4: Schematic view of a laboratory XRCT scanner

A schematic view of a XRCT system is shown in Fig. 1.4. The elements of an X-ray computed tomography scanner comprise an X-ray source, a detector that measures X-ray intensity along multiple beam paths, and a rotating stage supporting the object being imaged. Different configurations of these components can be used to create XRCT scanners optimized for imaging objects of various sizes and compositions.

The great majority of XRCT systems use X-ray tubes, although tomography can also be done using a synchrotron or gamma-ray emitter as a monochromatic X-ray source. Important tube characteristics are the target material and peak X-ray energy, which determine the X-ray spectrum that is generated; current, which determines X-ray intensity; and the focal spot size, which impacts the spatial resolution of the tomography.

Most XRCT detectors utilize scintillators. Important parameters are scintillator material, size and geometry, and the means by which scintillation events are detected and counted. In general, smaller detectors provide better image resolution, but reduced count rates because of their reduced area compared to larger ones. To compensate, longer acquisition times are used to reduce the signal to noise ratio. Common scintillation materials are cesium iodide, gadolinium oxysulfide, and sodium metatungstate.

The diagram in Fig. 1.4 illustrates the cone-beam configuration for laboratory XRCT scanners. In cone-beam scanning, the linear array is replaced by a planar detector, and the beam is no longer collimated. Data for an entire object, or a considerable thickness of it, can be acquired in a single rotation. The data are reconstructed into images using a cone-beam algorithm. Besides, planar-beam and parallel-beam configurations are also

the most common configurations for CT scanners. Further details of the equipment and applications can be found in Banhart [134], and Hsied [135].

However, as the resolution is limited to about 1000-2000 voxels along the object cross-sectional diameter, high resolution requires small objects. Finite resolution causes some blurring of material boundaries. The calibration of gray levels to attenuation coefficients is complicated by the presence of polychromatic X-rays. For the large (decimeter) scale, geological specimens cannot be penetrated by low-energy X-rays, reducing resolving capability. Not all features have sufficiently large attenuation contrasts for useful imaging (e.g. carbonate fossils in carbonate matrix, quartz versus plagioclase...). Image artefacts (beam hardening) can complicate data acquisition and interpretation. Large data volumes (in the order of a few gigabytes) can require considerable computer resources for visualization and analysis.

1.2.2 Typical observations

One of the most popular and basic method to observe the plasticity of granular materials is the standard one-dimensional compression test. Here, an example of the one-dimensional compression test, performed in 1990 by Golightly [136], to analyze the yielding and plastic hardening of carbonate and silica sands, is shown in Fig. 1.5. At low stresses (region 1), the behavior is quasi-elastic, beyond yield (region 2), an approximately linear normal compression line emerges.

We present here typical studies using the XRCT to investigate the mechanical properties of wet granular material, from macroscopic to microscopic level.

Several authors reported on the liquid capillary bridges between grains and their effects on the mechanical behavior of wet granular materials [33, 125, 12]. The specimens were prepared in the pendular state (with very small water content, $< 1\%$) by using the random loose/ dense packing method. An example of the liquid bridges between grains was clearly observed in Fig. 1.6 by using the Fluorescence Microscope by Fournier *et al.* [12]. The average number of bridges per bead was then obtained by zooming with the microscope through the sample and counting the bridges. Besides, they also described experiments on the dynamic deformation of a wet granular material, which reveal a type of shear-thinning behavior that they attributed to the shear-rate dependence of liquid bridge volumes.

More recently, ESEM has been used to observe wet granular materials [137, 138, 123, 139, 130]. This method allows observing water inside the materials. An example [130] of the use of this method to show clearly the water menisci at contacts of sand grains, is illustrated in Fig. 1.7. Fig. 1.7(a) shows predominantly concave menisci (corresponding to tensile capillary pressure) and Fig. 1.7(b) shows predominantly convex menisci (corresponding to compressive capillary water pressure). Lourenço *et al.* [130] observed the curvature of water menisci in both idealized and natural granular materials with vari-

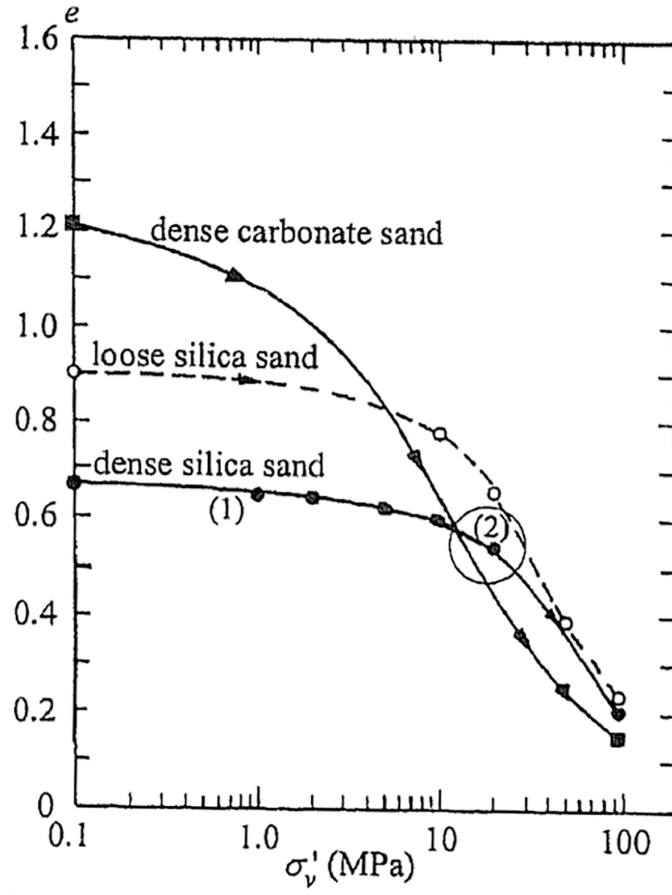


Figure 1.5: One-dimensional compression plots for carbonate and silica sands (from Golightly [136]).

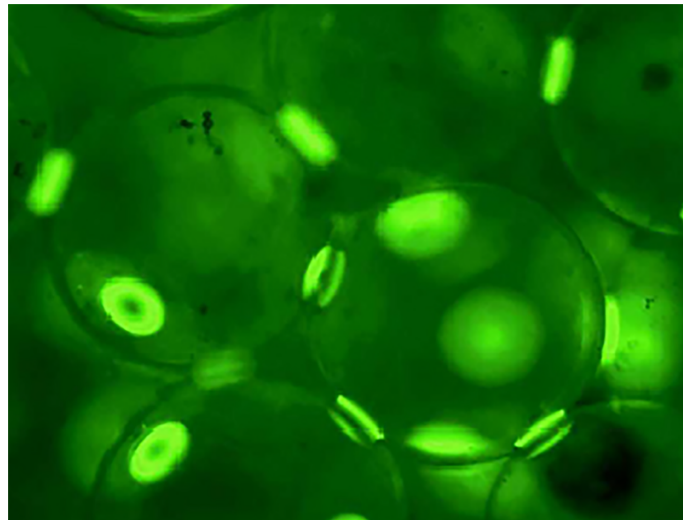


Figure 1.6: Capillary bridges in glass beads (from Fournier *et al.* [12])

able particle sizes, shapes and nature. They found that the curvature could vary along the border of a single meniscus or differ from one point to another separated at the micrometer scale, and that it is also dependent on the nature of materials and wetting

history. They confirm the importance of surface tension in the air/water interfaces (or “contractile skin”) in holding particles together.

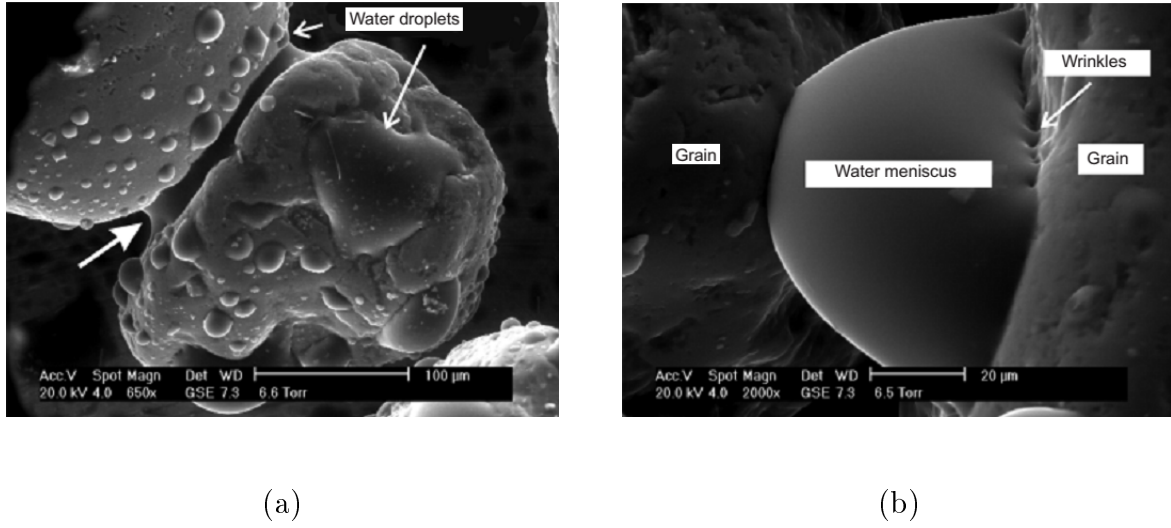


Figure 1.7: Water menisci form at contacts of sand grains (from Lourenço *et al.* [130]): (a) concave menisci; (b) convex menisci.

Maeda *et al.* [138] also studied the formation and disappearance of liquid bridges between two surfaces of grains. They reported the slow evaporation and rupture of liquid bridges relatively to low vapor pressure. They also studied the mechanical (as opposed to the thermodynamic) stability of liquid bridges. These results shown clearly the importance of adhesion between surfaces in the presence of liquid bridges. For example, the rupture distance of such bridges is an important parameter in describing the dynamic mechanical properties of moist granular materials. This problem was reported in Ref. [140] and then confirmed by Seville *et al.* [141].

Early study performed by Crestana *et al.* [103], in 1985, used the XRCT to measure the water content of soil. They also showed that the XRCT can be applied to measure and follow dynamically the motion of water in soil in three dimensions. An example using the third-generation of the XRCT for spatial and real-time (dynamic) measurement is shown in Fig. 1.8. It is seen that in the region of interest (ROI) box 1 the water content quickly became constant; in ROI box 2, heterogeneities can be seen from the XRCT scan, but the average water content increases with time and attains a smaller average value. In ROI 3, there is a continuous increase in water content with a more drastic relative change. Finally, in ROI 4 where the water had not yet arrived, there was no change in attenuation [103].

Up to now, XRCT has become a widely used technique and is appropriate for numerous types of materials including particulate and porous materials [124, 142]. Moreover, this technique has been widely used in several studies to investigate wet granular materials [143, 144, 145, 146, 147, 35]. Figure 1.9 shows an example of XRCT scans of Hostun

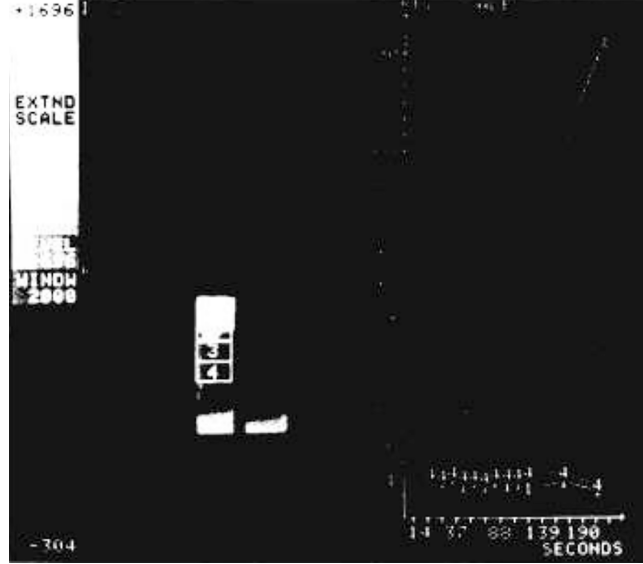


Figure 1.8: The differences of water content for different regions 1, 2, 3, and 4 as a function of time (from Crestana *et al.* [103]).

sand [148]. Bruchon *et al.* [35] characterized in 3D the capillary collapse phenomenon during water infiltration into a loose unsaturated sand. They used the volumetric digital image correlation tool to assess the volume of water-filled pores and deformation of the granular skeleton.

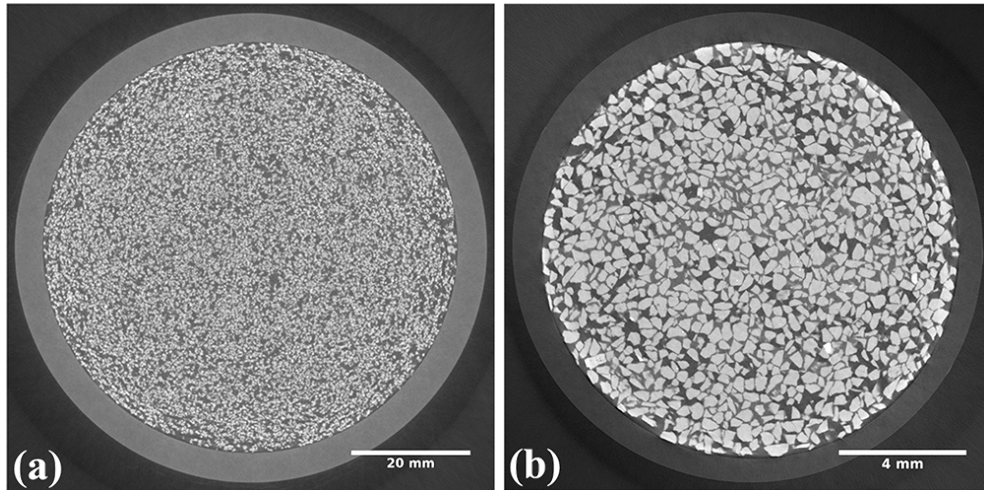


Figure 1.9: An example of XRCT scans of Hostun sand, with D is the diameter of cell and r is the resolution of image: (a) $D=70$ mm, $r=50$ μ m, (b) $D=13$ mm, $r=10$ μ m (from Bruchon [148])

Wildenschild *et al.* [143] also used this technique to characterize phase distribution and pore geometry for partially saturated media. They obtained qualitative and quantitative results with different scanning systems and sample sizes. Furthermore, Wildenschild and Sheppard [147] used this technique for quantifying the pore-scale structure

and processes in subsurface porous medium systems. A pore-network reconstruction is shown in Fig. 1.10, illustrating the results of applying watershed partitioning and region merging on the pore and grain space of an unconsolidated sand. However, this method reveals a major weakness which is the use of spherical structure elements that breaks down when the grain shapes are very oblate or prolate [147].

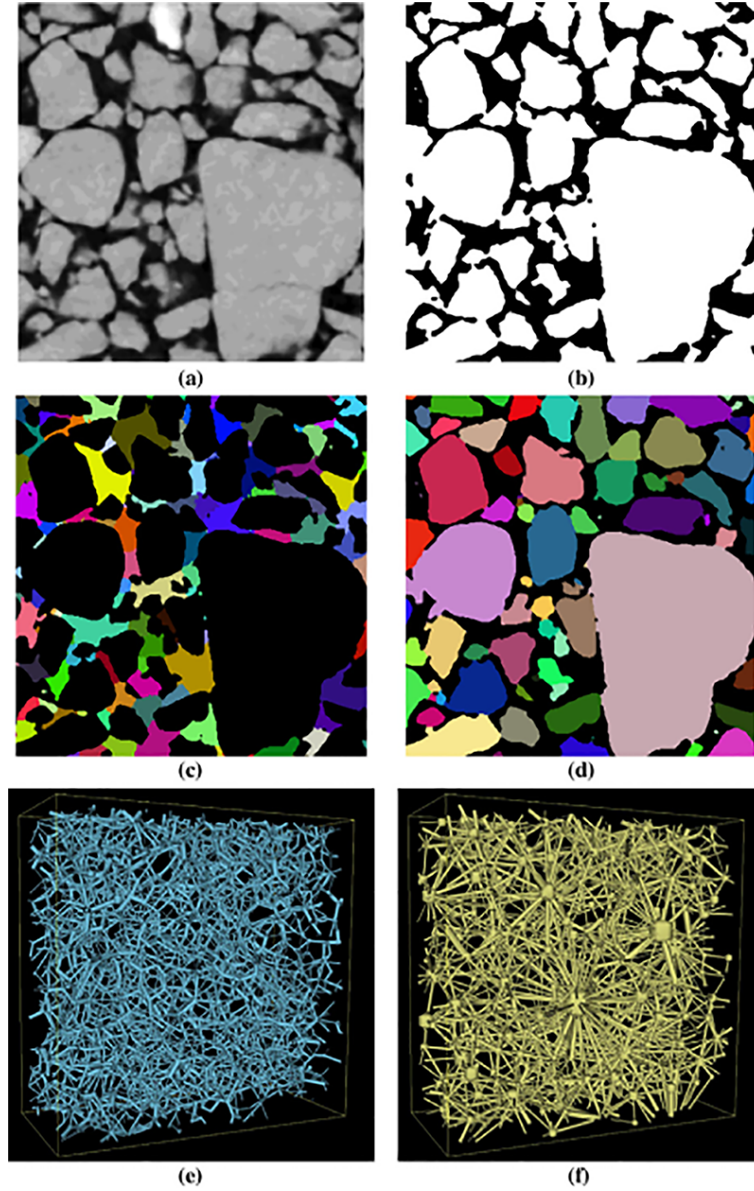


Figure 1.10: Examples of partitioning and subsequent ball-and-stick network construction, applied to an unconsolidated sand imaged at $2.8 \mu\text{m}$. (a) Zoom into slice from original image, (b) segmented image, (c) partition of the pore space using watershed transform, (d) partition of the grain space, (e) equivalent pore-network of 3D region surrounding the 2D slice, and (f) equivalent grain network (from Wildenschild and Sheppard [147]).

Farber *et al.* [144] studied the porosity, pore size distribution, and geometric structure of pores in granulates by using different conditions and materials. In addition, the mor-

phological information such as pore shape, spatial distribution, and connectivity were also observed by combining with mercury porosimetry. Kim *et al.* [145] reported the effect of particle morphology on water distribution in partially saturated granular porous media. They also investigated the influence of water content in order to evaluate the water phase-distribution spatially for compacted sand specimens in a aluminum cylinder. Riedel *et al.* [146] characterized experimentally the link between partial water saturation and suction in a sand sample at the micro scale. Four different levels of imposed suction of a sample (with Hostun sand) obtained from trinarised 3D images, as shown in Fig. 1.11 [146]. The vertical location of the slices is chosen to best highlight different water retention states. The two slices on the top row show liquid phase continuity for both saturations. At higher suction, the pendular domain is reached in some parts of the sample (in bottom left of Fig. 1.11), complete continuity of the liquid phase is lost, with liquid bridges between the grains. At bottom right of Fig. 1.11, the hygroscopic domain with only adsorbed water on the surface of the grains. The hygroscopic domain was also observed in some regions of the sample [146].

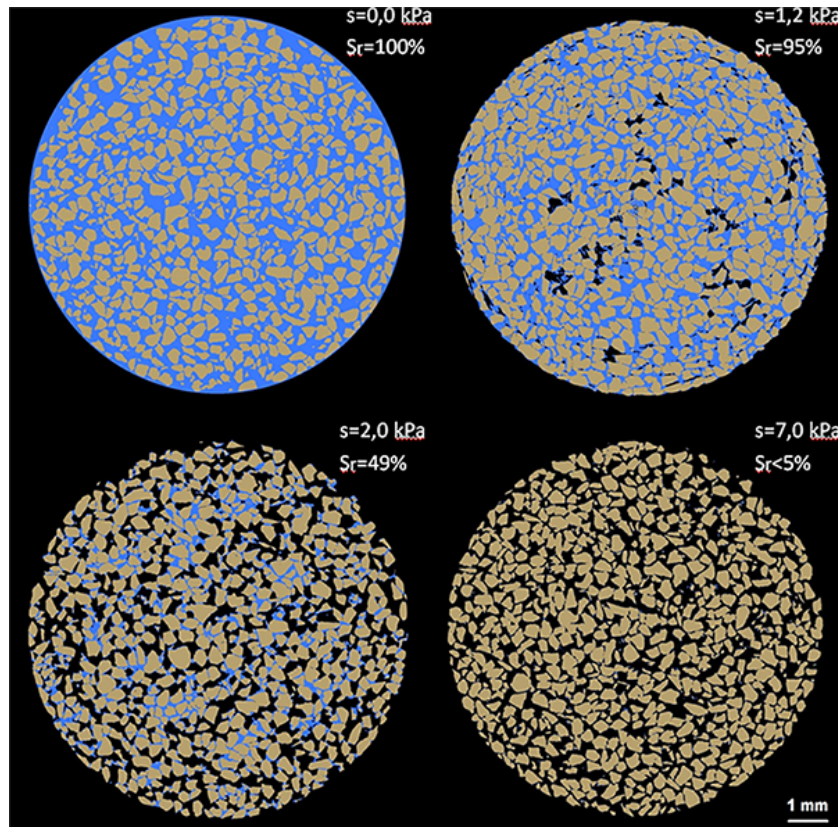


Figure 1.11: Four different domains (fully saturated, funicular, pendular and hygroscopic) shown in slices from trinarised 3D images of Hostun sand; water in light blue, air in black and solid in light brown. The degrees of saturation noted are global (from Riedel *et al.* [146]).

In a more recent study, Menon *et al.* [149] used XRCT combined with numerical sim-

ulation, to quantify the impact of compaction on macroaggregates, mainly on the pore size distribution and water flow. The impact of compaction on interpores and intrapores is presented in the proportion of inter- and intrapores, as shown in Fig. 1.12. Note that interpores or inter-aggregate pores, are the pores between soil aggregates; intrapores or intra-aggregates pores, are within soil aggregates (within the solid matrix of soil aggregates). Interpores dominated the total pores volume in comparison to the intrapores, representing $> 90\%$ of the total pore volume before compaction in pre-compacted samples. However, after compaction, there was an increase in intrapores proportion in all cases. In addition, the total surface area of interpores and intrapores were also calculated. They concluded that in all cases, the decrease in interpores proportion produced a corresponding increase in intrapores fraction [149]. Moreover, the size distribution of interpores volumes (i.e. volume of individual interpore) before and after compaction was also reported. They showed that the soil compaction and moisture content increased the total number of individual (very small) interpores ($< 0.001 \text{ mm}^3$) although the total volume of interpores decreased sharply [149].

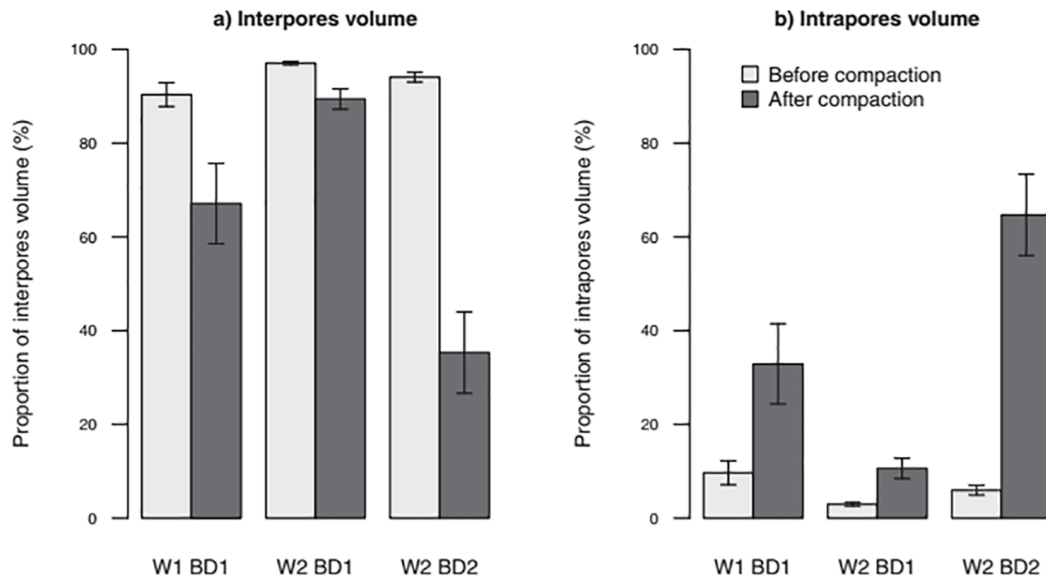


Figure 1.12: Effect of soil compaction on interpores (a) and intrapores (b) volumes from soil aggregates with varying levels of soil moisture and compaction. Note: W1 refers to moisture content of 9.3 %, W2 represents 18.3 %; BD1 and BD2 refer to bulk density increment of 0.28 and 0.71 g.cm^{-3} , respectively (from Menon *et al.* [149]).

1.3 Numerical investigations

1.3.1 Numerical methods

Over the last decades of the last century, numerical simulations were introduced to study granular materials. Since then, numerical methods have become a valuable tool to in-

investigate the mechanical behavior of granular systems. There were a lot of numerical methods for analysis of granular and porous materials such as: Smoothed Particles Hydrodynamic (SPH), Particle Finite Element Method (PFEM), Material Point Method (MPM), Lattice Boltzmann Method (LBM), Random Walk Simulation (RWS), Molecular Dynamics (MD), and Discrete (Distinct) Element Method (DEM). In general, these methods have been widely used to investigate the macroscopic properties as well as the internal states of granular systems. In other words, these methods allow to investigate the behavior of granular systems from the macroscale to the microscale (and even the nanoscale); this is hardly made possible by using experimental methods.

The most common computer simulation method used to determine fluid flow and analyze transport properties through porous media is the LBM [150, 151]. LBM may be regarded as a digital method equivalent to the traditional Computational Fluid Dynamics. Several authors used the LBM to investigate fluid flow and permeability in porous materials [118, 152, 153, 154, 155, 156]. The permeability and tortuosity of porous materials were also studied by the RWS [157, 158]. SPH is a meshless Lagrangian computational technique that was introduced in the astrophysics community to simulate the movement of masses of material in an unbounded three-dimensional space [159, 160, 161, 162, 163]. SPH is used to obtain approximate numerical solutions of the equations of fluid dynamics by replacing the fluid by a set of particles. MPM, known as the particle-in-cell method, combines the strengths of Eulerian and Lagrangian descriptions of the material. The Lagrangian description is provided by discretizing each body by a collection of material points, and the Eulerian description is based on a background computational mesh. The MPM extends these capabilities to materials modeling [164, 165, 166, 167]. PFEM uses a Lagrangian description to model the motion of nodes (particles) in both the fluid and the structure domains. Nodes are thus viewed as particles which can freely move and even separate from the main analysis domain representing, for instance, the effect of water drops. A mesh connects the nodes defining the discretized domain where the governing equations, expressed in an integral form, are solved as in the standard Finite Element Method (FEM) [168, 169].

The most popular computer simulation methods used to calculate the contact and the displacement of particles in granular materials is the “discrete element” type. This method was firstly introduced in 1979 [43] and has proved to be an efficient and widespread tool to observe the micro-structure and micro-mechanical behavior of granular systems. Two versions of the molecular dynamics simulation method are introduced. The first is the so-called soft sphere molecular dynamic (MD=DEM). It is a straightforward implementation to solve the equations of motion for a system of many interacting particles [170, 171]. For DEM, both normal and tangential interactions, like friction, are discussed for spherical spheres. The integration of the dynamic equation is illustrated in Fig. 1.13. The second method is the so-called Event-Driven (ED) or Contact Dynamics (see Jean in [172]) simulation, which is conceptually different from DEM, since

collisions are dealt with using a collision matrix that determines the momentum change on physical grounds. For the sake of brevity, the ED method (see McNamara in [172]) is only discussed for smooth spherical particles. In addition, the quasi-static method is developed based on the stiffness matrices of the granular assemblages. This method is appropriate to analyze the granular assemblages at the equilibrium or in the quasi-static deformation (see Roux and Combe in [172]).

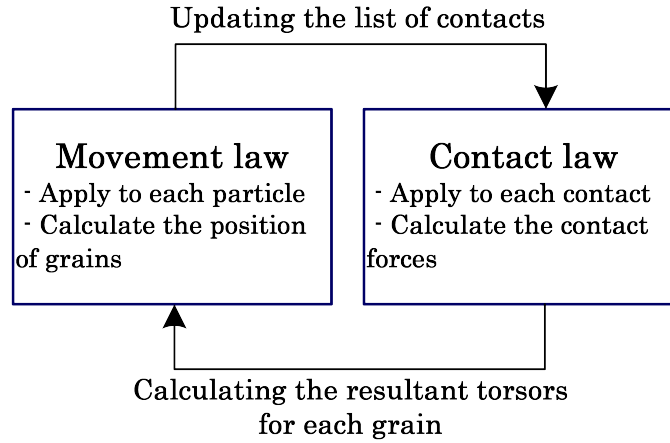


Figure 1.13: The cycle of the DEM calculation

In some cases, a computational method coupling two methods is necessarily applied to study simultaneously two objects, for instance the fluid and particles flows. Hence, a coupling of the SPH and the DEM was proposed in order to simulate the liquid-solid flows in granular materials [159, 160]. Another coupling of two methods, used in mechanics of granular media and fluid dynamics, are the LBM and the DEM, respectively [173, 174, 175, 176, 177, 178]. Besides, several authors proposed a coupling of the DEM and the FEM to tackle the behavior of granular assemblies from the microscale to the macroscale. The concept of Representative Elementary Volume (REV) is applied to bridge the micro- and macro-scales. This computational homogenization (FEM \times DEM) has been use to simulate biaxial tests [179, 180, 181], triaxial tests [182], and for the dynamic analysis of geomechanics problems [183]. In addition, a coupling between the MPM and the FEM was implemented to demonstrate a good agreement between explicit and implicit solutions to the problem of stress wave propagation [166].

1.3.2 Typical observations

The DEM or MD simulation are getting more and more popular in granular material science, for 2D and 3D applications. However, studies of cohesive granular materials, especially in loose states, have been investigated less frequently than dense or non-cohesive granular materials. For instance, Onoda and Liniger [184] studied the random-loose-packing fraction of uniform spheres at the limit of zero gravitational force. Dong *et*

al. [15] then reported on the loose structures formed by particle packed under gravity and stabilized by adhesion, as illustrated in Fig. 1.14. It can be seen from Fig. 1.14 that the DEM can reasonably reproduce the experimental results for all sized particles, confirming the validity of the proposed simulation technique [15].

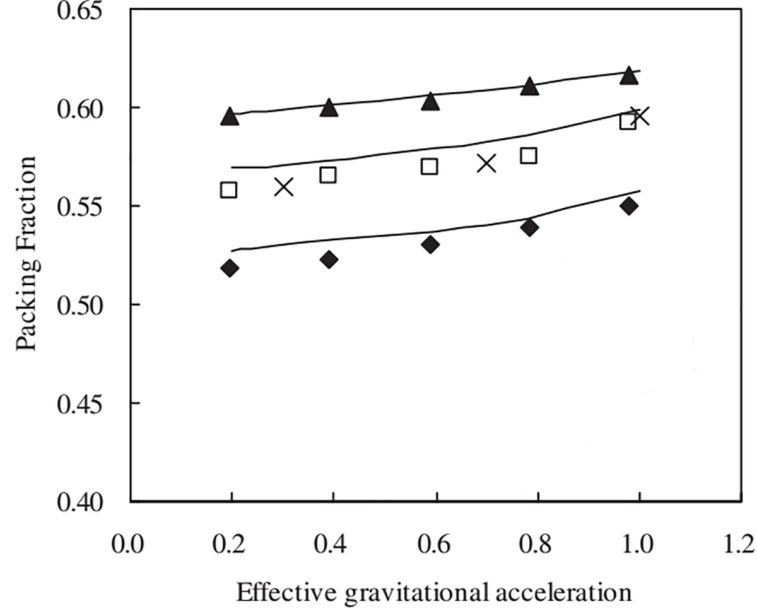


Figure 1.14: The packing fraction of different sized glass beads as a function of the effective gravitational acceleration. Points are the measured results: triangle, $d = 500 \mu\text{m}$; square, $d = 250 \mu\text{m}$; lozenge, $d = 110 \mu\text{m}$; and \times , result of [184]. Lines are the simulated results (from Dong *et al.* [15]).

Other authors investigated loose packing stabilized by cohesion and the collapse of such materials under growing loads during compression tests [16, 17, 18, 19]. These authors studied a dynamical compression regime, and observed a shock wave propagating through the samples. Fig. 1.15 [17] shows a simulation of a ballistic deposit containing 2746 monodisperse spherical particles, the top figure is the initial arrangement, the bottom figure is the final configuration. The contact between particles includes Coulomb friction, rolling friction and cohesion. They also compared with the case using only Coulomb and rolling friction. This comparison confirms that the effect of cohesion on the porosity is higher if one uses Coulomb and rolling friction. Moreover, the low cohesive forces lead to similar packings as without cohesion [17].

Gilabert *et al.* performed a 2D investigation into the microstructure and mechanical properties of model cohesive powders [13], and also the quasi-static behavior of the cohesive powders under an isotropic compression test [14]. Fig. 1.16 [14] shows how this initial influence affects the beginning of compression curves and fades out later on. Compression curves are shown in Fig. 1.16 for two values of initial agitation level and rolling resistance. An increase of rolling resistance (μ_R/a) stabilizes looser systems under

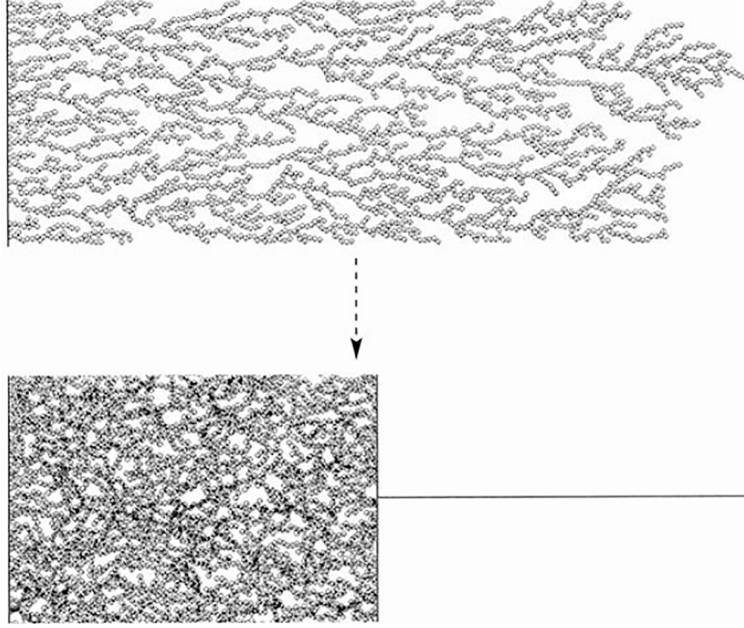


Figure 1.15: Ballistic deposit before and after compaction by a constant external force on the piston. Contact properties include Coulomb friction, rolling friction and cohesion (from Kadau *et al.* [17]).

low pressure P^* , as does a decrease of agitation level (V_0/V^*). However, such a change in material properties affects not only the initial stage (first plateau of compaction curve) but also the macroscopic mechanical behavior at larger densities. As a consequence, the slope of the compaction curve is lower for larger rolling resistances [14].

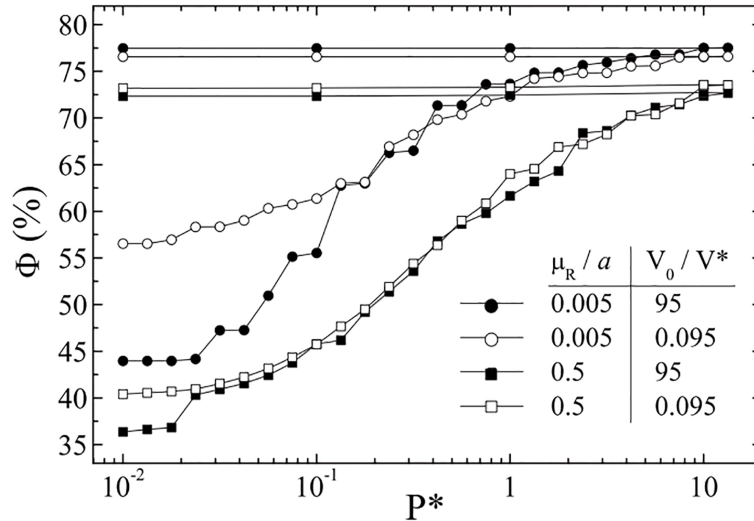


Figure 1.16: Compression and decompression curves: effect of initial agitation level in aggregation stage and influence of rolling resistance parameter (from Gilibert *et al.* [14]).

In addition, several studies focused on the fracture of bound particle assemblies in static [20, 21] or dynamic conditions [22]. The others studied wet beads packs in

which neighboring particles are joined by liquid bridges, and investigated the structure of poured samples [23], or shear strength of this material [24]. Besides, the shear flows of cohesive granular materials have been also simulated [25, 26, 27, 185, 186]. This means that with the DEM, it is easily to simulate all the tests with any material.

In the microscopic point of view, the DEM simulation give easily access to the microstructure of wet granular materials, thus allowing the measurement of intergranular forces between grains, contact networks, etc. For instance, Richefeu *et al.* [187] analyzed stress transmission in wet granular media in the pendular state by means of 3D molecular dynamics simulations. Fig. 1.17 shows the force network in a narrow slice whose thickness is nearly three particle diameters. The tensile and compressive forces are represented by segments of different colors joining particle centers. The line thickness is proportional to the force. It is remarkable that tensile and compressive force chains could be obviously observed although the slice is quite narrow [187]. Besides, the distribution of forces and the connectivity of the bond network are the main properties, that most often are characterized in studies using DEM simulations.

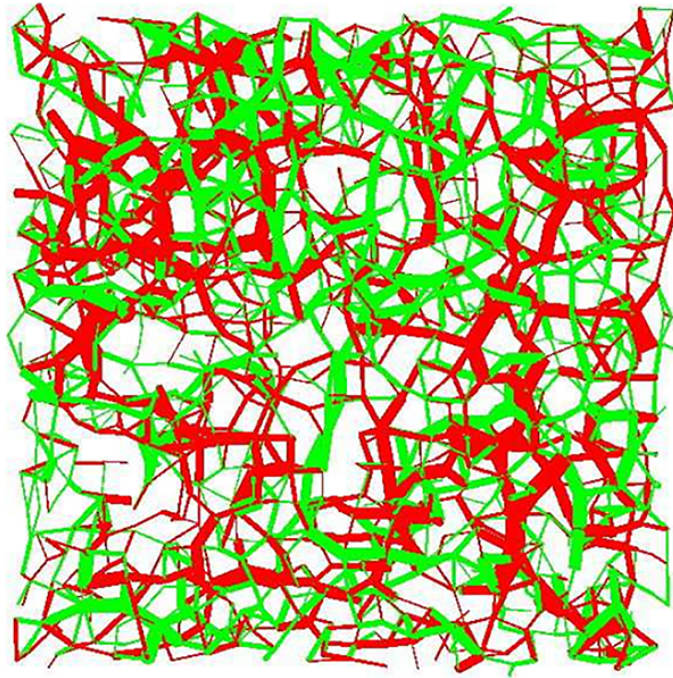


Figure 1.17: A map of tensile (green) and compressive (red) forces in a thin layer cut out in the packing. Line thickness is proportional to the magnitude of the force (from Richefeu *et al.* [187]).

1.3.3 Some characteristics of wet granular material in DEM simulation

1.3.3.1 Capillary forces

The appearance of a small quantity of water in the intergranular voids, will preferentially accumulate near the contacts or the narrow interstices, forming liquid bridges that join contacting grains or near neighbors. These bridges are formed by assuming the shape of the meniscus as illustrated in Fig. 1.18. This formation may be spontaneous if the liquid has exchanges with its vapor, present in the surrounding atmosphere. The pressure difference between two sides of a curved liquid-air or liquid-solid interface is determined by the Laplace-Young equation which is the product of the surface tension Γ and principal radii of curvature r_1 and r_2 (as shown in Fig. 1.18(a)):

$$\Delta u = u_a - u_w = \Gamma \left(\frac{1}{r_2} - \frac{1}{r_1} \right), \quad (1.4)$$

in which $u_a - u_w$ is the pressure difference across the fluid interface and Γ is the surface tension of the air-liquid interface.

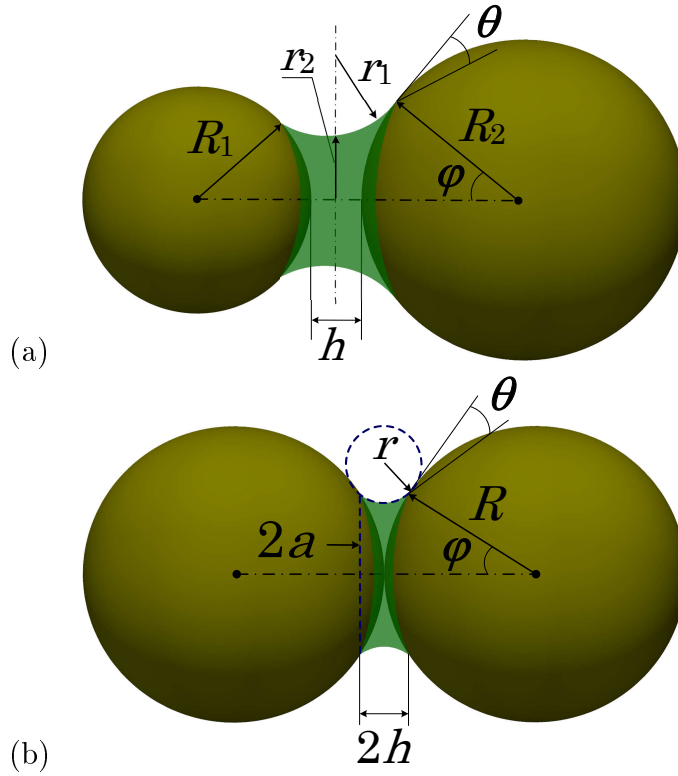


Figure 1.18: Schematic view of liquid bridge between two smooth (a) polydisperse spheres and (b) monodisperse spheres (not to scale).

The capillary force F_{cap} due to the liquid bridge can be also calculated according to the “gorge method” [188]. This force involves effects of both the capillary pressure Δu and the surface tension Γ over the bridge section, as

$$F_{cap}^G = \pi r_2^2 \Delta u + 2\pi r_2 \Gamma = \pi \Gamma r_2 \left(1 + \frac{r_2}{r_1} \right). \quad (1.5)$$

For the monodisperse case, r_1 and r_2 , respectively denote the radius of the meridian profile and the radius at the neck (Fig. 1.18(b)), are given by

$$\begin{cases} r_1 = \frac{h/2 + R(1 - \cos \varphi)}{\cos(\varphi + \theta)}, \\ r_2 = R \sin \varphi + [1 - \sin(\varphi + \theta)]r_1. \end{cases} \quad (1.6)$$

The filling angle φ cannot be calculated explicitly and an iterative procedure must be used to get it as a function of the other parameters. The contact angle θ is illustrated in the relationship between capillary force, suction, and the gorge's radius (see Fig. 1.19). The contact angle is null when the gorge's radius is larger than 0.01 to 0.1 mm, the capillary force varies from 78 μN to 57 μN , and the suction from 23 kPa to 0.3 kPa. Therefore, the strong variation of suction slightly affects the capillary force. Moreover, when the contact angle increases, the capillary force decreases at the constant of gorge's radius, and the capillary force reaches a maximum value of $2\pi\Gamma R \cos \theta$. In experiments on granular materials, it is really difficult to determine this contact angle. Hence, for the simplification, the contact angle is usually considered null in many different models.

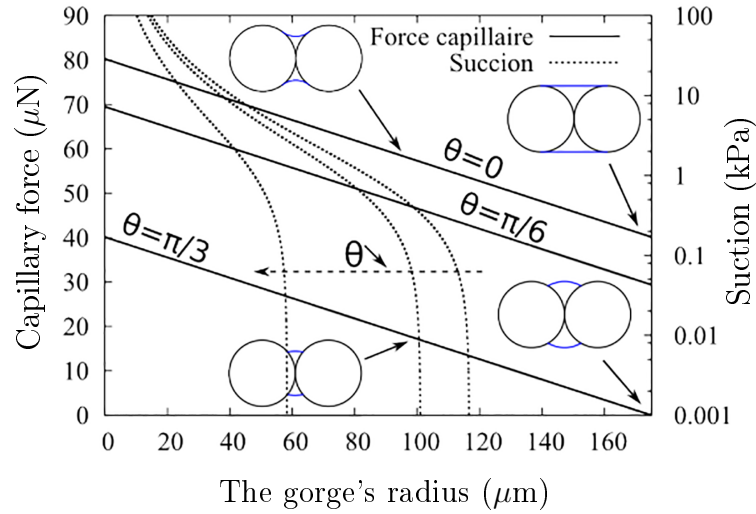


Figure 1.19: Capillary force and capillary pressure as a function of the gorge's radius for different values of contact angle θ (from Bruchon [148]).

Besides, Soulié *et al.* [91] also proposed a numerical solution to calculate the capillary force, as below

$$F_{cap} = \pi\Gamma\sqrt{R_1R_2}\left[c + \exp\left(a\frac{h}{R_2} + b\right)\right], \quad (1.7)$$

where R_1 and R_2 are the radii of particles and h is also the interparticle distance. The coefficients a, b, c are functions of the volume of liquid bridge V_m , the contact angle θ ,

and R_2 :

$$\begin{cases} a = -1.1 \left(\frac{V_m}{R_2^3} \right)^{-0.53} \\ b = \left(-0.148 \ln \left(\frac{V_m}{R_2^3} \right) - 0.96 \right) \theta^2 - 0.0082 \ln \left(\frac{V_m}{R_2^3} \right) + 0.48 \\ c = 0.0018 \ln \left(\frac{V_m}{R_2^3} \right) + 0.078 \end{cases} \quad (1.8)$$

In the case of a capillary bridge at the contact point between two equally-sized spheres with radius R (see Fig. 1.18(b)), assuming that the principal radii of curvature are denoted a and r , relation (1.4) can be rewritten as:

$$\Delta u = \Gamma \left(\frac{1}{a} - \frac{1}{r} \right). \quad (1.9)$$

As the diameter a of the meniscus is much larger than its meridian radius of curvature r , Δu is negative. The liquid is sucked towards the contact region. The angle θ is the equilibrium contact angle between the liquid and the grain surfaces. In the case of perfect wettable materials, this contact angle is equal to zero.

The capillary force between equal-sized spheres is approximately equal to the suction force $\pi a^2 \Delta u$. If we assume $a \gg r$, the pressure difference is proportional to $-\Gamma/r$. For the very small grain size, assuming $h \ll R$ ($2h$ is the distance between grain surfaces), we finally obtain the capillary force,

$$F_{cap} \simeq 2\pi\Gamma R \cos \theta. \quad (1.10)$$

The capillary force between two equal-sized spheres in contact is proportional to surface tension Γ and particle radius R . This relation is remarkably independent of the volume of meniscus V_m . When the particles are small enough, the influence of gravity on the curvature of the liquid bridge and on the capillary force is negligible [96].

In order to calculate approximately the capillary force, Maugis [189] proposed a simpler formula but less accurate, also called Maugis approximation, by which the capillary force is expressed as a function of the meniscus volume V_m and the interparticle distance h (also called separation distance) as below,

$$F_{cap} = 2\pi\Gamma R \cos \theta \left[1 - \frac{1}{\sqrt{1 + \frac{2V_m}{\pi R h^2}}} \right]. \quad (1.11)$$

This formula is chosen to calculate the capillary force of the monodisperse grains in the present works.

Fig. 1.20 shows a typical example of the evolution of the capillary force with the relative displacement between two interacting grains for a given capillary pressure. The capillary force acts exclusively in the axial direction of the interaction (the normal to the contact plane). F_{cap} is maximum and remains constant for grains strictly in contact

($h \leq 0$), assuming small deformations of the contact zone compared with the grain size. D_r (rupture distance) is the debonding distance defined as the maximum distance h beyond which the Laplace-Young equation has no solution. A hydraulic hysteresis can be introduced by defining D_c (creation distance) as the distance below which a liquid bridge can form. For numerical simulation, a possible choice is to allow a bridge to form when particles come strictly in contact $D_c = 0$, hence neglecting the possible effect of adsorbed water on the grain surface. This assumption is used in our study.

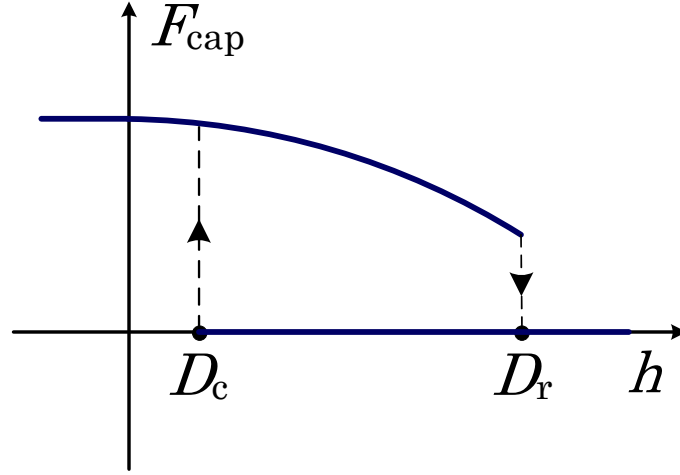


Figure 1.20: Evolution of the capillary force F_{cap} as a function of the interparticle distance h for a given capillary pressure Δu : a meniscus can form when $h \leq D_c$ and breaks down when $h \geq D_r$ (from Chareyre and Scholtès in [172]).

The rupture distance D_r can be found in several studies existing. Lian *et al.* [140] proposed the following relation between the rupture distance D_r , the liquid bridge volume V_m and the contact angle θ :

$$D_r = \left(1 + \frac{\theta}{2}\right) V_m^{1/3}. \quad (1.12)$$

The formula proposed by Herminghaus [84] also related to meniscus volume V_m and contact angle θ , as follows:

$$D_r = \left(1 + \frac{\theta}{2}\right) (V_m^{1/3} + 0.1 V_m^{2/3}). \quad (1.13)$$

The approximate formula of rupture distance, $D_r \simeq V_m^{1/3}$, was also proposed by Willett *et al.* [90], and Maeda *et al.* [138]. This approximate equation has been widely used in the numerical simulations and it is applied in the present study. An experimental study by Pitois *et al.* [190] shows that the rupture distance also varies with the separation velocity.

1.3.3.2 Loose configuration of adhesive particles

Adhesive particles tend to form tenuous aggregates, which may sustain the increasing confining stress without rearranging, as shown for a 2D model [13] in Fig. 1.21. The

authors observed that the equilibrated configurations of cohesive packing are sensitive to the applied pressure. The structures can be stabilized for very small applied pressure, but then collapse when increasing the pressure in some pressure range. This can be found in the first regime of compression curves in 2D models of loose systems [14], and in 3D ones [47], as shown in Fig. 1.22. Indeed, the first part of the compression curves (see rectangle boxes) confirms that the initial structure is able to sustain the increasing pressure without rearranging. Note that the compression curve of Gilabert *et al.* [14] is expressed as the relationship between solid fraction Φ and reduced pressure P^* instead of the $e - \log(P^*)$ curve conventionally used in soil mechanics.

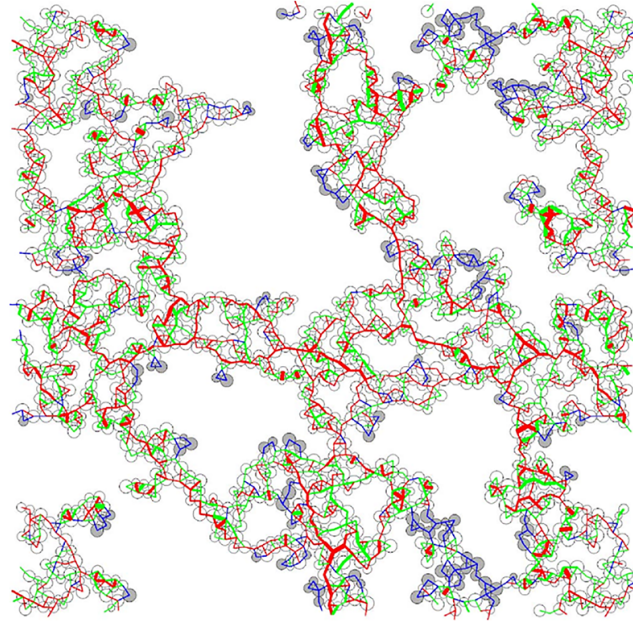


Figure 1.21: Loose cohesive assembly of disks (from Gilabert *et al.* [13]). Force magnitude is encoded as line thickness, with compressive forces in red and tensile ones in green. Blue lines correspond to null normal contact forces.

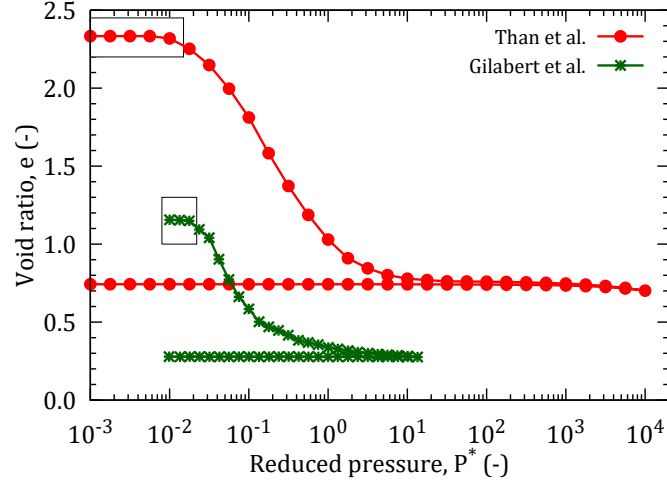


Figure 1.22: An example of compression curve of loose systems obtained with 2D [14] and 3D [47] models.

1.4 Experimental investigation versus numerical investigation

1.4.1 Existing studies combining experimental and numerical methods

It is well recognized that experimental methods hardly enable to get insight into the microstructure of specimens, especially to measure precisely intergranular forces between particles subjected to growing external forces. However, with the advanced techniques, we can count accurately the capillary bridges between particles (using FM for instance), or capture and distinguish clearly convex and concave menisci (using ESEM for instance), or access and reconstruct completely the microstructure of specimens at dimensions from millimeters to micrometers (using XRCT for instance). In practice, some factors can considerably and directly affect the results. Among other factors, one can cite the technique itself, the quality and the inherent noise of the equipment, or the environment, which is of critical importance in the case of in-situ observations. Therefore, we sometimes need to perform several tests for measuring a given quantity. Generally, it is really difficult to overcome the inconvenience of external factors. Conversely, with the numerical simulations, we can idealize the materials and the testing conditions, with minimal disturbance from external factors. Alternatively, we can simulate in a realistic manner the imperfect conditions applied or observed while testing physically the specimens. Therefore, the numerical results will be helpful to get information on unmeasurable quantities or to interpret non-ideal experiments.

Each method, either numerical or experimental investigations, has its own strengths as well as inherent limitations. Both could provide useful observations to improve the general knowledge. As a consequence, the combination of numerical and experimental observations is not only a way to overcome the shortcomings of each method but also

an opportunity to complete and validate each other. A summary of the main applications that have utilized the combination of experimental observations and computer simulations to study the behavior of porous or granular materials is provided in Table 1.3 (partially succeeding from Moreno-Atanasio *et al.* [50]). Selected examples (typical studies) found in the literature are shown in Table 1.3, where are indicated the application, material and parameter used to link experiment and computer simulation, and appropriate referenced works.

The link between experiments and computer simulations is always established through the exchange of structural information between the two techniques. In Table 1.3, the link between experimental and numerical investigations mainly focuses on the following phenomena: fluid flow and transport properties, mechanical loading of granules and granular beds, and particle packing. A brief summary of the most characteristic parameters obtained from XRCT and computer simulations is described below.

Firstly, the study on oil and water distribution within the beads, reported by Sukop *et al.* [156], has shown one of the most robust ways of coupling XRCT with computer simulations. In this study, the initial structure was transferred into the computer software. The authors then compared the distribution of oil and water by comparing the relative content of each fluid plane by plane. The distribution of the two phases within specific pores was then visualized. In addition, Selomulya *et al.* [153] also presented the transport properties (permeability and tortuosity) of filter cakes of which XRCT digital images were transferred into a LBM software. The simulated relative permeabilities were calculated according to Darcy's law. Moreover, Wang *et al.* [154], using the LBM simulations, obtained a similar value of permeability for exactly the same bead which was used in the experiments by Nakashima and Watanabe [157].

Secondly, Golchert *et al.* [49, 196] studied the influence of the structure of granules made of glass beads on the compressive behavior of the granule using XRCT and DEM. They determined particle sizes and positions from the XRCT images and this information was used to create the computer simulated granule. Besides, Stock [197] suggested that the displacement of marker particles in powder beads allows the determination of the field displacement. For instance, Fu *et al.* [193] used marker particles in the study of the compressive behavior of a bead of sugar particles mixed with some glass particles. They observed that the markers at the bottom of the bead were displaced less than the markers near the top of the bead. The authors stated that their results were in agreement with computer simulation results obtained by other authors using FEM [198]. Therefore, the comparison was purely qualitative.

Finally, the combination of XRCT and computer simulations allows a direct and easy comparison and validation of the particle packing predictions by computer models [48, 193]. The investigated materials include the monodisperse glass spheres, polydisperse glass spheres, and irregular polydisperse microcrystalline cellulose particles. By obtaining different cross sections from the XRCT, the particle size distribution was ob-

tained, compared to SEM results and provided to DEM simulations. They found a good agreement for the radial distribution function between experiment and simulation, except the case for cellulose particles. This work shows a typical case in which limitations in the computer models are the origin of the differences between the data obtained from XRCT and the predicted simulation data. In contrast to Fu *et al.* [48, 193], Jia *et al.* [194, 195] studied the predicted packing of irregular particles by using the real particle shape as an input for the computer simulations. Therefore, the link between simulation and experiments presented by these authors is a combination of parametric and imaging link. Furthermore, a sophisticated algorithm able to produce particulate beads with a specific value of coordination number and packing fraction distribution has been developed [191]. The results were compared to the values obtained from XRCT for a bead made of glass beads [101]. They also found a good agreement between simulations and experiments in all cases of monodisperse and polydisperse spheres.

Table 1.3: Combining experimental observations with computer simulations

Application	Material	Simulation	Experiment	EXP-SIM link	Reference
Bed structure, coordination number and packing distribution	Glass beads	Optimization method	XRCT	Homogeneity and isotropy	Al-Raoush, Al-Raoush and Alsaleh [191, 192]
Bed structure, packing, bed compression	Glass mono, glass poly and MCC	DEM	XRCT	Input structure, pair correlation function	Fu <i>et al.</i> [48, 193]
Bed structure, packing	Industrial powders	Digital model	XRCT	Comparison of porosity and structure between real and simulated	Jia <i>et al.</i> [194, 195]
Granule compression	Glass beads	DEM	XRCT	Input structure	Golchert <i>et al.</i> [49, 196]
Stress–dilatancy and strength	Cemented sand	DEM	Triaxial test	Input parameters	Wang and Leung [36, 37]
Fluid saturation	Sand, oil and water	LBM	XRCT	Input structure and visual observations	Sukop <i>et al.</i> [156]
Permeability of porous materials	Bentheimer sandstone, water, oil	LBM	XRCT	Input structure	Harting <i>et al.</i> [152]
Permeability of filter cakes	Glass beads	LBM	XRCT	Input structure	Selomulya <i>et al.</i> [155]
Permeability of flocs and sediments	Glass beads	LBM	XRCT	Input structure	Selomulya <i>et al.</i> [153]
Permeability and tortuosity of porous materials	Glass beads	RWS	XRCT	Transport properties by tracking ion displacement	Nakashima and Watanabe [157]
Permeability and tortuosity of porous materials	Sandstone	RWS	XRCT	Comparison with medical CT	Nakashima <i>et al.</i> [158]
Permeability and tortuosity of porous materials	Glass beads	LBM	XRCT	Input structure	Wang <i>et al.</i> [154]
Fluid–particle interactions	Gravel (quartz)	bed LBM \times DEM	Vacuum dredging system	Comparison	Feng <i>et al.</i> [175]

Note: EXP, Experiment; SIM, Simulation; MCC, MicroCrystalline Cellulose; CT, Computed Tomography

1.4.2 Combination between the XRCT and the DEM

One of the most suitable simulation techniques to couple with the XRCT in the study of mechanical properties of granular materials is the DEM. DEM considers particles as individual entities with physical and geometrical properties (elastic modulus, density, particle size distribution and different shapes). The DEM simulation could provide a direct correlation between external load and internal granular behavior with realistic contact deformation [13]. Therefore, we present briefly here some of the most important parameters that are obtained by combining XRCT and DEM, such as particle shape, porosity distribution and structures of pores, characterization of contact network, radial distribution function, and particle displacements.

1.4.2.1 Particle shape

The most common way to simplify particle shape is to consider irregular particles as ellipsoids. Wang *et al.* [199] applied this technique to study the irregular particles (limestone and sandstone), whose shapes were obtained from XRCT. The model particles were then characterized by having the same mass and inertia moments as the original particles. This method was described in terms of a spherical harmonic expansion [200, 201]. By applying the volume of the equivalent ellipsoids, Wang *et al.* [199] shown that the ellipsoid volume overestimated the real particle volume meanwhile the reconstructed images of limestone and sandstone were reproduced qualitatively well by the equivalent ellipsoidal simulation. Therefore, this combination is extremely useful because it allows an easy manipulation of irregular particle without making the codes very complex. Several algorithms used to describe different particle shape properties (such as roundness and inertia moments) were also proposed by Al-Raoush [192] and Lin and Miller [127].

Wang *et al.* [199] also proposed the clumping of spheres method, using XRCT images to simplify particle shapes, and they can be easily handled by simulations. Fig. 1.23 shows two schematic representations of the clumping of spheres method in which the tomographic image of a real particle was used to create a computational equivalent particle. Fig. 1.23(a) illustrates the equivalent particle using the non-overlapping technique. The overlapping method of clumping the spheres is presented in Fig. 1.23(b). In the first method, the shape and volume of the final modeled particle are very different from the real one because of the presence of pores between the clumped spheres, unlike the real object. Therefore, the final structure is made of clusters of spheres which do not show a relative motion between them, in principle [199]. However, with the second method, it allows the overlap of the individual spheres, and therefore avoiding the interstitial artificial pores. Nevertheless, this method may be computationally very expensive depending on the irregularity of the real particle and on the requirement of accuracy of the simulated particle [50].

Other authors proposed a simple solution and ignored the non-sphericity of particles

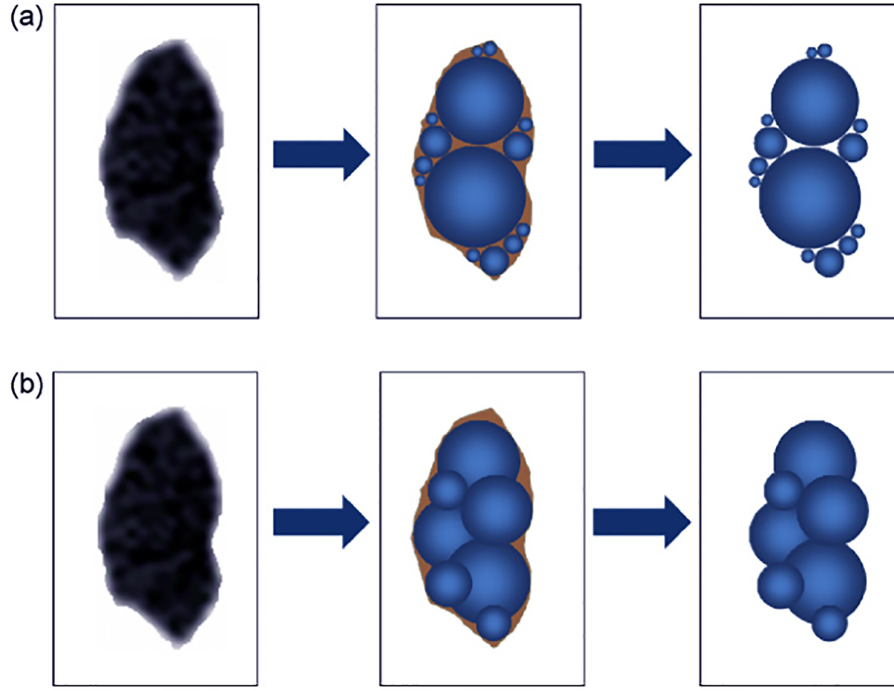


Figure 1.23: (a) Illustration of the clumping of spheres method with no overlapping particles. From left to right: the tomographic image, the actual clumping method, and the simplification of particle shape used by DEM. (b) Illustration of the clumping of shapes method with overlapping particles (from Moreno-Atanasio *et al.* [50]).

if the particle shape was not strongly elongated [49, 196]. In these cases, the centers and radii of particles can be obtained directly from XRCT and these parameters are straightforwardly transferred to computer simulation.

1.4.2.2 Porosity, porosity distribution and structures of pores

Porosity and distribution of porosity in a sample is probably the most common parameter used to link XRCT and DEM. This parameter strongly affects the mechanical and physical behavior of materials, such as mechanical strength, flow-ability, or permeability. Therefore, the porosity predicted by simulations necessarily has to be compared and validated with the values obtained from XRCT. Some typical works reported here have not been linked with simulations but these works provide the possibility to relate XRCT and numerical simulations in future works.

The analysis of the bulk or local porosity of the samples exposes some problems: the scanned areas may not be representative of the whole specimen, the identified algorithm for differentiation between grains and pores (namely, the segmentation process) may be inaccurate, and the resolution of XRCT images may not be high enough. Therefore, we can consider different local scans from different parts of the specimen as a representative value of porosity. We use this value to compare with the bulk porosity of whole sample.

Selumulya *et al.* [153] performed six scans of different sample region in order to obtain an appropriate value of bulk porosity of the material, and compared with the porosity of the real sample. The authors analyzed the porosity of the sample versus height. This is the most common way of characterizing the porosity of materials. Interesting studies regarding the analysis of porosity distribution with height within a cylindrical specimen has been performed [202, 203].

The characterization of the porosity of samples was also analyzed by the pore network structure in term of the number of pore bodies, pore throat, and the coordination number of pores [101, 204]. Al-Raoush and Willson [101] considered eight different systems mainly made of glass beads although some of them were made of natural marine sand. They found that the differences in the number of pores, body pore sizes and pore coordination number is approximately 50 % despite the fact that the macroscopic value of porosity was similar in all samples. Interestingly, they also compared the results with low and high resolution XRCT images and concluded that a good resolution is needed to minimize the error of the estimation. This is one of the most detailed study in literature which analyzes clearly pore properties.

Other studies using XRCT, with no comparison with simulation, were performed to determine parameters such as the average pore diameter, number of pores per cross sectional area [144, 205]. XRCT results are also compared with the ones obtained from mercury intrusion porosimetry. One of the most interesting parameter is the pore size distribution analyzed directly from the tomographic images, as illustrated in Fig. 1.24 [144]. By analyzing different samples with the two techniques, the authors concluded that XRCT and mercury intrusion porosimetry yield very similar overall porosities; noteworthy is the fact that only the largest pores (so-called macropores) were analyzed [144].

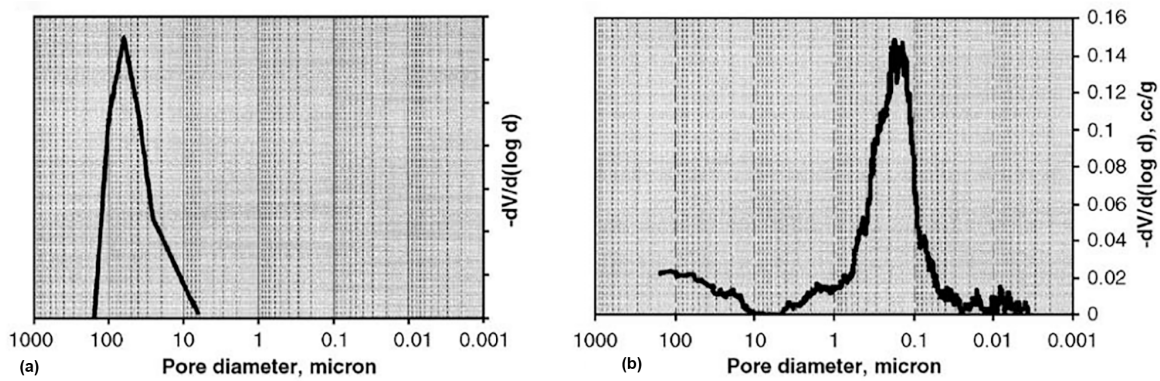


Figure 1.24: Pore size distributions of granules produced under high shear (a) calculated from tomographic images; (b) measured by mercury porosimetry (from Farber *et al.* [144]).

Finally, the porosity of granular materials can be characterized in many possible

ways and using various metrics, such as bulk and local void ratio, spatial distribution of density, number and size of pores, etc. These quantities do not only complement each other but also can be favourably injected into computer simulations in general, and the DEM in particular in order to provide a detailed comparison with XRCT.

1.4.2.3 Microstructure characterization

The characterization of the contact network of granular materials is very important to understand how the material behaves under an external applied force. One of the most important characteristic of the contact network is the coordination number of the system. The coordination number is defined as the number of contacts per grain. A contact network can be characterized not only by the total coordination number of the whole structure but also by the local values of the number of contacts. In fact, the coordination number has been characterized in many studies using XRCT [206, 101, 207, 208, 209], in studies using XRCT and optimization methods [191, 192], and many studies using the DEM. However, one of the most interesting combination of XRCT and DEM for analyzing the coordination number can be found in Marmottant *et al.* [210]. The authors observed the structure of compacted NaCl irregular powders, the coordination number is shown in Fig. 1.25.

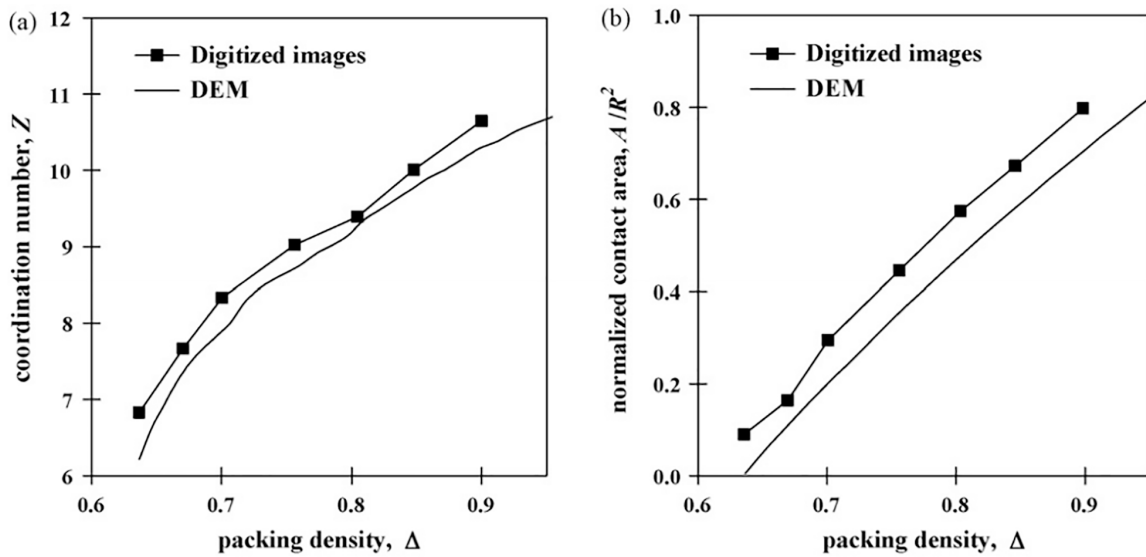


Figure 1.25: Comparison of coordination measurements on numerical sphere packings produced by DEM and by analysis of XRCT images of (a) the mean coordination number z , and (b) the mean contact area A between touching particles normalized by the square of the particle radius R (from Marmottant *et al.* [210]).

They show that the coordination number obtained from the digitization algorithm slightly overestimate the one obtained from DEM computations (see Fig. 1.25(a)). The measured mean contact areas are also somewhat greater than those given by the DEM

calculations (see Fig. 1.25(b)). This discrepancy is due to the digitization procedure, which artificially increases the measured area (because of the finite voxel volume), causing for example a nonzero area for a point-contact between two particles [210].

The determination of the coordination number in granular media is also a typical subject in stereology and algorithms for extracting this parameter from digital images [211]. Nevertheless, the estimation of the coordination number and the characterization of the contact network have not been extensively investigated in engineering applications in spite of the key role of these parameters to understand comprehensively the behavior of granular materials under different loading conditions.

1.4.2.4 Radial distribution function

Radial distribution function (RDF) or pair correlation function is also a common way of comparing the structures obtained from simulations with those from experiments. The RDF is the probability of finding a particle center in a spherical shell. Many examples of the use of RDF can be found in the literature [212]. The detailed information of the RDF will be also described in Chapters 2 and 3. In this section, we only present a typical study using both of XRCT and DEM for the RDF.

The influence of particle shape on the local packing of particles is studied by Fu *et al.* [48, 193]. These authors observed that the first peak of the RDF, obtained from XRCT, was lower than the one obtained from DEM simulations, as illustrated in Fig. 1.26. The oscillations in the RDF extended through a longer distance in densely packed states and were quickly damped in the loosely packed states. This fact was attributed to the presence of large disordered structures when the system was loosely packed.

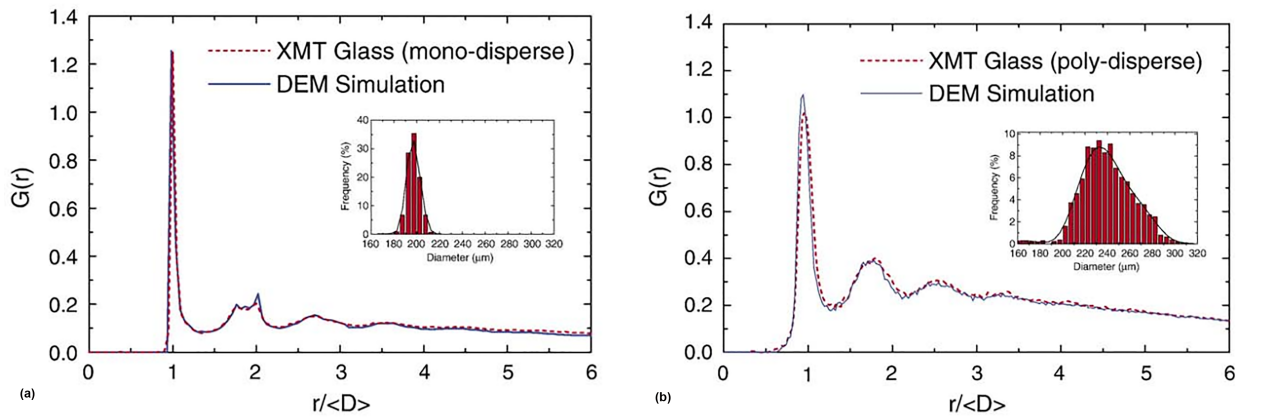


Figure 1.26: Comparison of the RDFs of (a) the monodisperse glass packing structure, and (b) polydisperse glass packing structure obtained from XMT (solid curve) and DEM simulation (dashed curve).

Other studies also observed the RDF, such as the study of bead compression [213], characterization of packing structure [206], and the analysis of the influence of particle

shape [192]. In summary, the RDF obtained from XRCT can provide extensive information for the corroboration of the DEM.

1.4.2.5 Particle displacements

The determination of particle displacements is usually applied in XRCT and DEM to visualize the changes in the structure of a granular material. Although in most cases, particle displacements have not been used in conjunction with DEM, it offers a direct way of linking simulations and experiments. Here, Fig. 1.27 shows an example of the comparison between the DEM and the experiment under triaxial tests of cemented sand. Fig. 1.27 shows the final numerical specimen (a) [86], alongside the equivalent laboratory sample (b) [214]. A conjugate shear plane can be observed clearly in the laboratory sample. A similar failure can be seen in the corresponding image of the numerical sample, which has fairly distinctive non-uniform deformations.

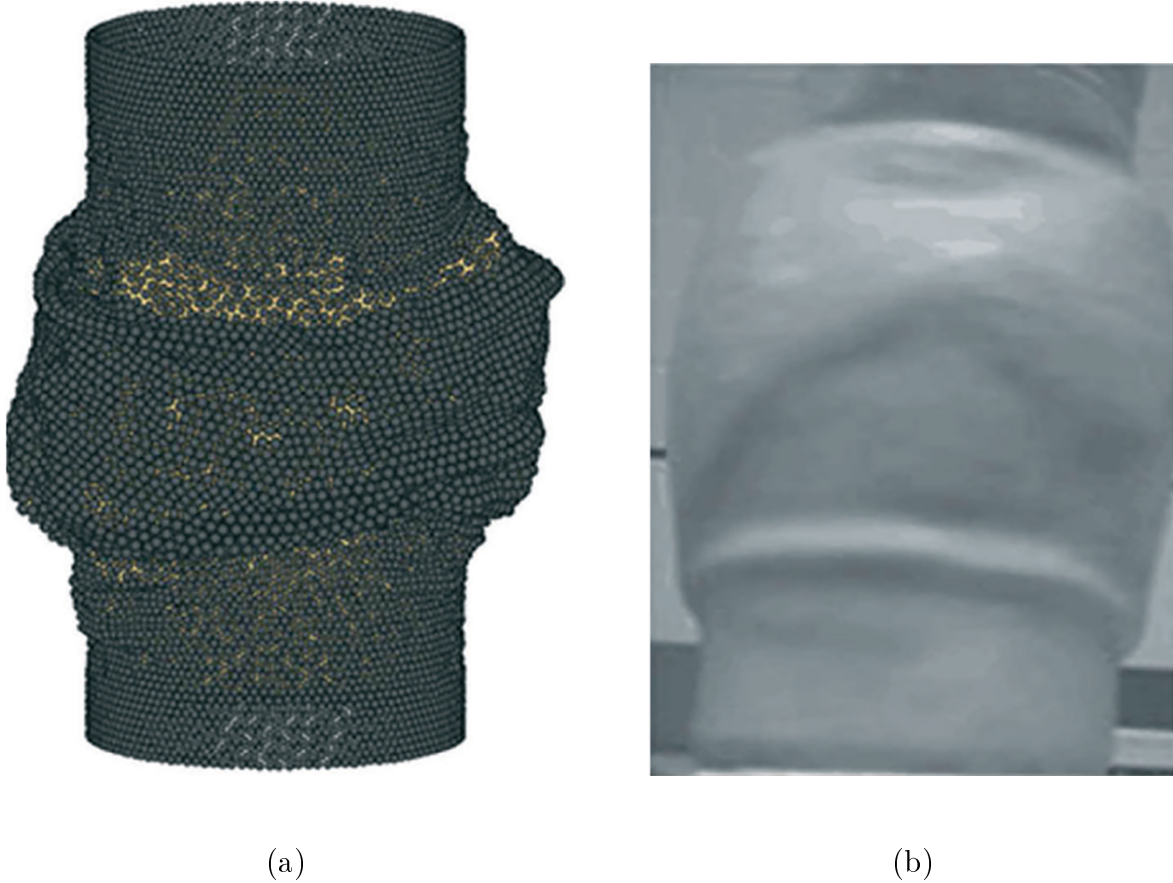


Figure 1.27: (a) Cemented numerical sample (from de Bono *et al.* [86]) and (b) laboratory sample (from Marri *et al.* [214]) after shearing to 20 % axial strain under 1 MPa confining pressure.

In many studies using XRCT, the 2D/3D Digital Image Correlation (DIC) method has been extensively applied to analyze the micro-macroscopic displacements of particles

under different loading conditions [129, 215, 209, 56, 216]. This approach provides an ideal framework to compare experiments on granular materials and DEM simulations at both macroscopic and microscopic scales.

In our study, the DEM and the XRCT are chosen to observe the mechanical behavior of wet granular materials from macroscopic level to microscopic level. We performed oedometric compression tests in order to investigate the differences between the irreversible behavior observed experimentally and the one predicted by numerical simulations.

1.5 Conclusion

In this chapter, we have reviewed the mechanical behavior of bonded granular materials which were observed by using both experimental and numerical investigations, with a particular focus put on wet granular materials. A brief description of the behavior of granular materials is also given. Three common non-destructive experimental methods and several computer simulation methods which were usually applied to approach the behavior and the structure of granular materials, from macroscopic to microscopic levels, are succinctly presented. Among various numerical methods, the DEM is one of the most popular applied to investigate the behavior of wet granular materials. We have introduced the following remarks: *(i)* adhesive granular materials have been observed less frequently than cohesionless ones; *(ii)* dense states of granular materials were studied significantly more than loose or very loose states; *(iii)* the association of the DEM and the XRCT is still limited in the study of granular materials in general and wet granular materials in particular. Therefore, the work presented here will combine DEM and XRCT to investigate wet granular materials, in very loose states stabilized by the presence of a very small amount of interstitial liquid. In the following chapters, we will present experimental and numerical evidences, which will be analyzed at both macroscopic and microscopic scales.

Experimental investigations

In this chapter, we present the observations of grain-scale behavior of a wet granular material in very loose state under one-dimensional compression tests, combined with X-ray computed tomography. We first describe the global compaction behavior of this material. A procedure to process images is then presented. It involves an algorithm to detect spherical structures from 3D tomography images, and the analysis of microstructure properties. A link between micro and macroscopic behavior is finally discussed to get a better insight into the macroscale behavior based on the microscale one.

Contents

2.1	Introduction	53
2.2	Material and methods	53
2.2.1	Material	53
2.2.2	Specimen preparation	54
2.2.3	Oedometric compression tests	57
2.2.4	X-ray computed tomography tests	59
2.3	Mechanical behavior under increasing vertical stress	62
2.4	Global scan observations	63
2.4.1	3D reconstruction from the image stack	63
2.4.2	Segmentation process	65
2.4.3	Heterogeneity	66
2.4.4	Pore scale deformation	71

2.5	Local scan observations	74
2.5.1	General principles	74
2.5.2	Algorithm to detect spherical structures	76
2.5.3	3D reconstruction after detection process	80
2.5.4	Grain size distribution after the detection process	82
2.5.5	General description of the structure at grain-scale	82
2.5.6	Heterogeneity	85
2.5.7	Geometrical structure analysis	86
2.5.8	Contact networks	92
2.6	Links between macro and microscopic behaviors	94
2.7	Conclusion	95

2.1 Introduction

So far, many authors investigated the macro- and micro-mechanical behavior of wet granular materials [10, 33, 12, 34, 32, 35] (among others). These works evidenced the link between the macroscopic mechanical behavior and the changes of microstructure. However, few works have focused on the grain-scale behavior.

Moreover, among various non-destructive experimental techniques, the XRCT is a high-resolution non-destructive 3D observation method, that does not require any sample pre-treatment. This technique can advantageously be combined with mechanical loading tests. Such a combination constitutes a clear strength of this method. Therefore, several recent studies used this technique to investigate the microstructure of granular materials with / without combining mechanical loading or any other test [144, 217, 218, 128, 191, 192, 209, 56, 35]. However, most of these works focus on the analysis of dense packing of cohesionless particles of large size.

In this chapter, we present an experimental investigation of a wet granular material assembled in a very loose state by means of XRCT. A cylindrical sample constituted of thousands of glass beads (average diameter: 100 micron) with liquid bonds in the pendular state was submitted to an oedometric compression test, which consisted in various compression steps. At every step, a XRCT scan was performed.

2.2 Material and methods

2.2.1 Material

The studied material is composed by spherical glass beads, an industrial product. Beads with diameters ranging from 80 μm to 104 μm were chosen. With these diameters, particle weight loses relevance with respect to capillary forces [96]. Furthermore, the beads are large enough to be satisfactorily resolved by the XRCT. The specific density of this material is equal to 2,460 kg.m^{-3} . The grain size distribution of the chosen glass beads is shown in Fig. 2.1.

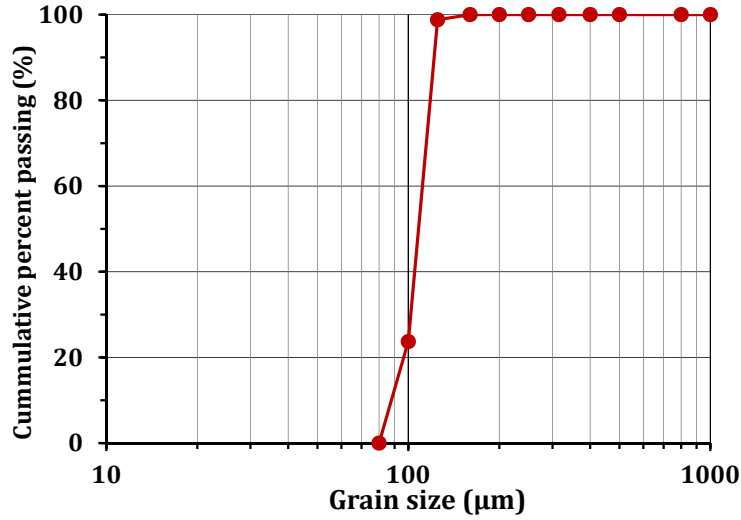


Figure 2.1: Cumulative grain size distribution of glass beads.

2.2.2 Specimen preparation

Two types of oedometric cells were used for compression tests. The first one is a metallic cell with 50 mm of internal diameter and 20 mm of height – hereafter called cell $\phi 50$, shown in Fig. 2.2. The second one is a polymethyl methacrylate (PMMA) cell with 20 mm of internal diameter and 10 mm of height – hereafter called cell $\phi 20$, shown in Fig. 2.3. The oedometric cell $\phi 20$ mm was made of PMMA to minimize X-ray absorption through the testing device. This cell was used in combination with XRCT.

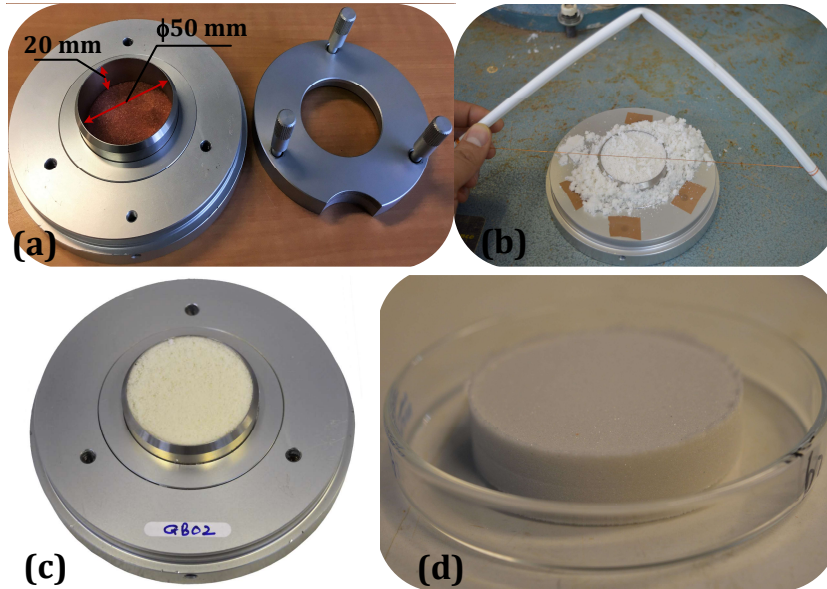


Figure 2.2: Specimen preparation for cell $\phi 50$. (a) Metallic cell $\phi 50$, (b) specimen preparation, (c) specimen before testing, and (d) specimen after testing.

The specimens were prepared with the following steps:

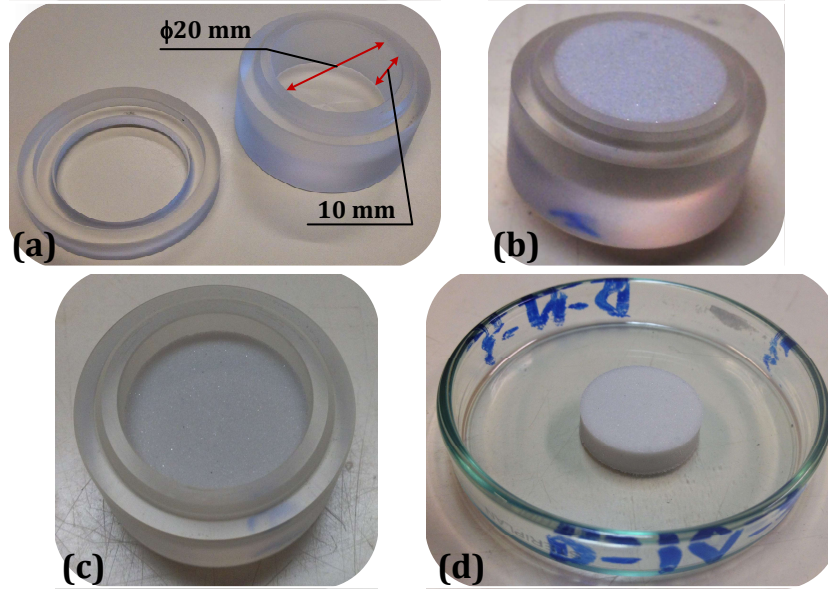


Figure 2.3: Specimen preparation for cell $\phi 20$. (a) PMMA cell $\phi 20$, (b) specimen before testing, and (c) and (d) specimens after testing.

- The glass beads were mixed with water at an initial water content of $w_0 = 3.5 \%$, to ensure that the specimens remained in the pendular regime at any time.
- The oedometric cell was placed on the support system (see Fig. 2.4). It was then filled with the wetted glass beads by using a controlled pluviation method, described hereafter. The filling was performed by placing the wetted glass beads on a fixed sieve with a $200 \mu\text{m}$ opening. The sieve was vibrated vertically with a vibration machine. Thanks to the vibration, clusters of glass beads passed sequentially through the sieve to finally fall into the cell. The height of free fall (h_f) from the sieve bottom to the cell bottom was varied between 80 mm and 260 mm.
- All specimens were prepared in an air-conditioned room. The preparation of each specimen took approximately from 30 to 45 minutes.
- The top surface of the specimen was then perfected by using a small iron wire to cut the excess soil (see Fig. 2.2(b)). This action must be done carefully and gently in order to avoid any perturbation to the initial structure. Height of specimen is 20 mm in the case of cell $\phi 50$ and 10 mm in the case of cell $\phi 20$ (see Figs. 2.2(a) and 2.3(a)). The specimens before testing are shown in Figs. 2.2(c) and 2.3(b).
- After the compaction test, the water content of the specimens was measured by oven-drying (w_{ap}).

The initial parameters of specimens after preparation are listed in Table 2.1. In this table, the tests named using prefix OD are performed with cell $\phi 50$ and the tests named using prefix CT are carried out with cell $\phi 20$. The water content of all specimens

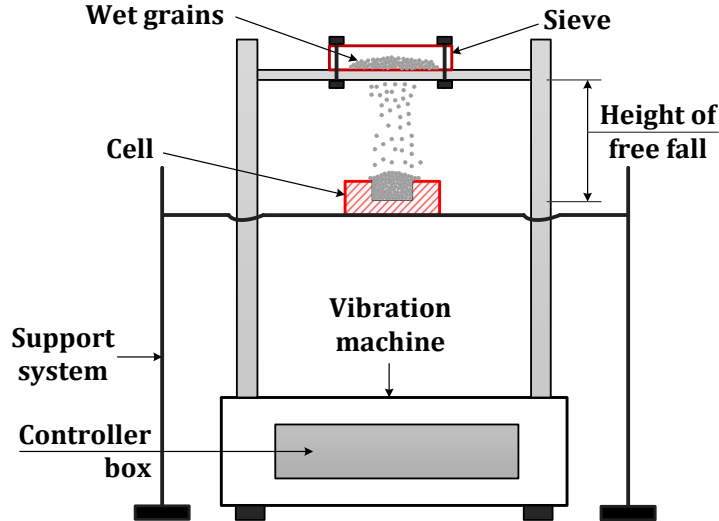


Figure 2.4: Schematic view of the system for preparing the specimen.

after preparation is strongly affected by the height of free fall (h_f). For instance, the water content after testing is $w_{ap} = 1.60$ % for the highest height ($h_f = 260$ mm), and $w_{ap} = 2.71$ % for the smallest height ($h_f = 80$ mm). Indeed, with same initial conditions, the evaporation of samples is proportional to the height of free fall. Clear evidences are given in Table 2.1: the maximal evaporation amounts to 1.90 % of water content (relative reduction of ≈ 54.29 %) for the highest height and the minimal evaporation corresponds to 0.79 % of water content (relative reduction of ≈ 22.57 %) for to smallest height. Although the water contents after preparation were quite small, the specimens were still stable in very loose states. The calculated degree of saturation ($S < 5$ %) confirms that the specimens are always maintained in the pendular state. This confirms that the capillary forces between grains play a key role to maintain the stability of specimen's structure.

Moreover, the relationship between initial void ratio e_0 , initial porosity n and the height of free fall h_f is illustrated in Fig. 2.5. The circle-red points represent the specimens with cell $\phi 50$, the square-blue points represent the specimens with cell $\phi 20$, and the triangle-green points represent other specimens which were not used for further analysis. Fig. 2.5 confirms that the higher is the height of free fall, the smaller the initial void ratios are.

Table 2.1: Initial parameters of selected specimens after preparation. The sample CT03 was prepared for the XRCT tests. w_{ap} was measured after testing.

Tests	Parameters				
	h_f (mm)	n (%)	w_{ap} (%)	e_0 (-)	S (%)
OD01	80	70.19	2.71	2.35	1.91
OD02	80	70.12	2.70	2.35	2.12
OD03	120	66.56	2.00	1.99	1.91
OD04	120	66.86	2.30	2.02	2.49
OD05	150	63.72	2.50	1.76	2.49
OD06	150	63.95	2.20	1.77	2.48
OD07	260	60.60	1.80	1.54	1.68
OD08	260	60.02	1.60	1.50	2.19
CT01	80	70.05	2.89	2.34	1.92
CT02	80	69.93	2.85	2.33	1.42
CT03	80	69.67	-	2.30	-

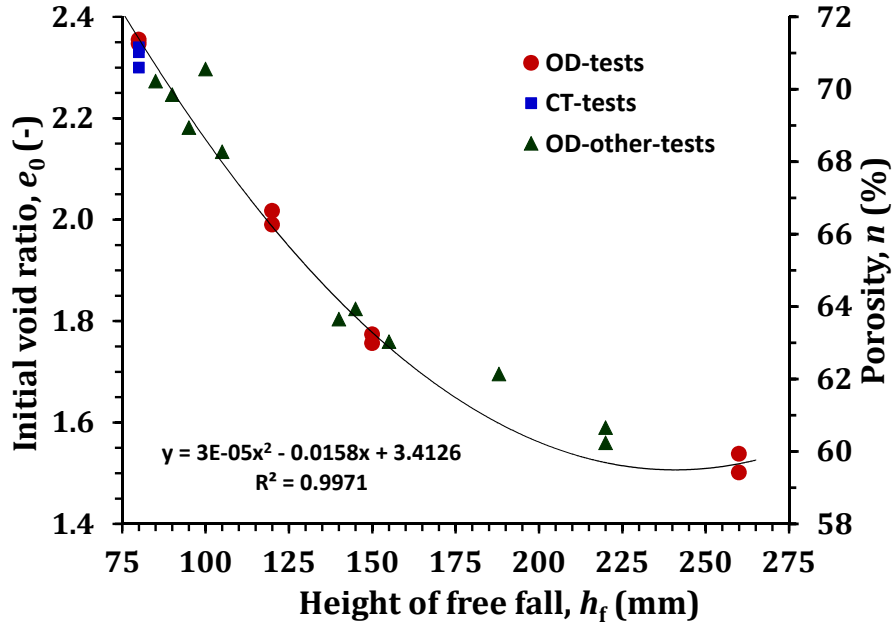


Figure 2.5: Initial void ratio e_0 and initial porosity n versus height of free fall h_f .

2.2.3 Oedometric compression tests

After its preparation, the specimen was carefully placed on the loading platform of the compression system, as shown in Fig. 2.6. In this system, the piston was fixed to the load cell which has a maximum capacity of 1,000 N. A linear variable differential transformer (LVDT) was installed to measure the displacement of the loading platform. Before

recording the signals, the cell was moved upward in order to approach the piston. A rate of 0.5 mm/min was set up for the loading cycle. The maximal applied force was limited approximately to 700 N. All signals of load cell and LVDT were received by the data logging system using the software LabVIEW.

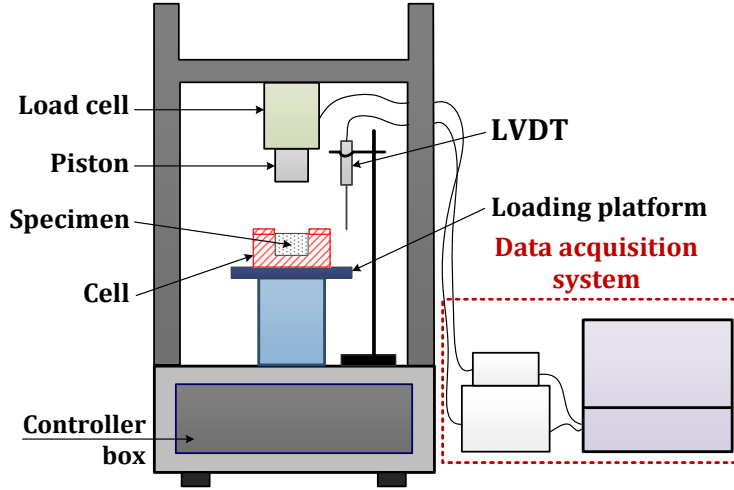


Figure 2.6: Schematic view of oedometric compression system.

After compression, all specimens were taken out from the cell (see Figs. 2.2(d) and 2.3(d)) to measure their mass and final height. These measures were then used to validate the quantities measured after preparation and shown in Table 2.1. These final measurements allows verifying the final state of the specimens after compression.

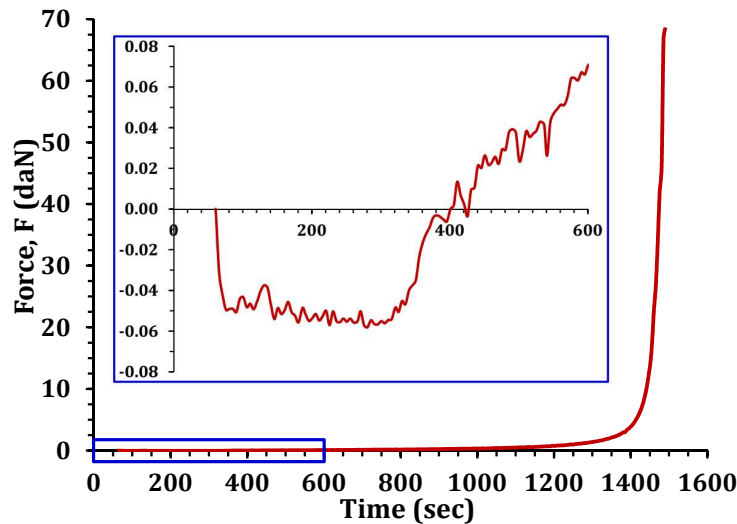


Figure 2.7: Applied force versus time during compression process. The inset shows the signal noise during the initial stage when the specimen approached and touched the piston.

Fig. 2.7 illustrates a typical evolution of the applied force with time during the compression process. Based on this curve, the initial vertical stress was specified after

removing the effect of noise (see inset of Fig. 2.7), specifically at the moment when the specimen surface touched the piston. The settlement of specimens was then determined from the displacement measured by the LVDT. The void ratio was finally calculated from the settlement and the initial void ratio of specimens.

2.2.4 X-ray computed tomography tests

2.2.4.1 X-ray scanner in Laboratoire Navier

The CT images of this work were captured on the XRCT laboratory scanner available at Laboratoire Navier (UltraTom microtomograph from RX-Solutions) using a micro-focus source Hamamatsu L10801 (230 kV, 200 W, 5 μm) and a “flat-panel” imager Paxscan Varian 2520 V (1920x1560 pixels, pixel size 127 μm). The hollow rotation stage is able to support heavy samples (up to 100 kg) and was designed to receive in-situ experiments. A view of the in-situ experiments performed in the laboratory is illustrated in Fig. 2.8.

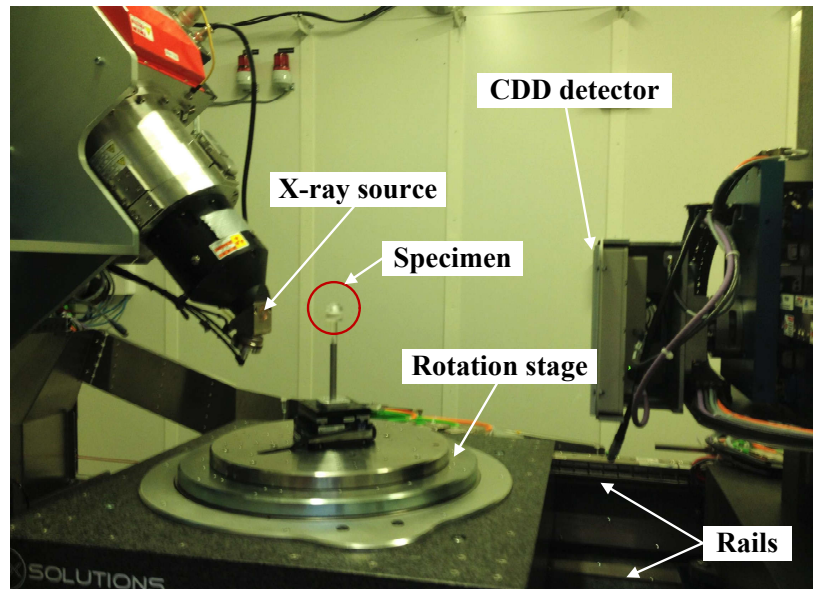


Figure 2.8: Global view of in-situ compression test combined with XRCT at Laboratoire Navier.

The XRCT images are reconstructed by using the GPU-based reconstruction software Xact developed by RX-Solutions. Some filters may be used to correct some artifacts as ring artifacts.

2.2.4.2 Apparatus

Apart from the cell $\phi 20$, several gaskets and pistons were also designed for performing XRCT scans, as shown in Fig. 2.9. The height of pistons were manufactured with different values in millimeter, as written in Fig. 2.9(a). Several wedges in paper were

also made with different values of thickness, as shown in Fig. 2.9(b). These wedges are used to alter accurately the compressed height during the in-situ compression tests.

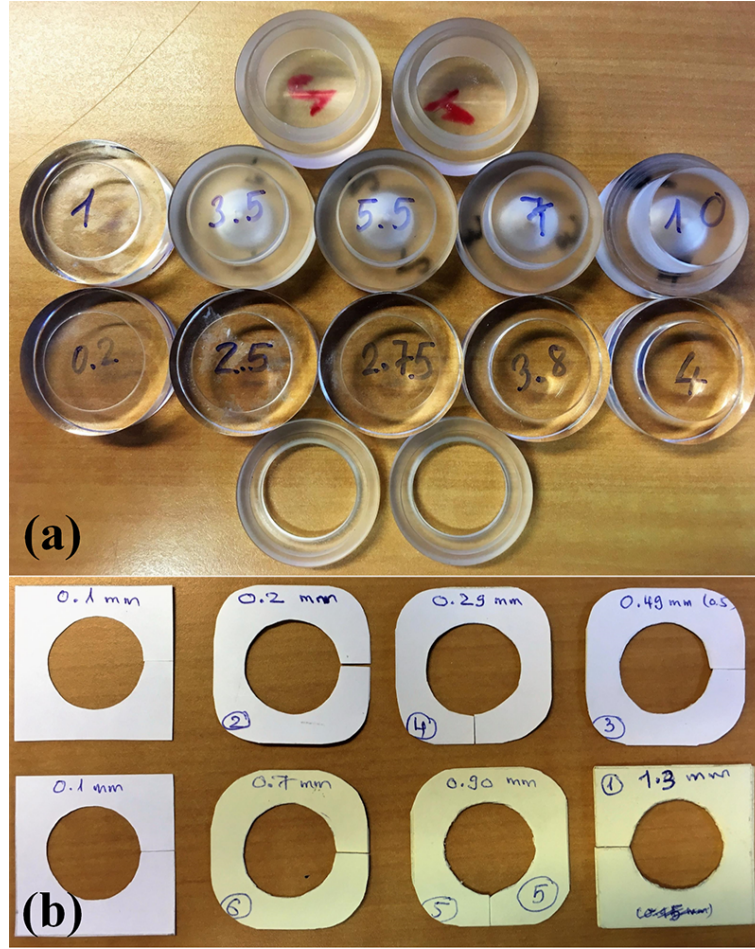


Figure 2.9: (a) The PMMA cell with several gaskets and pistons (heights δ given in mm, see Fig. 2.10 for definition of δ). (b) Several wedges with different values of thickness.

2.2.4.3 Scanning procedure

The scanning procedure combined with an in-situ compression test for the sample CT03 (mentioned in Table 2.1) is now described. The specimen was scanned at various stages of compression; the order of scanned compressed heights is depicted in Fig. 2.10. The detailed scanning program is given in Table 2.2, in which the void ratio was calculated from the compressed height and initial parameters of sample CT03. The height of pistons δ is given in Fig. 2.9.

At each level of the compressed height, a 3D image was scanned at the scale of the whole specimen (scans hereafter referred to as “global scan” or GS). Besides, at the levels corresponding to heights h_1 , h_3 , h_5 , and h_7 , 3D images of the central part of the specimen (see the 10-mm diameter dashed-region in Fig. 2.10) were also scanned at a finer scale for a more detailed view of the grains and the pores (scans hereafter referred to as “local

scan” or LS). For the global scans, X-ray source voltage and current were respectively 70 kV and 130 μA ; the voxel size was 13 μm and a single scan lasted 80 min. For the local scans, X-ray source voltage and current were respectively 70 kV and 95 μA ; the voxel size was 6.5 μm and a single scan lasted 240 min. 3D images were saved in 16 bits and subsequently converted into 8 bits in order to reduce memory usage for subsequent image analyses.

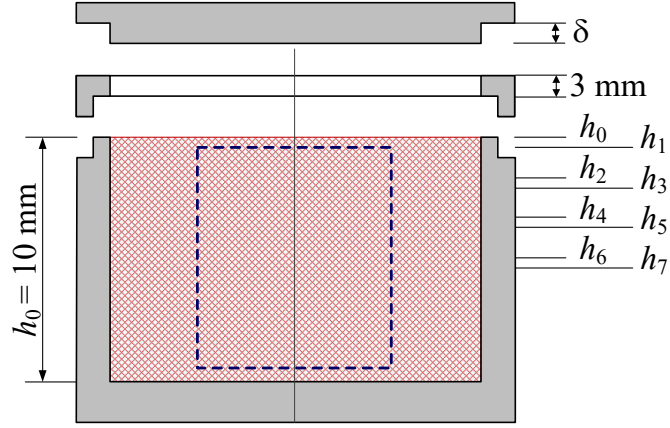


Figure 2.10: Illustration of the compressed heights of in-situ compaction test that were scanned for XRCT. The dashed-region corresponds to a 10-mm diameter cylinder and denotes the central part of specimen imaged during local scans.

Table 2.2: Details of the scanning program. G: global scan, L: local scan.

Scan	h_i (mm)	e_i (-)	Notation
01	h_0 10	2.2963	S01G
02	h_1 9.8	2.2303	S02G
03	h_1 9.8	-	S03L
04	h_2 8.7	1.8678	S04G
05	h_3 8.5	1.8678	S05G
06	h_3 8.5	-	S06L
07	h_4 7.5	1.4722	S07G
08	h_5 7.3	1.4063	S08G
09	h_5 7.3	-	S09L
10	h_6 6.4	1.1096	S10G
11	h_7 6.2	1.0437	S11G
12	h_7 6.2	-	S12L

2.3 Mechanical behavior under increasing vertical stress

All the tests were carried out on specimens with very loose initial structures, from $e_0 = 2.35$ to $e_0 = 1.50$. Fig. 2.11 shows the compression curves for different values of initial void ratios. All the tests were duplicated to check repeatability. The initial stress at the bottom of specimens including their weight varies equals 0.048 kPa and 0.024 kPa for cells $\phi 50$ and $\phi 20$, respectively.

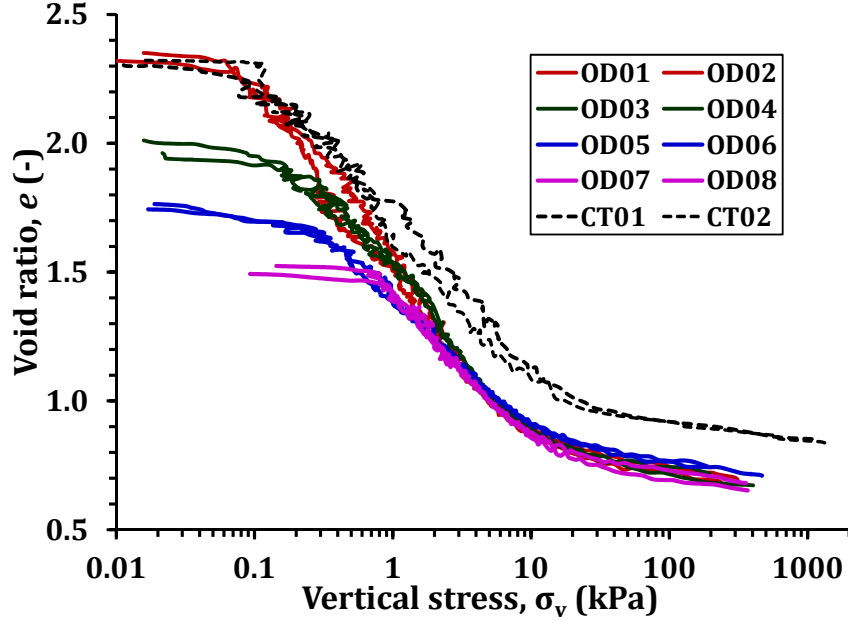


Figure 2.11: Void ratio versus vertical stress during oedometric compression tests for cells $\phi 50$ and $\phi 20$.

Based on the shape of these curves and the range of vertical stress, three stages can be identified. During the first stage, under low stresses (< 0.1 kPa), void ratio e slightly decreased. Void ratio then sharply decreased in the intermediate stage. Finally, in the third stage, void ratio gradually decreased for vertical stresses larger than 10 kPa. In particular, all curves (except those for cell $\phi 20$) are very close in this stage, irrespectively of the initial void ratio. In other words, when almost no further rearrangement is possible, the decrease of void ratio was very small and almost limited to the elastic deformation of grains at the contact points.

For the cell $\phi 20$, upon growing of the vertical stress, the decrease of void ratio is slower than for the cell $\phi 50$. This can be explained by the effect of the diameter (20 mm against 50 mm) and the height (10 mm against 20 mm) of the cell, which tend to increase lateral friction.

It should be recognized that the macroscopic behavior of the studied material under 1D compression tests is very special. Indeed, in soil mechanics [1, 5, 219, 30], only the first two stages are observed in oedometric compression curves. Interestingly, the last stage

observed in the compaction curve in the present study was also described in the S-shape curves obtained by Tang *et al.* [219]. Similarly, three stages are also observed in the numerical results of isotropic compression with the same material [47].

2.4 Global scan observations

Eight global scans (Table 2.2) were successively captured at various the compaction steps, and were named as follows: S01G, S02G, S04G, S05G, S07G, S078G, S10G and S11G. 3D image analyses were carried out by using the open source software Fiji.

2.4.1 3D reconstruction from the image stack

After converting to the 8-bit images, the 3D sample volume at different states of compaction was reconstructed, as shown in Fig. 2.12. These 3D images, with diameter 20 mm and height h_i , correspond to the global scans given in Table 2.2. A quarter of these 3D images was removed to observe the inside of the specimen. Pores and grains can be distinguished thanks to grey levels. Lighter grey levels typically correspond to more absorbing materials, while darker grey levels correspond to less absorbing materials.

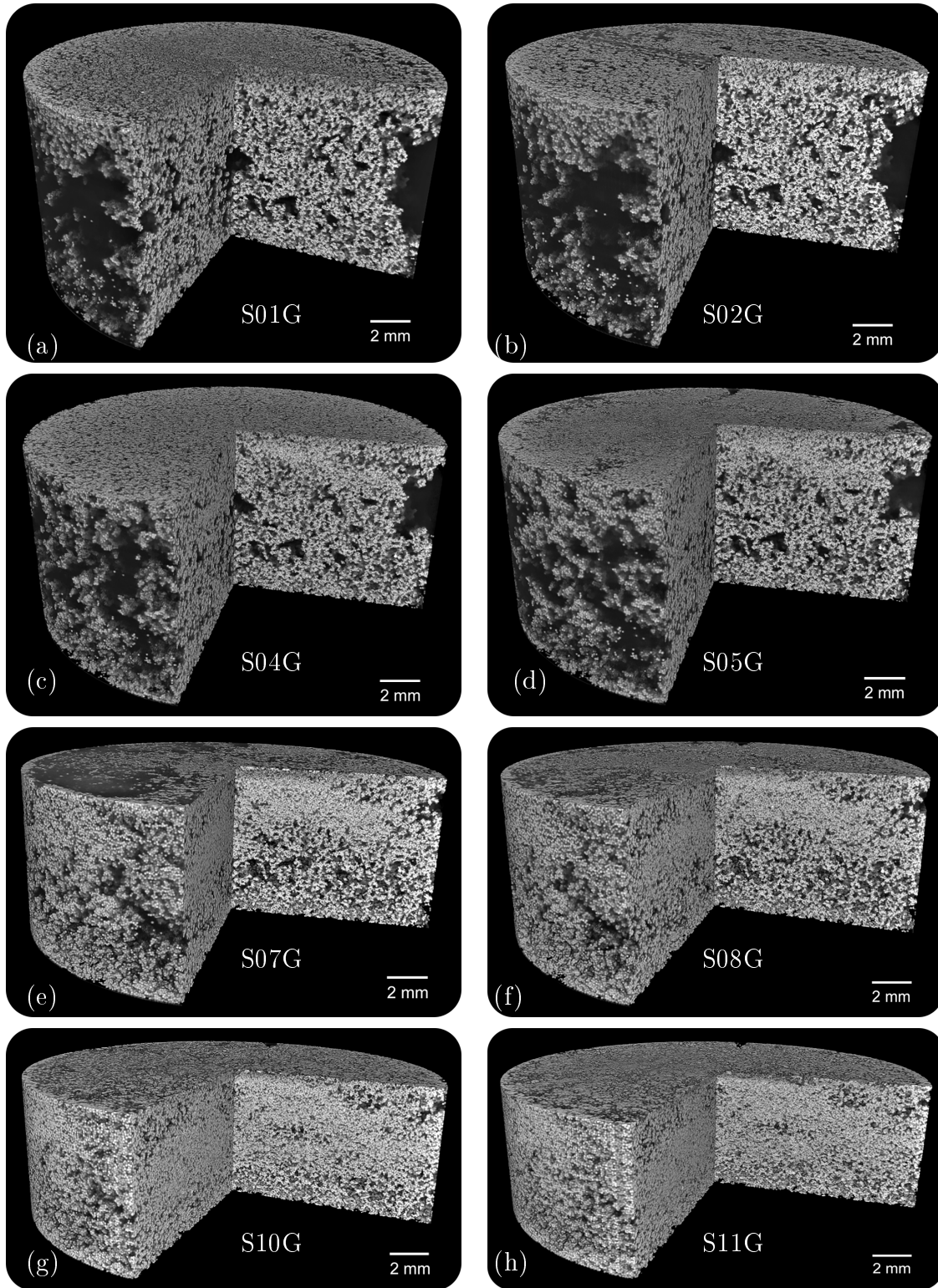


Figure 2.12: 3D reconstructed images of the specimen at different stages of compaction. From (a) to (h), the images correspond to the global scans in Table 2.2.

2.4.2 Segmentation process

From the 3D image stacks of all global scans, the grey level histograms were successively extracted, as shown in Fig. 2.13. For 8-bit images, grey levels range from 0 to 255. Depending on compaction steps, the two peaks more or less visible on each histogram are progressively changed. The first one on the left-hand side strongly decreases while the second one on the right-hand side increases. At the highest level of compaction, the left peaks of the dark-green curves (continuous and dashed lines) almost no longer exist. Meanwhile the peaks of these curves on the right-hand side reach the highest level. This confirms that the specimen approached a very dense state.

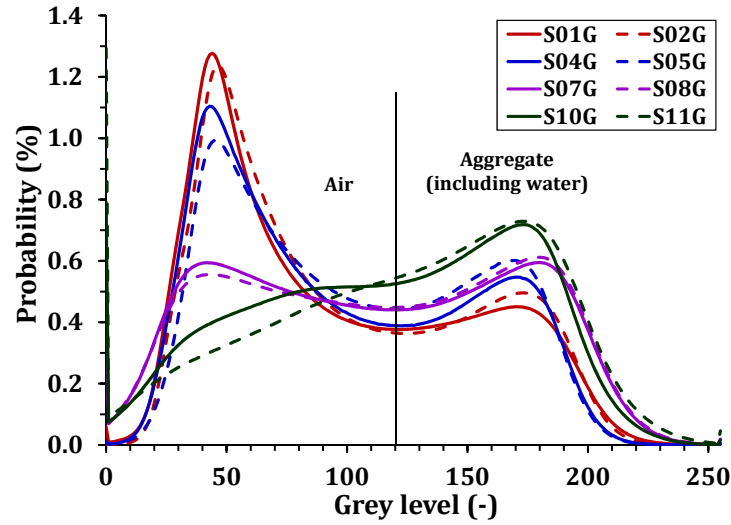


Figure 2.13: Illustration of grey level histograms for all global scans.

Furthermore, a threshold, shown for illustrative purpose on the same figure, was used to delineate a border between air dominated portions of the sample (left of the line) and aggregates (including water) on the right of the line. Distinct grey-level threshold values were found in the interval [105:135], depending on the considered compression step. With this piece of information, the images were segmented to recalculate the total void ratio, as well as the void ratio distribution during the compaction test. Grey-level threshold values of 128, 129, 121, 127, 131, 132, 128 and 133 were selected for scans S01G, S02G, S04G, S05G, S07G, S08G, S10G, and S11G, respectively.

There exist a lot of segmentation methods in the Fiji software. In the present study, the IsoData algorithm, proposed by Ridler and Calvard [220], was chosen for all analyses. The procedure divides the image into object and background by taking an initial threshold, then the averages of the pixels at or below the threshold and pixels above are computed. The averages of those two values are computed, the threshold is incremented and the process is repeated until the threshold is larger than the composite average. That is, $\text{THRESHOLD} = (\text{AVERAGE BACKGROUND} + \text{AVERAGE OBJECTS})/2$. Fig. 2.14 shows an example (horizontal slice) of the segmentation process corresponding to two

consecutive stages: a) initial state (original image) and b) segmented image (or binarized image). After thresholding, the aggregates (black) and the air (white) are clearly distinguished. The void ratio is then recalculated by dividing the number of black voxels by the total number of voxels of the 3D segmented image.

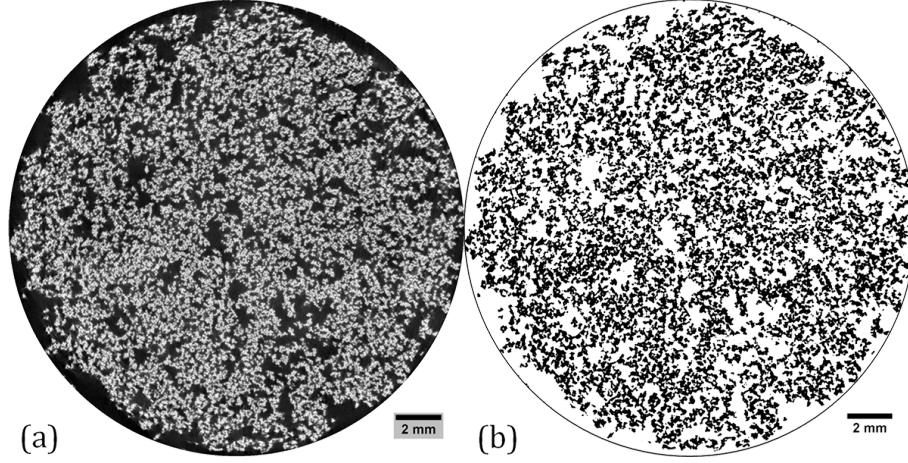


Figure 2.14: Images at different steps of segmentation: (a) original image, (b) segmented image (or binarized image).

2.4.3 Heterogeneity

2.4.3.1 General description

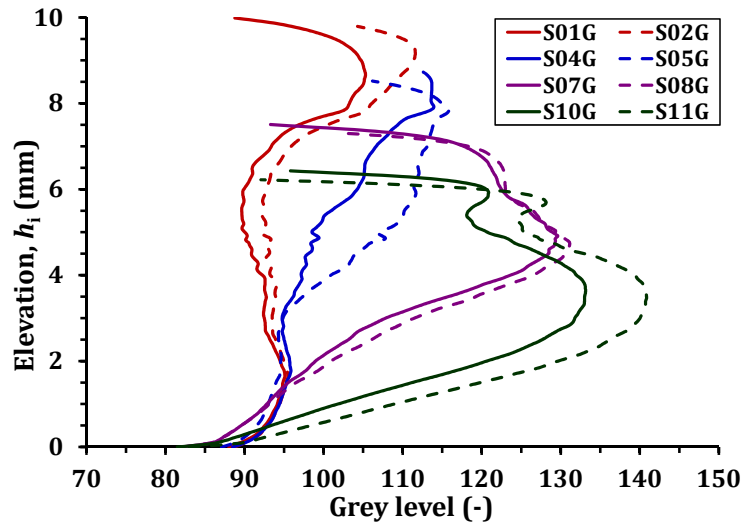


Figure 2.15: Illustration of grey level as a function of the height of specimen.

As shown in Fig. 2.12, it appears clearly that the density is not homogeneous within the cylindrical sample, especially at the periphery where more voids are observed. A larger density with less voids at the top and bottom of the specimen is also observed.

There exist also several large holes in the center of the specimen in the first compression steps (S01G, S02G, S04G, and S05G). This is due to the specimen preparation, and also to the boundary conditions imposed by the ring. In other words, during the specimen preparation, the friction between the external ring and the grains opposes to the displacement of other particles. The cohesion of grains also plays a remarkable role to limit the movement of particles.

At higher levels of compaction (Figs. 2.12(e, f, g, and h)), the structure is strongly rearranged in the central layers because the densest state is obtained in this region (horizontal band). Reversely, the structure is slightly affected at the bottom and top layers.

Moreover, the average grey level distributions of all global scans were also extracted to observe the change of density during compaction. Fig. 2.15 illustrates the average grey level according to the elevation (h) of all scans during compaction. In general, the specimen is not homogeneous. Initially, the specimen is fairly homogeneous from $h = 1$ mm to $h = 7$ mm (from bottom to top of specimen). After a slight compaction (S02G), the density of the upper part of specimen slightly increases while the one at the lower part (from 0 to 2 mm) is not changed. The upper part of specimen is continuously compressed at higher compaction (S04G and S05G) while the lower part is negligibly disturbed. For the highest compaction (S07G, S08G, S10G, and S11G), the central layers of the specimen are strongly settled, while the bottom layers are insignificantly rearranged.

2.4.3.2 Spatial distribution of void ratio

In order to observe the spatial distribution of void ratio of all global scans during the compaction test, five types of diagram are proposed in Fig. 2.16. Firstly, the sample is divided in ten equal layers h_i (Fig. 2.16(a)). Ten concentric hollow cylinders with average diameter R_i are then distinguished (Fig. 2.16(b)). Thirdly, the sample is split into eight equal sectors (Fig. 2.16(c)). Fourthly, five different volumes, with the size $L \times B \times H = 10 \times 10 \times H$ mm³ = $770 \times 770 \times H$ voxels³ (H is specimen's height) are investigated (Fig. 2.16(d)). Twelve different volumes according to X and Y directions are finally identified (Fig. 2.16(e)). Their size is $L \times B \times H \simeq 3.25 \times 3.25 \times H$ mm³ = $250 \times 250 \times H$ voxels³. Hereafter, the five above diagrams are referred to as diagram 1, diagram 2, diagram 3, diagram 4, and diagram 5, respectively.

For the diagram 1 (Fig. 2.16(a)), the void ratio distribution according to the elevation for different compaction steps is depicted in Fig. 2.17. At the initial state (S01G and S02G), from bottom to top, the void ratio is largest at the sixth layer ($e_{\max} = 2.65$) because of the influence of the wall in the specimen preparation process. Meanwhile the sample is denser at the bottom layers and densest at the top layers. This is caused by the end of preparation process when the grains were widely spread on the surface of

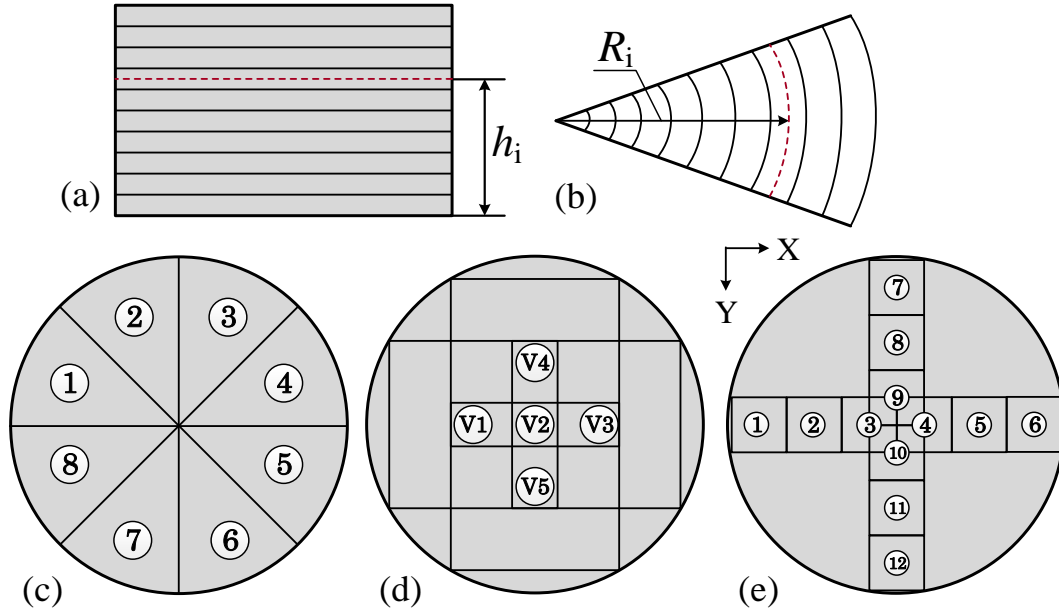


Figure 2.16: Schematic view of several types of diagram for calculating the heterogeneity. (a) Ten equal layers, (b) ten concentric cylinders, (c) eight equal sectors, (d) five different volumes, and (e) different volumes according to X and Y directions.

the cell. The top layers are therefore more homogeneous than the other layers. These observations confirm that the void ratio in this region is the smallest initially. For the higher compaction level (S04G and S05G), the structure is notably compacted and rearranged. Void ratio in the central and top layers is reduced, especially the central layers of scan S05G. Up to scans S07G and S08G, the structure is significantly perturbed. The void ratio in the central layers strongly decreases (from $e = 2.25$ to $e = 1.15$, $\approx 49.80\%$). This reduction is larger than the one observed in the bottom layers and the top layers (from $e = 1.51$ to $e = 1.15$, $\approx 23.25\%$). At the densest states (S10G and S11G), a strong decrease of void ratio is obtained in the central layers ($e_{\min} = 0.7$) while the structure in the bottom layers is slightly rearranged. Actually, when the specimen becomes denser in the center, the corresponding layers seem to prevent the displacement of the top layers. This explains why it is really difficult to compact this specimen at S11G although the total void ratio is decreased by approximately 50 % (from $e = 2.23$ to $e = 1.11$). This is already confirmed via the decrease in the total void ratio in Fig. 2.11 from the loosest state (S01G) to the densest state (S11G).

For the diagram 2 (Fig. 2.16(b)), Fig. 2.18 depicts the spatial distribution of void ratio which is investigated as a radial function, considering different concentric hollow cylinders having the same height for each scan. In general, the mean distribution of void is rather regular, except the center and periphery of the cylinders in the first four scans. Once again, this demonstrates the remarkable effect of the wall friction which is already mentioned above. In the last four scans, void ratio e variation with the distance to the center is negligible. This reflects the homogeneity of the specimen under the higher

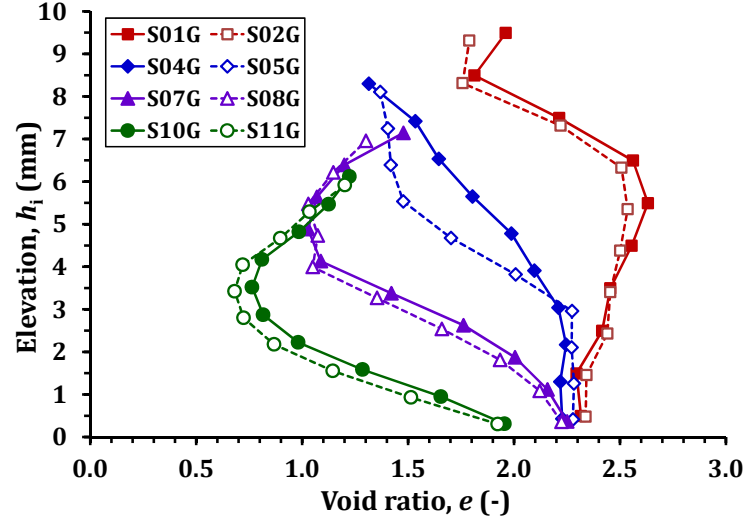


Figure 2.17: Void ratio distribution according to the compressed height of sample for different compaction steps (diagram 1).

compaction levels.

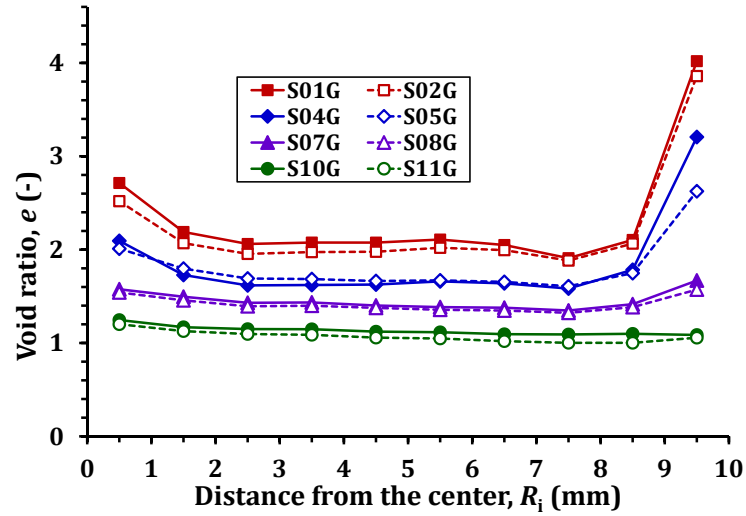


Figure 2.18: Void ratio distribution according to the average radii of the selected cylinders for different compaction steps (diagram 2).

For the diagram 3 (Fig. 2.16(c)), the void ratio distribution according to eight equal sectors for different compaction steps is illustrated in Fig. 2.19. In general, the distribution of void ratio is fairly regular at the initial state, except for sectors S1 and S8 in first four steps (S01G, S02G, S04G and S05G). In these sectors, there exist several large pores between grains and the wall (see Fig. 2.12). For the denser states (last four steps), the structure is really homogeneous.

For the diagram 4 (Fig. 2.16(d)), the void ratio distribution according to five equal volumes for different compaction levels is depicted in Fig. 2.20. With this diagram, the

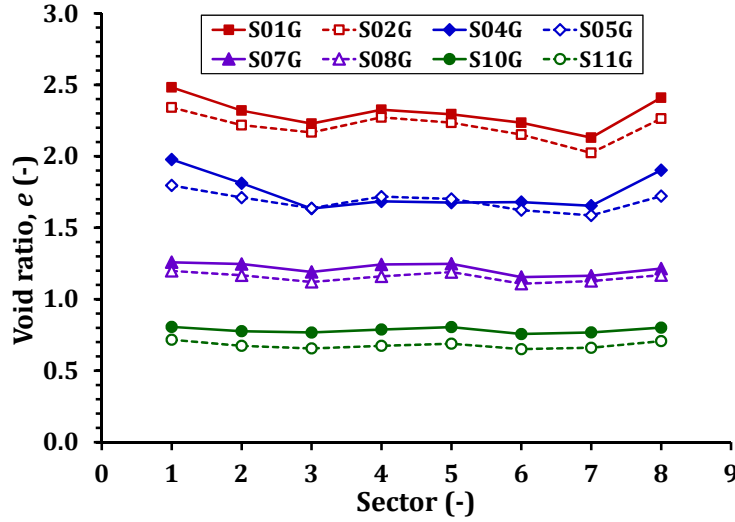


Figure 2.19: Void ratio distribution according to eight equal sectors for different compaction steps (diagram 3).

distribution of void ratio is always homogeneous upon growing of compaction level. Each volume is approximately equal to one-third of the total volume of the specimen. It can therefore be considered as a Representative Elementary Volume (REV). We use these REV for the analyses in Sec. 2.4.4.

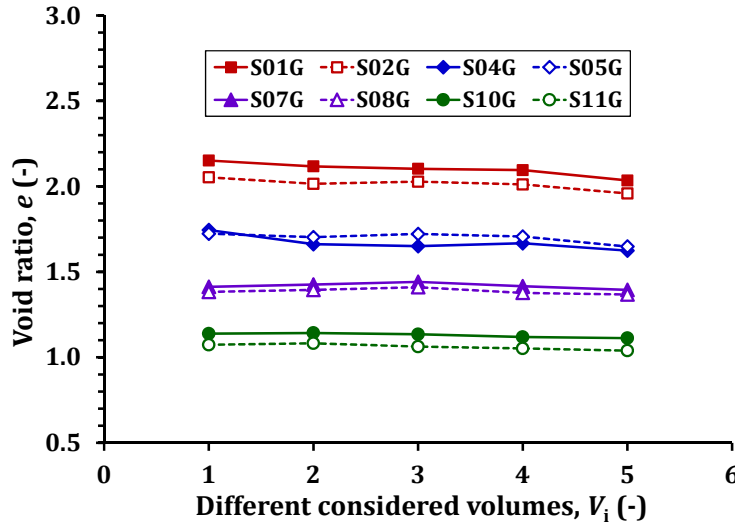


Figure 2.20: Void ratio distribution according to five equal volumes for different compaction steps (diagram 4).

For the diagram 5 (Fig. 2.16(e)), the void ratio distribution at different small volumes along the x and y directions for different compaction steps is shown in Fig. 2.21. At low compaction steps, a clear difference is observed in the void ratio values between the borders ($x = y = 2$ mm and 18 mm) and the center along the x direction. A significant difference is noticed along the x direction. It corresponds to the sectors S1 and S8 in

Fig. 2.16(c). Meanwhile, along the y direction, the distribution of void ratio e is smoother than the one in x direction.

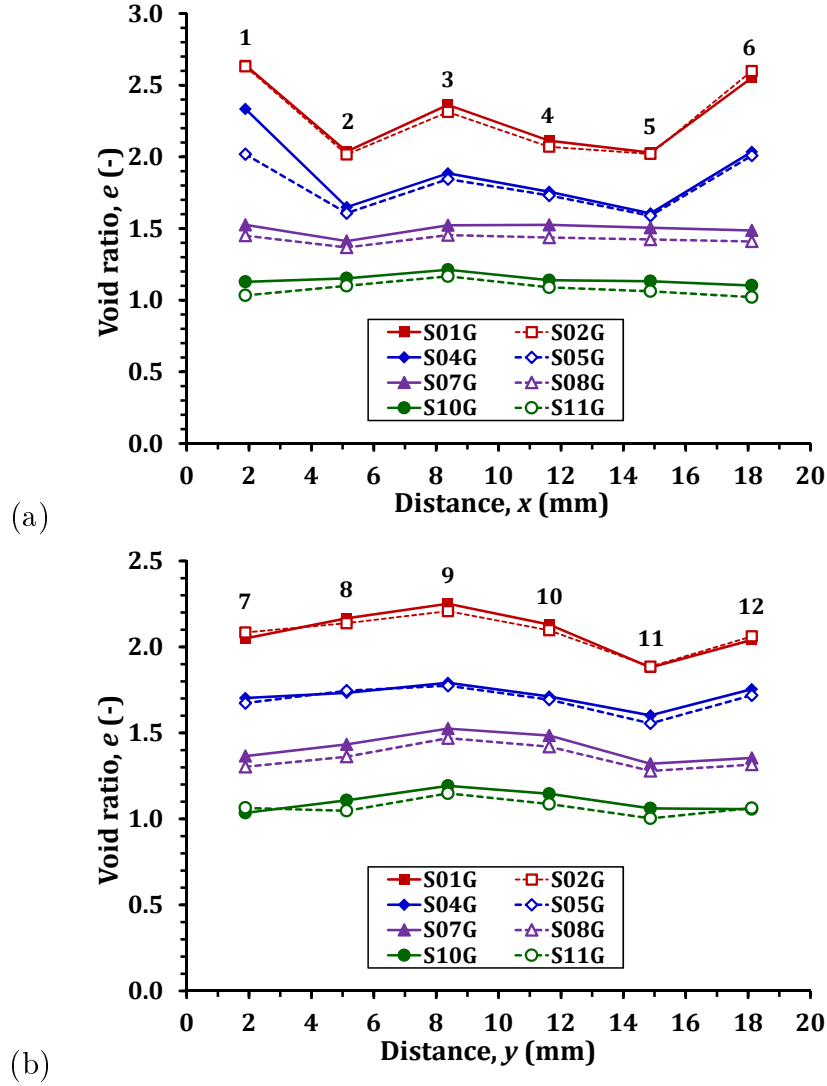


Figure 2.21: Void ratio distribution according to the x (a) and y (b) directions for different compaction steps (diagram 5).

2.4.4 Pore scale deformation

In order to ensure the homogeneity of the specimen during the compaction, the REV is used to analyze the pore scale deformation. The volume V2, already mentioned in the diagram 4 (Fig. 2.16(d)), is chosen for this analysis. Moreover, the use of smaller volume instead of the entire specimen aims to reduce the memory usage during image processing.

The total volume and the total pore volume of V2 for different compaction steps is shown in Fig. 2.22. The total pore volume is calculated by method already described in Sec. 2.4.3. With two adjacent scans, we can obviously observe a slight difference of the

total pore volume (see the blue columns in Fig. 2.22). The variation of the total volume is also obtained.

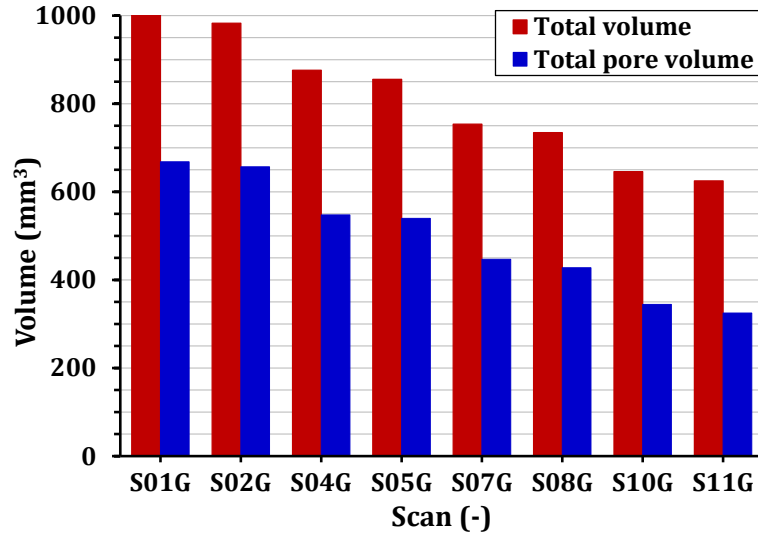


Figure 2.22: Total volume and total pore volume of volume V2 for different steps of compaction.

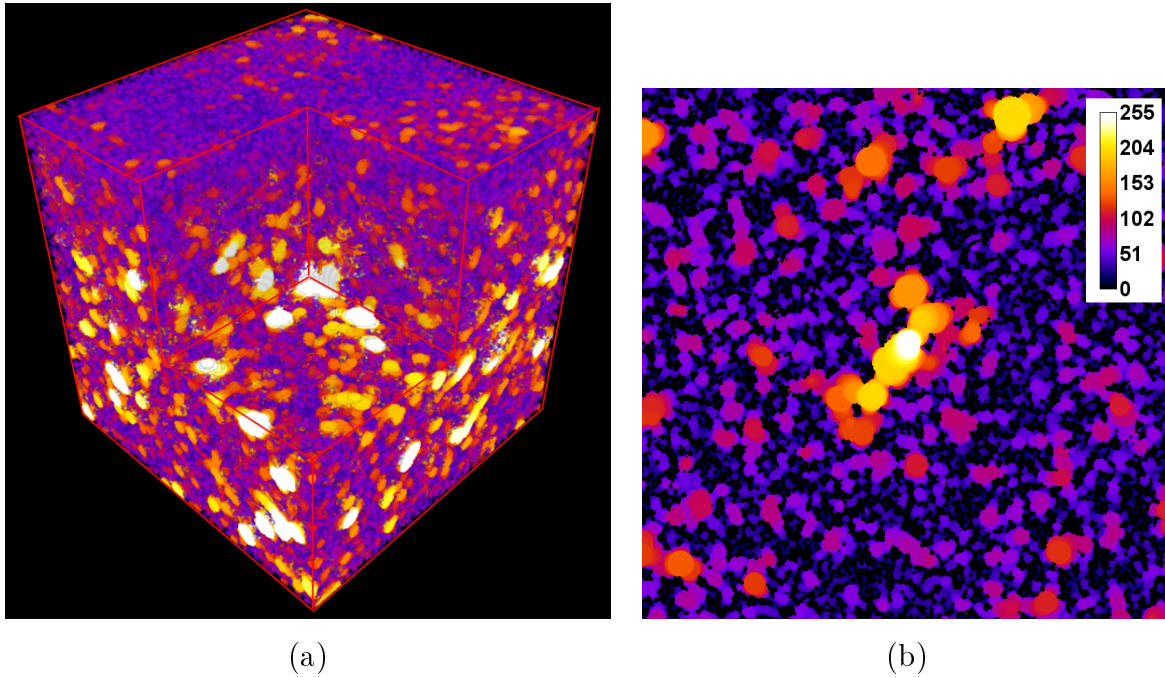


Figure 2.23: An example of the local thickness for volume V2 (a) at step S01G and a slice (b) extracted from (a).

Besides, the distribution of pore volume is also analyzed. The algorithm “thickness” [221, 222] in the plugin BoneJ of Fiji is applied to compute the local thickness of 3D structures in 3D images. It defines the thickness at a point as the diameter of the

greatest sphere that fits within the structure and which contains the point. In other words, the grains and the pores are precisely separated by this algorithm.

Fig. 2.23 shows an example of volume V2 at step S01G after applying the local thickness algorithm. In Fig. 2.23, the grains (only the black color) and the pores (the other colors) are clearly distinguished. Bright colors represent the larger pores. This can be easily observed via the bright volume in Fig. 2.23(a). Based on the histogram of the 3D images, the volumes of different pores are quickly calculated. Nevertheless, we can only compute the volume of the pores having the same size (or same color). Therefore, we cannot distinguish exactly the volume of every pore in the volume V2.

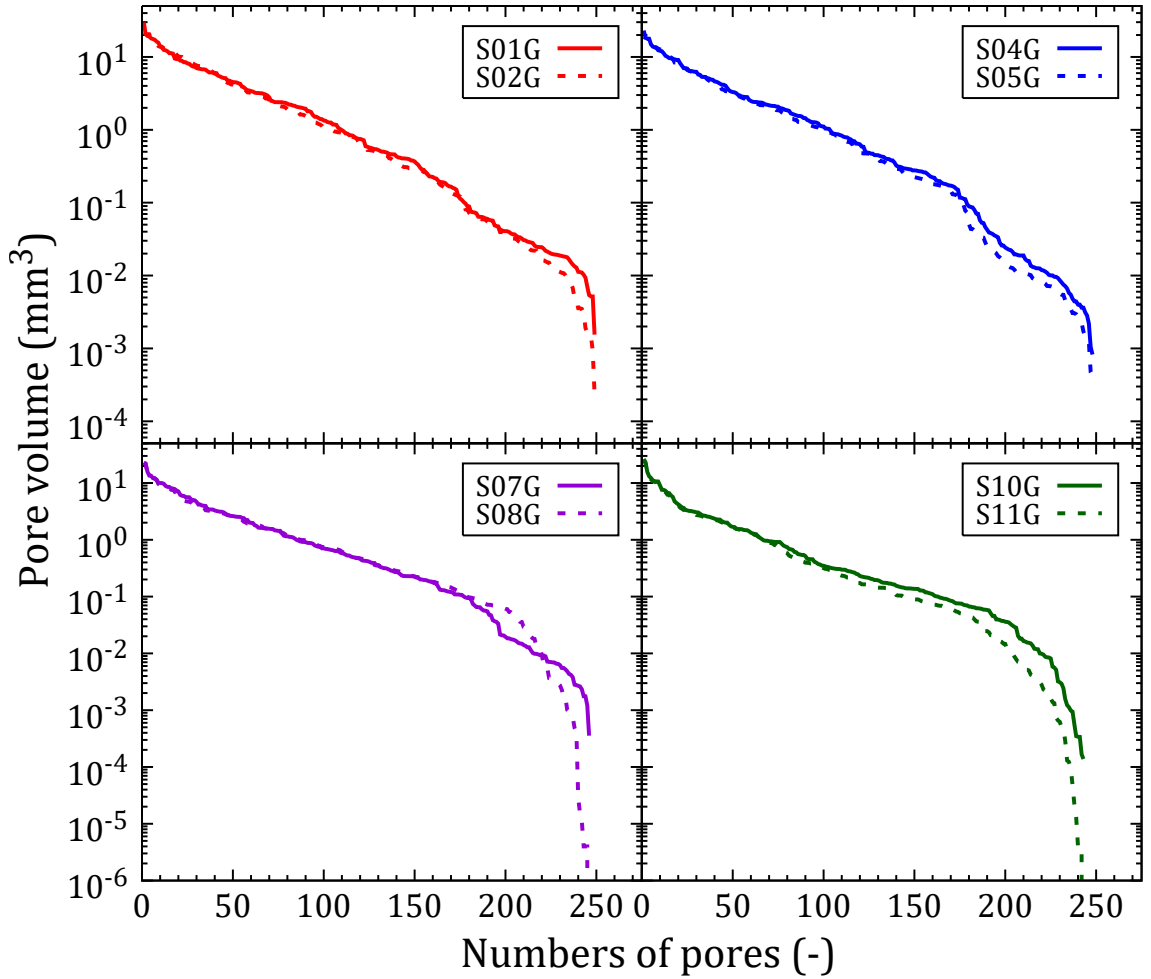


Figure 2.24: Distribution of pore volume of the volume V2 for different levels of compaction.

The distribution of pore volume in volume V2 for each of two adjacent scans is illustrated in Fig. 2.24. Numbers of pores mean the number of all the pores which have the same size (same colored voxels). In general, the shape of the distribution of pore volume in all cases is almost similar. More small pore volumes are created under growing of the compaction step. In each of two adjacent scans, the larger pore volumes are negligibly decreased while the smaller ones are significantly reduced (see the continuous

line and the dashed line in Fig. 2.24). For instance, in the initial stages (S01G and S02G – red curves), the smallest pore volume varies from $3 \times 10^{-4} \text{ mm}^3$ to $2 \times 10^{-3} \text{ mm}^3$, and in the final stages (S10G and S11G – green curves), the smallest one varies from 10^{-6} mm^3 to $2 \times 10^{-4} \text{ mm}^3$. Interestingly, in the larger compaction levels (S07G and S08G – violet curves), several pore volumes from the scan S08G (dashed curve) are larger than the ones from the scan S07G. This reflects a strong perturbation of the structure in these stages. The evidence in Fig. 2.17 also confirms this phenomenon.

2.5 Local scan observations

2.5.1 General principles

As described in Sec. 2.2.4.3, four local scans, with 10 mm in diameter, were captured from the central region of the global scans. An example of 3D reconstructed image from local scan is illustrated in Fig. 2.25. From the 3D tomography images of the local scans, cubical subregions (edge length = 1.95 mm) were extracted. One such subdomain is shown in Fig. 2.25(c). Ten such cubes (hereafter so-called *Standard Volume*, or SV) were randomly extracted at different positions within the local scan, to take into account the sample microstructure heterogeneity.

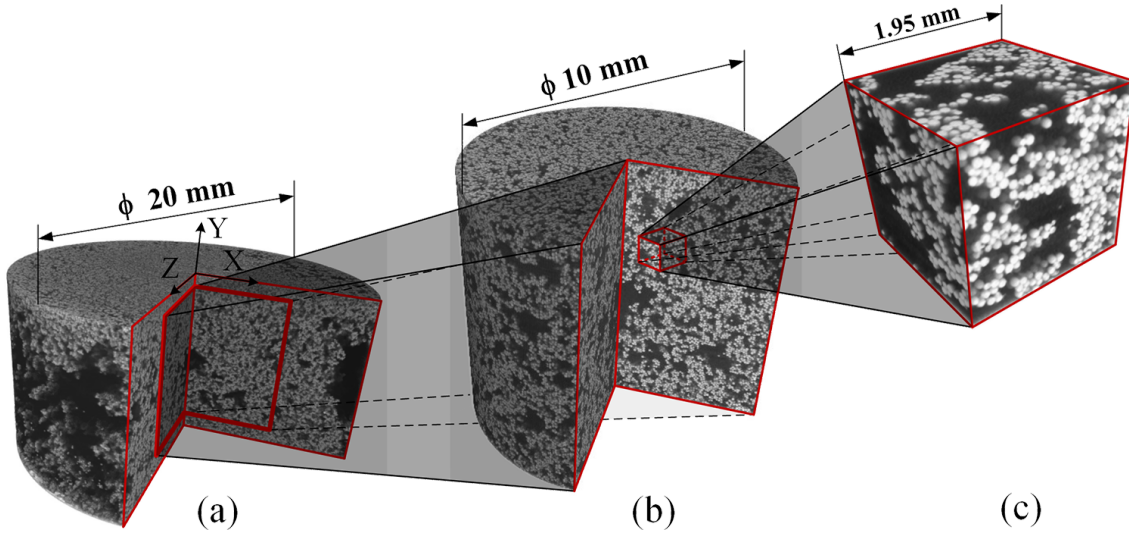


Figure 2.25: Position of the local scan (b) from the global scan (a) and an example of investigated cube (c).

The 3D reconstructed image of four local scans is shown in Fig. 2.26. The order of these scans is already given in Table 2.2. The quarter of each image is also cut for easily observing the structure. In general, these local scans are fairly homogeneous although there still exist several macropores at initial stages (S03L and S06L). For the denser stage, S09L, some of the pores are compressed, and the density is increased, especially in the central layers. The structure seems very homogeneous at the densest

stage, S12L. Therefore, the local scans are principally used to analyze the connectivity as well as the geometrical change induced by compaction. For the reason of computer's configuration, several small cubes instead of the entire local scan are extracted to perform the calculations.

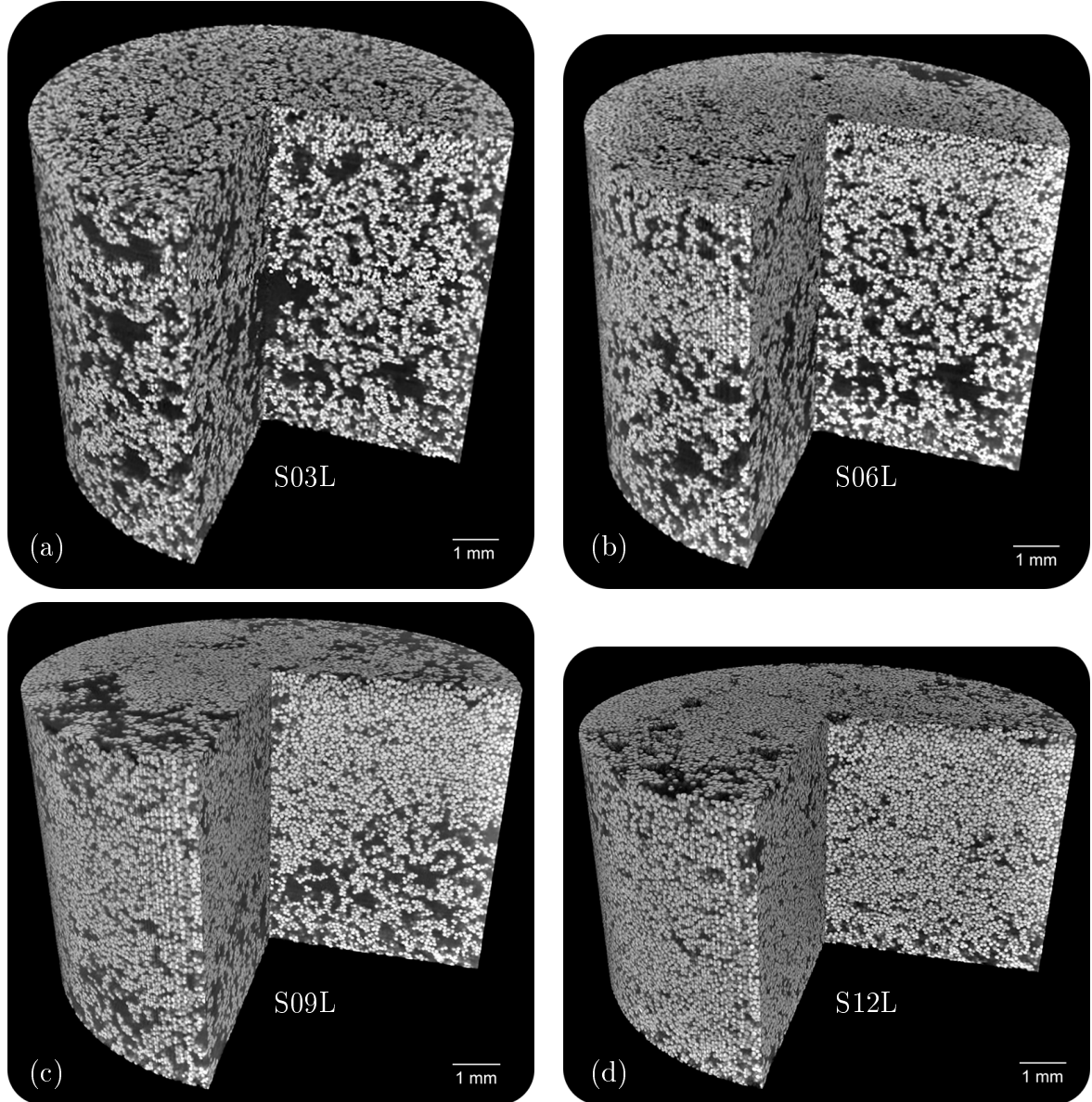


Figure 2.26: 3D reconstructed image of four local scans. (a) S03L, (b) S06L, (c) S09L, and (d) S12L.

Image processing was also performed by using the open-source software Fiji. Besides, the author's codes (using Matlab software, the programming language Python and the open-source software ParaView) were mainly used for the image analysis. The algorithm used to detect spherical structures of 3D images, developed by Xie *et al.* [223] in 3D is applied with a suitable development. This algorithm was modified from the one of Peng *et al.* [224] in 2D and the Adaptive Hough Transform algorithm (original algorithm)

of Illingworth and Kittler [225]. Furthermore, a 3D skeletonization algorithm, proposed by Lee *et al.* [226] and then developed into a plugin of BoneJ in Fiji by Doube *et al.* [227], is also applied to plot the contact network of particles.

2.5.2 Algorithm to detect spherical structures

The algorithm to detect spherical structures from tomography images is illustrated in Fig. 2.27. A 3D image with a cubic shape, and formatted as a 3D array, was first extracted from the local scans. The center's positions of spheres were then directly located within the 3D array. Afterward, the radii of the spheres (with identified central position) were identified. Finally, the 3D reconstruction process and analysis were carried out from the detected spheres.

The detailed description of the main algorithm (the dashed-red square in Fig. 2.27) will be given in the following subsections.

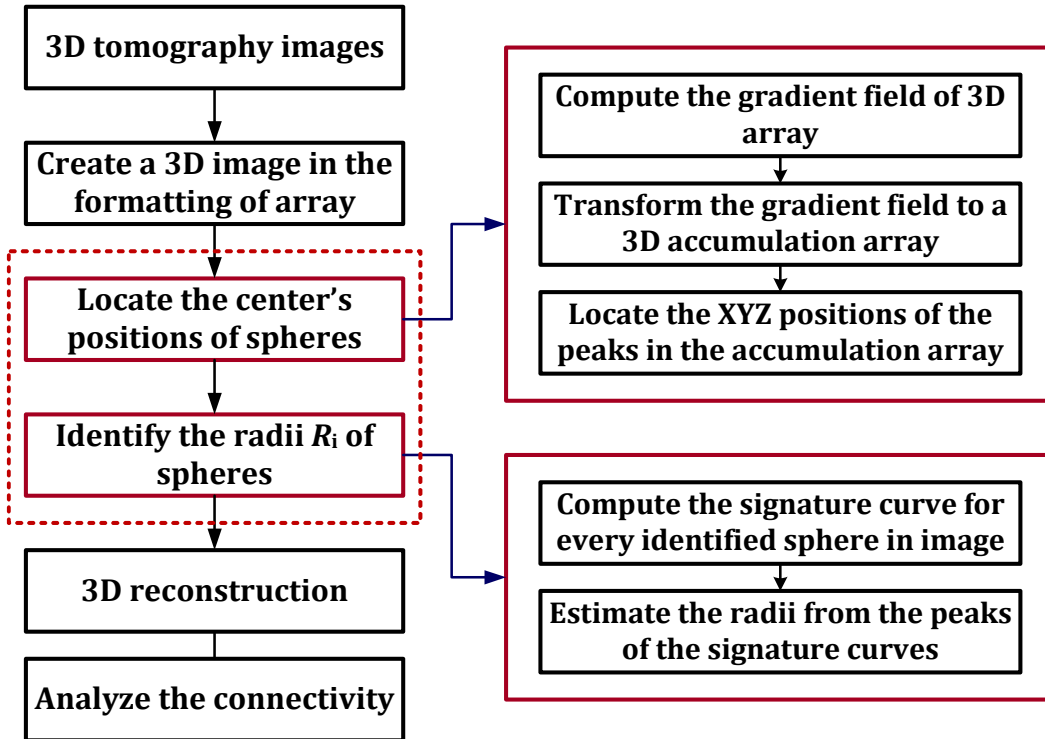


Figure 2.27: The algorithm to detect the spherical structures.

2.5.2.1 Locating the center's position of spheres

The method to compute the center's position of a sphere in the 3D image is first to identify the voxels that belong to that sphere, and then to compute the centroid of those voxels. The gradient field of image intensity is firstly computed using the following

equation:

$$\begin{aligned}\nabla I(i, j, k) &= (V_x, V_y, V_z)|_{(x,y,z)} \\ &= [I(i, j, k) - I(i, j, k - 1), I(i, j, k) - I(i, j - 1, k), I(i, j, k) - I(i - 1, j, k)]\end{aligned}\quad (2.1)$$

where (i, j, k) are the voxel indices, $\nabla I(i, j, k)$ is the gradient vector at voxel (i, j, k) , which consists of x , y and z components, and $I(i, j, k)$ is the image intensity at voxel (i, j, k) .

In a gradient field, the nonzero gradient vectors are either pointing toward the center of a sphere or away from it. So, a transform is defined to convert the gradient field to an accumulation array, in which the voxel intensity corresponds to the probability of that voxel being the center of a sphere. The accumulation array has the same dimension as the gradient field. In the accumulation image, the maximum intensity represents the center position of a sphere. The accumulation array is constructed by an adding process, as shown in Fig. 2.28. In the gradient field, for each nonzero gradient vector $\nabla I(i, j, k)$, a weight value is added to the voxels in the accumulation array upon the line segment which is defined by the vector $\nabla I(i, j, k)$. The length of the line segment is set to be the possible maximum diameter of the spheres, and the magnitude of $\nabla I(i, j, k)$ is used as the weight value. The accumulation array is built from the collecting of all nonzero gradient vectors from many directions. In Fig. 2.28, the darkest voxel has the maximum weight.

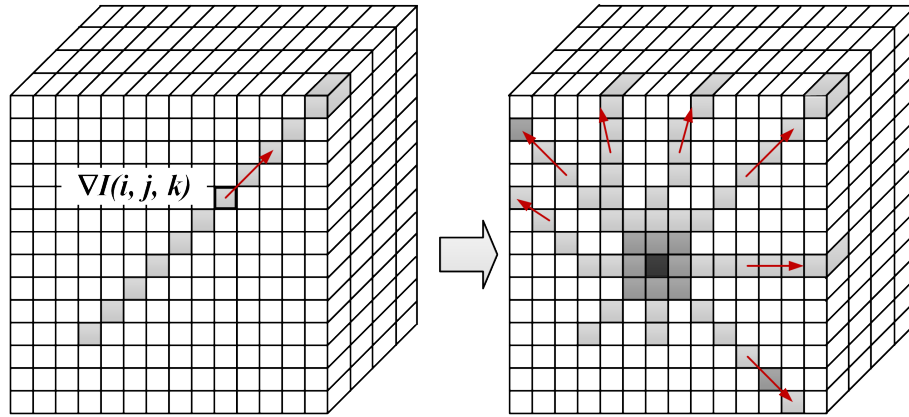


Figure 2.28: Construction of the accumulation array from the gradient field (the added nonzero gradient vector to the accumulation array for the left, and the accumulation array after adding the nonzero gradient vector in different directions for the right) (not to scale).

2.5.2.2 Estimating the radii of spheres

In order to determine the radii of spheres, a signature curve $f(r)$ is defined over the gradient field of the sphere's image, where r is the distance to the center position of the sphere and $f(r)$ is the averaged dot product of the gradient vector and the radial vector.

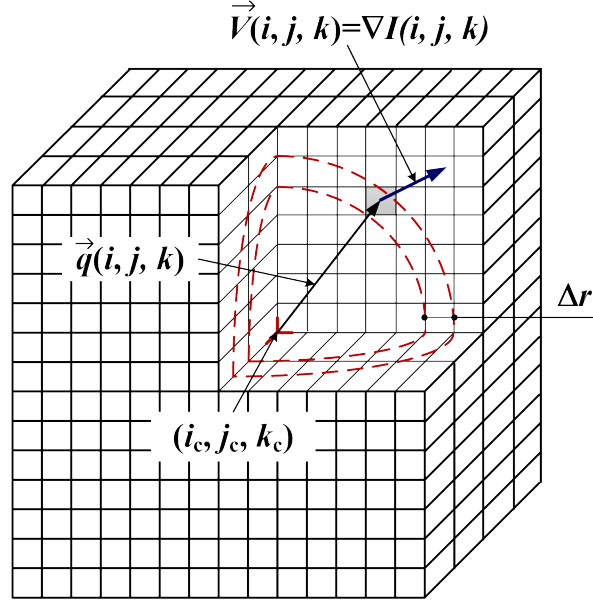


Figure 2.29: Definition of the signature curve (not to scale).

Fig. 2.29 depicts the definition of the signature curve, in which (i_c, j_c, k_c) is the center position of a detected sphere. For a voxel (i, j, k) in the neighborhood of (i_c, j_c, k_c) , let $V(i, j, k)$ be the gradient vector of the voxel, (i, j, k) and $q(i, j, k)$ be the vector joining (i_c, j_c, k_c) to the center of the voxel (i, j, k) . A sequence of discrete r values with fixed interval is selected. It represents distances to the sphere center (i_c, j_c, k_c) . For each r value, $f(r)$ is defined by the following equation:

$$f(r) = \frac{\sum_{||\vec{q}(i,j,k)|-r|<\Delta r/2} \left[\frac{\vec{V}(i,j,k) \cdot \vec{q}(i,j,k)}{|\vec{q}(i,j,k)|} \right]}{\sum_{||\vec{q}(i,j,k)|-r|<\Delta r/2} 1}, \quad (2.2)$$

where the sum is over all the voxels whose distance from (i_c, j_c, k_c) is within the range $[r - \Delta r/2, r + \Delta r/2]$.

Fig. 2.30 shows an example of the signature curve. From this curve, the radius of the sphere corresponds to the distance to center position having the highest value of $f(r)$. In the example shown, the radius equals seven times the voxel size. It is equivalent to 45.5 microns. Besides, other values of radius are also detected: 6 and 8 times the voxel size (equivalently 39 microns and 52 microns). Note that, in the present work, only rounded valued of radius were considered.

Fig. 2.31 illustrates an example for one slice in a 3D image. The blue disks are the detected spheres, and the red points represent their centers. Incomplete white disks at

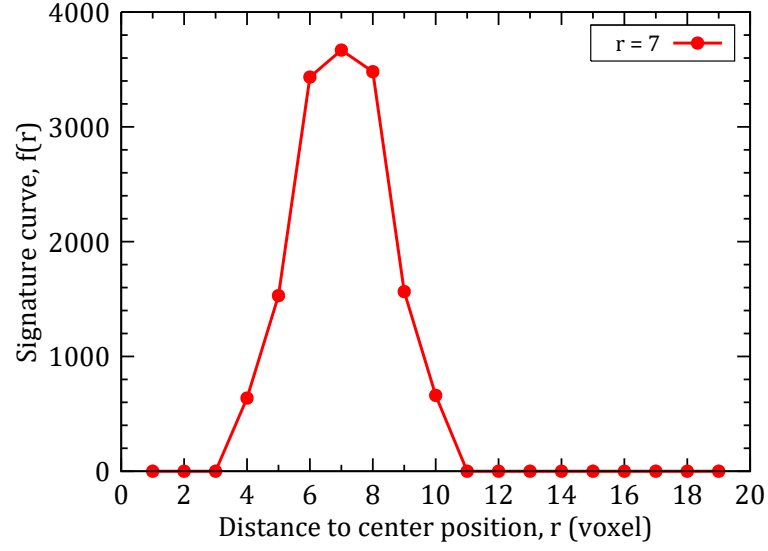


Figure 2.30: An example of a signature curve computed from the 3D image.

the border are not used for center detection.

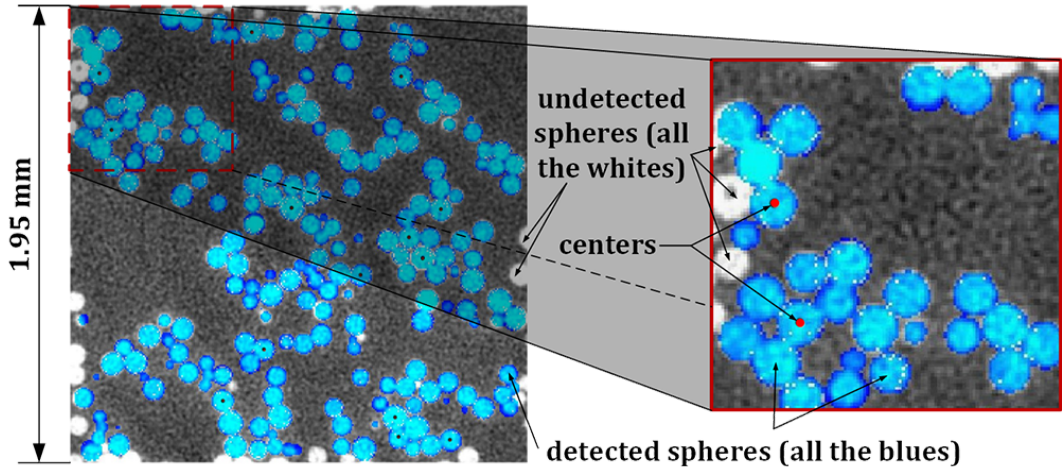


Figure 2.31: A slice in a 3D detected image (not to scale).

2.5.2.3 Estimating the lost contacts after the detection process

After the detection process, the spheres which have a part located outside of the border of the cube were not identified (see Figs. 2.25(c) and 2.31). Hence, the contacts between these spheres and their neighbors inside the standard volume were lost. In order to estimate the lost contacts, a method is proposed as follows. A new cube which is larger than the SV (see definition in Sec. 2.5.1) is created. It is called the Extended Volume (or EV) with the size b (see Fig. 2.32) which $b = a + 2d_{\max}$, where a is the size of the SV, d_{\max} is the maximum diameter of the detected spheres. The EVs were then detected with the same input parameters and compared with the SVs. All grains inside the SVs and the

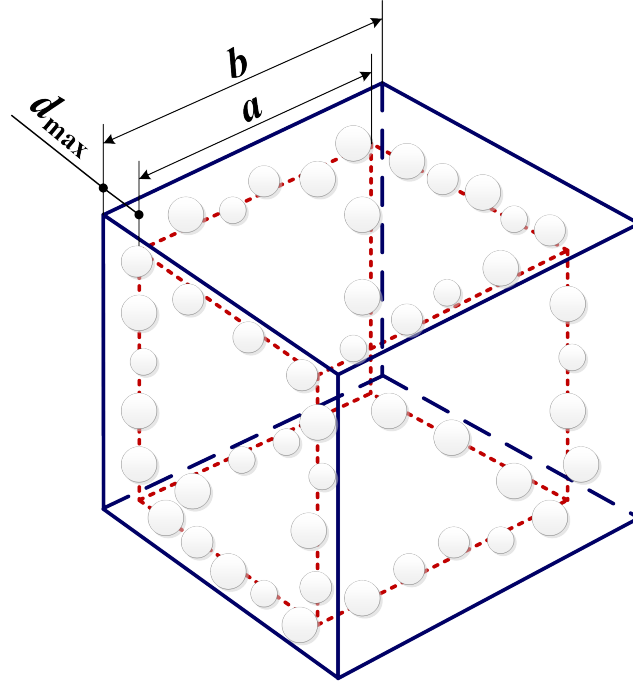


Figure 2.32: Method to find the lost contacts, inside cube is the standard volume; outside cube is the extended volume (not to scale).

EVs having the same coordinates were first identified. The grains, around the border of the EVs, which have contacts with the ones inside the SVs, were then distinguished. The lost contacts N_C^l of the SVs were finally found. They will be used in the analyses of geometrical changes in the following sections.

2.5.3 3D reconstruction after detection process

Fig. 2.33 shows an example of a 3D reconstructed cube before and after detection. Each cube, from top to bottom, corresponds to each local scan. On the left-hand side, the cubes are directly reconstructed from 3D images (before detection); on the right-hand side, the cubes are reconstructed from the detected spherical structures. As mentioned in Sec. 2.5.2.3, the incomplete spheres, located on the border of the SVs, are not identified. Hence, they cannot be seen in the cubes on the right-hand side in Fig. 2.33 (b, d, f, and h).

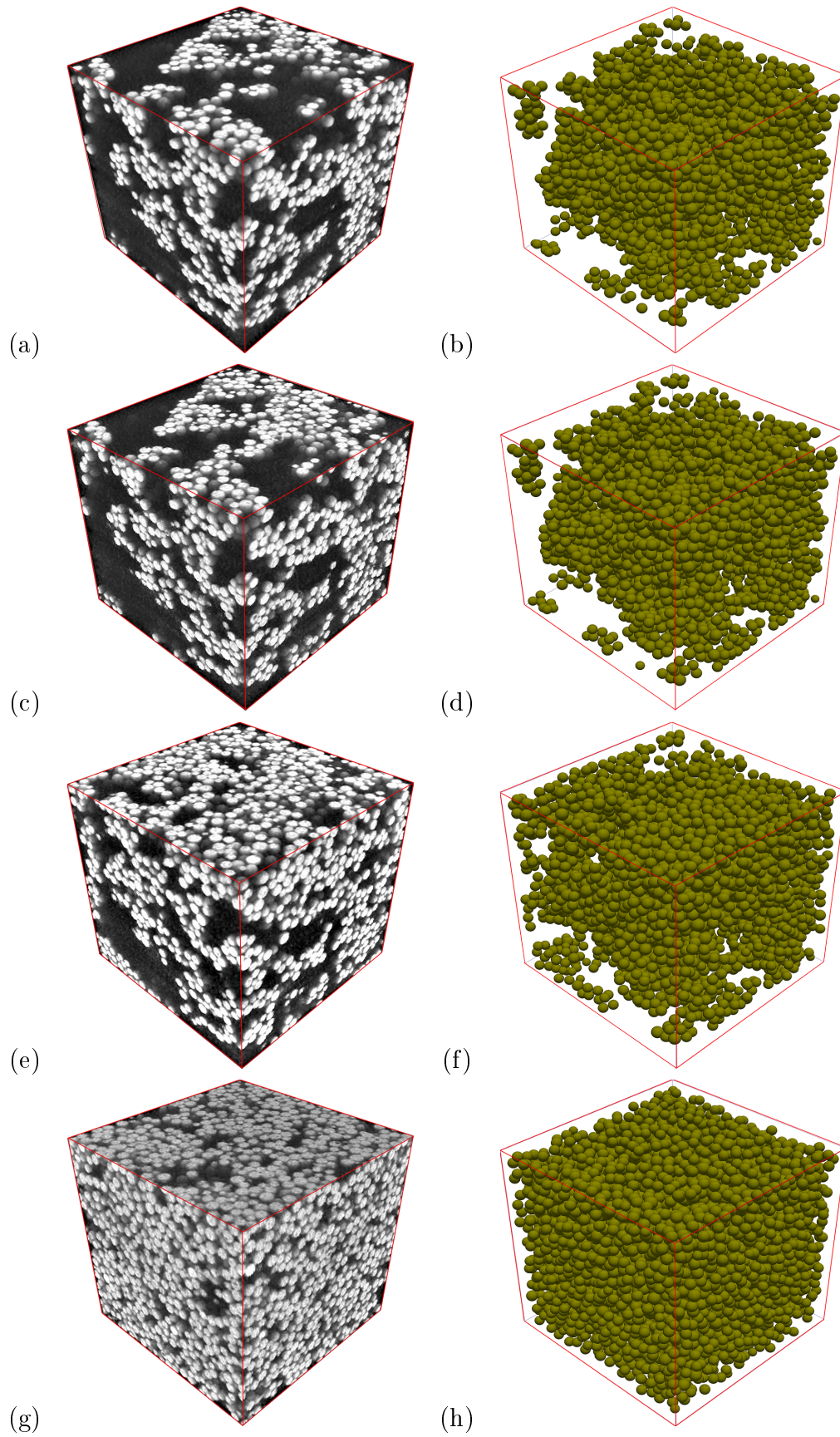


Figure 2.33: Example of 3D reconstructed cubes of four local scans. Left-hand side: before detection, right-hand side: after detection. Edge length = 1.95 mm.

2.5.4 Grain size distribution after the detection process

Fig. 2.34 shows the grain size distribution of all the SVs for the four local scans. Three values of radii (6, 7, and 8 voxels) were obtained after the detection process. In this process, the 7 voxels-radius occupied a maximum proportion, approximately 80 %, and the 6 voxels one occupied a minimum proportion, nearly 2.5 %. From the loosest state (S03L) to the densest state (S12L), the percentage of 7 voxels-radii increases and it reaches a maximum at S12L. Meanwhile, the percentage of 6 and 8 voxels-radii decreases and reaches a minimum also at S12L.

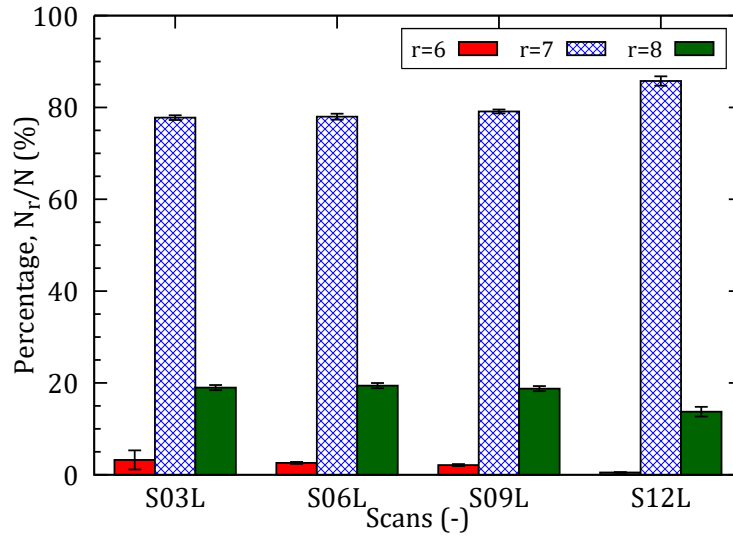


Figure 2.34: Grain size distribution of the 3D reconstructed specimens.

2.5.5 General description of the structure at grain-scale

Fig. 2.35 illustrates an example of 3D reconstruction for the SV before and after the detection. The specimens (a) and (b) were directly reconstructed from 3D tomography images, in which the small cube (b) was extracted from the specimen (a). The specimens (c) and (d) are reconstructed from 3D binary images, (d) is also a small cube extracted from the (c). The specimens (e) and (g) were reconstructed from the exact positions of particles after detection with tolerances of 0 and 1 voxel, respectively. The small cubes (f) and (h) were extracted from the (e) and (g), respectively.

Fig. 2.35(a) shows the assembled spheres within the specimen, including the stacks (lighter grey levels) of spheres and the pores (darker grey levels). In this specimen, several large pores exist corresponding to a size up to 1 mm and a lot of stacks created from the spheres have dimension ranging from 0.3 to 0.5 mm. X-ray diffraction (the opaque layers around the spheres) can be precisely shown in Fig. 2.35(b), by zooming in several spheres in the specimen (a) and reducing the noise of original images. All small cubes (Figs. 2.35(b, d, f, and h)) show clearly the contact region at the boundary of particles.

Moreover, the voxel size obtained in the XRCT tests is around 6.5 micrometers. Hence, as the average diameter of spheres is 100 micrometers, the spheres reconstructed in 3D tomography images are recomposed by a thickness around 15 voxels (equivalent to 15 layers). It is well observed that these layers are clearly distinguished in Fig. 2.35(d), but there is no more sphericity due to binarisation. In fact, these thicknesses always have a spherical shape (see Fig. 2.35(b)).

The contact between spheres can be clearly seen in Figs. 2.35(b) and (d). Some typical contacts are denoted by the positions (from 1 to 5) to see its change before and after the detection. It is well recognized that these spheres are always kept in contact at these positions in the specimen (see Figs. 2.35(b) and (d)). However, because of the error after the detection, these spheres are no longer in contact, as shown in Figs. 2.35(f). Hence, after adding a tolerance of 1 voxel to the diameter of all spheres, the contacts of these spheres are similar to the ones before the detection. A clear evidence is shown in Figs. 2.35(h). The change of contacts can be easily seen by the color of spheres, as follows: the red, green, blue, yellow, magenta are represented the spheres have zero, one, two, three, and four contacts, respectively.

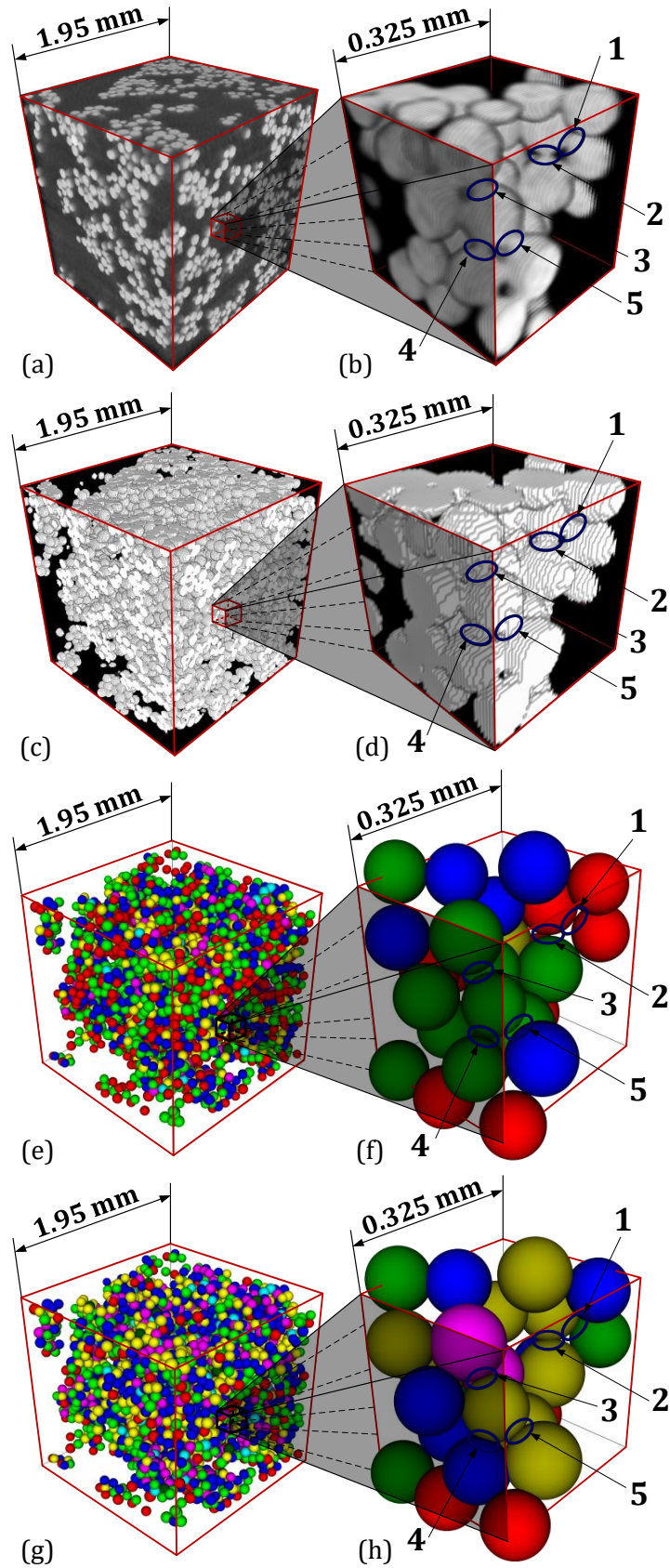


Figure 2.35: Example of 3D reconstructed specimen: (a) whole specimen in original images, (b) small cube extracted from (a), (c) solid part of specimen (binarized images), (d) small cube extracted from (c), (e) and (g) whole reconstructed specimens with tolerance 0 and 1 voxel, and (f) and (h) small reconstructed cubes extracted from (e) and (g).

2.5.6 Heterogeneity

As mentioned in Sec. 2.5.1, ten SVs were randomly extracted at ten different positions for each local scan. After the detection process, the number of particles for the ten SVs considering four steps (S03L, S06L, S09L, and S12L) are obtained, as shown in Fig. 2.36. During the detection process, all the SVs were set up with the same input parameters. The results show that the average number of particles at a denser state is higher: at the loosest state, S03L ($e = 2.23$), there are approximately 4000 particles in one cube, while at the densest state, S12L ($e = 1.04$), there are approximately 7500 particles.

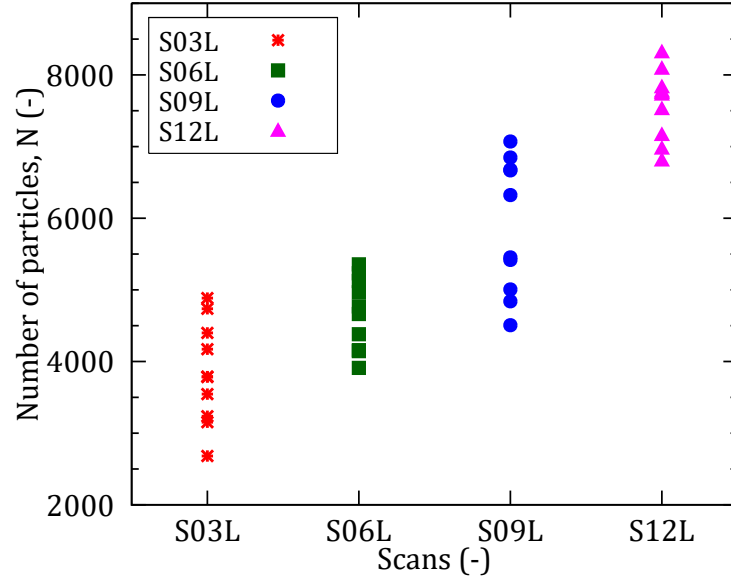


Figure 2.36: Number of particles of the ten SVs for four local scans after detection process.

Besides, the macroscopic solid fraction and the average solid fraction of ten SVs are illustrated in Fig. 2.37. The triangle points are computed from the void ratio of the whole specimen (see Sec. 2.4.3). The circle points show the average values, which were directly calculated from the tomography images. In addition, after the detection process, the solid fraction is easily computed by the volume of all particles and the volume of the cube. The results show that the macroscopic solid fraction is different from that estimated at the center of the specimen. That can be partly explained by the heterogeneity of the microstructure of the sample. Besides, the solid fraction obtained after the detection process is smaller than that before the detection; the decrease equals to 0.05, 0.06, 0.07, and 0.1 for the scans S03L, S06L, S09L, and S12L, respectively. It seems that the detection process underestimate the radii of the spheres and this problem is more serious at a denser state.

Furthermore, the solid fraction after the detection process is also recalculated with a tolerance of 1 voxel (6.5 micron) added in the diameter of spheres (the diamond-shaped-

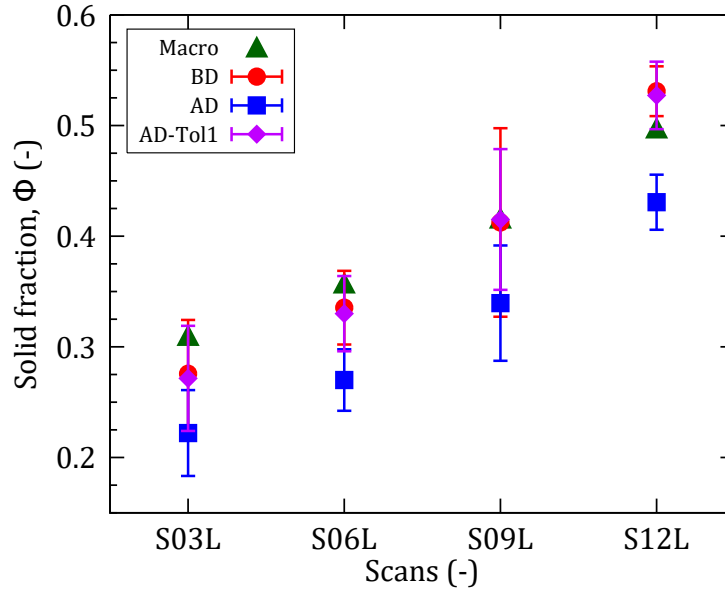


Figure 2.37: Macroscopic solid fraction (triangle) and the average solid fraction of 4 local scans before and after the detection process with a tolerance of 0 and 1 voxel. BD denote before detection, AD denotes after detection.

magenta points). These values are very close to the ones before detection (the circle-red points). This confirms that the use of a tolerance of 1 voxel for all analyses of the 3D images after the detection process is quite suitable.

2.5.7 Geometrical structure analysis

2.5.7.1 Total coordination number

In granular materials, the coordination number z is defined as the average number of force-carrying contacts per grains. If N_C is the number of force-carrying contacts between N grains, then the coordination number is $z = 2N_C/N$ – as product zN counts each contact twice. In the present analysis, N_C is redefined as the number of pairs of contacts between N grains. Pairs of contacts mean two particles which have a distance between two centers smaller than or equal to the sum of its radii. In order to reduce the error of the rounded value of diameters in voxel during the detection process, the effect of the resolution of tomography images, a tolerance in voxel value is used when estimating the coordination number. This tolerance is defined as the distance between two surfaces of particles. Therefore, in the present part, z is called the total coordination numbers. As mentioned in Sec. 2.5.2.3, the diameters after the detection process are smaller than the real diameters of material. Hence, a tolerance of 1 voxel is chosen for the reference error of all calculations.

Fig. 2.38 plots the average total coordination number of four steps for three values of tolerance (0, 1, and 2 voxels). For a tolerance of 0, z tends to decrease under growing

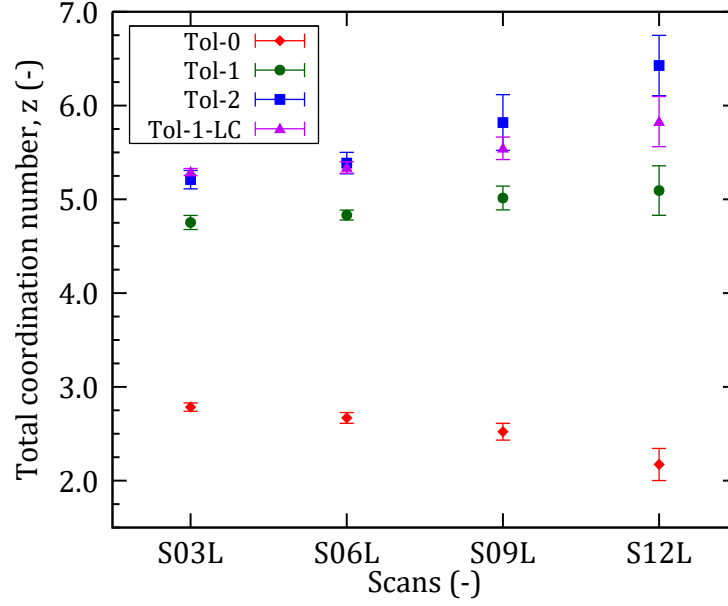


Figure 2.38: Average total coordination numbers of 4 local scan with three values of tolerance (0, 1 and 2 voxels). LC denotes the lost contacts.

stress. This is not reasonable but this confirms once again the error mentioned above. z then increases twofold and nearly threefold when the tolerance changes from 0 to 1 voxel. However, from 1 to 2 voxels, z is gradually raised from a half to nearly one and a half. The error bars are wider at a denser state or with a higher tolerance.

The new z (with lost contacts) of four steps is also plotted in Fig. 2.38 for the tolerance of 1 voxel (the triangle-magenta points). The results show that this correction (i.e. using lost contacts) increases the total coordination number by approximately 10 % for the four cases. For the following analysis, the lost contacts were not considered for the sake of simplification.

2.5.7.2 Coordination number of close neighbors

The coordination number of close neighbors, $z(h)$, is the average number of neighbors of one particle separated by an interstice narrower than h . $z(0)$ is the usual total coordination number z with tolerance 0. Fig. 2.39 illustrates the average coordination number of close neighbors of four scans with the dimensionless interparticle distance $h/\langle d \rangle$, in which $\langle d \rangle$ is defined as follows:

$$\langle d \rangle = \frac{2d_{\max}d_{\min}}{d_{\max} + d_{\min}}. \quad (2.3)$$

This distance is equivalently from 0 to 2 voxels.

For each scan, there is a threshold of h below which $z(h)$ increases quickly when h increases; above this threshold, the $z(h)$ increases with a lower rate. Based on the shape of these curves, we can suggest that this threshold is around 1 voxel (equivalently

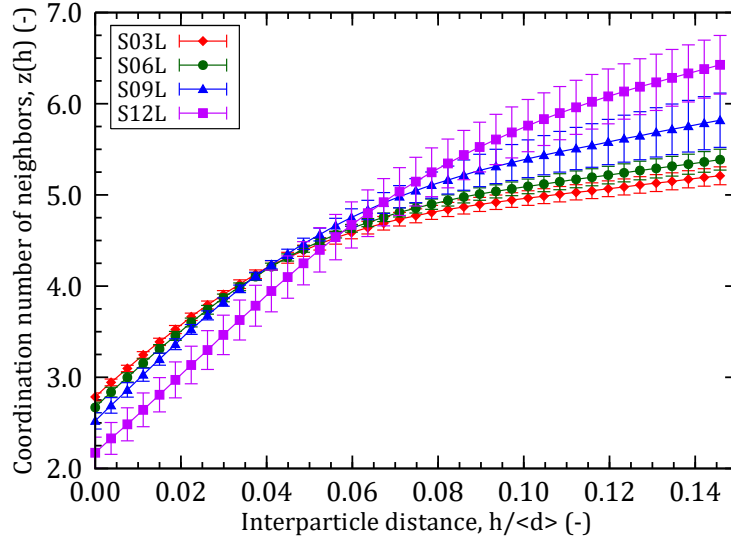


Figure 2.39: Coordination numbers of close neighbors for four local scans.

$h/\langle d \rangle \approx 0.07$). At this point, four curves start to diverge and the $z(h)$ of the lower compaction level is smaller than the one of the higher compaction level. This threshold, applied for all the scans, corresponds to the error induced by the detection process. Below the threshold, the rate at which $z(h)$ increases with h is independent of the compaction state because it is related to the error of the detection process. Above the threshold, the rate at which $z(h)$ increases with h is higher for a denser state. Actually, this rate depends on the structure of the samples. The denser the states, the higher the numbers of close neighbors.

2.5.7.3 Number of contacts per grain

Fig. 2.40 shows the number of contacts per grain for the three tolerances 0, 1, and 2 voxels. In general, the grains have from one to eight contacts. Firstly, with a tolerance of 0 voxel, the grains having zero contact occupy the highest quantities, from 30 % to nearly 40 %. The denser the stages, the higher the percentage of grains without contact. This is due to the error of the detection algorithm as already mentioned above.

For the tolerance of 1 voxel, the grains having two and three contacts occupy the most quantities, about 27.5 % for each series. Meanwhile, the quantities of the grains without contact decrease from threefold to fourfold corresponding to growing of compaction. For the denser state, the probability to have a high value of N_C (3, 4, 5, and 6) is higher than for the other states. Reversely, the probability to have low values of N_C (0, 1, and 2) is lower for denser states than for looser states. The probability to have $N_C = 0$ is approximately 6 % to 8 %. That can be attributed to the lost contacts mentioned above, which are not considered in this analysis, where the red spheres have $N_C = 0$ (see Figs. 2.35(e) and (g)). They are mainly located close to the border of the cube. $N_C = 7$ is the maximal value and it occupies a minimal probability, nearly 0.2 %.

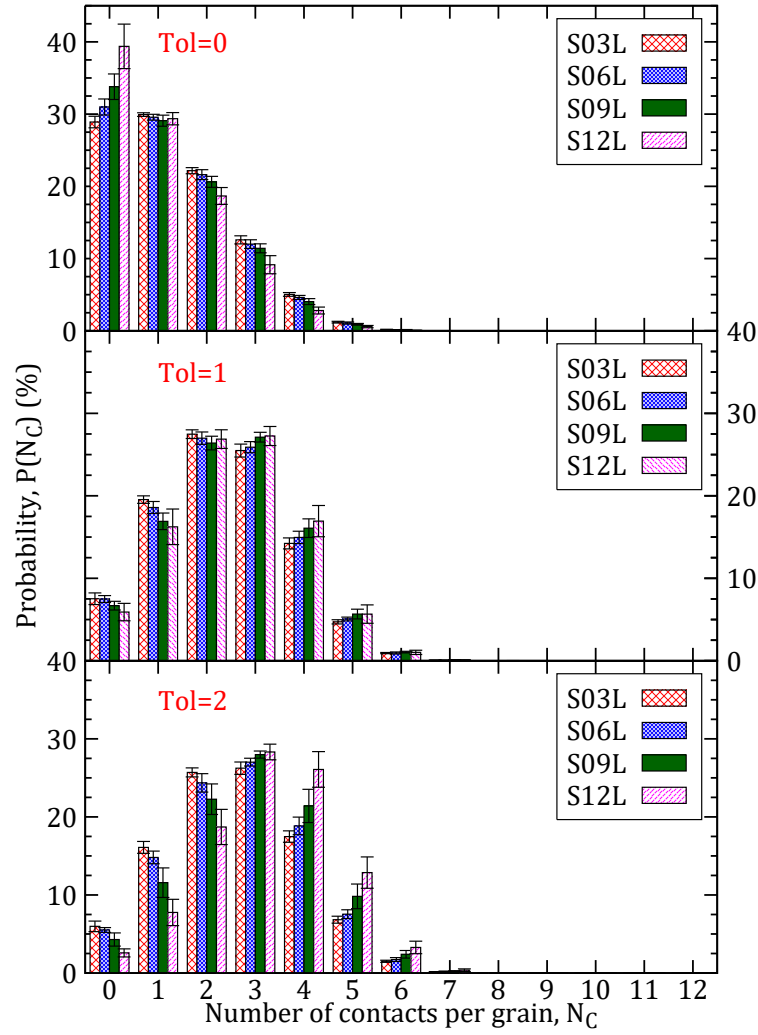


Figure 2.40: Number of contacts per grain for three tolerances of 0, 1 and 2 voxels.

For the tolerance of 2 voxels, the probabilities $P(N_C)$ of four states are significantly changed for the ones of tolerance of 1 voxel, in which the $P(N_C)$ at $N_C = 3$ is negligibly changed. For the denser state, low value of N_C (0, 1, and 2), the $P(N_C)$ is notably decreased while it is considerably increased at high value of N_C (4, 5, and 6). The grains having nine contact exist but the corresponding quantity is very small, approximately 0.004 %.

Several authors reported the distribution of number of contacts (i.e. the coordination number) [192, 101, 228, 210, 50] by using different methods to detect the contacts between the spheres. However, calculating the number of contacts is difficult due to the uncertainty (due to the diffraction of X-rays at the boundary) when calculating the accurate position of the center of the particle, especially with the small size of grains and low resolution of the tomography images. That is why the tolerance of 1 voxel is chosen for all calculations in the present study. This tolerance is close to the interval tolerance by 1-2 voxels^{1/3} of Aste *et al.* [128, 228] while their size of particles is bigger than our grains, and the resolution is not too much different. In several packing studies [191, 218, 228],

the spheres are at maximum in contact with 11 particles and at minimum with 2. Meanwhile, in our study, the maximum number of contacts is 8 with an average percentage of 0.01 %, and there still exists a significant percentage (around 7 %) of spheres that have no contact. We think that this can be explained by two reasons. Firstly, during the specimen preparation, the spheres are automatically stuck in groups of two or more grains after passing through the sieve. When falling into the cell, the cohesion of spheres tends to resist the interpenetration of the other groups, especially in some closed pores. Hence the structure of the specimen is not homogeneous. Secondly, as mentioned in Sec. 2.5.2, the spheres located close to the borders of the analyzed volumes are partly outside the analyzed cubes and thus not detected. Hence some spheres which are in contact with “incomplete” spheres will be isolated after the detection process.

Interestingly, the sphere having one contact can exist in this structure, as illustrated in Fig. 2.41. This is a small cube extracted from the Fig. 2.35(a). Furthermore, from the loosest state (S03L) to the densest state (S12L), $N_C = 1$ occupies a significant amount, approximately 30 % (tolerance of 0 voxel), 17 % (tolerance of 1 voxel), and 11 % (tolerance of 2 voxels). These spheres (in green) can be clearly seen in Figs. 2.35(e) and (g). This is explained by the fact that the capillary force between spheres is higher than the weight of the spheres. Indeed, with the size of diameters is 100 μm , the particle weight loses relevance with respect to capillary forces [96].

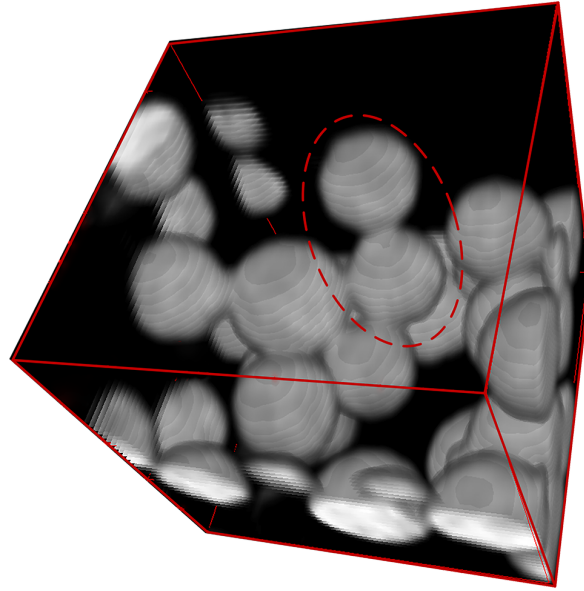


Figure 2.41: An example of a sphere with one contact.

2.5.7.4 Radial distribution function

The Radial Distribution Function (hereafter referred to as RDF), $g(r)$, is the probability of finding a particle center in a spherical shell of a radius r , given that there is another

particle at the origin of the spherical shell [212]. The RDF is related to the average number of particles by

$$p(r_2) - p(r_1) = \int_{r_1}^{r_2} g(r) 4\pi r^2 dr, \quad (2.4)$$

where $p(r)$ is the average number density of particles in a spherical shell of radius r . In this formula, the radial distances will be normalized by the average diameter $\langle d \rangle$ (given in Eq. 2.3). The RDF is a useful tool to describe the structure of a system, and it has been used widely for granular materials, especially in the numerical simulations.

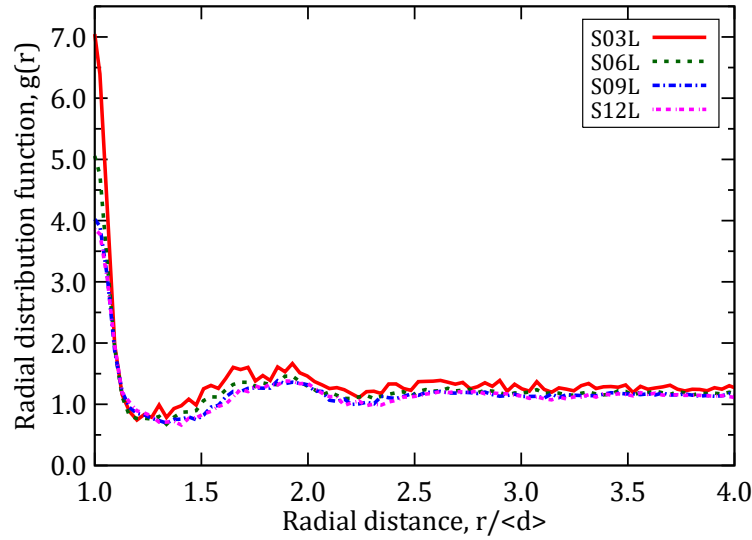


Figure 2.42: Radial distribution functions for particle centers of four local scans.

Fig. 2.42 shows the radial distribution of particle centers in a spherical shell for four steps of the dimensionless distance $r/\langle d \rangle$. Each curve is represented by the average value of ten SVs. The probability distribution function is nearly similar at various states with their oscillations and peaks due to large size distribution. At very short r ($r/\langle d \rangle < 1$) the RDF must be zero, because two particles cannot occupy the same space.

The RDF for S03L is rougher than for the other ones. The functions start from maximum probability of the contact particles at first peak $r = \langle d \rangle$ with different amplitudes. The functions then decrease to minimum probability at $r = 1.2\langle d \rangle$, $r = 1.3\langle d \rangle$, $r = 1.35\langle d \rangle$, and $r = 1.4\langle d \rangle$ upon growing of compaction S03L, S06L, S09L, and S12L, respectively. These functions increase subsequently to another local peak at $r \approx 1.9\langle d \rangle$. From this peak, these functions continue to vibrate slightly until they approach a constant value at $r = 3.0\langle d \rangle$. It is clear that $g(r)$ should go to 1 for large r . However, these RDFs in Fig. 2.42 go asymptotically to 1 for large r . This can explain why spherical shell cannot include the spheres which are located in the corner of the cube. Besides, due to the heterogeneity of the SVs, these RDFs slightly oscillate until their value is close to unity.

2.5.8 Contact networks

Fig. 2.43 illustrates the contact networks of a typical SV, represented in a narrow slice of nearly four average particle diameters ($4\langle d \rangle \approx 50$ voxels) thick before detection (on the left-hand side) and after detection (on the right-hand side). Each pair (before and after detection) from (a and b) to (g and h) corresponds to growing of compaction, from S03L to S12L. The contact between particles are represented by segments of different colors (only for after detection) joining particle centers.

Before detection, the contact network is directly analyzed from the 3D binarized images by joining the particle centroids. On the left-hand side of Figs. 2.43(a, c, e, and g), there are still a lot of small blocks. This is due to some small pieces of incomplete spheres at the borders that are not identified. After detection, the contacts are plotted in two types (on the right-hand side of Fig. 2.43). The first one (red lines) is the contacted particles including one voxel of diameter (tolerance of 1 voxel). The second one (blue lines) is the neighbors with their interstitial distance of 1 voxel.

In general, the contacts obtained before the detection process are more than the ones after detection. This is due to the grains loss during the detection process, already mentioned in the above sections. Moreover, the lines, joining two particle centroids on the left-hand side, are spatially connected from many voxels so the contact networks are rather complex for observing. This confirms that these lines are not straight. Furthermore, on the right-hand side of Fig. 2.43, the contact between neighbors with their interstice of 1 voxel are also drawn in order to reduce the effect of detection process. Indeed, the general shape of the contact networks before and after detection are fairly similar.

A supplemental illustration of contact networks between grains is shown in Fig. 2.44. A typical slice ($4\langle d \rangle$) of the typical SV is extracted. It has the same position of the thickness in Fig. 2.43. For depicting the number of contacts per grains, a tolerance of 1 voxel is computed to the diameters of particles. The number of contacts per grains are illustrated by different colors. The red, green, blue, dark-yellow, magenta, dark-cyan, dark-green, dark-purple, black and dark-red represent the spheres having zero, one, two, three, four, five, six, seven, eight, and nine contacts, respectively. In these slices, the dark-purple, black, and dark-red spheres do not exist but the dark-green spheres having 6 contacts can be easily found. Nevertheless, the red spheres still exist significantly. Therefore, we can conclude that the number of contact is underestimated because of the significant influence of the lost contacts.

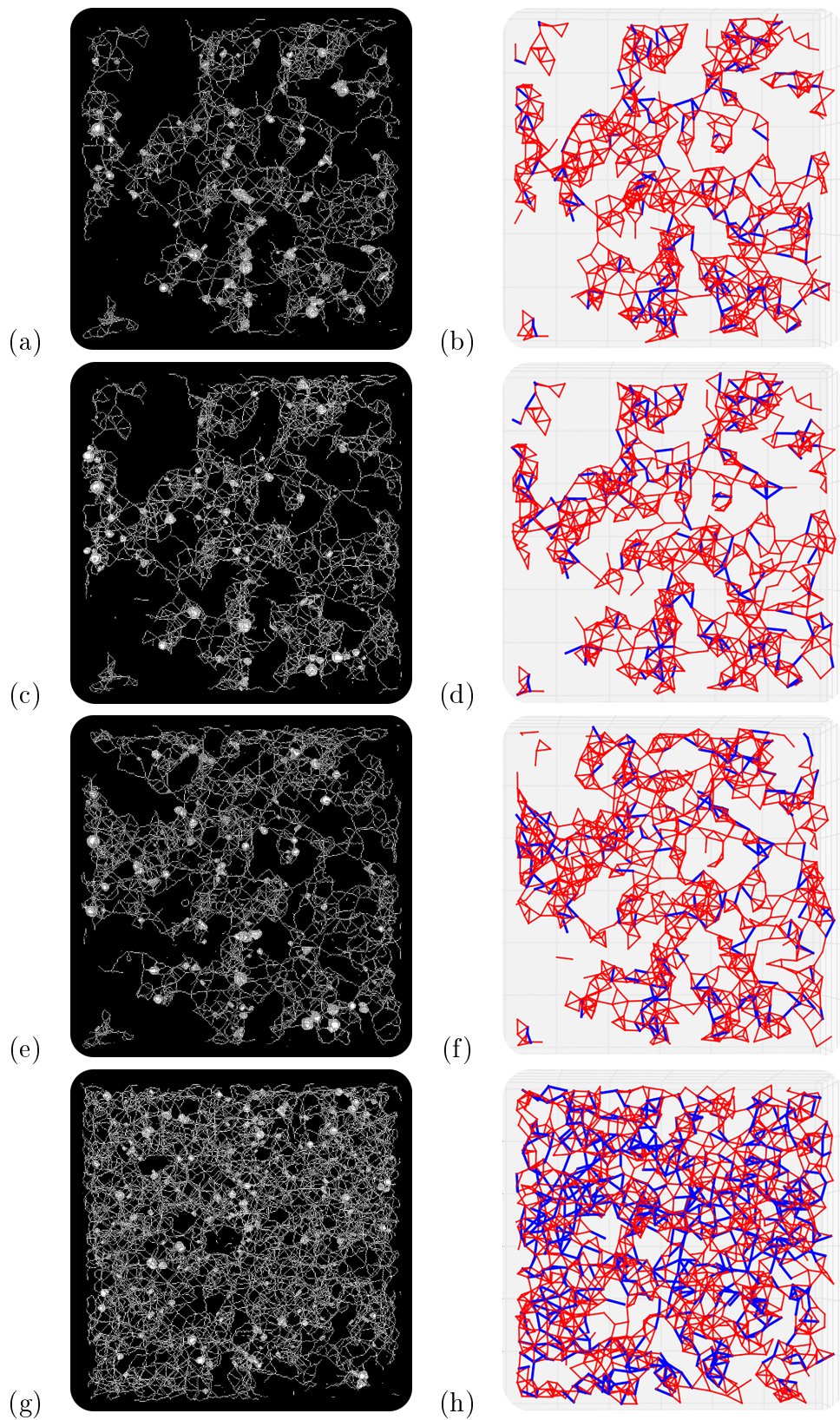


Figure 2.43: Contact network of a typical SV under growing of compaction. Red lines denote the contacted grains with tolerance of 1 voxel, blue lines denote the neighbors of grains with their interstice of 1 voxel.

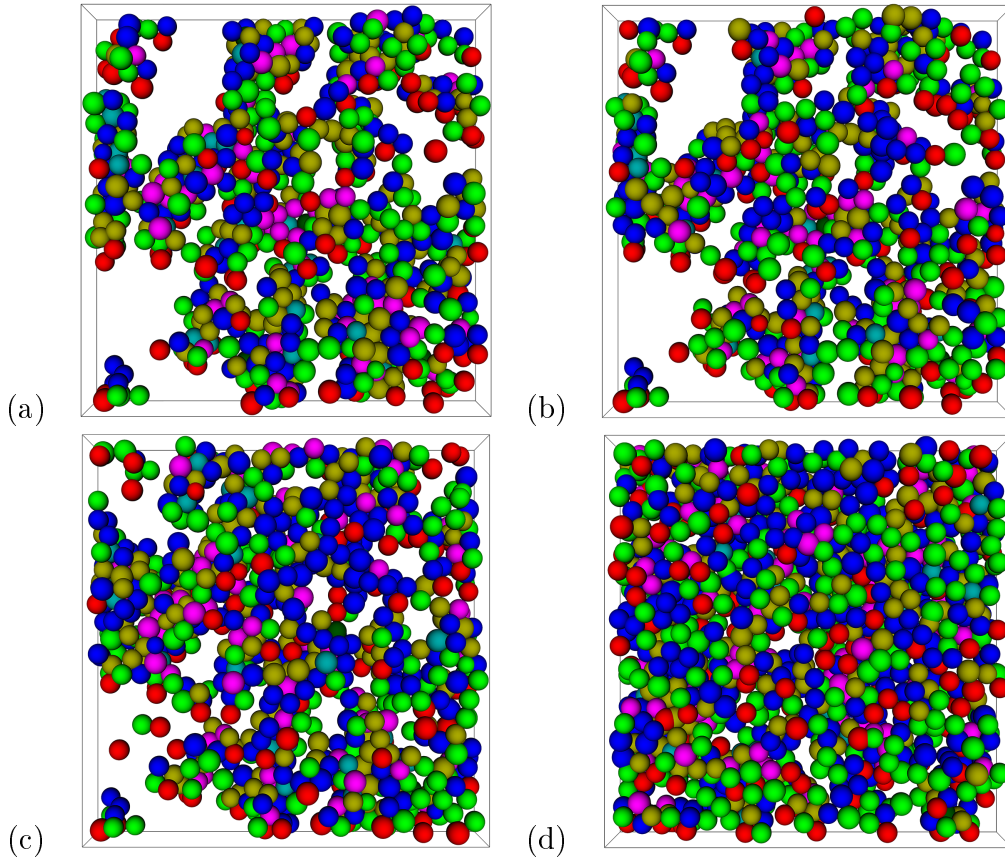


Figure 2.44: 3d-slices of the typical SV under growing of compaction. (a) SO3L, (b) S06L, (c) S09L, and (d) S12L.

2.6 Links between macro and microscopic behaviors

The links between macro and microscopic behavior of specimen under growing of compaction can be observed via the compression curves, the global and local observations. In other words, these links are successively depicted by the Figs. 2.11, 2.12, 2.17, 2.26, 2.36, 2.38, and 2.39.

In the stage 1 of the compaction curve (Fig. 2.11), the void ratio remains nearly constant and slightly decreases at the end of this regime (equivalently the position of the scan S02G). This is depicted well by the distribution of void ratio of scans S01G and S02G in Fig. 2.17.

Under growing of stress in stage 2, the structure of specimen quickly collapses. This is evidently reflected by a twofold decrease of void ratio in the central layers of specimen (see Fig. 2.17). At these regions, there are several big pores which are located at the periphery and the central zones of the specimen (see Figs. 2.12 and 2.26). Besides, at higher densities, the number of contacts is larger than the one at lower densities (see Figs. 2.38 and 2.39).

In the stage 3 of the compaction curve, starting from the S11G and S12L, the structure

collapses negligibly because of the elastic deformation of grains at contact regions. This is completely demonstrated by the highest density of S12L and the slight increases of z and $z(h)$ from the tolerance of 1 voxel (see Figs. 2.38 and 2.39). Furthermore, the highest density of grains at the central layers of the specimen is also a main factor to sustain the settlement of the top layers. This is confirmed by the smallest void ratio of S11G in Fig. 2.17 and a band in specimen of the scans S10G and S11G (see Fig. 2.12).

2.7 Conclusion

In this chapter, we have performed two observations of wetted glass beads: the first one is the 1D compression test, the second one is the XRCT test combined with in-situ compression test. Two different scales of scans were performed in order to quantify the degree of homogeneity and to observe the microstructural changes of specimen under growing of compaction levels.

Firstly, the results show that a very loose yet stable state of wet granular soils can be made in laboratory for tests, even using very small water content. This is one the most interesting aspects of this work as compared to the past studies which were focused on denser states and/or higher water contents (e.g. Bruchon *et al.* [35]). Evidently, the structure of the specimen is heterogeneous but it seems very difficult to make the specimen more homogeneous with so low densities.

Secondly, the macroscopic behavior of wet beads at loose state obtained from oedometric compression tests has usually three regimes: (i) at stresses lower than the preconsolidation stress, the initial structure can sustain these stresses with a very small rearrangement; (ii) when the stresses exceed the preconsolidation stress, the loose structures collapse and restructure; and (iii) at higher stresses, the elastic deformation of grains at contact points occurs.

Thirdly, the XRCT investigations of the microstructure allowed quantifying the degree of homogeneity, the distribution of porosity in the specimen as well as the pore-scale behavior under growing of compaction level.

Finally, a new approach for detecting the spherical structures from tomography images is proposed in order to characterize the microstructures of loose systems. Several fundamental microstructural properties are obtained such as total coordination number, number of close neighbors, and distribution of number of contacts, contact network, and radial distribution function. Although our results show an underestimated prediction of several microstructural properties for the other studies, the method presented in this work provides an interesting characterization of the grain-scale compression behavior of wet granular soils (with type of spherical shape) at loose state.

Isotropic compression: DEM study

This chapter reports on a 3D numerical study, using the discrete element method, to investigate the quasistatic response of very loose assemblies of frictional spherical grains to an isotropic compression. The grains are mixed with a small amount of an interstitial wetting liquid, which forms capillary menisci causing an attractive intergranular forces. Under growing pressure, the influence of the initial assembling process and of various micromechanical parameters on the plastic compression curves are firstly studied. The plastic responses along those compression curves are then shown in particular without and with the appearance of rolling and pivoting resistances in contacts and also the effect of size polydispersity. The evolution of microstructure and force transmission along the compression curve are finally characterized.

Contents

3.1	Introduction	99
3.2	Model material and interaction laws	99
3.2.1	Particle shape and size distribution	99
3.2.2	Interaction law: normal forces	100
3.2.3	Tangential forces	104
3.2.4	Resistance to rolling and pivoting (RPR)	105
3.3	Basic definitions and properties	106
3.3.1	DEM equations, boundary conditions and stress control	106
3.3.2	Equilibrium condition	108
3.3.3	Coordination numbers	109

3.3.4	Liquid content and limit of pendular state	110
3.3.5	Average normal force	111
3.3.6	Dimensionless control parameters	112
3.4	Simulation procedures for the compression test	113
3.4.1	Specimen preparation	113
3.4.2	Simulation parameters	115
3.4.3	Compression cycle	118
3.5	Material behavior in isotropic compression	118
3.5.1	A reference case	118
3.5.2	Influence of drying or of saturating	130
3.5.3	Influence of initial state	131
3.5.4	Effects of polydispersity	138
3.6	The case of wet beads with RPR	143
3.6.1	Influence of initial solid fraction	143
3.6.2	Influence of initial agitation intensity	145
3.6.3	Influence of rolling and pivoting friction coefficients	149
3.6.4	Comparison of bead assemblies with and without RPR	151
3.7	Conclusion	153

3.1 Introduction

This chapter presents the results of a discrete numerical simulation study of wet beads under isotropic compression. Capillary cohesion due to the liquid bridges between neighboring grains stabilizes very loose structures which tend to collapse under growing pressure. The material behavior in compression is thus characterized by strongly irreversible plastic effects, which are investigated at the macroscopic and microscopic levels. This study is similar to the one carried out by Gilabert *et al.* [13, 14] in 2D. However, the numerical model is designed to quantitatively simulate a real material and enables direct comparisons with laboratory experiments.

The model material, which is the same as in the numerical simulations of Khamseh *et al.* [29], is described in Sec. 3.2. Some basic properties and important relations in the DEM approach to the mechanical behavior of granular materials are recalled in Sec. 3.3. The numerical procedure and the choice of parameters use to simulate isotropic compression are presented in Sec. 3.4. Then the results both for the macroscopic behavior and the microstructure evolution are given in Sec. 3.5 in which the influence of various parameters is investigated. The material in which the contacts are endowed with resistance to rolling and pivoting (RPR), a micromechanical feature which is known to strongly affect the mechanical behavior, is studied in Sec. 3.6.

3.2 Model material and interaction laws

A granular material is defined by the grain geometry and the intergranular forces. The *contact law* in a granular material is the relationship between the relative motion of two contacting grains and the contact force. As we deal with particles that may attract one another at short distance without touching, the law governing intergranular forces and moments is best referred to simply as the *interaction law*. Such elements of the numerical model, designed to simulate wet solid beads, are given here.

3.2.1 Particle shape and size distribution

Effects of angularity on internal friction are known to be important, and the morphology of the liquid phase is also expected to be strongly affected by the geometry of the solid grains. Nevertheless this study focusses on spherical grains, as the simplest model material for which laboratory studies are possible.

One possible way to represent non-spherical particle shape is to implement rolling and pivoting resistance (RPR), as dealt with in Sec. 3.6, Ref. [229] established a correspondence between rolling resistance of spherical grains and a certain shape parameter for non-spherical grains. The material behavior reported in Sec. 3.6 might thus be expected to be similar to the one of assemblies of grains departing from the spherical shape, although the change in the geometry of liquid menisci is not accounted for.

Moreover, we mainly consider equal-sized, identical spherical beads of diameter d . The actual value of d is not relevant for our results, if they are expressed in dimensionless form. However, in order to provide physical orders of magnitude, results will also often be reported in dimensional form (e.g. pressures in kPa), in which case they pertain to glass beads of diameter $d = 0.118$ mm.

The influence of a (moderate) grain polydispersity will be assessed on dealing with the following probability distribution function (P.D.F) for the distribution of diameter d , varying between a minimum value d_{\min} and a maximum value d_{\max} :

$$p(d) = \frac{2d_{\min}^2 d_{\max}^2}{d_{\max}^3 - d_{\min}^3} \frac{1}{d^3}. \quad (3.1)$$

This distribution is thus uniform by volume, and its first moments are given by:

$$\langle d \rangle = \frac{2d_{\min} d_{\max}}{d_{\max} - d_{\min}}; \quad \langle d^2 \rangle = \frac{2d_{\min}^2 d_{\max}^2}{d_{\max}^2 - d_{\min}^2} \ln \frac{d_{\max}}{d_{\min}}; \quad \langle d^3 \rangle = \frac{2d_{\min}^2 d_{\max}^2}{d_{\max} + d_{\min}}. \quad (3.2)$$

This diameter distribution is shown in Fig. 3.1, in the form of the cumulated probability function,

$$P(d) = \int_{d_{\min}}^d p(x) dx. \quad (3.3)$$

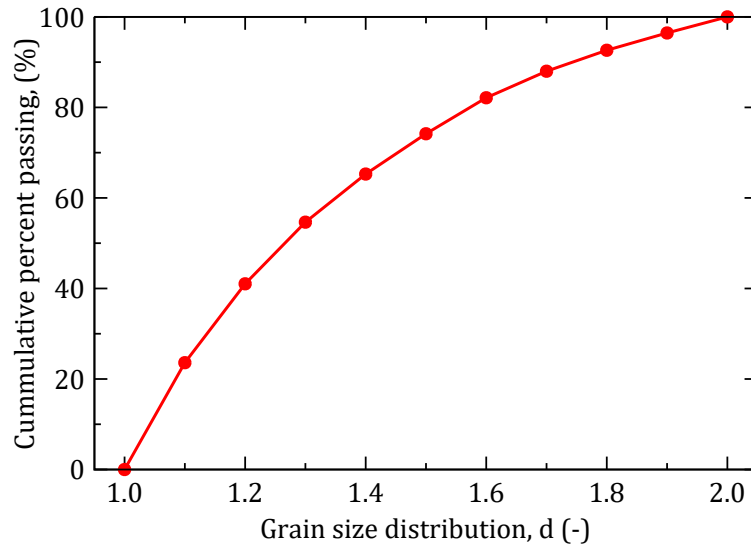


Figure 3.1: Grain size distribution of the polydisperse system.

3.2.2 Interaction law: normal forces

3.2.2.1 Elastic normal force: Hertz law

Consider two spherical beads i and j , with respective diameters d_i and d_j , made of a solid elastic material with Young modulus E and Poisson ratio ν . Using notations

$\tilde{E} = E/(1 - \nu^2)$ and $d_{ij} = 2d_i d_j / (d_i + d_j)$, the Hertz law, as implemented in a number of previous numerical studies [230, 29], adequately describes the normal elastic force, F_{ij}^{eN} , in their contact, depending on deflection h_{ij} , as

$$F_{ij}^{N,e} = \frac{\tilde{E}}{3} \sqrt{d_{ij}} |h_{ij}|^{3/2}. \quad (3.4)$$

This corresponds to a deflection-dependent (or force-dependent) normal stiffness

$$K_N^{ij} = \frac{dF_{ij}^{eN}}{d|h_{ij}|} = \frac{\tilde{E}}{2} \sqrt{d_{ij}} |h_{ij}|^{1/2}. \quad (3.5)$$

Although this choice does not entail any loss of generality, numerical results in physical units correspond here to glass beads, with Young modulus $E = 70$ GPa and Poisson ratio $\nu = 0.3$. Formulae (3.4) and (3.5) are used with monosized beads (with $d_i = d_j = d_{ij} = d$) or polydisperse ones with the diameter distribution given in (3.1).

3.2.2.2 Viscous damping

Just like in simulations of dry granular materials [230, 231, 232] we introduce a normal viscous force in intergranular contacts. The viscous normal force opposes the relative normal velocity $\delta V_N^{ij} = \dot{h}_{ij}$ of contacting beads, and is chosen as a constant fraction ζ of the critical damping coefficient in a linear oscillator with mass $m_{ij}^*/2$ (defining m_{ij}^* as the harmonic mean $2m_i m_j / (m_i + m_j)$ of masses m_i and m_j of the contacting grains), and stiffness constant K_N^{ij} as written in (3.5):

$$F_{N,v}^{ij} = 2\zeta \sqrt{m_{ij}^* K_N^{ij}} \delta V_N^{ij} = \zeta (m_{ij}^* \tilde{E})^{1/2} d_{ij} h_{ij}^{1/4} \delta V_N. \quad (3.6)$$

This model corresponds to a velocity-independent restitution coefficient in a binary collision [231]. Such a form of the viscous force is more justified by its computational convenience than by its physical relevance. In particular, it is not related to the viscosity of the liquid forming the menisci. The viscous forces, anyway, are quite irrelevant for the quasistatic mechanical properties of the wet bead assemblies, which are studied here. Their role, in the simulation practice, is to ease the obtaining of equilibrium states by dissipating the kinetic energy.

3.2.2.3 Capillary forces

The appearance of a small quantity of an interstitial wetting liquid introduces additional capillary forces, transmitted between contacting or neighboring grains by a liquid bridge, or meniscus, as depicted in the inset figure of Fig. 3.2. Our work is limited to the pendular state of isolated menisci [34], and the capillary forces are pairwise additive, acting on grains joined by such menisci. These forces are only present if grains have been in contact [125] and the meniscus has not broken since. A meniscus of volume V_m

remains until the separation distance reaches its rupture value $D_r \simeq V_m^{1/3}$, as a result of calculations by Willett *et al.* [90], Maeda *et al.* [138], and Herminghaus *et al.* [84].

In the case of monodisperse grains, the Maugis approximation [189] is chosen to calculate the attractive force which varies as a function of the distance h between particle surfaces:

$$F_{cap} = \begin{cases} -F_0 & h \leq 0 \\ -F_0 \left[1 - \frac{1}{\sqrt{1 + \frac{4V_m}{\pi d h^2}}} \right] & 0 < h \leq D_r \text{ (unbroken meniscus since last contact)} \\ 0 & 0 < h \leq D_r \text{ (no contact in the past, or broken meniscus)} \\ 0 & h > D_r. \end{cases} \quad (3.7)$$

Here, $h < 0$ corresponds to an elastic deflection of the particles in contact. $F_0 = \pi d \Gamma \cos \theta$ is the maximum tensile force, involving surface tension Γ of the liquid interface with the atmosphere (or the ambient continuous fluid phase), and wetting angle θ . Numerical results below are obtained with $\Gamma = 7.27 \times 10^{-2} \text{ N.m}^{-1}$ (an appropriate value for pure water at 20°C under atmospheric pressure), and $\theta = 0$, assuming perfect wetting. Fig. 3.2 shows how the static normal forces, with the repulsive, elastic (Hertzian) and the attractive, capillary contributions, vary with distance h .

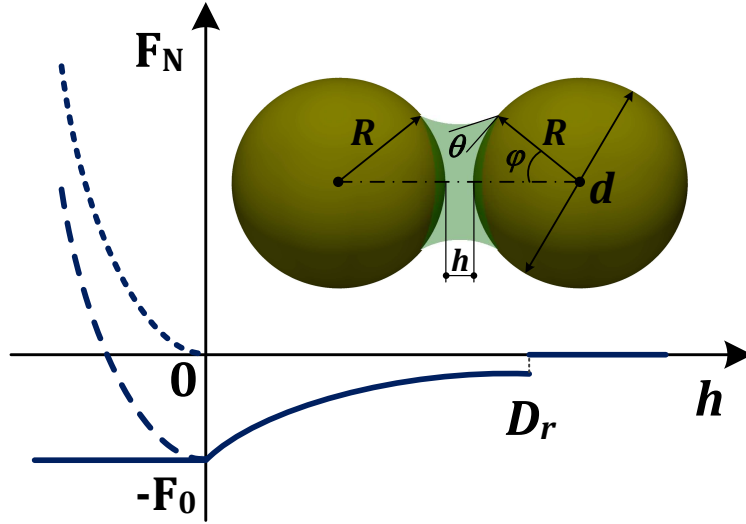


Figure 3.2: Static normal force, $F_N = F_N^e + F_{cap}$, as a function of the interparticle distance h . Inset: Geometry of a liquid bridge between two particles, with filling angle φ and contact angle θ . Short-dashed line: normal elastic repulsive force, long-dashed line: resultant normal force.

Two particles moving away from each other after a collision will only separate if their receding relative velocity is large enough to overcome the capillary attraction. The condition that the kinetic energy of the relative normal motion should be larger than

the potential energy of the capillary force, i.e. sets a threshold relative velocity V_{th} proportional to V^* [13], with

$$V^* = \sqrt{\frac{F_0 D_r}{m}}. \quad (3.8)$$

More precisely, one has

$$-\int_0^{D_r} F_{cap}(h)dh = F_0 \int_0^{D_r} \left(1 - \frac{1}{\sqrt{1 + \frac{4V_m}{\pi dh^2}}}\right)dh. \quad (3.9)$$

V^* is thus equal

$$V^* = \sqrt{\frac{kF_0 V_m^{1/3}}{m}}, \quad (3.10)$$

with $D_r \simeq V_m^{1/3}$ and k is a factor from the result of Eq. 3.9, as follows

$$k = \left[1 + \sqrt{\frac{4V_m^{1/3}}{\pi d}} - \sqrt{1 + \frac{4V_m^{1/3}}{\pi d}}\right]. \quad (3.11)$$

For polydisperse beads we resort to the Soulié formula [91], which is a fit to a numerical computation of the capillary force between particles with different diameters. Eq. (1.7) in Sec. 1.3.3.1 of Chapter 1 is rewritten, for two beads of radii R_1 and R_2 , as

$$F_{cap} = F_0 \sqrt{R_1 R_2} \left[c + \exp\left(a \frac{h}{R_2} + b\right) \right], \quad (3.12)$$

with

$$\begin{cases} a = -1.1 (V_m^*)^{-0.53} \\ b = (-0.148 \ln(V_m^*) - 0.96)\theta^2 - 0.0082 \ln(V_m^*) + 0.48 \\ c = 0.0018 \ln(V_m^*) + 0.078, \end{cases} \quad (3.13)$$

in which V_m^* is the dimensionless ratio of the meniscus volume (proportional to the surface area of the grain pair) to the cube of the maximum $R_{\max} = \max(R_1, R_2)$:

$$V_m^* = \frac{V_m}{R_{\max}^3} = \frac{V_m^{(0)}(R_i^2 + R_j^2)}{2R_{\min}^2}. \quad (3.14)$$

In all our simulations the volume meniscus is attributed a fixed value V_m : a meniscus is assumed to form, from the liquid layer coating isolated grains, as soon as a contact appears. The assumption of a constant volume, while not really justified on physical grounds, enables calculations to be carried out without having to model the liquid transport. While seemingly a gross oversimplification, it will be shown to have negligible influence on the results. In polydisperse systems, V_m varies according to the radii of the grains, and is proportional to the available surface area in the pair, as implied in (3.14), in which $V_m^{(0)}$ denotes the meniscus volume for two beads with the minimum diameter of the distribution.

3.2.3 Tangential forces

The tangential elastic force \mathbf{F}_{ij}^T , as in [230], relates to the relative tangential displacement in the contact, $\delta \mathbf{u}_{ij}^T$, involving a (deflection-dependent) tangential stiffness coefficient K^T assumed proportional to K^N :

$$d\mathbf{F}_{ij}^T = K_{ij}^T d(\delta \mathbf{u}_{ij}^T), \text{ with } K_{ij}^T = \frac{2-2\nu}{2-\nu} K_{ij}^N. \quad (3.15)$$

Tangential stiffness K^T has to be suitably adapted (rescaled) whenever the normal elastic force decreases, in order to avoid spurious elastic energy creation [233, 230].

Let us recall that the relative displacement at the contact point combines the displacements of both grains, \mathbf{u}_i and \mathbf{u}_j , and their (small) rotations $\vec{\theta}_i$ and $\vec{\theta}_j$, thus, with transparent notations for the radii, and \mathbf{n}_{ij} the unit normal vector, which for spherical objects points from the centre of i to the centre of j :

$$\delta \mathbf{u}_{ij} = \mathbf{u}_i - \mathbf{u}_j + (R_i \vec{\theta}_i + R_j \vec{\theta}_j) \times \mathbf{n}_{ij}. \quad (3.16)$$

The normal component of relative displacement (3.16) is subtracted to define the relative tangential displacement $\delta \mathbf{u}_{ij}^T$ appearing in the tangential contact law.

The Coulomb condition enforces inequality

$$\|\mathbf{F}_{ij}^T\| \leq \mu F_{ij}^{N,e}, \quad (3.17)$$

with the friction coefficient μ set to 0.3 in the present study. It is taken into account by suitably projecting \mathbf{F}_{ij}^T onto the circle of radius $\mu F_{ij}^{N,e}$ in the tangential plane, after applying incremental relation (3.15), whenever necessary.

Normal and tangential contact force components also follow the general motion of the grain pair in order to ensure the objectivity of the model [234, 230]. It is important

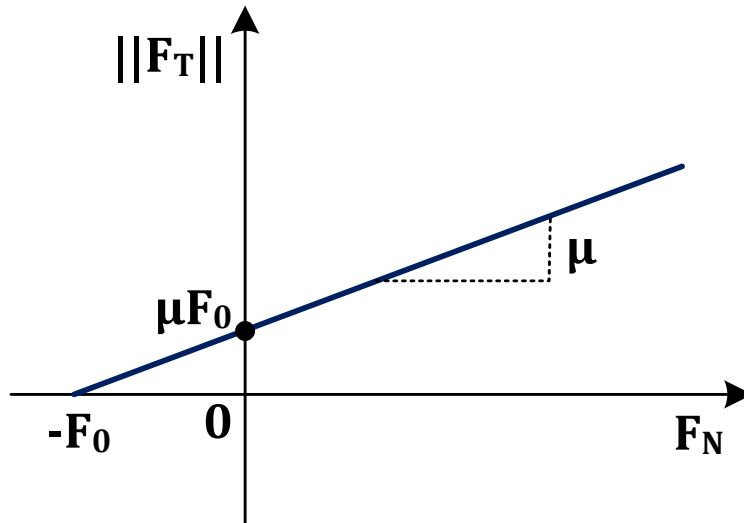


Figure 3.3: Coulomb cone limiting the value of the tangential force.

to note that the Coulomb condition (3.17) applies with the sole elastic contribution $F_{ij}^{N,e}$

to the normal force F_{ij}^N in the right-hand-side. As shown in Fig. 3.3, this entails that the Coulomb cone corresponding to total static contact forces in the space spanned by force components F_N, \mathbf{F}_T is shifted to the left, with its tip at $F_N = -F_0$, the maximum tensile force. As a consequence, in the contact between two grains of an isolated pair in equilibrium, the total normal force vanishes, but a sliding motion might be opposed by a tangential force as large as μF_0 .

In all the numerical computations of the present study the friction coefficient is set to $\mu = 0.3$.

3.2.4 Resistance to rolling and pivoting (RPR)

The influence of rolling and pivoting resistances (RPR) at contacts, as investigated in 2D by Gilabert *et al.* [14], is also studied. For simplicity, we only implement this feature with linear contact elasticity. Therefore, the linear elastic repulsive force, $F^{N,e}$, is defined as:

$$F^{N,e} = K_N |h|, \quad (3.18)$$

where $|h|$ is the normal deflection in the contact as the spheres are pressed against each other, K_N is the normal stiffness coefficient, related to the elastic moduli of the material that the grains are made of. In the present study, K_N is chosen such that $K_N d = 4.10^8$ Pa.m. Likewise, tangential stiffness K_T is deflection-independent in the linear elastic contact model, and chosen here equal to K_N .

The moment that sphere i exerts onto its contacting neighbour j , of radius R_j , at its centre, is denoted as $\mathbf{\Gamma}_{ij}$. It is first due to the tangential contact force, then to a possible moment $\mathbf{\Gamma}_{ij}^r$ of the force density distribution within the contact region, in its centre. One writes

$$\mathbf{\Gamma}_{ij} = \mathbf{F}_{ij}^T \times R_j \mathbf{n}_{ij} + \mathbf{\Gamma}_{ij}^r. \quad (3.19)$$

$\mathbf{\Gamma}_{ij}^r$ is most often neglected on dealing with smooth, convex particle shapes, because the contact region is very small on the scale of the particle radius.

However, non-negligible moments at the contact point $\mathbf{\Gamma}_{ij}^r$ might result from particle surface roughness, as contact regions become larger than the ones deduced from contact elasticity. Separating tangential and normal components of $\mathbf{\Gamma}^r$, one gets the *rolling* torque, $\mathbf{\Gamma}_R$ (a tangential vector), and the *pivoting* torque, scalar $\Gamma_P = \mathbf{n} \cdot \mathbf{\Gamma}^r$. Those moment components respectively work in rolling and pivoting relative motions. The rolling velocity $\delta \mathbf{\Omega}_{ij}^R$ in contact i - j is the tangential part of the difference in rotation velocities, $\delta \mathbf{\Omega}_{ij} = \mathbf{\Omega}_i - \mathbf{\Omega}_j$, while the pivoting velocity $\delta \mathbf{\Omega}_{ij}^P$ is its coordinate along normal vector \mathbf{n}_{ij} .

The contact law for contact moments, expressing RPR, is similar to the tangential contact law, it involves spring constants K_R, K_P and Coulomb-like thresholds with friction coefficients μ_R, μ_P . Just like the tangent elastic force, $\mathbf{\Gamma}_R$ and Γ_P are incrementally

updated in the bead motions, as

$$\begin{aligned}\Delta\Gamma_R &= K_R\delta\Omega^R\Delta t \\ \Delta\Gamma_P &= K_P\delta\Omega^P\Delta t\end{aligned}\tag{3.20}$$

in each time step Δt , while the following Coulomb inequalities are enforced whenever necessary by reducing the norm of vector $\mathbf{\Gamma}^R$ and the value of scalar Γ^P :

$$\begin{aligned}\|\mathbf{\Gamma}_R\| &\leq \mu_R F^{N,e} \\ |\Gamma_P| &\leq \mu_P F^{N,e}.\end{aligned}\tag{3.21}$$

“Friction coefficients” μ_R and μ_P have the dimension of a length. They are of the order of magnitude of the lateral dimension of the contact region, due to surface irregularities. In practice, they should be equal to a small fraction of the particle radii.

Stiffness constants K_R , K_P have the dimension of a force multiplied by a length, or of an ordinary linear spring stiffness multiplied by the square of a length. K_R and K_P should be such that equality in conditions (3.21) should be reached for small relative rotation angles (otherwise the integration of rotations should not be carried out as vectors). Values of order $\mu_R RK_N$ (R being the particle radius) are physically reasonable in this respect.

Just like sliding friction (with Coulomb condition (3.17)), rolling and pivoting friction involve the normal elastic force in the right-hand-side of inequalities (3.21). One could thus represent possible contact moment values versus this total static normal force as a Coulomb cone, with its tip shifted to negative values, at $-F_0$, similar to Fig. 3.3. A contact between two beads in which the total normal force vanishes may transmit torque components as large as $\mu_R F_0$ in a tangential direction or $\mu_P F_0$ in the normal direction.

3.3 Basic definitions and properties

Basic aspects of DEM simulations are recalled here, which prove useful in the design of the numerical tests and in the analysis of their results.

3.3.1 DEM equations, boundary conditions and stress control

DEM simulations consist in computing the collective motion of collections of N spherical beads (with $N = 4000$ in most cases in this study) by integration of the differential equations resulting from Newton’s laws and rigid-body mechanics. Grains are regarded as homogeneous solids, and thus a bead of diameter d has a mass m proportional to d^3 and a moment of inertia $I = md^2/10$.

The grains are enclosed in a cuboidal cell. The cell edges are parallel to the coordinate axes $(x_\alpha)_{\alpha=1,3}$, with respective lengths $(L_\alpha)_{\alpha=1,3}$. Periodic boundary conditions (PBC) are used, thereby avoiding wall effects. Two neighboring spheres, i and j , if brought into

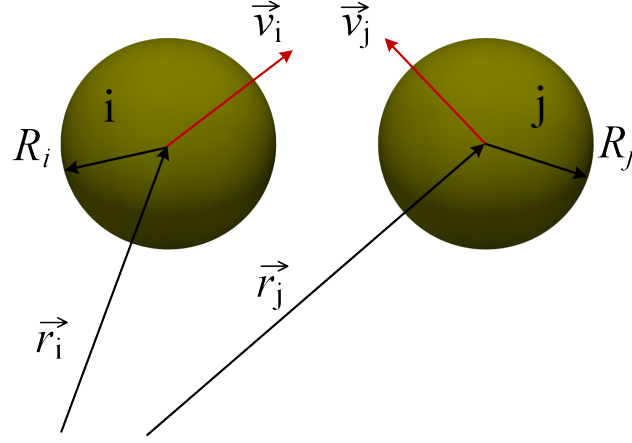


Figure 3.4: Motion of two spheres.

contact or very close to each other, transmit a force \vec{F}_{ij} and a moment Γ_{ij} onto each other. More precisely, \vec{F}_{ij} and Γ_{ij} are exerted by i onto j at the *contact point*. Simulations do not model material deformation in a contact region, but consider overlapping particles. The contact point is defined as the center of the intersecting region of the two spheres. In the case of the capillary interaction between spherical beads without contact, the force will be normal to the surfaces at the points of nearest approach and therefore carried by the line of centers.

Let \vec{r}_i and \vec{r}_j , respectively, denote the position of the centre of spheres i and j , as shown in Fig. 3.4. $\vec{r}_{ij} = \vec{r}_j - \vec{r}_i$ is the vector joining the centres of i and j and $h_{ij} = |\vec{r}_{ij}| - (d_i + d_j)/2$ is the overlap distance. The degrees of freedom, in addition to the positions \vec{r}_i are the angles of rotation θ_i , velocities \vec{v}_i , angular velocities ω_i of the grains ($1 \leq i \leq N$), the dimensions $(L_\alpha)_{\alpha=1,3}$ of the cell containing the grains and their time derivatives, through the strain rates

$$\dot{\varepsilon}_\alpha = -\frac{\dot{L}_\alpha}{L_\alpha^0}, \quad (3.22)$$

in which L_α^0 denotes the initial size for the corresponding compression process. The time evolution of the particle degrees of freedom are usually governed by the following equations:

$$\begin{aligned} m_i \frac{d^2 \vec{r}_i}{dt^2} &= \sum_{j=1}^N \vec{F}_{ij} \\ I_i \frac{d\omega_i}{dt} &= \sum_{j=1}^N \Gamma_{ij}. \end{aligned} \quad (3.23)$$

In Eqs. (3.23), only those spheres j interacting with i will contribute to the sums on the right-hand side. On dealing with periodic, deformable cells, those equations should be adapted: the linear velocities comprise two terms, one due to the variation of reduced coordinates $\tilde{x}_\alpha = x_\alpha/L_\alpha$, the other one due to the variation of L_α . One possibility, used

in Ref. [230], is to write down an equation for the vector of reduced coordinates exactly in the form of (3.23), with scaled down forces in the right-hand side. With appropriate choices of parameters (in particular, of the mass associated with the cell dimensions) the “classical” form (3.23) of the equations is only very slightly perturbed.

Stresses are measured using the standard formula: for all coordinate index pairs α, β ,

$$\sigma_{\alpha\beta} = \frac{1}{\Omega} \left[\sum_{i=1}^N m v_i^\alpha v_i^\beta + \sum_{i<j} F_{ij}^\alpha r_{ij}^\beta \right]. \quad (3.24)$$

Here, $\Omega = L_1 L_2 L_3$ is the sample volume. Cell lengths $(L_\alpha)_{\alpha=1,3}$ vary simultaneously with the grain positions. We use stress-controlled dynamics, requesting cell dimensions and particle positions to adjust until a mechanical equilibrium state is obtained in which the diagonal elements of the stress tensor take their prescribed values Σ_α , $1 \leq \alpha \leq 3$. Equations of motion for cell dimensions L_α are written as [230].

$$M \ddot{L}_\alpha = \frac{1}{L_\alpha} \left[L_\alpha^2 \sum_i m_i \left(\tilde{r}_i^{(\alpha)} \right)^2 + \sum_{i<j} F_{ij}^{(\alpha)} r_{ij}^{(\alpha)} \right] - \frac{\Omega}{L_\alpha} \Sigma_\alpha. \quad (3.25)$$

The right-hand-side of (3.25) is proportional to $\sigma_{\alpha\alpha} - \Sigma_\alpha$. M denotes a generalized mass associated with changes in the cell dimensions. It is usually chosen, in compression tests, of the order of the total mass of all particles in the system. Eq. (3.25) requests the cell to expand if the stress (evaluated with the sign convention of soil mechanics: tensile stresses are negative) is too large compared to the prescribed value, and to shrink if it is too small.

In all equations written here, the periodicity of the simulation cell has to be taken into account: particles exiting the cell through any boundary are being replaced by their image (or “copy”) entering the cell through the opposite boundary. Sums over interacting pairs involving “branch vectors” (centre-to-centre vectors) \mathbf{r}_{ij} , as in (3.24), are to be understood with the nearest-image convention: vector \mathbf{r}_{ij} actually points from the centre of grain i to the centre of the nearest copy of j within the periodic set of replica of grain j .

3.3.2 Equilibrium condition

Although numerical simulations of the quasistatic response of granular materials requires mechanical equilibrium to be reached, equilibrium criteria are sometimes left unspecified or quite vaguely stated in the literature. However, in order to report on usual quantities like the coordination number or the force distribution, it is essential to know which pairs of grains are in contact and which are not. Due to the frequent occurrence of small contact force values, this requires forces to balance with sufficient accuracy. We found that the following criteria allowed us to identify the force-carrying structure clearly enough.

A typical intergranular force value $F_1 = \max(F_0, Pd^2)$ sets the tolerance levels for individual grain equilibrium, where P is the applied pressure. A configuration is deemed equilibrated when the following conditions are simultaneously satisfied: (i) the net force (the total force) on each spherical grain is less than $10^{-4}F_1$; (ii) the total moment on each sphere is lower than $10^{-4}F_1d$; (iii) the difference between imposed and measured stresses is less than $10^{-4}F_1/d^2$; and (iv) the kinetic energy per grain is less than $10^{-8}F_1d$.

3.3.3 Coordination numbers

In static granular assemblies, the coordination number z is, after solid fraction Φ (which is the volume occupied by the solid grains divided by the total system volume), the most important and well-studied variable characterising the material state. It is defined as the average number of force-carrying contacts per grain. If N_c is the number of force-carrying contacts between N grains, then the coordination number is $z = 2N_c/N$ – as the product zN counts each contact twice. In general disordered systems, the coordination number has an upper bound well below the values it may reach in ideal, regular arrangements like perfect crystals. Thus, disordered packings of spherical beads, in the limit of small contact deflections (rigid contact limit), satisfy $z \leq 6$ [235, 236, 237, 230]. This upper bound to z is due to the absence, in generically disordered grain packings, of contact networks able to carry self-balanced normal forces (the degree of force indeterminacy or “degree of hyperstaticity” of the contact network is equal to zero if contacts are regarded as frictionless).

The coordination number z is split into two terms: the average number of contacts per grain, z_c , and the average number of the pairs interacting through a capillary bridge per grain, z_d , so $z = z_c + z_d$. Hence, z is also called the total coordination number.

Furthermore, it is interesting to define and to measure a coordination number of close neighbors, $z(h)$, as the average number of neighbors of one sphere separated by an interstice $\leq h$. $z(0)$ is the usual contact coordination number z_c , and $z(h)$ characterizes the packing geometry in terms of position correlations.

A decomposition of the coordination number of contacts z_c is:

$$z_c = z_+ + z_-, \quad (3.26)$$

in which z_+ is the coordination number of compressive bonds (positive forces) and z_- is the coordination number of tensile bonds (negative forces). Note that z_+ includes only the contacts in which the repulsive elastic force is larger than the capillary force, and z_- includes all the distant interacting pairs and also all the contacts in which the capillary force dominates.

particles so far, $h = 2R(1 - \cos \varphi)$, and hence [140]

$$V_m = \pi a^2 h - 2v_i = \frac{2\pi R^3}{3}(2 \cos^3 \varphi - 3 \cos^2 \varphi + 1). \quad (3.29)$$

The volume of the meniscus is therefore approximately $8 \cdot 10^{-3} d^3$ when the filling angle reaches its maximum value $\varphi = \pi/6$. Note that, here, the so-called *toroidal approximation* is used: the curves limiting the meniscus in a plane containing its axis of symmetry are approximated as circular arcs. Formula (3.29) also assumes a contact angle equal to zero. Eq. (3.28) then predicts a maximum saturation between 0.05 and 0.1, similar to experimental observations [84, 34]. With the selected value of $V_m/d^3 = 10^{-3}$, used, as a reference value, in most simulations of this study, Eq. (3.28) predicts the degree of saturation in this work to be of the order of 10^{-3} .

3.3.5 Average normal force

Given the formula (3.24) for the stress tensor, it is easy to deduce a convenient expression for the average intergranular normal force [13, 230]. From

$$\mathcal{P} = \frac{1}{3\Omega} \sum_{i < j} \vec{F}_{ij} \cdot \vec{r}_{ij}, \quad (3.30)$$

one gets, $\vec{r}_{ij} = (d + h_{ij})\vec{n}_{ij}$, in which \vec{n}_{ij} denotes the normal unit vector pointing in contact $i - j$.

Eq. (3.30) can be rewritten as:

$$\mathcal{P} = \frac{1}{3\Omega} \sum_{i < j} (R_i + R_j) F_{ij}^N + \frac{1}{3\Omega} \sum_{i < j} h_{ij} F_{ij}^N \quad (3.31)$$

The second term is usually neglected with grains in contact (as the elastic deflection $h_{ij} < 0$ is very small). For distant interactions through menisci ($h_{ij} > 0$) it was also observed [29] to be very small for the range of meniscus volumes corresponding to the pendular state. Replacing the sums with the average values and using the definitions of Φ , z , and z_d gives us:

$$\mathcal{P} = \frac{\Phi z}{\pi d^2} \langle F_N \rangle \quad (3.32)$$

The relation (3.32) can be accurate in all simulated states with or without cohesion [13]. However, in the presence of cohesion, it cannot be used to predict the typical contact force when the confining pressure is dominated by the attractive forces. Then, contact forces of order F_0 are quite common [187], while the average force is smaller.

In a moderately polydisperse system, (3.32) becomes

$$\mathcal{P} \simeq \frac{z\Phi \langle d \rangle}{\pi \langle d^3 \rangle} \langle F_N \rangle, \quad (3.33)$$

provided the correlation between the force value and the diameters is neglected.

3.3.6 Dimensionless control parameters

In order to achieve greater generality, dimensionless parameters are used in the presentation of all simulation results. Some are immediately apparent in the contact law: friction coefficient μ , damping coefficient ζ . From numerical observations [172], it is known that, while the influence of μ on the macroscopic mechanical behavior of model granular materials is always quite important, ζ is rather irrelevant in the quasistatic regime. Under a pressure P , the typical contact deflection $|h|$, relative to the grain diameter d , is related to a dimensionless stiffness parameter, which is conveniently defined as

$$\kappa = \left(\frac{\tilde{E}}{P} \right)^{2/3}. \quad (3.34)$$

It is such that typical values of $|h|/d$ are of order κ^{-1} [230]. If a linear contact elasticity is used instead of the Hertz law, then one may simply use $\kappa = K_N/(dP)$. In all simulations carried out here, κ is kept large enough along the whole compression curve that the elastic deflections are kept very small ($\kappa \geq 4000$). Such κ values hardly affect coordination numbers (due to contact recruitment caused by shrinking intergranular distances) [239].

To those parameters ruling the behavior of dry grains, one should add three new dimensionless groups which become relevant in the context of the present study, involving attractive forces.

With capillary forces, an additional dimensionless control parameter associated with the force law is the ratio of meniscus volume V_m to d^3 , determining the range of the corresponding capillary attraction, and consequently the number of liquid bonds. Fig. 3.6 compares function $F_{cap}(h)$ according to Maugis model and to the Soulié formula.

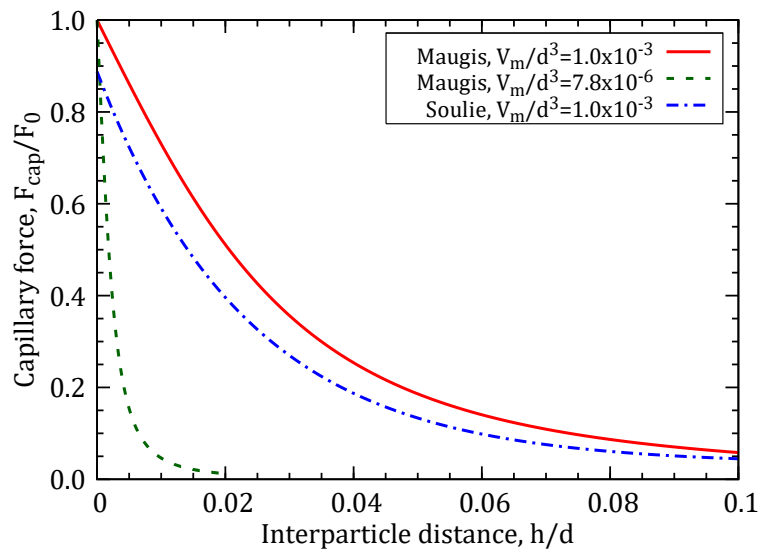


Figure 3.6: Capillary force law $F_{cap}(h)$, for two different meniscus values, according to the Maugis approximation and the Soulié formula.

Our simulation procedure, to be detailed below, involves an aggregation stage to form low pressure initial states, in which grains are agitated with a characteristic velocity V_0 . The microstructure of the resulting aggregates, as the initial kinetic energy is gradually dissipated, depends on whether the initial agitation is strong enough to cause breakage and restructuration of the contact networks, and thus on dimensionless ratio V_0/V^* , with V^* defined in Eq. (3.8). This ratio will be observed to have a strong influence on the initial coordination number.

The third dimensionless group introduced by capillary cohesion, an important control parameter, is the reduced pressure,

$$P^* = \frac{d^2 P}{F_0}, \quad (3.35)$$

comparing the applied pressure to the tensile strength (maximum attractive force) in contacts. $P^* \ll 1$ signals cohesion-dominated systems, for which attractive forces may stabilize loose structures. Confining forces dominate for $P^* \gg 1$, and attractive forces become negligible – the bead assembly behaves as a dry granular material. The simulation parameters are chosen such that P^* reaches large values before κ^{-1} decreases to 10^{-3} , and thus the effect of pressure in this study is due to the competition between confining stress and capillary forces, not to compression induced contact deflections.

Additional parameters are $\mu_R/d = \mu_P/d$ in system with RPR, as well as the rotation angles for which rolling and pivoting friction thresholds are reached (small enough to be irrelevant in our case).

In the polydisperse system, a reduced pressure is redefined as

$$P_{po}^* = \frac{\langle d^2 \rangle P}{\pi \Gamma \langle d \rangle}. \quad (3.36)$$

With the chosen diameter distribution (Sec. 3.2.1), one has

$$P_{po}^* = \frac{P}{\pi \Gamma} \frac{d_{\min} d_{\max}}{d_{\max} - d_{\min}} \ln \left(\frac{d_{\max}}{d_{\min}} \right). \quad (3.37)$$

3.4 Simulation procedures for the compression test

3.4.1 Specimen preparation

Before applying a controlled external pressure, we first assemble disordered, loose configurations in which the grains form connected aggregates spanning the sample.

A preliminary step consists in placing the grains within the cubic, periodic simulation cell, forming a disordered configuration without contacts. We thus choose the initial solid fraction Φ_0 , which may be set to low values (down to 0.2) compared with the typical densities of dry granular systems (Φ hardly decreases below range 0.55–0.58, depending on the friction coefficient, in confined cohesionless bead packs). Several techniques can be used to obtain disordered configurations of non-contacting beads.

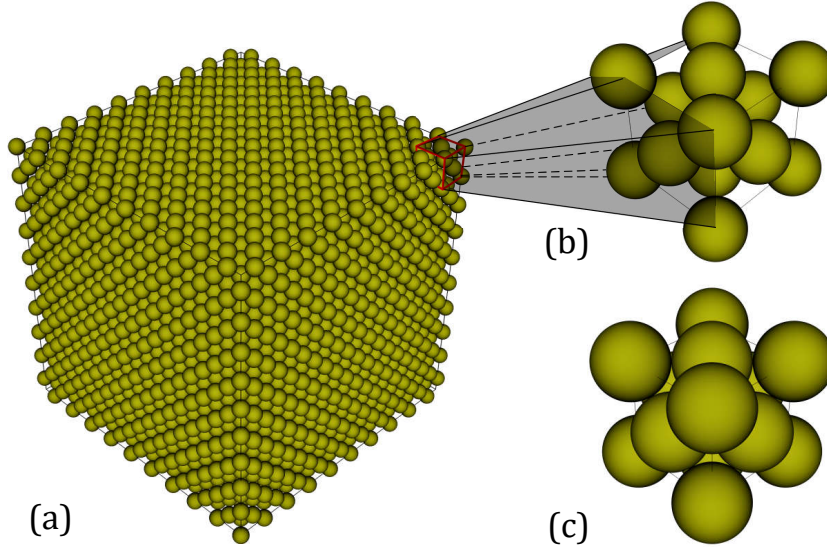


Figure 3.7: Monodisperse system on FCC lattice ($\Phi_0 = 0.3$): (a) whole specimen; (b) small cube extracted from (a); (c) a small cube of maximal density ($\Phi_0 = \frac{\pi}{3\sqrt{2}}$).

A convenient one uses the “melting” of a regular lattice [230]. In this study we use samples of $N = 4000$ (often monodisperse) beads, initially placed on the sites of a Face-Centered Cubic (FCC) lattice within the cubic cell, as shown in Fig. 3.7. In order to obtain a disordered system, the beads are first regarded as hard objects interacting with collisions that preserve kinetic energy. Once launched with random velocities, the initial order is quickly forgotten (provided Φ does not exceed the crystallization value 0.49 for monosized beads). This initial *mixing stage* is a purely numerical procedure in which the mechanical properties of the particles do not conform to the physical model.

Next comes an *aggregation stage*, for which the grains are endowed with all the properties of elasticity, friction (possibly RPR) and capillary cohesion as described in Sec. 3.2. This numerical procedure is supposed to mimic, in some idealized version, the physical process by which low density equilibrium configurations of wet beads are stabilized. Once attributed random velocities, which are Gaussian distributed with a mean quadratic velocity V_0 , particles collide, and the capillary attraction causes them stick to one another. A contact network gradually forms, and kinetic energy gets dissipated. The process is stopped when all particles are connected, forming one single cluster joined by liquid bonds, and when all particles reach equilibrium in the sense of Sec. 3.3.2. Typical resulting disordered configurations are shown in Fig. 3.8. The same aggregation procedure applies to polydisperse systems.

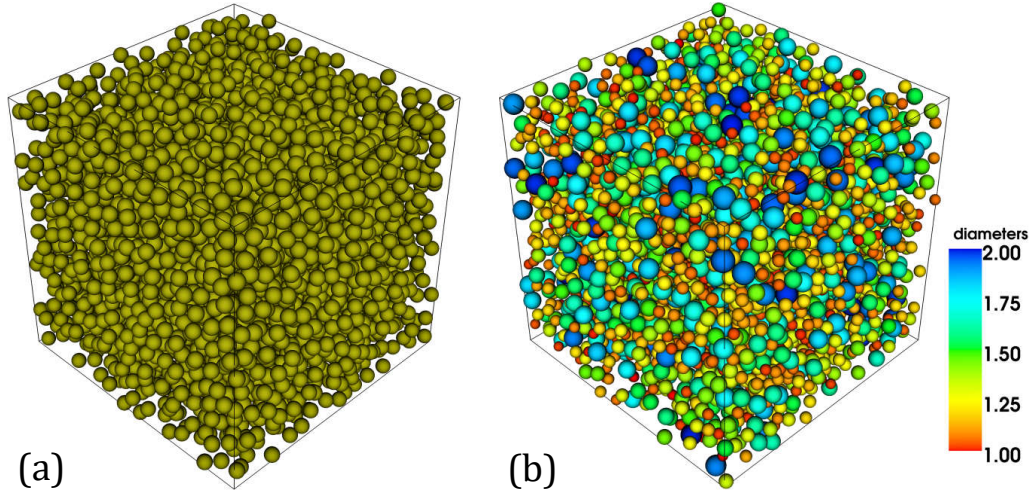


Figure 3.8: Typical specimens of (a) the monodisperse ($\Phi_0 = 0.30$) and (b) the polydisperse ($\Phi_0 = 0.24$) systems.

3.4.2 Simulation parameters

The sample series and the parameter values for the monodisperse material without RPR are listed in Table 3.1. Sample F30V1Vm3 is chosen as the reference case, from which the different control parameters are varied one by one: initial solid fraction Φ_0 , initial agitation level V_0/V^* in the aggregation process, meniscus volume V_m .

Polydisperse samples (without RPR) are prepared with six different initial agitation intensities, as listed in Table 3.2.

The sample series for the (monodisperse) material with RPR is given in Table 3.3. The dimensionless rolling friction coefficient, μ_R/d , and its pivoting friction counterpart μ_P/d are both set to 0.02 for most simulations.

Table 3.1: Initial parameters of the monodisperse system without RPR

Φ_0		V_0/V^*		V_m/d^3		Notation
0.25	F25	0.2041	V1	1.00×10^{-3}	Vm3	F25V1Vm3
0.30	F30	0.2041	V1	1.00×10^{-3}	Vm3	F30V1Vm3
		0.4082	V2			F30V2Vm3
		1.2247	V3			F30V3Vm3
		4.0825	V4			F30V4Vm3
		12.2474	V5			F30V5Vm3
		40.8248	V6			F30V6Vm3
0.30	F30	0.2041	V1	1.00×10^{-2}	Vm1	F30V1Vm1
				5.00×10^{-3}	Vm2	F30V1Vm2
				5.00×10^{-4}	Vm4	F30V1Vm4
				2.50×10^{-4}	Vm5	F30V1Vm5
				1.25×10^{-4}	Vm6	F30V1Vm6
				6.25×10^{-5}	Vm7	F30V1Vm7
				3.13×10^{-5}	Vm8	F30V1Vm8
				1.56×10^{-5}	Vm9	F30V1Vm9
				7.80×10^{-6}	Vm10	F30V1Vm10
0.32	F32	0.2041	V1	1.00×10^{-3}	Vm3	F32V1Vm3
0.35	F35	0.2041	V1	1.00×10^{-3}	Vm3	F35V1Vm3
0.40	F40	0.2041	V1	1.00×10^{-3}	Vm3	F40V1Vm3
0.45	F45	0.2041	V1	1.00×10^{-3}	Vm3	F45V1Vm3

Table 3.2: Initial parameters of the polydisperse system without RPR

Φ_0		V_0/V^*		V_m/d^3		Notation
0.24	Po	0.2041	V1	1.00×10^{-3}	Vm3	PoV1Vm3
		0.4082	V2			PoV2Vm3
		1.2247	V3			PoV3Vm3
		4.0825	V4			PoV4Vm3
		12.2474	V5			PoV5Vm3
		40.8248	V6			PoV6Vm3

Table 3.3: Initial parameters of the monodisperse system with RPR

Φ_0		V_0/V^*		V_m/d^3		$\mu_R/d = \mu_P/d$		Notation
0.25	F25	0.2041	V1	1.00×10^{-3}	Vm3	0.02	R2	F25R2V1Vm3
0.30	F30	0.2041	V1	1.00×10^{-3}	Vm3	0.02	R2	F30R2V1Vm3
		0.2041	V1			0.004	R1	F30R1V2Vm3
		0.2041	V1			0.1	R3	F30R3V2Vm3
		0.2041	V1			0.5	R4	F30R4V2Vm3
		0.4082	V2			0.02	R2	F30R2V2Vm3
		1.2247	V3			0.02		F30R2V3Vm3
		4.0825	V4			0.02		F30R2V4Vm3
		12.2474	V5			0.02		F30R2V5Vm3
		40.8248	V6			0.02		F30R2V6Vm3
0.32	F32	0.2041	V1	1.00×10^{-3}	Vm3	0.02	R2	F32R2V1Vm3
0.35	F35	0.2041	V1	1.00×10^{-3}	Vm3	0.02	R2	F35R2V1Vm3
0.40	F40	0.2041	V1	1.00×10^{-3}	Vm3	0.02	R2	F40R2V1Vm3
0.45	F45	0.2041	V1	1.00×10^{-3}	Vm3	0.02	R2	F45R2V1Vm3

3.4.3 Compression cycle

All assembled samples of the series of Tables 3.1, 3.2 and 3.3 are compressed under growing external isotropic pressure. A stepwise pressure-controlled loading path is applied. In each compression step, external reduced pressure P^* is multiplied by a constant factor $10^{1/4} \simeq 1.7783$, and one waits until the new equilibrium configuration is reached, with the criteria stated in Sec. 3.3.2. The main objective of the present work is to study of the effect of a gradual compression, starting from cohesion-dominated loose states at small P^* , and ending in confinement-dominated denser states at large P^* . The compression program is pursued up to $P_{\max}^* = 10^4$ (or for some systems, to $P_{\max}^* = 10^3$). Then, the reverse path of P^* back to minimum value $P^* = 10^{-3}$ from its highest value is also simulated.

3.5 Material behavior in isotropic compression

3.5.1 A reference case

3.5.1.1 Macroscopic behavior

The reference test is first run with a low initial solid fraction, $\Phi_0 = 0.30$. In the present works, the results are shown in the form of the conventional compression curve showing void index e versus $\log P^*$. The compression and decompression curves in the reference case is shown in Fig. 3.9.

Based on the range of the reduced pressure P^* , three regimes are identified from the compression curve (see the inset of Fig. 3.9(a)). A first regime (Regime I) is observed for low reduced pressures, $P^* \leq 10^{-2}$, in which the initial structure still sustains the increasing pressure without rearrangement, and void ratio e remains nearly constant (Fig. 3.9(a)). In a second stage (Regime II), roughly corresponding to interval $2 \times 10^{-2} \leq P^* \leq 2 \times 10^0$, the void ratio strongly decreases, and might be described as linearly varying with $\log P^*$. The loose structures formed at low P^* are no longer able to support the increasing confining pressure, they collapse and restructure. Finally, in Regime III, e gradually approaches some minimum void ratio e_{\min} at the end of the loading process. The slight decrease of e for $P^* \geq 10^2$ is similar to the behavior of cohesionless systems, and due to elastic deflections in a stable contact network. The chosen parameters are such that κ remains large enough not to influence the compression process taking place in Regime II.

The plastic compression behavior of the wet material is closely similar to the 2D results of Gilabert *et al.* [14], and to the experimental compression test results on metallic powders by Poquillon *et al.* [6]. The void ratio curve in Regime II might be represented with a linear variation with $\log P^*$, assuming e_{ref} is the void ratio for some reference

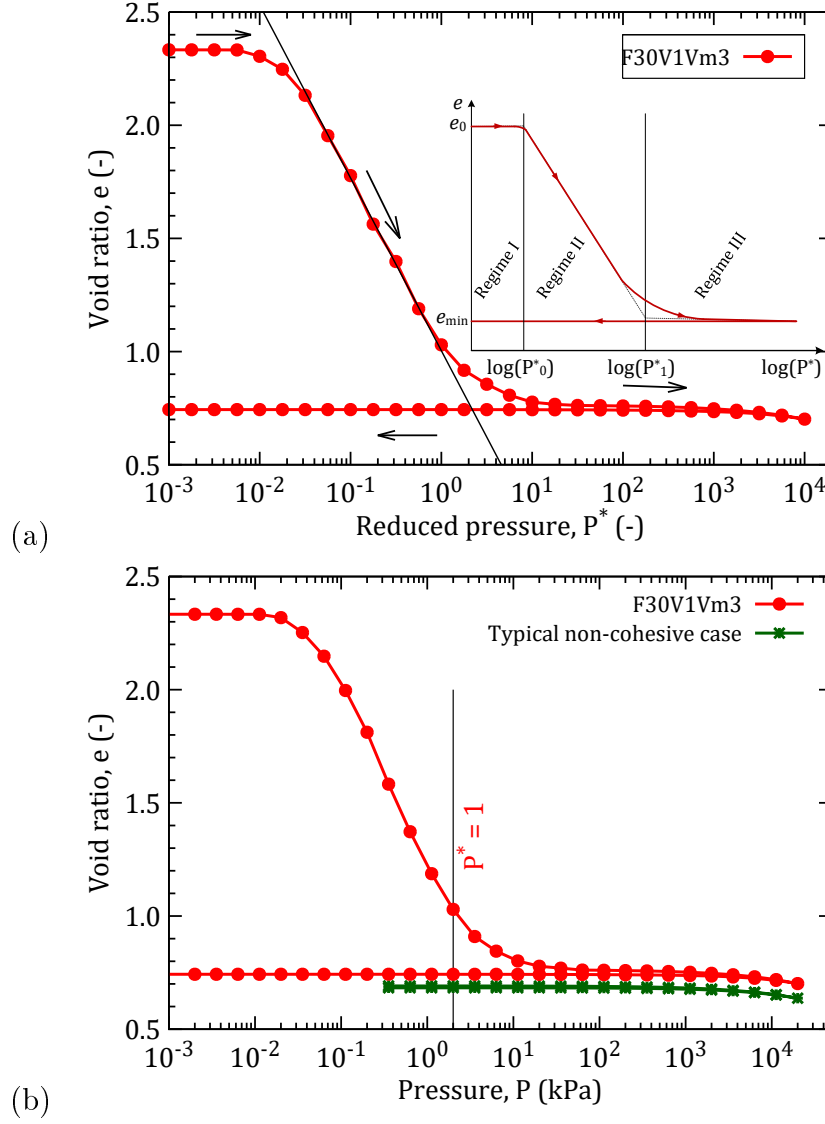


Figure 3.9: (a) e versus $\log P^*$ for reference system in compression cycle (with schematic view of three regimes in the inset); (b) comparison of reference case and typical non-cohesive behavior, with pressure in kPa for glass beads of diameter 0.118 mm wet by water.

reduced pressure, P_{ref}^*

$$e - e_{ref} = -\lambda \log \frac{P^*}{P_{ref}^*}. \quad (3.38)$$

Coefficient $\lambda \simeq 0.36$ successfully describes the curve in interval $4 \times 10^{-2} \leq P^* \leq 2 \times 10^0$. Eq. 3.38 is usually used in soil mechanics for cohesive materials [5].

Upon decompression, e increases slightly, remaining very close to e_{min} : the compaction is essentially irreversible, unlike in the cohesionless granular assembly of Fig. 3.9(b), for which loading and unloading branches are not distinguishable (as observed in the numerical study of compression cycles of cohesionless spherical beads reported in Ref. [239]). Note the use of a physical unit of pressure in Fig. 3.9(b), corresponding to glass beads of

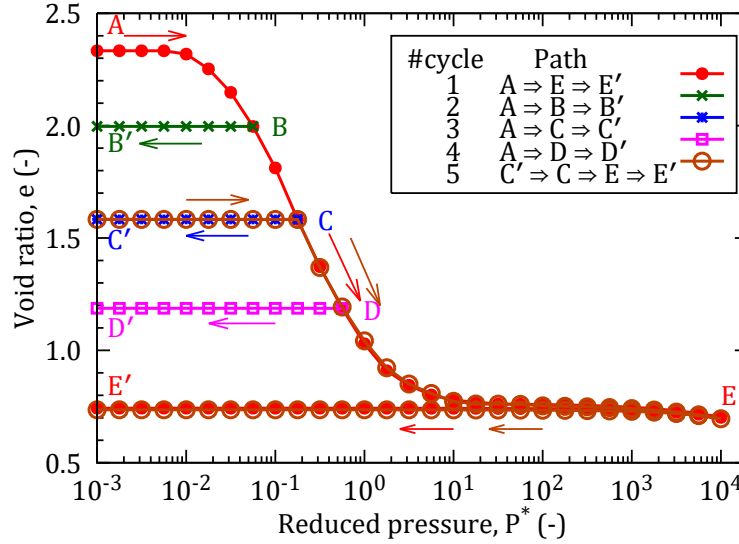


Figure 3.10: Effect of different (isotropic) unloading and reloading histories on void ratio; the system does not rearrange along unloading paths BB' , CC' , DD' , EE' , which are reversible; Path 5 causes plastic response in Section CE , along which pressure increases beyond its past maximum; the primary curves (Path 1) is then retraced.

diameter $118 \mu\text{m}$, perfect wetting, and the surface tension of water. With such a system $P^* = 1$ is obtained for $P = 2 \text{ kPa}$.

Upon unloading and reloading at various pressure levels along the compression curve, a plastic response (irreversible structural rearrangement with density change) under isotropic pressure is only observed (as illustrated in Fig. 3.10) if the maximum pressure the system has been subjected to in the past (the overconsolidation pressure of soil mechanics) is exceeded. This maximum pressure value appears to fully characterize the history dependence of the system in isotropic compression [47].

3.5.1.2 Contact networks and force transmission

As defined in Sec. 3.3.3, an important microstructural characteristic, the coordination number z , defined as the average number of interactions per grain, is the sum of the contact coordination number z_c and the coordination number of distant interactions, through menisci joining non-contacting grains, z_d .

Fig. 3.11(a) plots z_c , z_d , and z versus P^* in the compression cycle. Initially, one has $z_d = 0$, as the velocities in the aggregation process, in the reference case, are low, and do not allow contact opening (let us recall that distant interaction through menisci without intergranular contact only appear when contacts open – menisci do not spontaneously form between non-contacting grains). The obtaining of $z_c \simeq 4$ at low P^* is consistent with a minimally connected initial network, which does not reorganize or fold onto itself as aggregation proceeds. The value $z_c = 4$ is the one corresponding to isostaticity in a pack of frictional beads (although some limited simultaneous amount of force indeterminacy

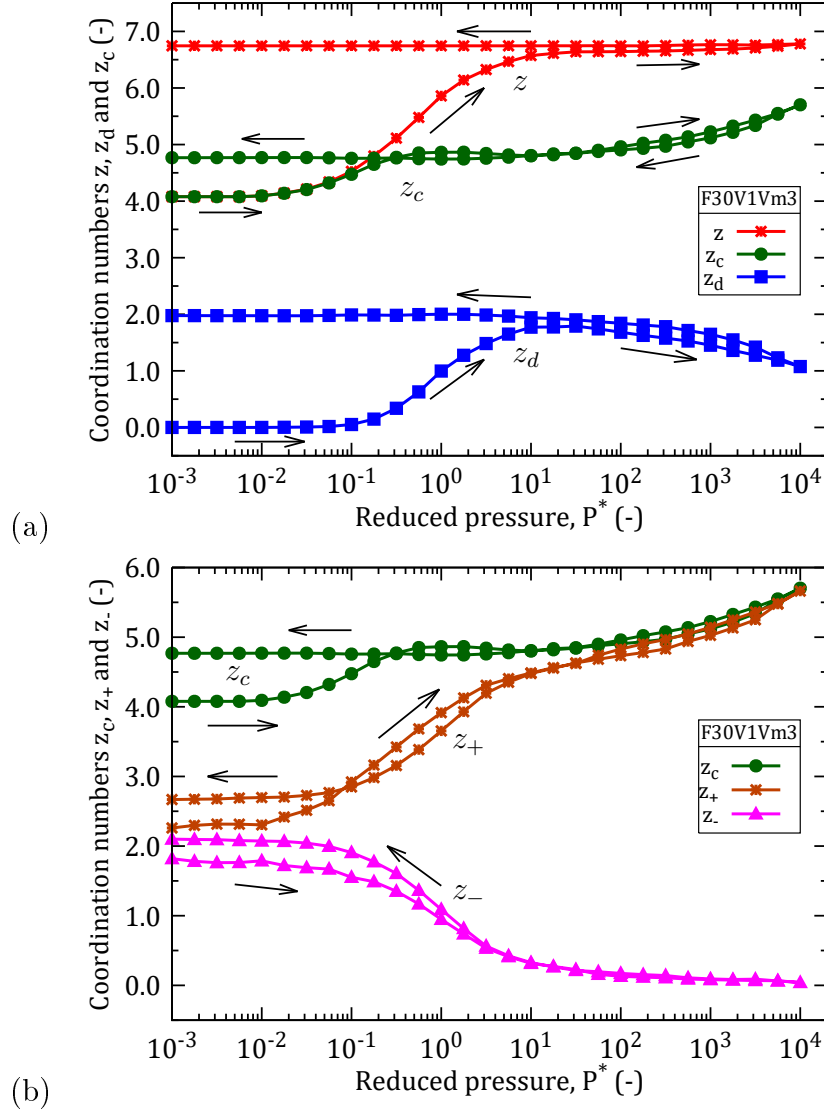


Figure 3.11: (a) Coordination numbers z , z_c and z_d ; and (b) coordination numbers z_c , z_+ , and z_- versus P^* in compression and decompression cycles.

and velocity indeterminacy – or hyperstaticity and hypostaticity – is not excluded, see Ref. [230]). z_c and z_d remain unchanged in Regime I ($P^* < 10^{-2}$), as the initial structure is maintained. Both coordination numbers start to increase as the structure collapses and reorganizes in Regime II ($10^{-2} < P^* \leq 2 \times 10^0$). z exhibits little change in Regime III ($P^* > 2 \times 10^0$), as the increase of the number of contacts is then mainly due to the closing of narrow gaps between pairs of grains joined by a meniscus, as the structure is further compressed – a moderate effect. Upon unloading, some contacts are opened and therefore z_d first increases while z_c decreases a little. Then both coordination numbers tend to remain constant till to the final state at low P^* , reflecting the stability of the dense structure formed at high P^* .

The coordination number of contacts z_c may be split into the contribution of compressive bonds, z_+ , and the one of tensile bonds, z_- . Coordination numbers z_c , z_+ , and

z_- are plotted versus reduced pressure P^* in Fig. 3.11(b). At low P^* , both compressive and tensile contact forces are present, with similar values of z_+ (slightly above 2) and z_- (slightly below 2). Nearly constant in regime I, they vary in opposite directions under growing P^* in regime II, with more and more compressive forces. At high pressure P^* , z_- gradually vanishes, as the system essentially behaves like a pack of compressed cohesionless beads. z_+ and z_- vary in opposite ways upon reducing P^* , without returning to their initial values.

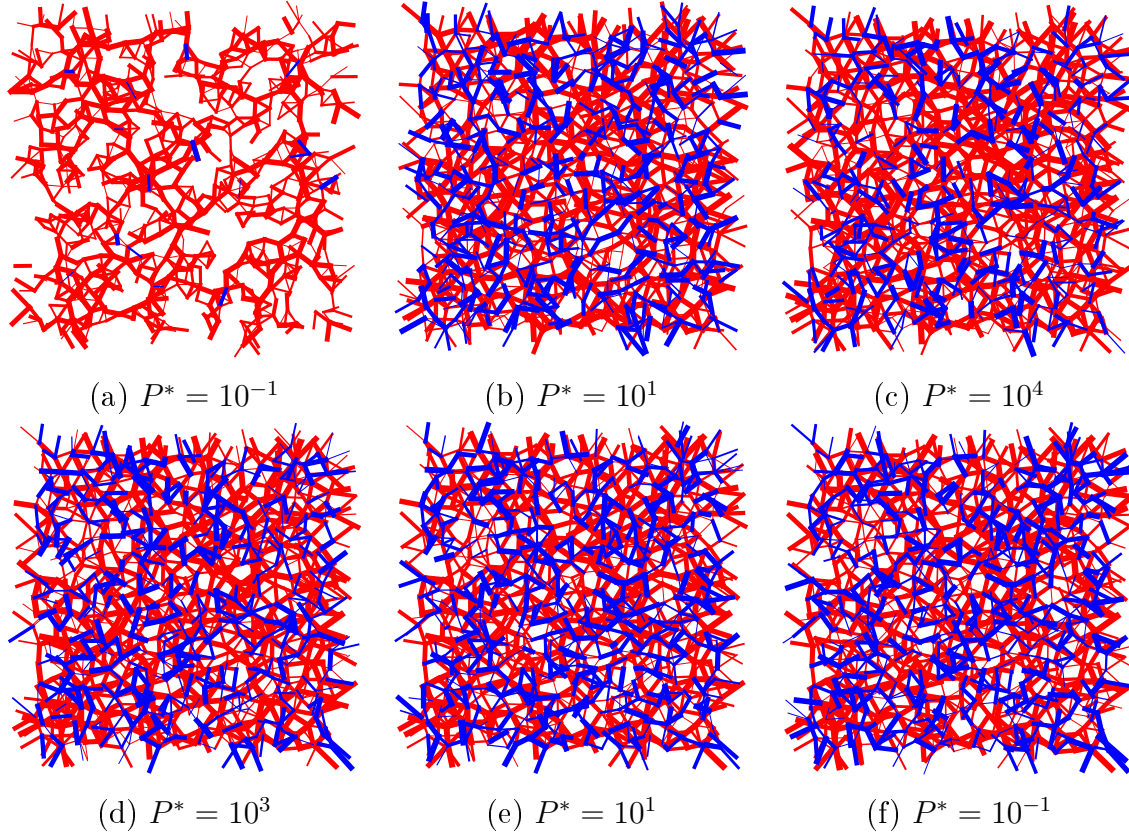


Figure 3.12: Contact networks in loading (a, b, and c) and unloading (d, e, and f) cycle. Line thicknesses for wet contacts (red lines), and for distant interaction (blue lines) are proportional to the normal force intensity $|F_N|$.

Contact networks may be visualized in order to provide insight on the structural changes and the evolutions of z_c and z_d under growing P^* . Fig. 3.12 shows the networks of wet contacts and of distant interactions through menisci at six typical stages of P^* in the compression cycle. A slice is extracted from the sample with width $3d$, its height and length being those of the whole cuboidal simulation cell. In Fig. 3.12, the red lines denote the wet contacts (the total normal force $F_N \neq 0$), and the blue lines denote the interactions through menisci, without direct contact. Along the loading path, under growing of pressure P^* , more distant interacting pairs are created, while the network density is increased (Figs. 3.12, a and b). Numbers of distant interacting pairs are slightly decreased till the end of loading path (Fig. 3.12(c)). The density of distant

interacting pairs reaches its maximum near $P^* = 10^1$, which corresponds to the end of Regime II. In unloading path, when the system is gradually opened, the numbers of distant interacting pairs are slightly increased. It remains nearly constant at the end of unloading path (beyond the stage $P^* = 10^{-1}$). We can see an insignificant change in the density of the blue lines in Figs. 3.12(d, e, and f).

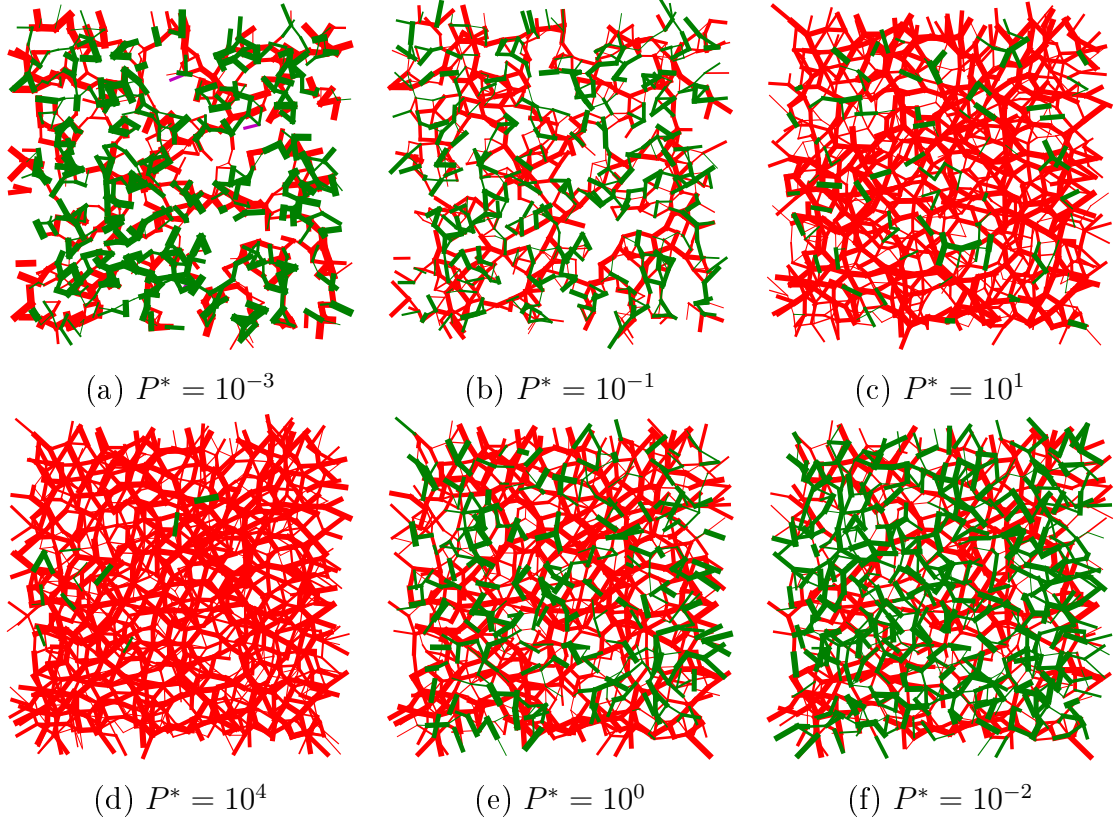


Figure 3.13: Networks of compressive contacts (red lines), tensile ones (green lines), and contacts with $F_N = 0$ (magenta). Line thicknesses are proportional to normal force intensity $|F_N|$. Loading path: (a), (b), (c) and (d); unloading path: (e) and (f).

Similarly, compressive and tensile bonds are also depicted in Fig. 3.13. The contact networks of the z_+ and z_- are selected at several values of P^* in compression path (Fig. 3.13(a, b, c, and d)) and decompression path (Fig. 3.13(e and d)). Initially, at the beginning of the compaction curve, the density of compressive bonds is higher than one of tensile bonds. There also exist several pairs having a null normal force (the magenta lines). This means the normal elastic force F_N^e is balanced with the capillary force F_{cap} . Upon growing of P^* , the compressive and tensile bonds are oppositely changed. While the compressive contacts are dramatically increased, the tensile ones are sharply decreased. We can obviously see the increase in the density of the red lines in Figs. 3.13(b and c). Until the maximal pressure ($P^* = 10^4$), the compressive ones reach to the maximum (at $z_+ = 5.75$, approximately 99 % of the contacts) while the tensile ones reduce to minimum corresponding to $z_- = 0.04$ (approximately 1 % of the contacts). For the

unloading cycle (see Figs. 3.13(e and f)), when the system is opened, the compressive and tensile contacts are inversely increased and reach to a constant values at the end of unloading path. The densities of the red and green lines at the stage $P^* = 10^{-2}$ are nearly equalized (Figs. 3.13(f)).

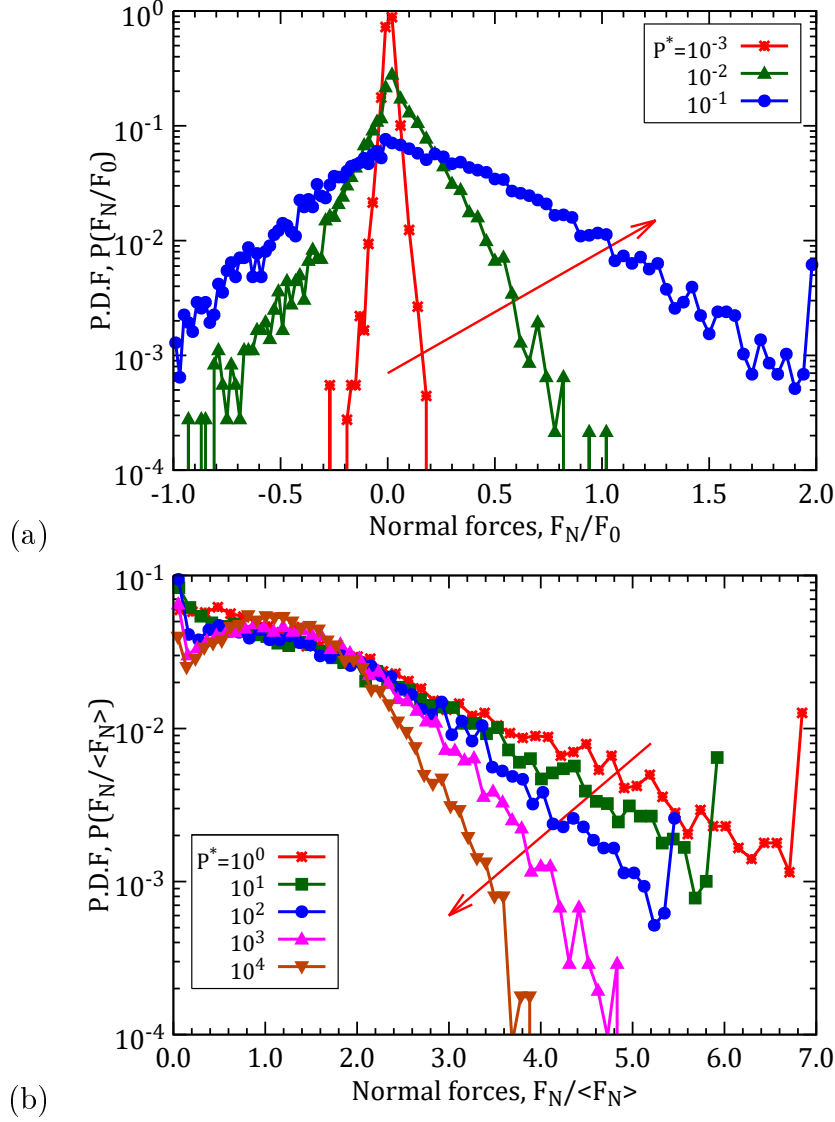


Figure 3.14: Distribution of normal forces for different values of P^* from the compression path, (a) normalized by the maximum tensile force F_0 , and (b) normalized by the average normal force $\langle F_N \rangle$. Red arrow indicates increasing P^* .

The distribution of intergranular force values in a granular material in equilibrium [62, 240, 237, 230, 231] has received a lot of attention in the recent literature. The probability distribution function (hereafter referred to as P.D.F) of normal forces in the reference system is also investigated, involving: distribution of forces between distant interacting pairs, distribution of repulsive contact forces and distribution of negative (tensile) contact forces (see Fig. 3.14). In cohesion dominated configurations ($F_0 \gg \langle F_N \rangle$), the P.D.F is normalized by the maximum tensile force F_0 . It is normalized by the average normal

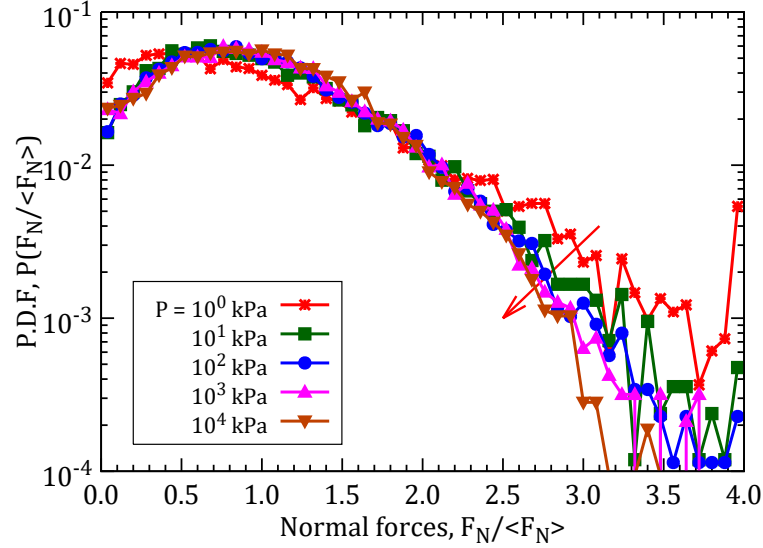


Figure 3.15: Distribution of normal forces for different values of P^* in non-cohesive case, normalized by the average normal force $\langle F_N \rangle$. Red arrow denotes increasing P^* values.

force $\langle F_N \rangle$ at larger reduced pressure P^* . The normal force distributions are roughly symmetric about zero in the initial states and under low P^* , (see e.g., the red and dark green curves). At the beginning of Regime I, $P^* = 10^{-3}$, all of the total normal forces F_N are very small. This is due to the near lack of force indeterminacy: if the network were exactly isostatic, all forces would vanish under zero pressure. These P.D.Fs widen and take notable values near $F_N = -F_0$ at the end of Regime I, signalling that more and more contacts are on the verge of opening. At pressure $P^* = 10^{-1}$, all P.D.Fs widen on the positive (repulsive) side, while the largest tensile force is fixed at F_0 , thus becoming dissymmetric, as shown in Fig. 3.14(a). Given relation (3.32), the average normal force tends to scale with pressure P (up to moderate effects of the variations of contact density $z\Phi$). In the last compression stage (regime III), these P.D.Fs, if normalized by the average $\langle F_N \rangle$, become narrower, as apparent in Fig. 3.14(b). This is similar to the behavior of cohesionless systems, in which those PDF's tend to decrease exponentially, on a scale given by the average $\langle F_N \rangle$, the faster the larger the pressure (or the smaller κ) – see Fig. 3.15. These results are quite similar to the ones obtained in other numerical studies on cohesive granular materials [187, 13, 14]

3.5.1.3 Influence of meniscus volume

We now report on investigations of the influence of meniscus volume V_m/d^3 , which is kept low enough for the material (with a saturation hardly exceeding 1%) to be maintained in the pendular state. Despite the importance of capillary bridges in the stabilization of loose structures, the change of meniscus volume seems to have no effect on the macroscopic behavior of the granular specimens under isotropic compression (no apparent change in the compression curve, e versus $\log P^*$), as shown in Fig. 3.16(a). This is cor-

roborated by the fact that very little change in the coordination number of contacts z_c is observed. Only the coordination number of distant interactions is notably influenced by such a change, especially in Regimes II and III, and in the decompression process, as depicted in Fig. 3.16(b). As menisci break at larger interparticle distance with larger meniscus volume, more liquid bonds are present.

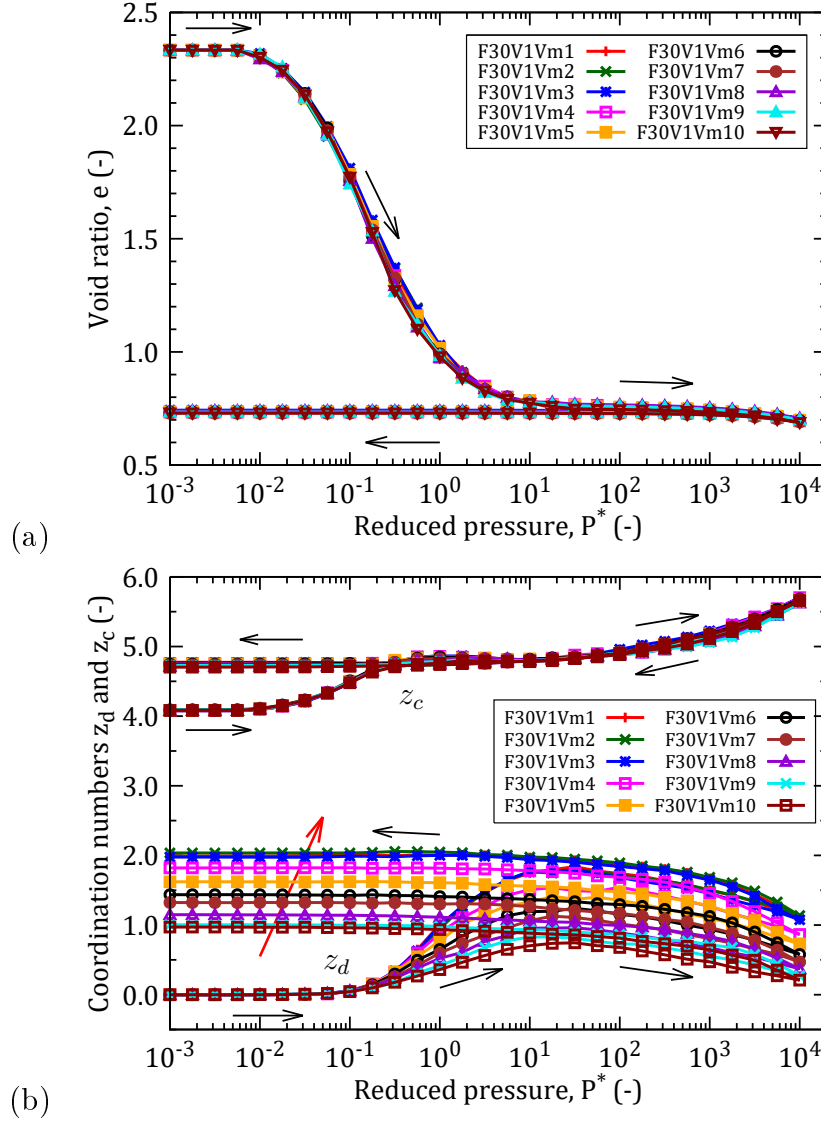


Figure 3.16: Void ratio (a), coordination numbers z_c and z_d (b) versus P^* of the reference case for different values of meniscus V_m/d^3 . Red arrow shows direction of increasing V_m values.

The coordination numbers of compressive bonds z_+ and tensile bonds z_- for different values of meniscus volume V_m/d^3 are also calculated, as shown in Fig. 3.17. In general, z_+ and z_- change similarly (increasing with V_m) in the loading path, upon entering regime II. However, they change in opposite directions in the end of unloading path ($P^* < 10^0$) (see the inset). While z_+ is reduced corresponding for decreasing meniscus volume, z_- is increased. The distant interactions through menisci joining non-contacting

grains are more numerous in systems with larger meniscus volume V_m . They contribute negatively to the pressure. For smaller V_m , their mechanical role is taken over by some of the contact forces, carrying net tensile forces.

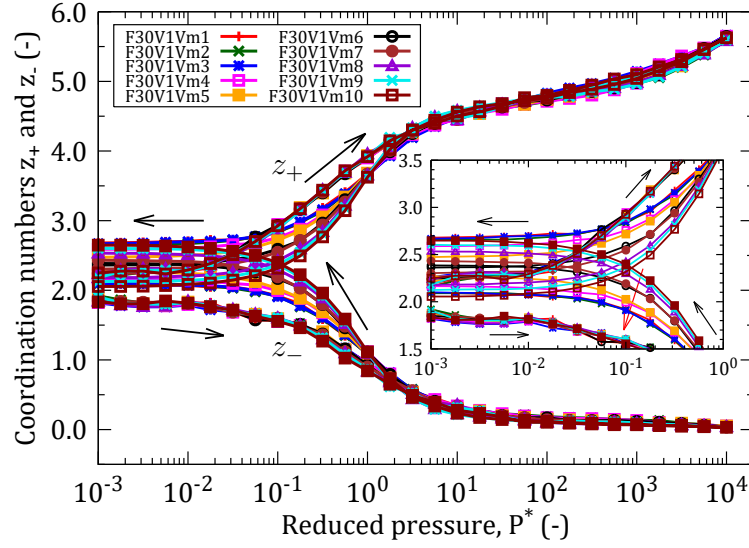


Figure 3.17: Coordination numbers of z_+ and z_- versus reduced pressure P^* for different values of V_m/d^3 . Inset shows detail with red arrow denoting increasing V_m .

The contact forces, including the wet contacts and contacts through meniscus for different values of V_m/d^3 are also analyzed. However, only the numbers of instant interacting pairs are changed, similar the change in Fig. 3.16. Furthermore, the compressive and tensile bonds are also analyzed. Nevertheless, they are nearly constant in loading cycle. They only change in the end of decompression path, when the pressure $P^* < 10^0$. The compressive bonds are decreased when the tensile ones are increased according to the decreasing of meniscus volumes.

Fig. 3.18 plots the distribution of the numbers of contacts per grains (connectivity) in the reference case for eight different values of meniscus volume during the compression process. Three representative stages of pressure P^* are observed in order to see clearly the rearrangement of microstructure due to the decrease in liquid content under growing pressure P^* . For $P^* = 10^{-3}$, close to the initial state, which is essentially V_m independent (because of the absence of distant interactions), the connectivity is not affected. For larger pressures, the structure gets somewhat depleted (although this is not a strong effect)

The effect of V_m on P.D.Fs of normal forces is also observed to be very small.

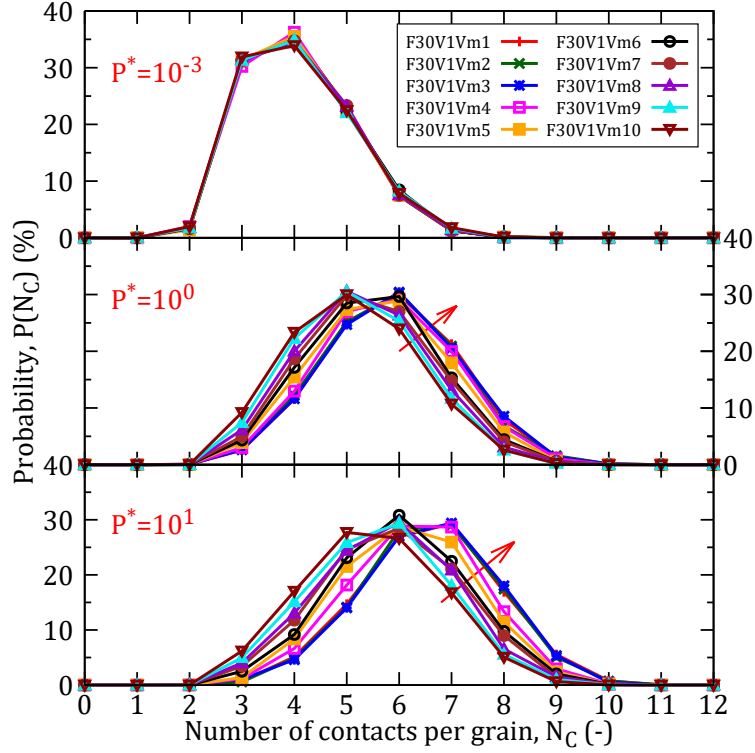


Figure 3.18: Distribution of the number of contacts per grain of the reference case for different values of V_m/d^3 at three typical states of P^* . Red arrow orders curves by increasing V_m .

3.5.1.4 Coordination number of close neighbors

Below the rupture distance D_r , the number of distant, interacting pairs in comparison with the total number of neighbor pairs is also mentioned. The coordination number of close neighbor $z(h)$ at distance below h (such that $z(0) = z_c$) increases with h as shown in Fig. 3.19.

Under low pressure $P^* \leq 10^{-2}$, $z(h)$ is almost similar (red and green curves) because hardly any structural change takes place in Regime I, and its increase with h is slow, with a slight upward curvature (convex curve). At $P^* = 10^{-1}$, $z(h)$ slightly increases. This corresponds to a slight increase of the z_c in Fig. 3.11(a). For growing P^* , function $z(h)$ gradually retrieves the concave shape observed in cohesionless systems [230], with larger contact coordination numbers, and correlatively less “incipient contacts” at short distance. Beyond a few times $d/100$, $z(h)$ steadily increases with density.

Within the interparticle the meniscus rupture distance D_r , each grain has on average $z(D_r) - z_c$ non-contacting neighbors, among which z_d neighbors are interacting by an attractive force. The ratio of z_d to $z(D_r) - z_c$ is the proportion of the neighbors within the range D_r that are bonded by a capillary bridge. This ratio for different values of P^* in loading path of the reference case are given in Table 3.4. These values are calculated for maximum and minimum initial agitation intensities of the loading cycle. For the

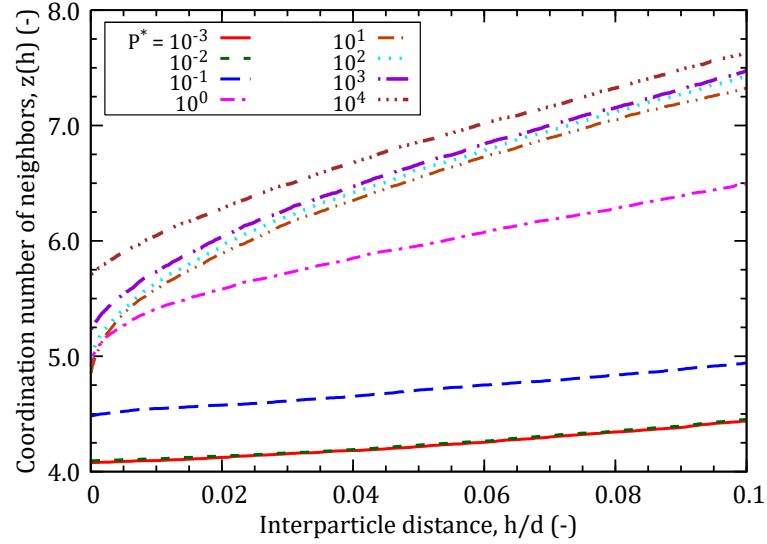


Figure 3.19: Evolution of coordination number of close neighbors $z(h)$ versus dimensionless interparticle distance h/d for different values of P^* in loading path.

unloading cycle, this proportion only negligibly changes.

Under low pressure $P^* \leq 10^{-2}$, $z(h)$ is almost similar (red and green curves) because no more contacts or distant interactions are created. At $P^* = 10^{-1}$, $z(h)$ slightly increases. This corresponds to a slight increase of the z_c in Fig. 3.11(a). At $P^* = 10$, $z(h)$, like the coordination number of contact, slightly decreases for very small h/d . This is the moment that z_c starts to increase in Regime III (see Fig. 3.11(a)). Beyond that distance, $z(h)$ increases with P^* . Once the interparticle distance h goes up to the meniscus rupture distance D_r , each grain has on average $z(D_r) - z_c$ non-contacting neighbors, among which z_d neighbors are interacting by an attractive force. The ratio of z_d to $z(D_r) - z_c$ is called as the proportion of the neighbors within the range D_r bonded by a capillary bridge. This ratio for different values of P^* in loading path of the reference case are given in Table 3.4. These values are calculated for maximum and minimum initial agitation intensities of the loading cycle. For the unloading cycle, this proportion is negligibly changed.

These values are similar to the ones of Khamseh *et al.* [29] and to the proportion of about 50% reported by Kohonen *et al.* [125] in static grain packs.

Table 3.4: Probability of meniscus formation between close neighbors versus P^* .

P^*	F30V1Vm3		F30V6Vm3	
	z_d	$z_d/[z(D_r) - z_c]$	z_d	$z_d/[z(D_r) - z_c]$
10^{-3}	0.0000	0.0000	0.2510	0.3990
10^{-2}	0.0005	0.0014	0.2510	0.3990
10^{-1}	0.0515	0.1102	0.2990	0.4262
10^0	0.9970	0.6115	1.1040	0.6404
10^1	1.7720	0.7018	1.7990	0.6909
10^2	1.6830	0.6826	1.8020	0.6875
10^3	1.4540	0.6462	1.5590	0.6509
10^4	1.0760	0.5565	1.1680	0.5713

3.5.2 Influence of drying or of saturating

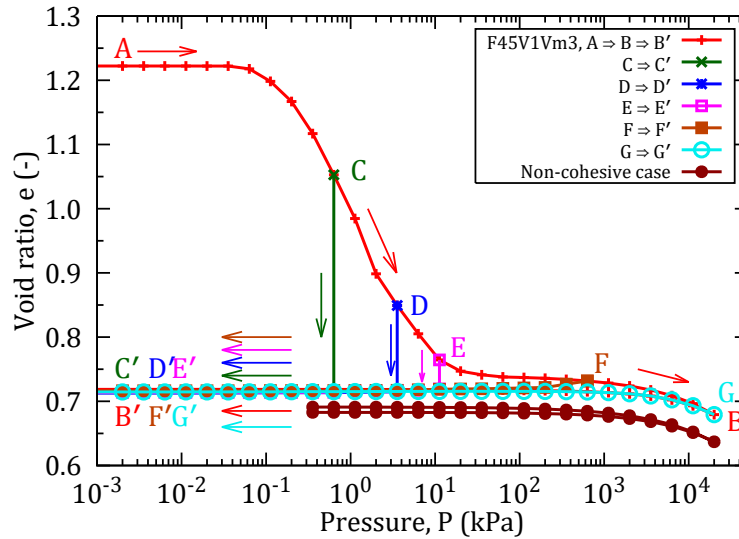


Figure 3.20: Void ratio versus pressure P , as cohesive forces are suppressed at the beginning of unloading, starting at different points on the primary compression curve (case with initial solid fraction $\Phi_0 = 0.45$).

In practice, one may act on a wet system by changing its saturation. The most drastic change should be obtained on entirely suppressing the capillary cohesion, either by drying, or by completely saturating the intergranular voids by the liquid. In numerical simulations, one may simply remove all capillary forces, leaving only the interactions present in a dry system. It is interesting to observe the effects of such an ideal transformation, carried out at various points along the irreversible compression curve. Fig. 3.20 illustrates the resulting void ratio evolution, if the system is suddenly deprived of capillary forces at different pressure levels. This ideal drying or saturation step produces

a sudden collapse (a brutal compression step), unless all irreversible compression has already taken place, as for Points F and G in Fig. 3.20. In such cases, one may remove all capillary forces, as their mechanical role, at high P , is negligible.

A more gradual collapse due to progressive imbibition is reported in some experiments [35].

Remarkably, the final state after decompression keeps the same density, whether or not the system has been deprived of capillary cohesion [47].

3.5.3 Influence of initial state

The assembling conditions notably affect the packing structure and microstructure under low pressure P^* . It is therefore necessary to assess the role of initial configurations, which are produced by the initial assembling process in the presence of with capillary bonds. The effects of various micromechanical parameters on the plastic compression curve are also discussed. The effects of both solid fraction Φ_0 and initial agitation intensity V_0/V^* are investigated.

3.5.3.1 Influence of initial solid fraction

Among the features affected by the assembling process, the competition between compression and aggregation is the most important one. Fig. 3.21, obtained with standard values $V_0/V^* = 0.2041$, $V_m/d^3 = 10^{-3}$, compares the compression curves of specimens with different initial solid fractions Φ_0 . Denser systems are able to support larger pressures before rearranging, whence larger Regime I plateaus (see Fig. 3.21(a)) in different intervals of reduced pressure P^* . For instance, from $10^{-3} \leq P^* \leq 4 \times 10^{-3}$ for the smallest Φ_0 value (F25V1Vm3) to $10^{-3} \leq P^* \leq 8 \times 10^{-2}$ for the largest one (F45V1Vm3). However, in Regime II, these compression curves tend to converge and they very nearly coincide at the end of the collapse (for $P^* = 2 \times 10^0$ to $P^* = 5 \times 10^0$), as clearly apparent in Fig. 3.21(a), with the different slopes of the six curves corresponding to different Φ_0 . In Regime III ($P^* > 5 \times 10^0$) and along the unloading path, the void ratio of the initially denser systems is only very slightly lower than the one of the looser systems.

Furthermore, the evolution of coordination numbers of z_c and z_d remain very similar during the loading and unloading paths whatever the initial solid fraction Φ_0 (see Fig. 3.21(b)). z_c is only very slightly different in Regime II, depending on the moment when the collapse started. Meanwhile, in the second half of Regime II, the difference in z_d is also quite insignificant, with slightly less contact openings leading to distant interactions in the denser systems. Along the unloading path, the denser the systems, the lower z_d too – but this difference is also quite small. One essential conclusion of these observations is that the coordination numbers depend much more on the system history (assembling process, loading path), than on its current density.

Looking at the coordination numbers of compressive and tensile bonds (Fig. 3.22),

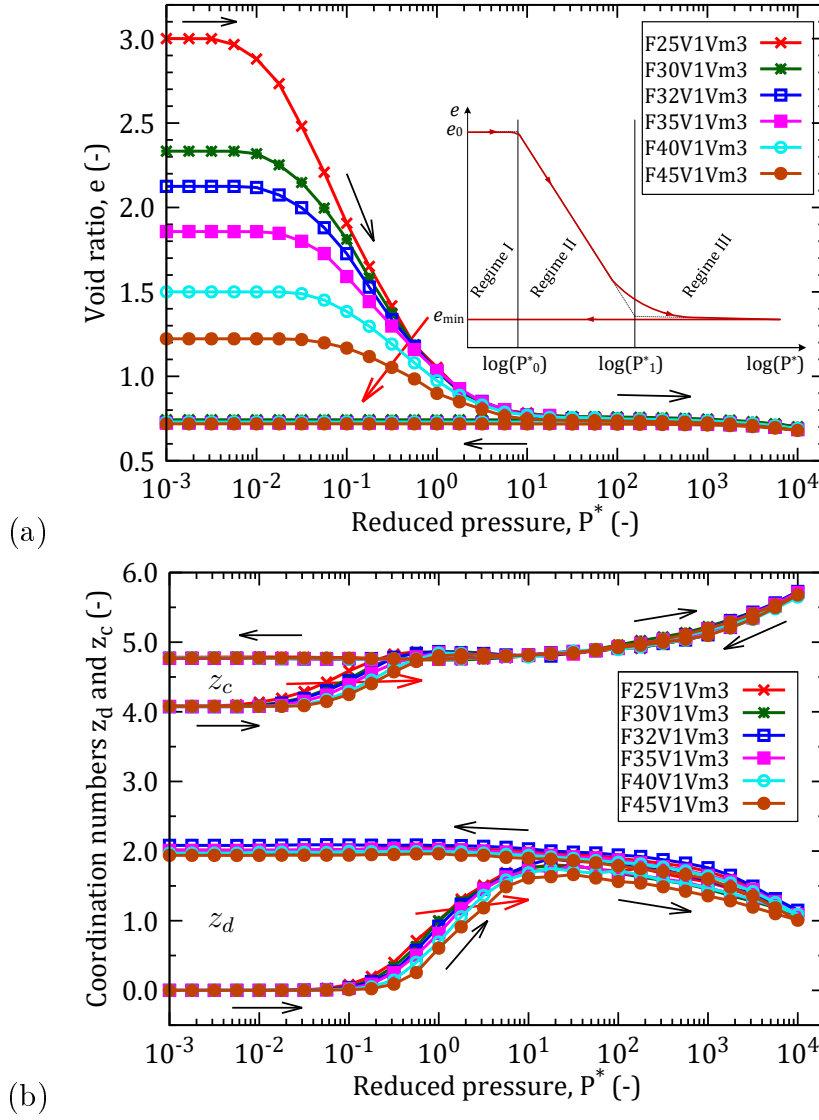


Figure 3.21: (a) Void ratio e , and (b) coordination numbers z_c and z_d versus P^* for different values of initial solid fraction Φ_0 . Red arrow denotes increasing Φ_0 .

one also observes quite insignificant differences for different initial solid fractions. z_+ and z_- at the beginning of loading curves ($P^* < 10^{-1}$), despite the different configuration geometry. z_+ increases to extent, while z_- decreases, for larger initial solid fraction Φ_0 (see clearly in the inset). Under growing pressure, z_+ and z_- evolve in opposite directions, similarly for all compression curves. System states appear no longer to be influenced at all by the initial density in Regime III and in unloading.

The connectivity, or distribution of the number of contacts per grain, $P(N_C)$, is shown in Fig. 3.23 for different values of Φ_0 (similarly to Fig. 3.18). Three figures correspond to three typical states of compaction path $P^* = 10^{-3}$, $P^* = 10^0$ and $P^* = 10^1$ (see the label on figure). At very low pressure $P^* = 10^{-3}$, the $P(N_C)$ is almost similar whatever the initial Φ_0 – confirming, in a more detailed form, the absence of correlation between density and contact numbers. $P(N_C)$ peaks at $N_C = 4$, with a value of approximately

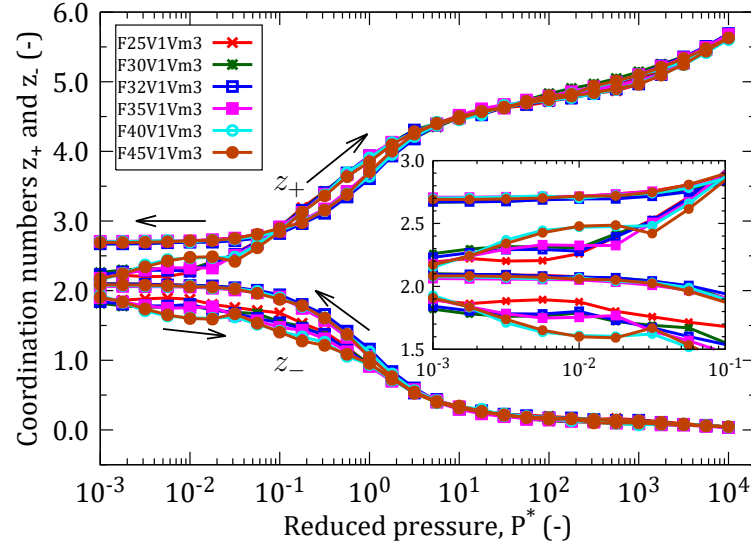


Figure 3.22: Coordination numbers z_+ and z_- versus P^* for different values of Φ_0 .

35 % for low pressure. The $P(N_C)$ is remarkably changed at $P^* = 1$, as its peak moves towards $N_C = 6$, except in the densest system $\Phi_0 = 0.45$. $P(N_C)$ curves tend to get shifted to larger N_C values in initially looser systems. In other words, at the end of the collapse, less contacts are created in the denser systems. This is confirmed via the variations of z_c and z_d in Fig. 3.21(b). At pressure $P^* = 10$, $P(N_C)$ reaches its maximum at $N_C = 7$ in the looser systems, while peaking at $N_C = 6$ in the denser ones. This tendency is in agreement with the small difference in z_d observed in Fig. 3.21(b). Then, like other state variables, connectivities signal no difference in Regime III and upon unloading.

Fig. 3.24 shows the distributions of normal forces for different values of initial solid fraction Φ_0 at $P^* = 10^{-2}$. At the lowest pressure $P^* = 10^{-3}$, the P.D.Fs are nearly symmetric about 0 and very similar to one another. At $P^* = 10^{-2}$, these P.D.Fs are also roughly symmetric about 0, except the P.D.F of case $\Phi_0 = 0.25$, because it already transited to the Regime II, as indicated by the extension of the positive wing to 1.5 and the finite value in -1. The delayed approach to Regime II for larger densities causes narrower P.D.Fs (as indicated according to red arrow in this figure). For increasing pressure, these P.D.Fs widen and undergo similar evolutions, approaching the characteristic force PDF shape of cohesionless systems already described in Sec. 3.5.1.2.

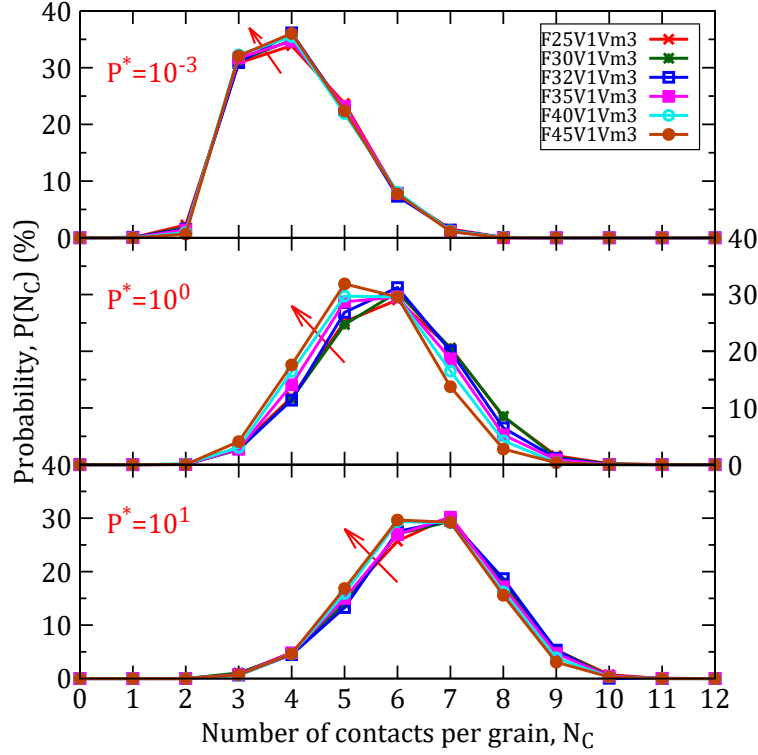


Figure 3.23: Distribution of the number of contacts per grain for different values of Φ_0 at three typical states of P^* . Red arrow denotes increasing Φ_0 .

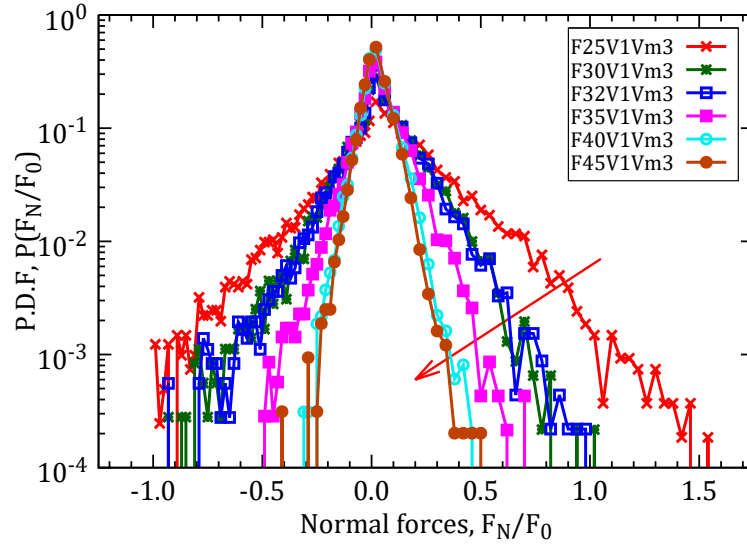


Figure 3.24: Distribution of normal forces for different values of Φ_0 under low pressure $P^* = 10^{-2}$, is normalized by the F_0 . Red arrow denotes increasing Φ_0 .

3.5.3.2 Influence of initial agitation intensity

Ratio V_0/V^* , characterizing the intensity of initial agitation and its ability to break adhesive contacts, significantly influences the initial assembling process and the resulting coordination number.

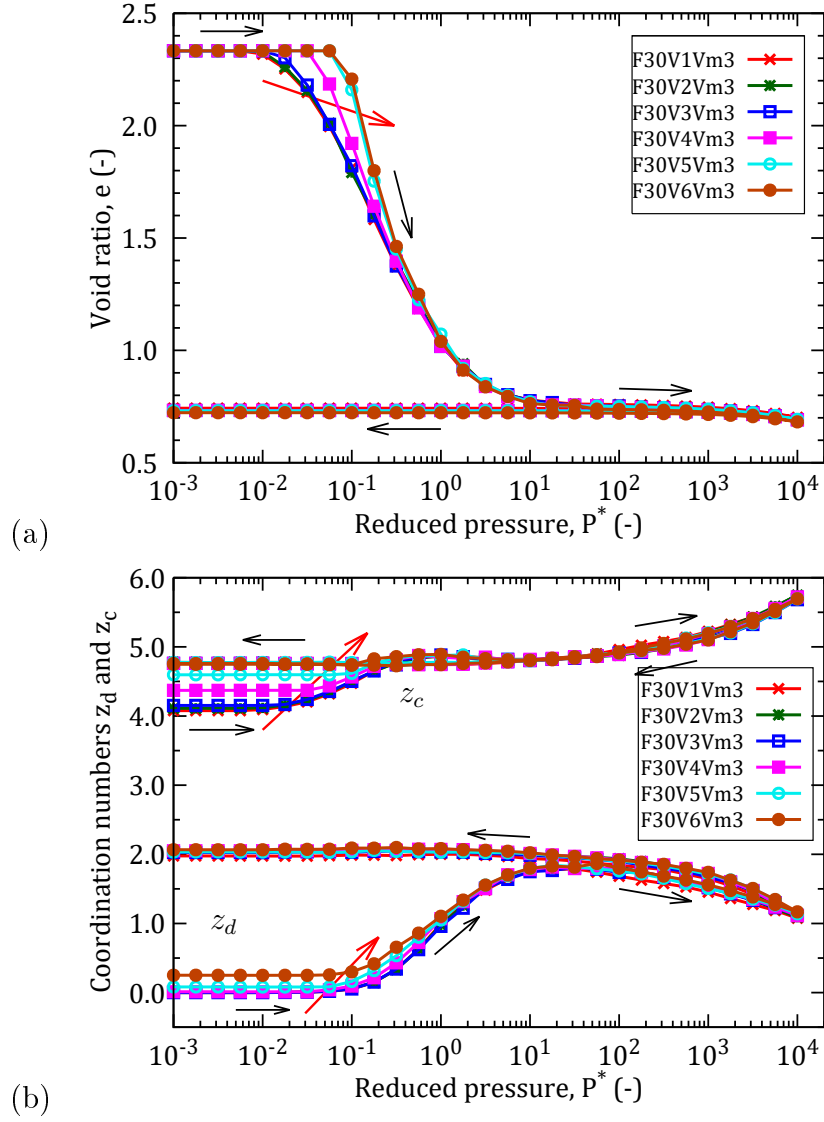


Figure 3.25: (a) Compression and decompression curves, and (b) coordination numbers z_c and z_d for different values of V_0/V^* . Red arrow denotes increasing V_0/V^* .

Fig. 3.25 shows that this parameter mainly affects the beginning of the compression curve. Six different values of V_0/V^* are used, and the difference between minimum and maximum values is two-hundredfold. Under low P^* , higher initial agitation velocities entail wider Regime I plateaus. This corresponds to the intervals of reduced pressure from $10^{-3} \leq P^* \leq 10^{-2}$ to $10^{-3} \leq P^* \leq 6 \times 10^{-2}$. If initial velocity V_0 is of the order of V^* , the initial packing structure is strongly perturbed. z_c values in the initial state depart then from the minimum, one observes $z_c > 4$, reaching $z_c = 4.75$ for the largest V_0 . z_d is also no longer equal to zero in the initial states. In other words, the larger the velocities, the stronger the initial structures (see Fig. 3.25(a)). More contacts are created, larger initial coordination numbers z_c and z_d are observed at low P^* (see Fig. 3.25(b)). Conversely, with low agitation velocities ($V_0 \leq V^*$), grains gently stick to one another and clusters of aggregated grains, once formed, are not disturbed. Lower

agitation velocities induce more tenuous aggregates.

As complementary evidence for the change in the numbers of contacts, the coordination numbers of compressive and tensile bonds are shown in Fig. 3.26. In the compression cycle, the z_+ and z_- only differ in Regime I (see inset). The larger the initial agitation intensities, the denser the initial network, with more compressive and more tensile bonds. The subsequent variations of z_+ and z_- in Regime II, and in the rest of the compression cycle, cease to be affected by the initial V_0 .

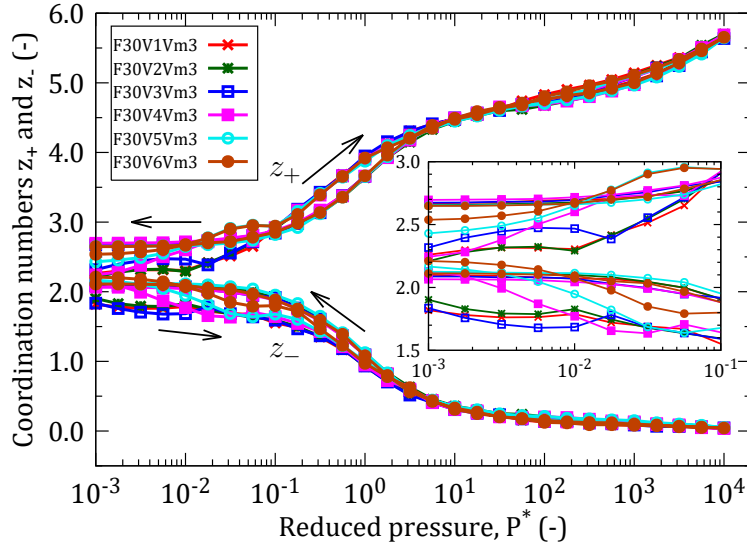


Figure 3.26: Coordination numbers z_+ and z_- versus P^* for different values of V_0/V^* .

The effect of the initial agitation intensity on the initial structure is visualized in Fig. 3.27, showing the grains contained in a slice of thickness $3d$ cut through the specimen (like in Fig. 3.13), at $P^* = 10^{-3}$, for different values of V_0/V^* . For the smaller V_0 values, initial structures are both more tenuous and more homogeneous. Stronger aggregates formed with larger V_0/V^* values (corresponding to longer Regime I plateaus, as shown in Fig. 3.25(a)), are also more heterogeneous, with larger pores. Besides, views of contact networks would reveal similar features as in Fig. 3.12 and Fig. 3.13.

Connectivities at different pressure levels, $P^* = 10^{-3}$, $P^* = 10^{-1}$, and $P^* = 10^0$ are shown in Fig. 3.28 for varying initial V_0 . The influence of initial agitation is quite conspicuous in the shift of the distribution to larger N_C values at $P^* = 10^{-3}$, and gradually fades out upon increasing P^* .

The effects of initial agitation velocities V_0/V^* on the distribution of normal forces at initial low-pressure states $P^* = 10^{-3}$ are shown in Fig. 3.29. P.D.F. are approximately symmetric about zero, except for the larger V_0 , as wider positive wings appear, extending to values above F_0 . Unlike in the case of Fig. 3.24, wider distributions do not signal here the approach to the plastic collapse of Regime II. These distribution shapes are characteristic of the self-balanced forces that appear for large V_0 as aggregates are restructured, fold onto themselves and acquire a significant level of force indeterminacy.

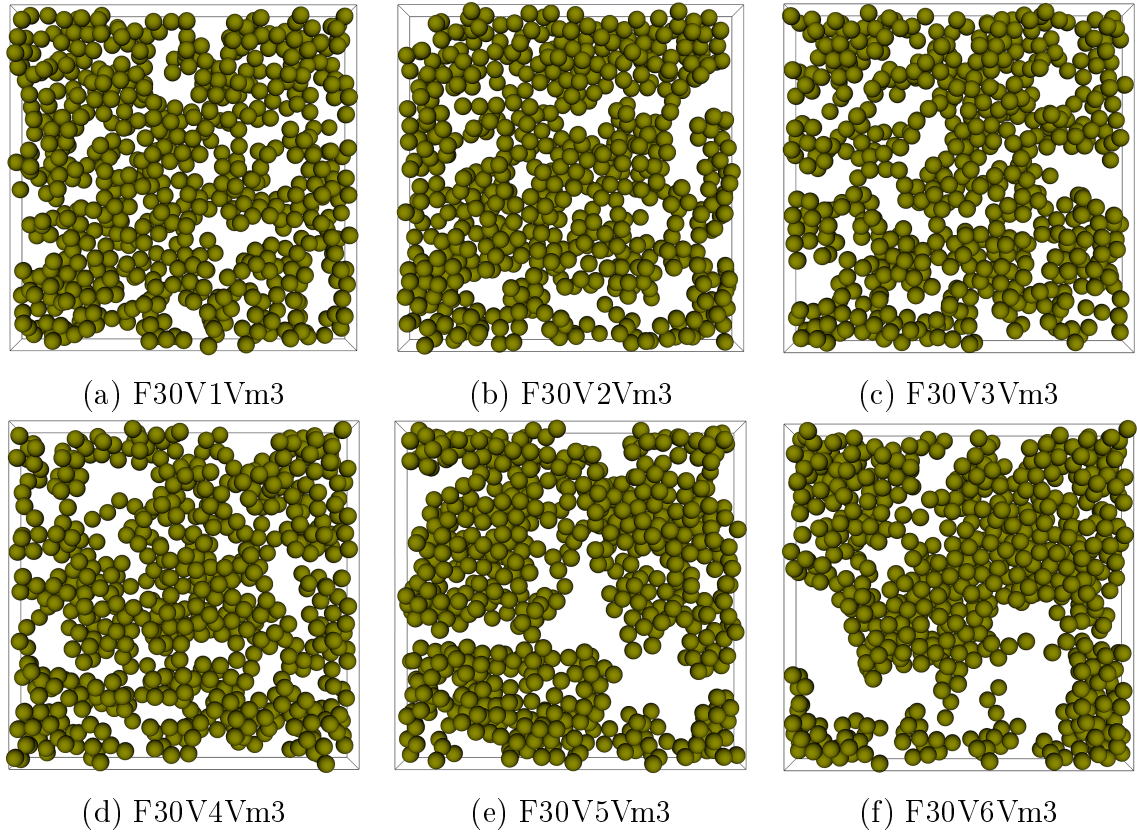


Figure 3.27: A 3D slice of specimen for different values of V_0/V^* at the beginning of loading path ($P^* = 10^{-3}$).

Under compression, those PDF's evolve as in the previous cases, and the initial influence of larger coordination numbers due to stronger agitation in the assembling stage are gradually forgotten.

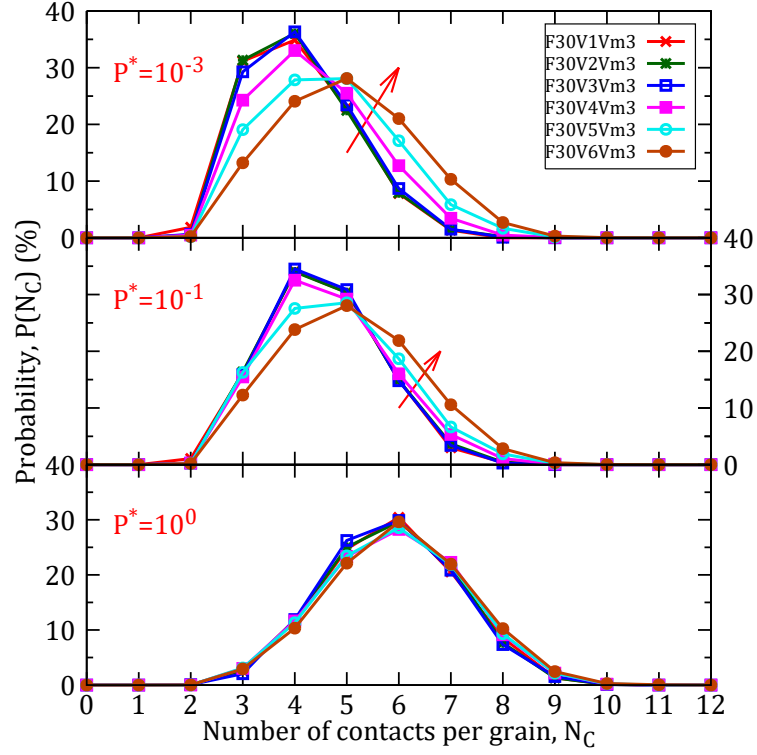


Figure 3.28: Number of contacts per grain for different values of V_0/V^* at three typical states of P^* .

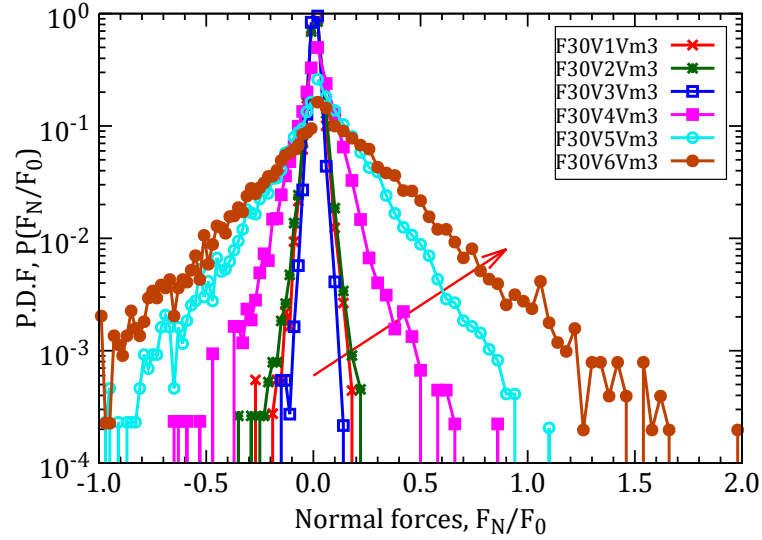


Figure 3.29: Distribution of normal forces of reference case for different values of V_0/V^* under low pressure $P^* = 10^{-3}$, normalized by F_0 . Red arrow denotes increasing V_0/V^* .

3.5.4 Effects of polydispersity

The polydisperse system (without RPR) is studied with the diameter distribution, such that $d_{\max} = 2d_{\min}$, presented in Sec. 3.2.1, and the values of initial parameters given in Table 3.2. The main objective of this study is to assess whether and to what extent

a grain size distribution affects the main results concerning the compression curve, the irreversible plastic compression and the correlative internal state evolution and their dependence on initial state and several control parameters. Note that the reduced pressure P^* as used in this section is in fact defined as P_{po}^* by relation (3.36).

3.5.4.1 Some observations on behavior and parameter dependence

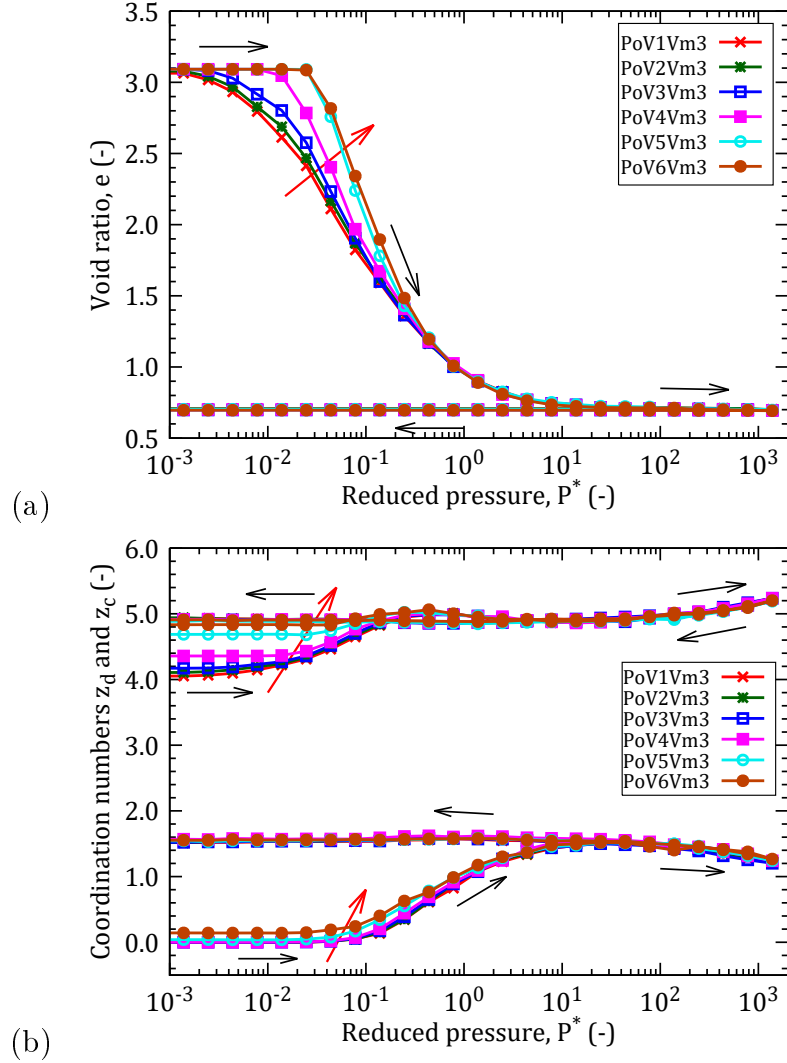


Figure 3.30: (a) Void ratio e and (b) coordination numbers z_c and z_d versus P^* for different values of V_0/V^* . Red arrow denotes increasing V_0/V^* .

The compression curve, displayed in Fig. 3.30(a), for different values of initial agitation velocity in the aggregation stage, exhibits the same three regimes as in the monodisperse case. One apparent difference is the reduction of the Regime I plateau for gently assembled systems (low V_0). The evolution of the coordination numbers z_c and z_d is plotted in Fig. 3.30(b). Under growing pressure P^* , more contacts are created, z_c increases notably. The evolution of z_c and z_d is qualitatively the same as in the monodisperse

case. Towards the end of the irreversible compression stage, as Regime III is reached, z_c and z_d are similarly changed whatever the initial values of V_0/V^* .

The contact networks for different values of initial agitations at $P^* = 10^{-3}$ are shown in Fig. 3.31, within a slice of thickness $3d_{min}$. In Fig. 3.31, the wet contacts are represented by the red lines, and the distant interactions by the blue lines – both with a thickness proportional to force intensity. Similarly to the monodisperse case, in the initial stages, more contacts and distant interactions are created with the larger agitations (V5 and V6). Observations – albeit, due to the choice of thickness $3d_{min}$, pertaining to a relatively thinner slice, relative to the average diameter – do not show any qualitative difference with those made in connection with Fig. 3.27: with larger V_0 , initial aggregates are better connected, forming a structure apt to withstand larger pressures, although comprising larger voids. Similar observations regarding density heterogeneities can be

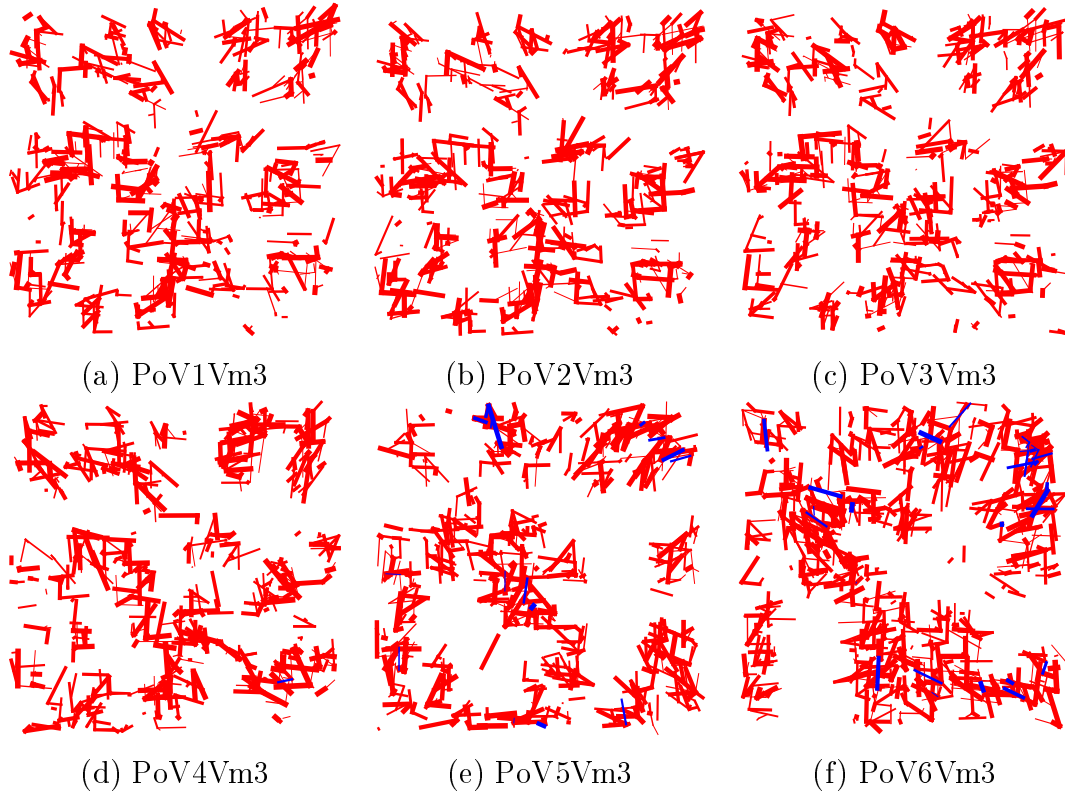


Figure 3.31: Contacts (red lines) and distant interactions (blue lines) for different values of V_0/V^* at $P^* = 10^{-3}$. Line thicknesses proportional to normal force intensity.

gathered from Fig. 3.32, visualizing grains rather than contacts and liquid bonds.

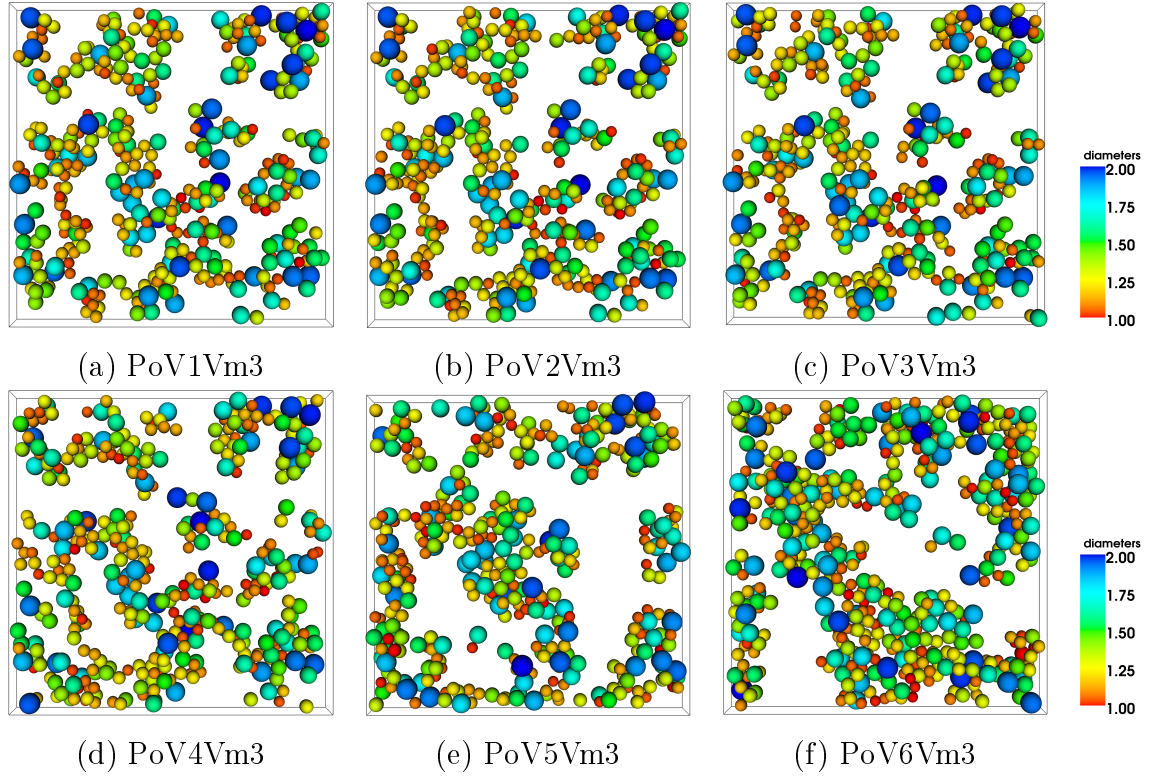


Figure 3.32: Grains contained in a slice (thickness $3d_{\min}$), at low P^* , for different values of V_0/V^* .

3.5.4.2 Comparison between polydisperse and monodisperse systems

Previous results show that the introduction of polydispersity does not very notably change the observed behavior and microstructure evolution of initially loose systems subjected to a pressure cycle. We now turn to more quantitative comparisons. The monodisperse case with the initial solid fraction $\Phi_0 = 0.25$ is selected to compare with the polydisperse one. These two cases are compared with the same values of initial agitation intensity and meniscus volume. One may note that both quantities should perhaps be adequately redefined, accounting for the different grain scale: the meniscus volume, as mentioned here, is actually the value of V_m corresponding to a pair of particles of equal diameter d_{\min} , while the meniscus volume is actually proportional to the surface area of the particle pair; and the value of V^* should in principle be modified too, accounting for size dependences of the mass and of the meniscus rupture distance. However, reference parameter values pertain to the limit of gentle aggregation, without cluster restructuration, and to a range of meniscus volumes with very little influence on the behavior, and, consequently, we dispense with rescaling V_0 and V_m . Fig. 3.33 directly confronts the variations of void ratio and of coordination numbers in the compression cycle for those two different materials, the monodisperse (MDS) and the polydisperse (PDS) ones.

This comparison reveals quantitatively close behaviors. Slight differences can be

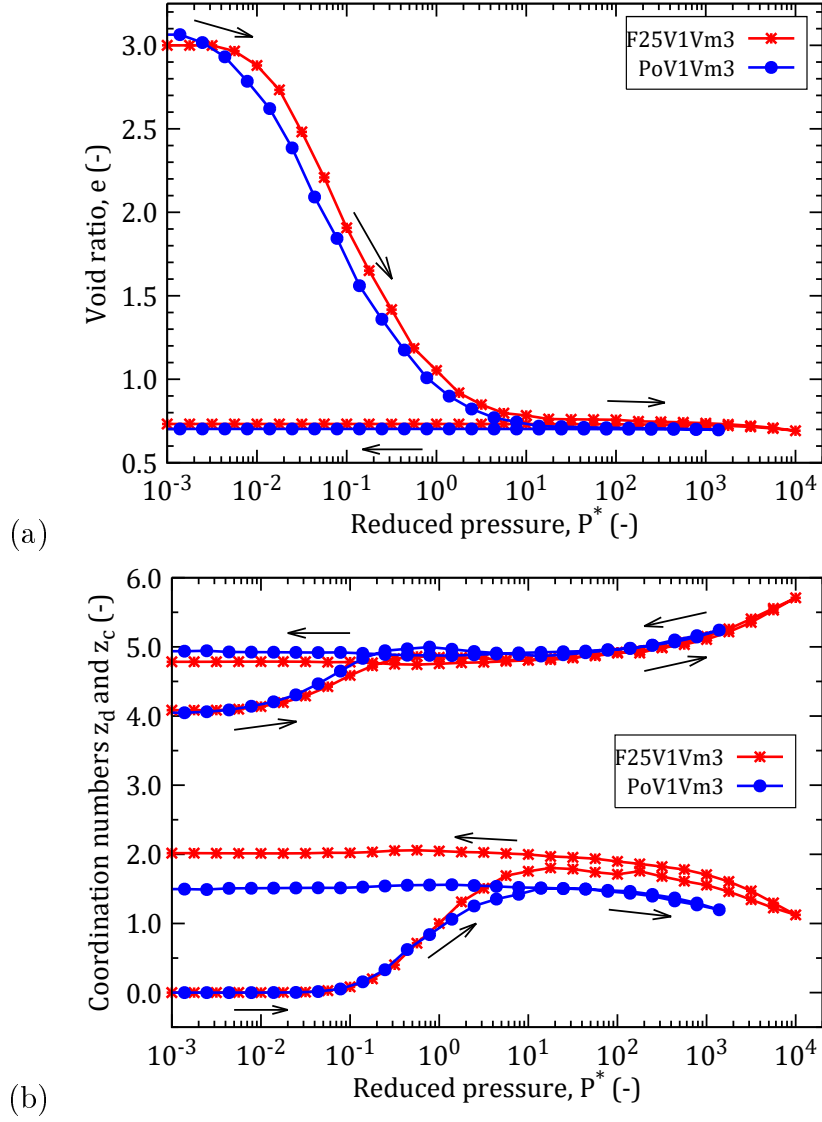


Figure 3.33: (a) Void ratio e and (b) coordination numbers z_c and z_d versus P^* for MDS and PDS.

noted: the Regime I plateau is narrower and less well defined for the PDS, showing a more fragile initial structure. In Regime II, the structure of PDS appears to collapse somewhat earlier than for the MDS, but not faster (both curves are nearly parallel). And the minimum void ratio e_{min} is slightly smaller for the PDS – the solid fraction of a polydisperse system is usually larger than for monosized grains.

The evolutions of coordination numbers z_c and z_d for both systems, plotted in Fig. 3.33(b), are also very close. At the end of the compression z_d is somewhat smaller in the PDS – this could be due to the difference in ratios D_r/d . In final dense states after decompression, small differences are maintained for z_c . Generally, given the geometric differences between monodisperse bead packs, and polydisperse ones with diameters varying by a factor of 2, it should be concluded that the observed behaviors do not exhibit very significant size distribution effects, and thus the study of a monodisperse model

gives meaningful results which might be applicable in rather generic situations involving spherical beads with moderate polydispersity.

3.6 The case of wet beads with RPR

Rolling resistance was observed in two-dimensional [17, 13, 14] and three-dimensional [19] DEM studies to have strong effects on loose cohesive granular materials for small P^* . We now report on the results of the isotropic compression cycle applied to the systems of Table [13, 14]. In all simulations with RPR, we set $K_R/(K_N d^2) = 2.5 \times 10^{-2}$, while $K_T/K_N = 1$ and $K_N/d = 400$ GPa.

3.6.1 Influence of initial solid fraction

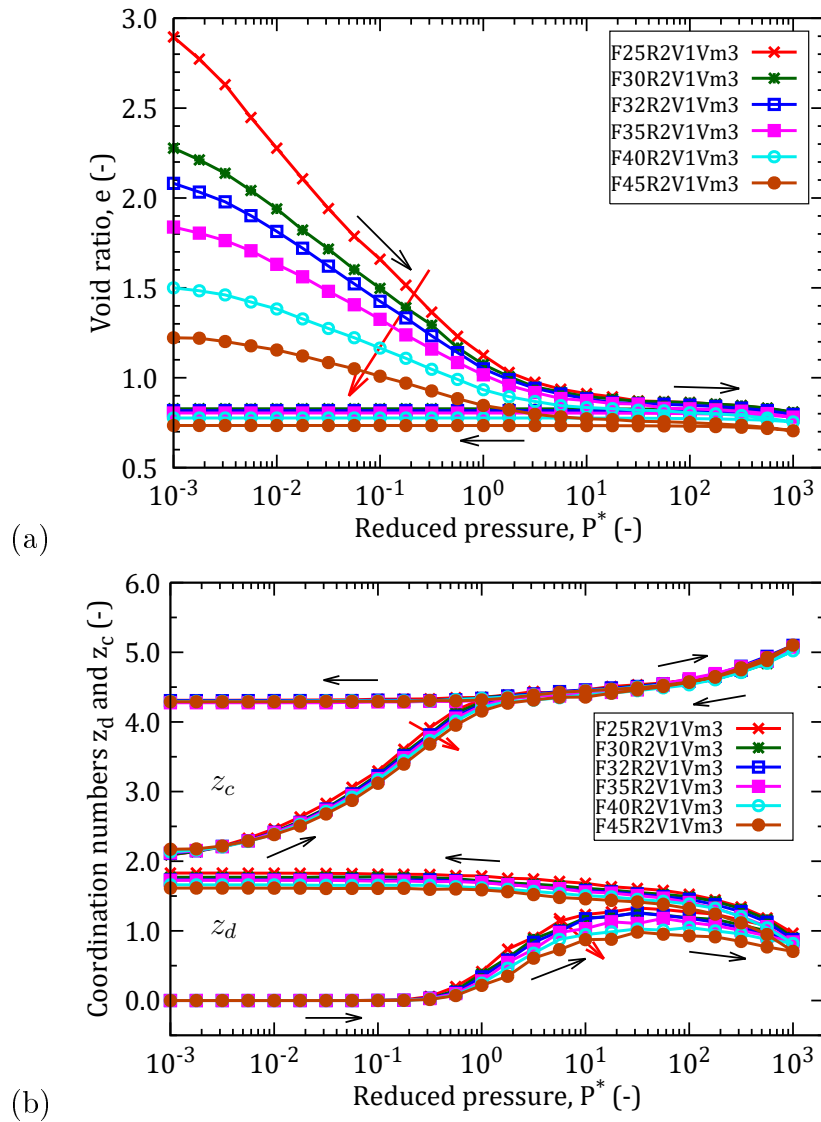


Figure 3.34: (a) Void ratio e and (b) coordination numbers z_c and z_d versus P^* in compression cycle for different values of Φ_0 . Red arrow denotes increasing Φ_0 .

Systems with RPR, assembled six different values of the initial solid fraction Φ_0 , are subjected to the compression test, with the same procedure as the material without RPR. The compression cycle is limited to $P^* \leq 10^3$. Fig. 3.34 shows the resulting behavior, in terms of void ratio and coordination numbers.

A first observation is, in general, the absence of a plateau for Regime I, except in the densest case $\Phi_0 = 0.45$. The irreversible density increase gradually takes place from the lowest investigated values of P^* , (of order 10^{-3}). Under growing pressure P^* , curves pertaining to different initial densities converge, until they nearly coincide in Regime III. The slope of the linear part of the e versus $\log P^*$ curve is no more an intrinsic material parameter as in the material without RPR, as it varies with Φ_0 . The final (minimum) value of the void ratio, reached for large enough P^* , and (approximately) maintained upon reducing the pressure, is also dependent on Φ_0 : one gets $e_{\min} = 0.75$ for $\Phi_0 = 0.40$ and $e_{\min} = 0.70$ for $\Phi_0 = 0.45$ (see Fig. 3.34(a)). The coordination numbers of contacts are still equal to the minimum value, which is 2 instead of 4 for systems with RPR: as noted in 2D systems [13], aggregates of particles with rolling resistance are rigid objects, and if they do not restructure due to the collisions while additional particles stick to the growing clusters in the formation stage, as in the case of a small initial agitation velocity V_0 , they should be generically devoid of loops, whence $z_c = 2$. Contact loops entails force indeterminacy. The initial aggregate is an isostatic structure in the limit of small V_0 . Fig. 3.34(b) shows that this applies to “V1” (small initial V_0) systems whatever the value of Φ_0 , and the variation of coordination numbers in the pressure cycle are remarkably independent on Φ_0 . Distant interaction coordination numbers, initially equal to zero, due to the instantaneous stability of aggregated structures, vary a little with Φ_0 in the later stages of the pressure cycle, with slightly less contact openings in denser systems.

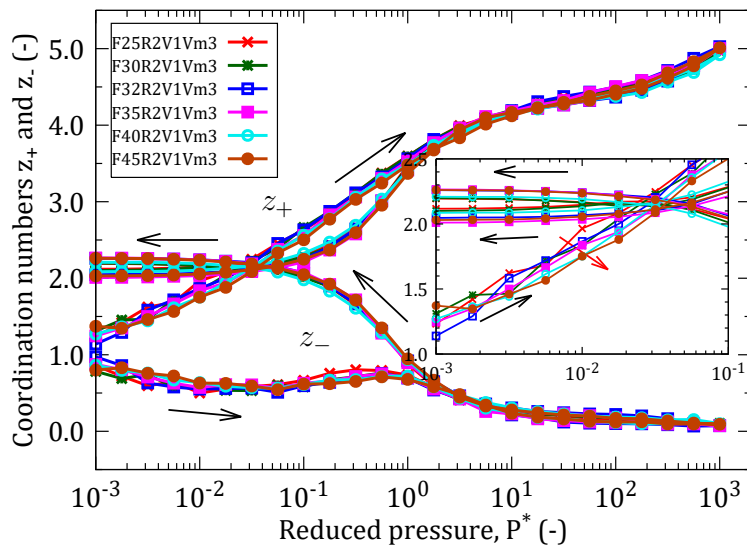


Figure 3.35: Coordination numbers z_+ and z_- versus reduced pressure P^* for different values of Φ_0 . Red arrow denotes increasing Φ_0 .

As to coordination numbers z_+ and z_- associated to compressive and tensile contact forces, Fig. 3.35 shows, apart from a smaller number of contacts, very similar evolutions as in systems without RPR, and are remarkably insensitive to Φ_0 .

3.6.2 Influence of initial agitation intensity

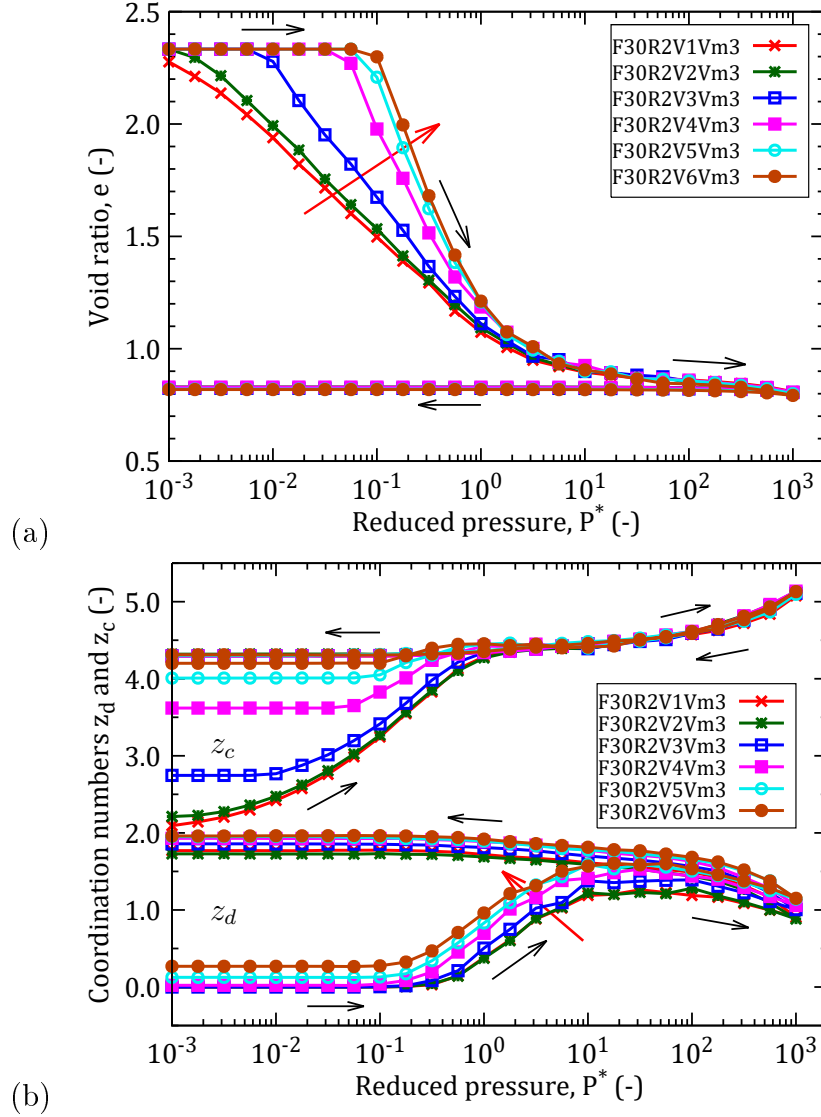


Figure 3.36: (a) Void ratio e and (b) coordination numbers z_c and z_d versus P^* in compression cycle for different values of V_0/V^* . Red arrow indicates increasing V_0/V^* .

As in the systems without RPR, the initial agitation intensity strongly affects the initial structures under low pressure P^* . Fig. 3.36 shows the variations of void ratio e and coordination numbers z_c and z_d in the compression cycle for different values of V_0/V^* .

As noted before Regime I does not exist as a plateau in the compression curves for small initial agitation level (this applies to two first cases – red and green curves

in Fig. 3.36). The initial tenuous structures (with coordination number approaching 2, i.e., virtually no loop) formed with RPR and low V_0 respond with some amount of plastic collapse at the first pressure increment, as shown in Fig. 3.36(a). Regime I reappears on the pressure scale of Fig. 3.36(a) in systems assembled with larger initial agitation velocities, which are better coordinated (see Fig. 3.36(b)), and collapse more abruptly in plastic compression. This large change in the compression curve is due to strong variations of the initial values of coordination number z_c , which nearly doubles, from approximately 2.15 to nearly 4.25, for increasing initial agitation. Interestingly, the system assembled with the lower coordination numbers first react by plastic compression with no contact loss, as z_d remains equal to zero (no contact opening creating a distant interaction). As in the 2D systems of Ref. [14], irrecoverable plastic restructuring may take the form of bending or folding deformation of single particle strands.

Distant interactions are present from the beginning in better coordinated, initially more strongly agitated systems, with $z_d = 0.25$ for the largest V_0 . At intermediate pressures $1 \leq P^* \leq 10$, while z_c slightly increases, z_d increases faster, before slightly decreasing in Regime III. z_c then reaches its maximum at the end of the loading path. Upon unloading, many distant interactions replace interparticle contacts. Finally z_c and z_d remain constant when P^* is smaller than 10.

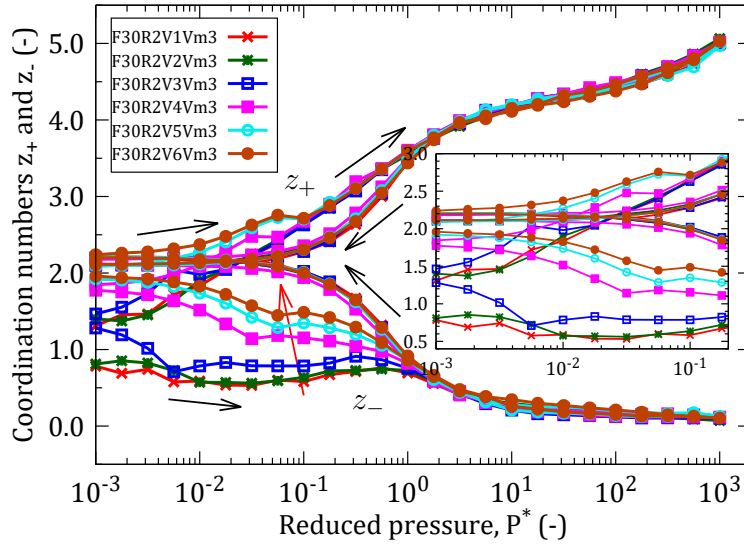


Figure 3.37: Coordination numbers z_+ and z_- versus P^* for different values of V_0/V^* (increasing according to red arrow).

Fig. 3.37 displays the variations of z_+ and z_- in the compression cycle for six values of initial agitation level. z_+ and z_- , just like $z_c = z_+ + z_-$, strongly depend on V_0 in the beginning of the compression cycle, and increase in parallel with V_0 , from $z_- = 0.82$ and $z_+ = 1.30$ to $z_- = 1.95$ and $z_+ = 2.30$. As Regime III is approached ($P^* > 10^0$), the system becomes denser, the tensile contacts gradually vanish while z_+ approach its maximum. Part of this evolution is reversed along the decompression path, with,

however, is no longer sensitive to the initial state.

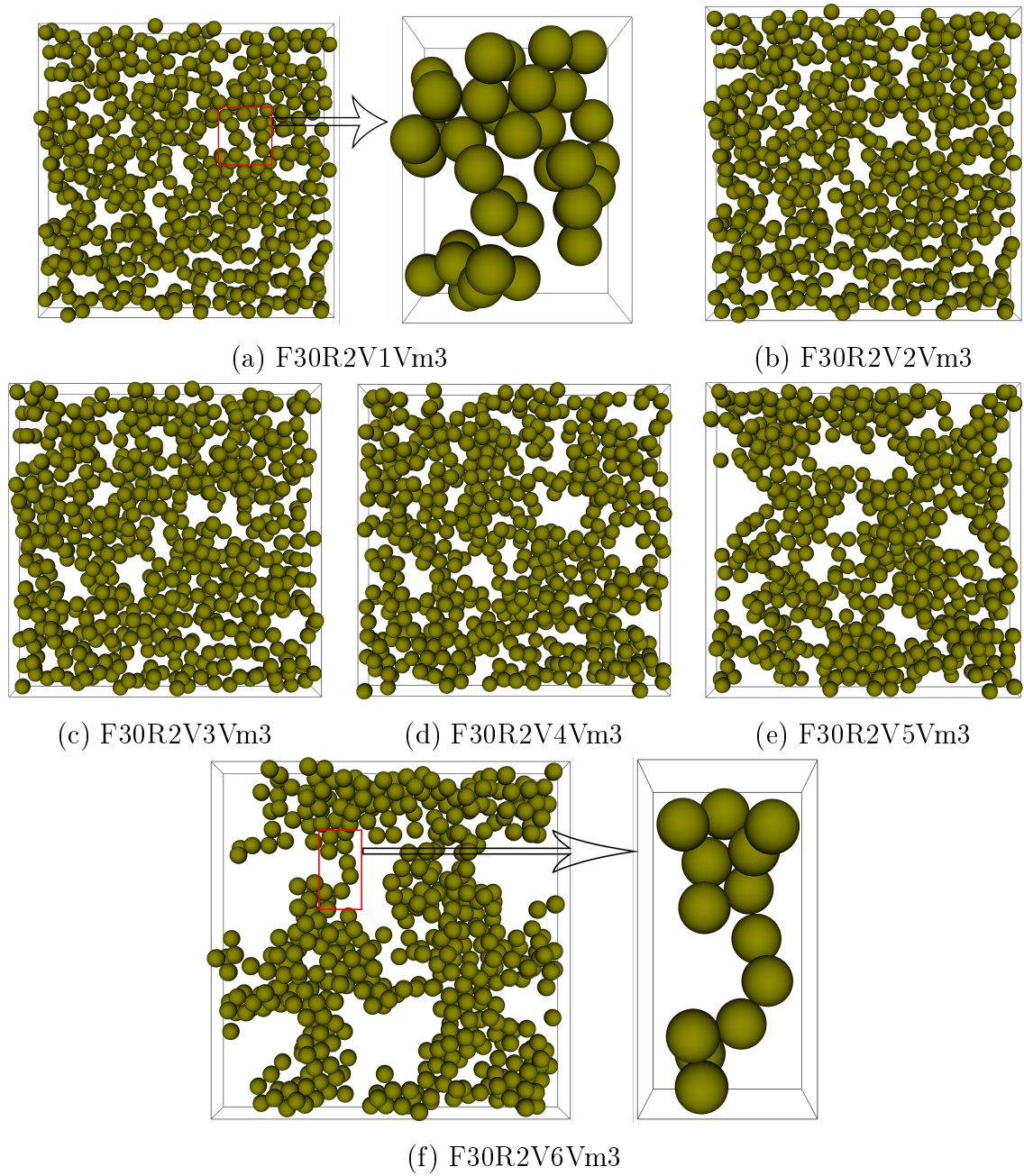


Figure 3.38: 3d-slices of specimens assembled with RPR for different values of V_0/V^* , under $P^* = 10^{-3}$

As in the previous sections, a slice (still with thickness $3d$) of the samples obtained for different values of V_0/V^* , under small pressure, $P^* = 10^{-3}$ is shown in Fig. 3.38. Fairly homogeneous for low V_0 (Fig. 3.38(a, b, and c)), the system exhibits larger dense regions and larger voids if initially more strongly agitated (Fig. 3.38(d, e, and f)). Meanwhile – see Fig. 3.36(b) – the coordination number changes from a value near 2 to slightly larger than 4. Remarkably, despite the larger number of contacts, structures formed under stronger agitation still exhibit strands (or chains) of single particles – see the blown up

detail of Fig. 3.38(f) are still present.

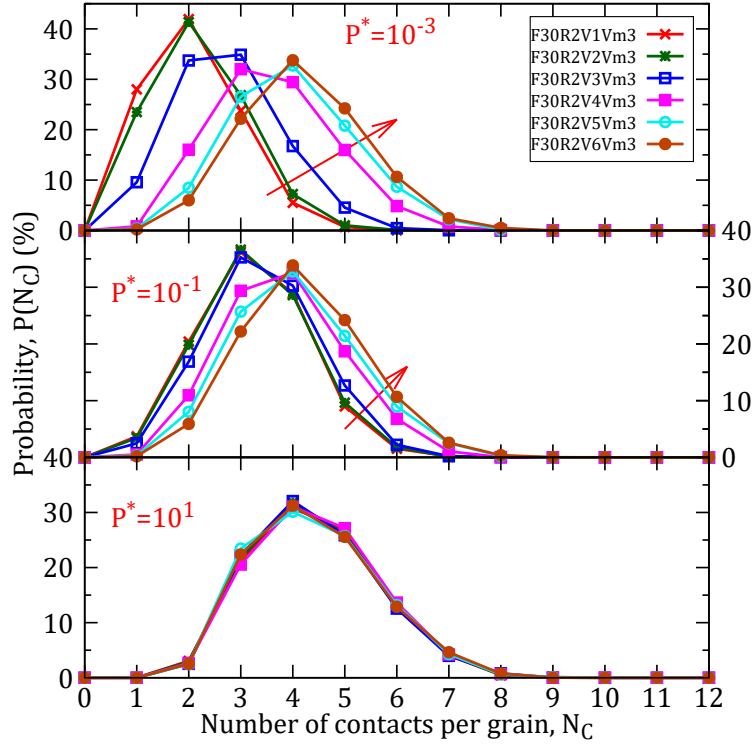


Figure 3.39: Number of contacts per grain for six values of V_0/V^* at three typical states $P^* = 10^{-3}$, $P^* = 10^{-1}$, and $P^* = 10^1$. Red arrow denotes increasing V_0/V^* .

The effects of V_0/V^* on connectivity are shown in Fig. 3.39. In the initial state ($P^* = 10^{-3}$), grains with just one contact represent $\approx 28\%$ of the whole population. Those grains are “dead ends” in the network of forces, and are joined to the network by a single bond carrying, necessarily, a force equal to zero. As discussed in Sec. 3.6.3, this bond is however able to transmit finite tangential forces and rolling and pivoting moments, so that those grains are rigidly fixed to the continuous aggregate. Such 1-coordinated grains no longer exist in the better coordinated systems assembled with the largest agitation levels. $P(N_C)$ distributions peak at increasing values of N_C as the agitation level increases, from $N_C = 2$ (V1 and V2), to $N_C = 3$ (V3 and V4), and then $N_C = 4$ (V5 and V6). Under the higher pressure $P^* = 10^{-1}$, the first four distributions (for V1, V2, V3, and V4) shift to larger values, while the ones of V5 and V6 hardly change, which is typical for the absence of evolution in Regime I. When all systems have almost completely collapsed ($P^* = 10^1$), all connectivities become similar as the memory of initial states fades out.

P.D.F. of normal forces in low-pressure states $P^* = 10^{-3}$ are plotted in Fig. 3.40. The effect of varying V_0/V^* is quite similar as in the systems devoid of RPR (Fig. 3.29), with a distribution, roughly symmetric about zero except for the largest values of V_0 , which correspond to the largest force indeterminacy, while the distribution width tends

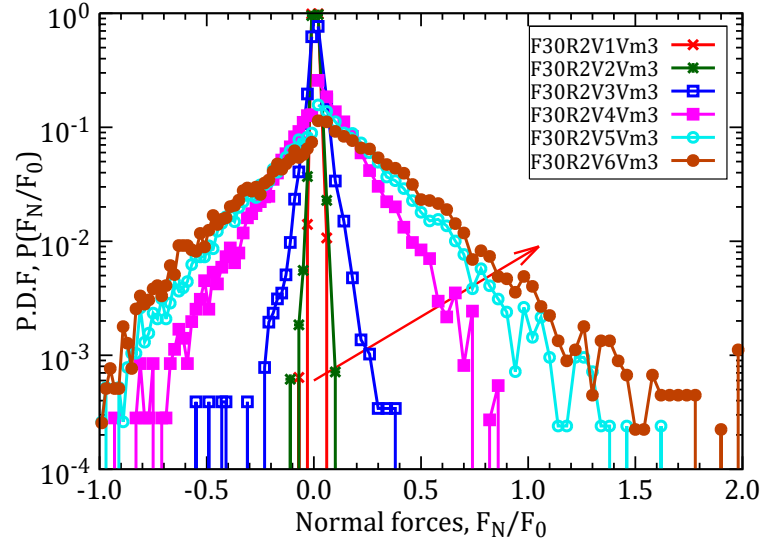


Figure 3.40: Distribution of normal forces at low pressure $P^* = 10^{-3}$ for different V_0/V^* (increasing according to red arrow) P.D.F. normalized by F_0 .

to vanish with the degree of force indeterminacy (hyperstaticity), for decreasing V_0 . The positive forces between grains dominate the maximum attractive forces at the maximum velocity (the cyan and brown curves). Like other cases of cohesive and non-cohesive grains, the stronger the pressure, the wider the P.D.Fs and the influence of initial velocities to force distributions then fade out after the granular structure are compressed to higher pressures and densities.

3.6.3 Influence of rolling and pivoting friction coefficients

Different values of the rolling and pivoting friction coefficients, μ_R/d and μ_P/d , are also tested in the same systems. The compression curves for four values of $\mu_R = \mu_P$ (see Table 3.3) ranging from $0.004d$ (R1) to $0.5d$ (R4) are shown in Fig. 3.41.

As regards Regime I, for the evolution of void ratio, the effect of larger RPR coefficients is somewhat similar to the one of a larger V_0 , creating more stable initial configurations. That does not exist in the systems of low μ_R/d (R1 and R2). Coordination numbers, however, tend to decrease for increasing RPR, with initial states closer and closer to the isostatic, loopless limit $z_c = 2$. The plastic compression of systems with larger RPR tends to be slower, both for void ratio and coordination numbers. As the irreversible compression proceeds, the differences between small and large RPR persist, and survive the complete pressure cycle – high $\mu_R = \mu_P$ values resulting in looser configurations with smaller coordination numbers. Increasing RPR also alters the microscopic mechanical behavior which determines the slope of the compression curves.

The distribution of normal forces, normalized by F_0 , for different values of μ_R/d , are shown in Fig. 3.42 under $P^* = 10^{-2}$. Despite the lower contact coordination number,

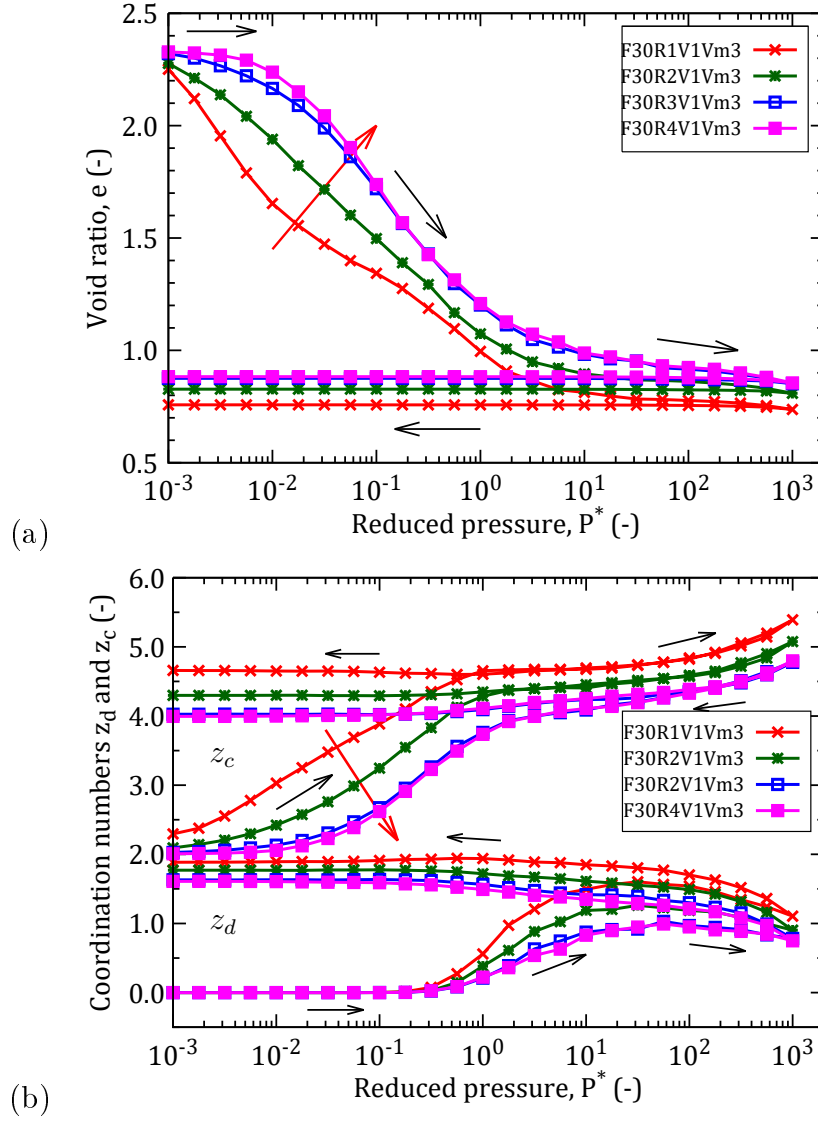


Figure 3.41: (a) Void ratio e and (b) coordination numbers z_c and z_d versus P^* for different values of $\mu_R = \mu_P$. Red arrow denotes increasing μ_R/d .

the systems with larger RPR tend to exhibit wider force distributions. This implies some influence of the different density, as large RPR maintains lower densities under $P^* = 10^{-2}$. Note the large values of the P.D.F. at $F_N = 0$: this should correspond to grains with one single contact, as remarked in connection with Fig. 3.39.

Some further analysis of the plastic mechanisms by which network break or rearrange as the system is irreversibly compressed would be necessary to explain the relations between the evolutions of density, coordination numbers, position correlations and force distributions. It was suggested in Ref. [14] that the dominant plastic mechanism transits from tensile rupture to rolling friction mobilization and “plastic bending” of particle chains as the level of RPR increases.

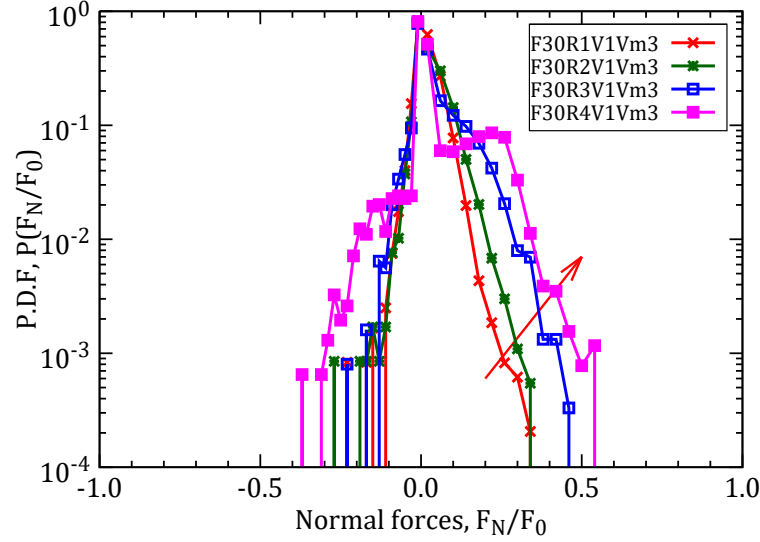


Figure 3.42: Distribution of normal forces for different values of μ_R/d at $P^* = 10^{-2}$. Red arrow denotes increasing μ_R/d .

3.6.4 Comparison of bead assemblies with and without RPR

A comparison of compression behavior between two reference systems with and without (small) RPR is made in Fig. 3.43. The effect of initial agitations V_0/V^* (both minimum and maximum values) are also shown. For the minimum agitation, the appearance of RPR in contacts creates denser systems under low P^* , because plastic collapse sets in earlier under increasing pressure, but smaller coordination numbers. While the initial loose structures formed without RPR, which can sustain a small non-vanishing pressure in Regime I, the compression curve of the tenuously connected structures formed with small RPR and low agitation tend to rearrange immediately. Such structures, are virtually loopless, with contact coordination numbers approaching 2. This different behaviour appears in Fig. 3.43(a). A Regime I plateau reappears on the pressure scale of Fig. 3.43(a) in systems assembled with larger initial agitations, which are better coordinated (Fig. 3.43(b)), and collapse more abruptly in plastic compression. With RPR, one may thus obtain a wider range of compression indices C_c in the sense of Eq. (1.1). Plastic compression, as the pressure increases, might be faster with RPR, for gently assembled systems with low coordination numbers; or slower with RPR, for systems assembled under strong agitation, into well connected structures.

Systems with or without RPR also widely differ by their initial coordination number, for which the introduction of RPR also entails a larger effect of the initial agitation. Between the minimum and the maximum agitation levels, at lowest pressure P^* , the contact coordination number z_c increases from 4.08 to 4.75 without RPR and from 2.09 to 4.20 with RPR. The coordination number of distant interactions z_d is also increased from 0.00 to 0.27 both without and with RPR. z_c and z_d , in both systems vary with

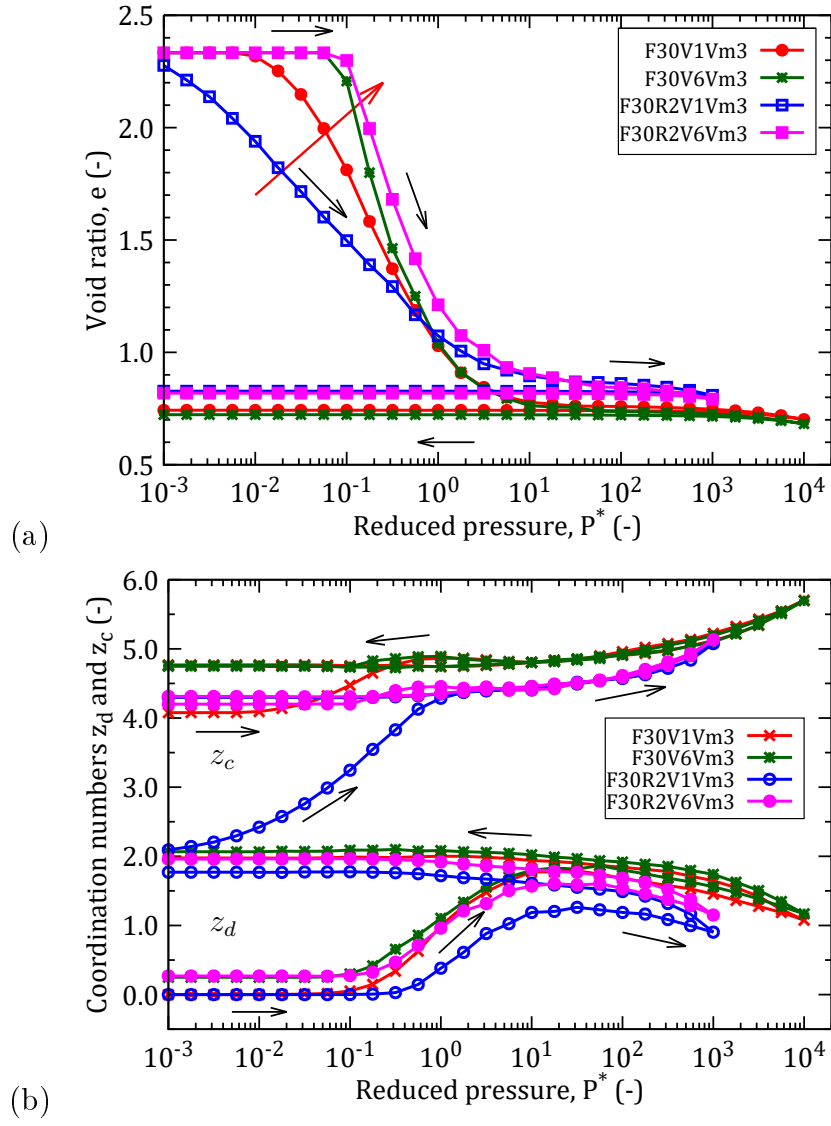


Figure 3.43: (a) Void ratio e and (b) coordination numbers z_c and z_d versus P^* in compression cycle for systems both without RPR and with RPR.

similar trends, remaining constant in unloading.

3.7 Conclusion

The numerical study of isotropic compression of initially loose wet bead systems, forming continuous, random aggregates stabilized by capillary cohesion, has been carried out for different model materials: monodisperse or not, possibly with some resistance to rolling and pivoting in the contacts, and with varying values of initial density, coordination and connectivity (the latter features being determined by the agitation intensity in the aggregation stage), and meniscus volume. The plastic behavior of such a model wet granular materials is characterized at both macroscopic and microscopic levels. The main conclusions of this chapter are summarized as follows.

Firstly, the irreversible, plastic compression process, controlled by the reduced pressure, P^* , goes through three regimes. In Regime I, which is sensitive to the assembling procedure, the microstructure can sustain small, finite pressure increments with strong enough without plastic collapse. Those increments are larger for denser initial states and for stronger initial structures, as obtained as agitation levels in the aggregation process entails cluster restructuration and reinforcement. Subsequent collapse as the confining pressure is increased and causes tensile contact rupture reduce the void volume in Regime II, for which the variation of void index with pressure has the same shape as reported in the soil mechanic literature. The preconsolidation pressure is a plastic threshold below which the quasistatic response of material is approximately elastic (similar to the behavior of a non-cohesive granular soils under isotropic load). The material eventually approaches a minimum void ratio (maximum density) in Regime III.

Secondly, our results emphasize the important differences between cohesive and non-cohesive granular assemblies. The most important differences, which are brought by cohesion in macroscopic behavior, are the existence of very loose stable structures (with solid fraction as low as 0.25 with identical spherical beads) and the plastic compression phenomenon. At the microscopic level, the attractive and repulsive contact forces are initially of the order of the maximum tensile strength F_0 , and tend to compensate each other under low pressure. The compaction path stabilizes self-balanced force networks with large compression forces.

Thirdly, our results show the remarkable, and somewhat unexpected, influence of two microscopic features. Both strongly affect the shape of the compression curve. One is a material characteristic, the rolling and pivoting resistances at contacts between grains. Even a small RPR has a strong microstructural role for small P^* . The other one is the initial coordination number and internal state of connectivity, as determined by the assembling process. Coordination and connectivity are quite independent of density, and also crucially influence the plasticity of loose materials.

Finally, the plastic behavior in compression is not very sensitive to the grain size distribution, as only a very moderate quantitative difference is observed between single-sized grains and polydisperse ones with a diameter distribution ranging from 1 to 2.

Oedometric compression: DEM study and experimental confrontation

This chapter reports on numerical simulations of oedometric compression tests with the model material (with monodisperse beads and no RPR). Some specific analyses are introduced to investigate stress anisotropy and its microscopic origins. Such simulations enable direct comparisons with experiments, both for the plastic behavior (compression curve) and for some microstructural characteristics.

Contents

4.1	Introduction	156
4.2	Simulation of oedometric compression tests	156
4.2.1	Compression of different initial states: initial V_0 and coordination.	157
4.2.2	Influence of initial solid fraction	162
4.3	Oedometric versus isotropic compression	166
4.4	Experiment versus simulation	168
4.4.1	Compaction behavior	168
4.4.2	Geometrical structure change	170
4.5	Conclusion	171

4.1 Introduction

The objective of this chapter is to investigate the behavior of the numerical material in oedometric compression, and then to quantitatively confront experiment and DEM simulation at macro- and microscopic levels, using the experimental results of Chapter 2. The DEM simulations are carried out with the simplest model material, the monodisperse one without RPR. The force model and the initial assembling procedure are the same as the ones defined in Chapter 3. Several results of the isotropic compression tests are also reused for the comparison.

4.2 Simulation of oedometric compression tests

To the same initial samples of 4000 mono-sized spherical beads as for isotropic compression tests, stress and strain conditions are applied in order to simulate oedometric compression: while σ_1 (the *axial stress*) is increased, $\varepsilon_2 = \varepsilon_3$, the *lateral strains* are maintained at zero. The axial strain rate is also constrained, during the compression, not to exceed a preset maximum value, in order to model a quasistatic test. This constraint is expressed through the inertial parameter $I = \dot{\varepsilon} \sqrt{m/d\sigma_1}$ where m is the particle mass. I is requested to remain below 10^{-3} throughout the compression tests simulation.

Like in the isotropic case, we use different values of material parameters in order to explore the parameter dependence of the plastic compression behavior: four values of initial solid fraction (Φ_0), different values of initial agitation intensity V_0/V^* for the reference initial solid fraction $\Phi_0 = 0.30$. As to the meniscus volume, one conclusion of Chapter 3 is its remarkably weak influence on the material behavior, and therefore it is fixed to $V_m/d^3 = 10^{-3}$ in all oedometric test simulations. The list of numerical samples subjected to oedometric compression, with the corresponding parameter choice, is given in Table 4.1.

Table 4.1: Initial parameters of the oedometric simulations (without RPR)

Φ_0		V_0/V^*		V_m/d^3		Notation
0.30	F30O	0.2041	V1	1.00×10^{-3}	Vm3	F30OV1Vm3
		0.4082	V2			F30OV2Vm3
		1.2247	V3			F30OV3Vm3
		4.0825	V4			F30OV4Vm3
		12.2474	V5			F30OV5Vm3
		40.8248	V6			F30OV6Vm3
0.32	F32O	0.0241	V1	1.00×10^{-3}	Vm3	F32OV1Vm3
0.35	F35O					F35OV1Vm3
0.40	F40O					F40OV1Vm3

The definition of a reduced stress used for pressure in Eq. (3.35) of Chapter 3, is applied, in the oedometric case, to the axial stress, compared to the tensile contact strength:

$$\sigma_1^* = \frac{d^2 \sigma_1}{F_0}, \quad (4.1)$$

The loading program, with controlled steps of externally applied axial stress, is similar to the isotropic compression cycles of Chapter 3.

4.2.1 Compression of different initial states: initial V_0 and coordination.

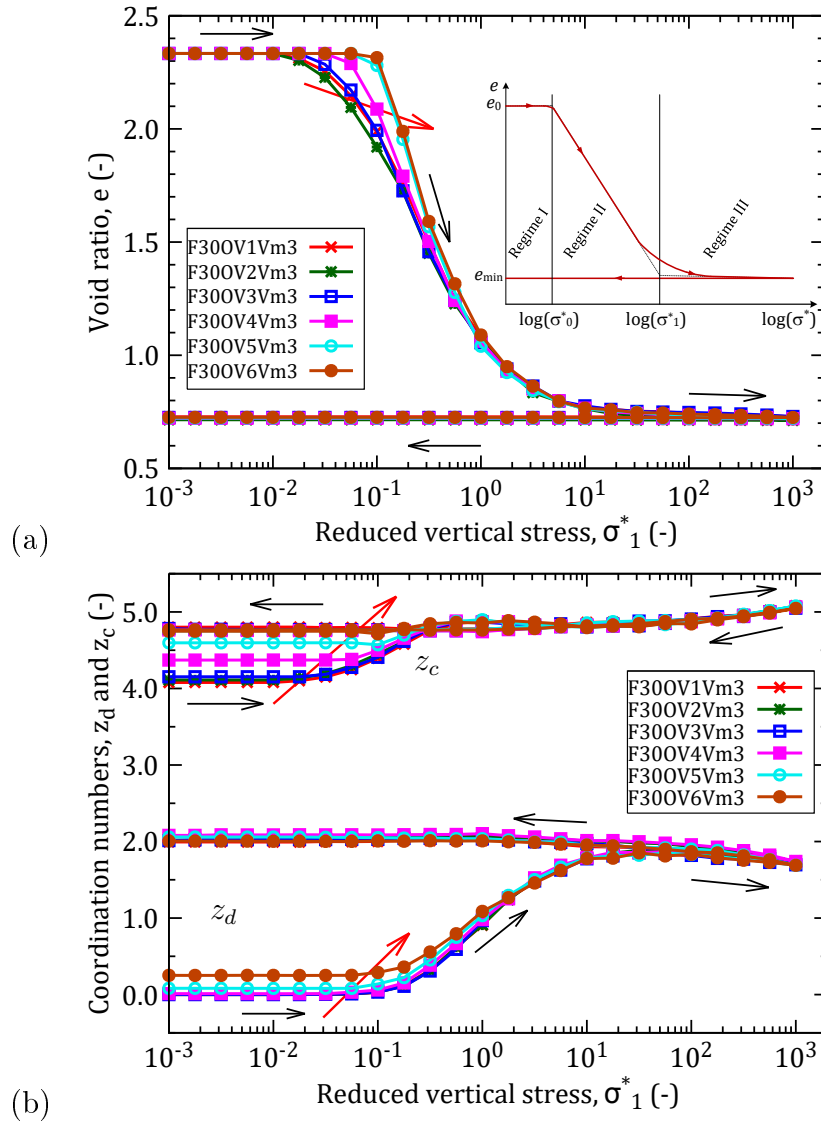


Figure 4.1: (a) Void ratio e , and (b) coordination numbers z_c and z_d versus σ_1^* for different values of V_0/V^* , in creasing as indicated by red arrow.

Initially assembled states of solid fraction $\Phi_0 = 0.30$ but varying values of initial agitation intensity V_0/V^* , and, consequently, connectivity, are subjected to the oedometric loading program. The compression curves are now shown as the relationship

between void ratio e and logarithm of reduced axial stress σ_1^* , $e - \log(\sigma_1^*)$, as plotted in Fig. 4.1, along with the variations of coordination numbers z_c and z_d . Three regimes are identified in the compression cycle (Fig. 4.1(a)), in close analogy with the isotropic compression behaviour. Let us recall that the initial states are isotropically assembled, and actually coincide with those studied in Chapter 3. The enduring effect, as σ_1^* increases through Regime I, of initial agitation, which creates stronger, better connected structures (Fig. 4.1(b)) is clearly visible and analogous to the isotropic case.

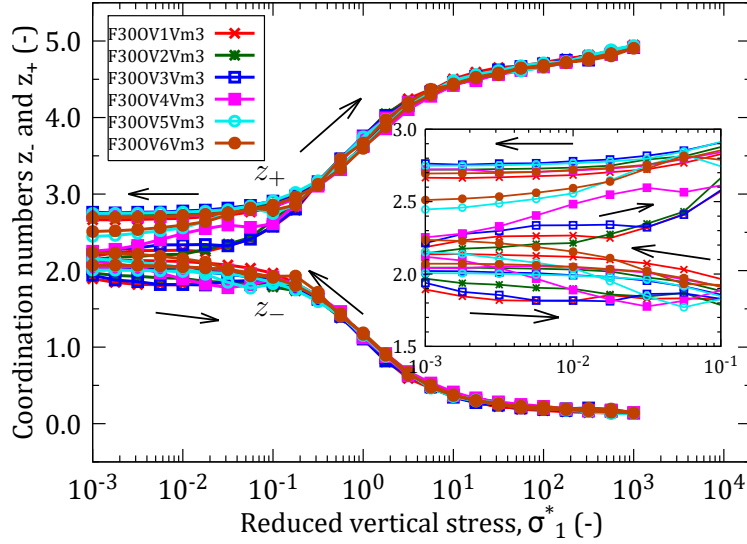


Figure 4.2: Coordination numbers of z_+ (compressive contacts) and z_- (tensile contacts) versus reduced vertical stress σ_1^* for different values of V_0/V^* , increasing as shown by read arrow.

Fig. 4.2, showing the σ_1^* dependence of coordination numbers z_- and z_+ associated to tensile and compressive contacts, is also closely analogous to its counterparts in the isotropic case.

The *coefficient of lateral pressure*, denoted as K_0 , is defined in oedometric compression as the ratio of lateral stress, to axial stress:

$$K_0 = \frac{\sigma_3}{\sigma_1}. \quad (4.2)$$

K_0 , in Fig. 4.3, is plotted on a logarithmic scale in order to observe clearly its variation along the compression and decompression curves. K_0 strongly depends on the initial state: it is about twice as large, under low σ_1^* , in the stronger systems (V4 to V6) than in the weaker ones (V1 to V3). This might be attributed to the initial isotropic organization of self-balanced forces of order F_0 , which cause the strong systems to transit less anisotropic stresses in Regime I. K_0 decreases slightly in Regime I, as the anisotropy of the loading process affects the initially isotropic microstructure more and more. Conversely, the collapse taking place in Regime II causes K_0 to gradually increase in all systems. K_0 values converge near the end of the collapse stage, at $P^* = 10^1$. At high

pressure, in Regime III, K_0 remains almost constant ($K_0 \approx 0.8$) whatever the initial connectivity. In the first part of the unloading path, K_0 slightly increases (from $K_0 \approx 0.7$ to $K_0 \approx 0.8$) with similar values in all cases (the influence of the initial state seems now forgotten). K_0 starts to diverge in the latter half of unloading path, when the vertical stress $\sigma_1^* < 10$, reaching values of several tens or several hundreds. This behavior is simply due to the existence of residual lateral stresses of order F_0/d^2 , while the axial stress is requested to decrease to much smaller values: $\sigma_1^* F_0/d^2$, by definition of σ_1^* . The different residual lateral stresses observed for different initial coordination (or initial agitation, V1 to V6) correlates with the different density of tensile contacts (see Fig. 4.2) at the end of the unloading curve in the six specimens.

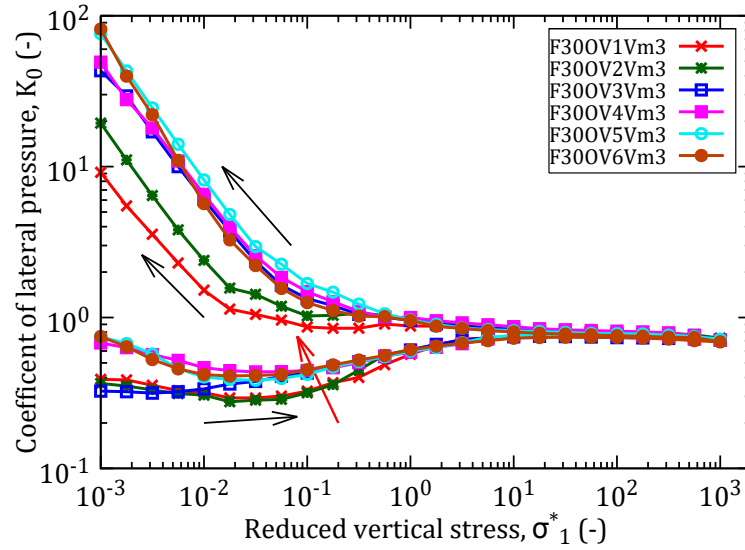


Figure 4.3: Coefficient of lateral pressure K_0 versus reduced vertical stress σ_1^* for different values of V_0/V^* . Red arrow denotes increasing V_0/V^* .

From the Eq. (3.24) of Chapter 3, the contribution of forces to the stress components can be split in various ways, depending on the distinction between different forces. First we consider the total stress as a sum of the contributions of the contacts and the distant interacting pairs, as

$$\sigma_{\alpha\beta} = \sigma_{\alpha\beta}^c + \sigma_{\alpha\beta}^d. \quad (4.3)$$

The contribution of distant interactions to σ_{22} is illustrated in Fig. 4.4. Due to the attractive nature of the capillary forces, σ_{22}^d is a tensile stress, negative with our sign convention. It is displayed in a logarithmic relation using the absolute value of σ_{22}^d in order to give a better observation of its contribution. As noted earlier (see Fig. 4.1(b)), distant interactions are initially absent in the systems with low initial coordination. σ_{22}^d is therefore very small in the first three cases (V1, V2, V3) at low axial stress, $\sigma_1^* \leq 10^{-2}$. Conversely, in systems V4 to V6, a significant amount of distant interactions are created in the aggregation stage. Their contribution to the stress components is naturally of

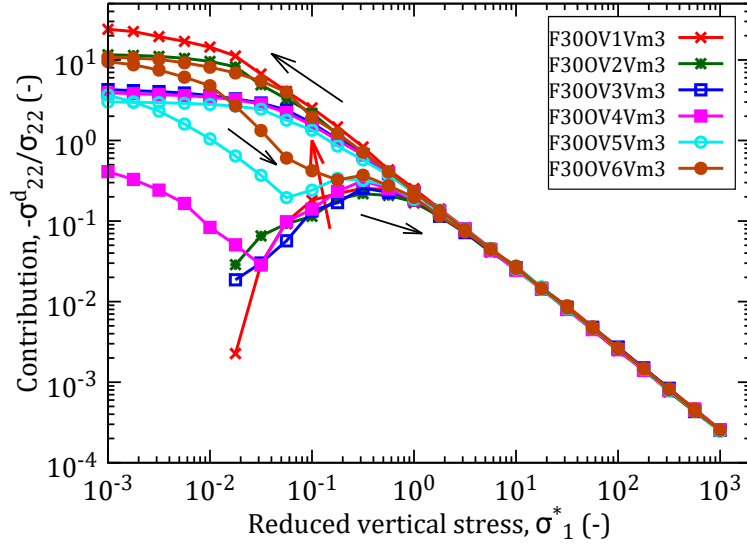


Figure 4.4: Contribution of distant interactions to normal stress σ_{22} . Red arrow denotes increasing V_0/V^* .

order $z_d F_0/d^2$, and therefore quite important compared to the total axial stress which is controlled at a small value of order $\sigma_1^* F_0/d^2$ (even considerably larger for well connected initial): at $\sigma_1^* = 10^{-3}$, values $\sigma_{22}^d/\sigma_{22} = -0.41$, $\sigma_{22}^d/\sigma_{22} = -3.65$, and $\sigma_{22}^d/\sigma_{22} = -9.53$ are respectively observed in tests F30OV4Vm3, F30OV5Vm3, and F30OV6Vm3. $\sigma_{22}^d/\sigma_{22}$, in these three cases, increases in Regime I, which ends, respectively, at $\sigma_1^* \simeq 3 \times 10^{-2}$, $\sigma_1^* \simeq 7 \times 10^{-2}$ and $\sigma_1^* \simeq 10^{-1}$ [Fig. 4.6(a)]. Nevertheless, it is well noted that the increase in $\sigma_{22}^d/\sigma_{22}$ is significantly induced by the increase in the total stress σ_{22} , certainly not by σ_{22}^d itself. The constant values of z_d demonstrate this phenomenon (see Fig. 4.6(b)). Upon growing of vertical stress, the system is compressed and more distant interacting pairs are created. σ_{22}^d is therefore decreased while σ_{22} is remarkably increased. This is why $\sigma_{22}^d/\sigma_{22}$ values significantly decrease in the range of vertical stress $2 \times 10^{-2} \leq \sigma_1^* \leq 3 \times 10^{-1}$ for first three cases (red, dark-green and blue curves) and in the shorter range of σ_1^* in the last three cases (magenta, cyan and dark-orange curves). When the confining forces dominate the attractive forces ($\sigma_1^* > 10^0$), this contribution is gradually increased until the end of loading path. Upon unloading, σ_{22}^d is steadily decreased until the end. This corresponds to the increase in the distant interactions in Fig. 4.1(b).

Another decomposition of total stress is given as follows:

$$\sigma_{\alpha\beta} = \sigma_{\alpha\beta}^{cap} + \sigma_{\alpha\beta}^{Ne} + \sigma_{\alpha\beta}^T, \quad (4.4)$$

in which $\sigma_{\alpha\beta}^{cap}$ is the contribution of capillary forces (either for the contacts or the distant interacting pairs), $\sigma_{\alpha\beta}^{Ne}$ is the contribution of normal elastic forces, and $\sigma_{\alpha\beta}^T$ is the contribution of tangential forces.

Fig. 4.5 displays the contributions of tangential forces and capillary forces to the normal stress σ_{22} . Remarkably, the contribution of tangential stress is almost negative

(Fig. 4.5(a)). Under growing of vertical stress, the ratio $\sigma_{22}^T/\sigma_{22}$ increases to approximately null values at the end of the loading path. It is then reincreased until the end of the unloading path. Besides, the capillary force being a tensile force, it is always negative. Its contribution to the total stress σ_{22} is illustrated in Fig. 4.5(b). As discussed in Chapter 3, the capillary forces play a key role for stabilizing the specimen in very loose states. Therefore, the capillary stress are considerably σ_{22} under low vertical stress. $-\sigma_{22}^{cap}/\sigma_{22}$ varies approximately from 2×10^2 to 10^3 at $\sigma_1^* = 10^{-3}$. This ratio strongly decreases to 2×10^{-3} at the end of the loading path. It then increases and recovers a dominant contribution when the system is unloaded.

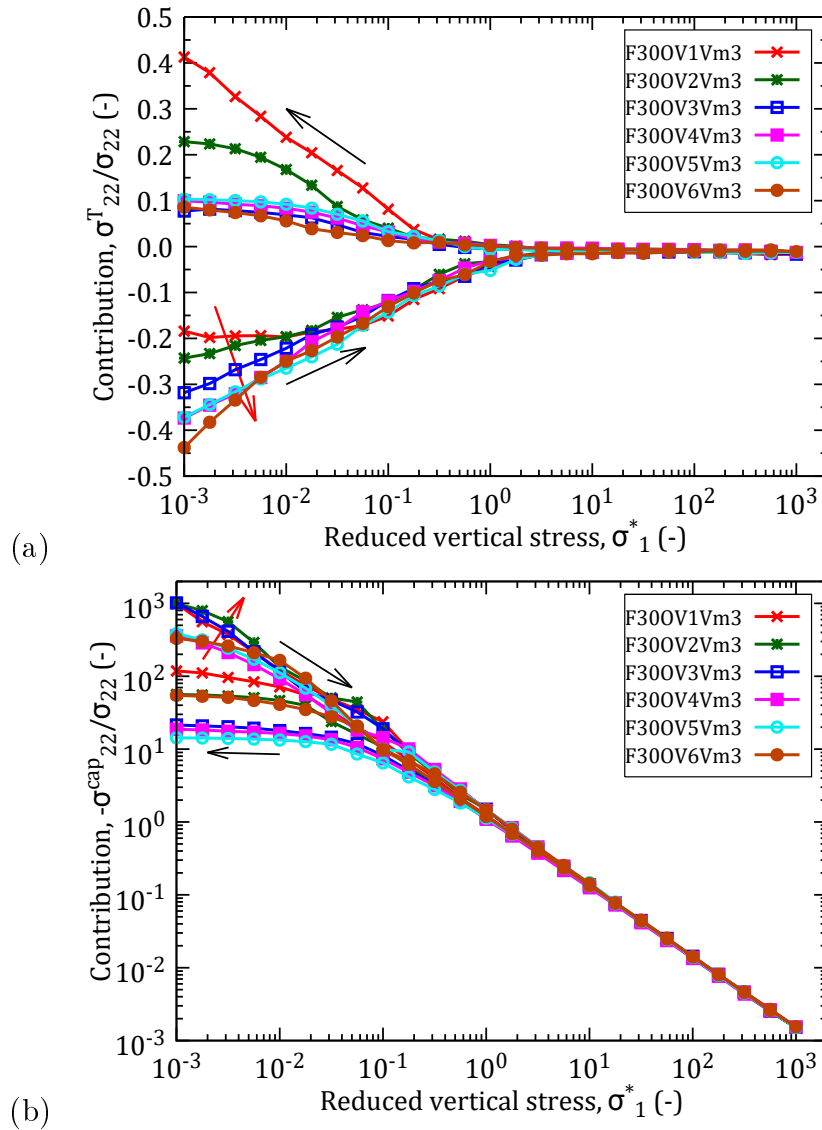


Figure 4.5: (a) Contributions of tangential (a) and capillary (b) interactions to normal stress σ_{22} . Red arrow denotes increasing V_0/V^* .

4.2.2 Influence of initial solid fraction

The influence of initial solid fraction Φ_0 on the variation of void ratio e and coordination numbers z_c and z_d in loading and unloading paths is depicted in Fig. 4.6. All four tests are started with the same values of initial agitation V_0/V^* and meniscus volume V_m/d^3 , given in Table 4.1. We can easily distinguish the usual three Regimes in the compression curve. The higher the densities, the larger the plateaus of Regime I (Fig. 4.6(a)). In the unloading path, void ratio e remains almost constant in the four systems. Furthermore, z_c and z_d numbers vary almost similarly during loading and unloading paths (Fig. 4.6(b)). They are negligibly different in Regime II, depending on the moment threshold of the collapse.

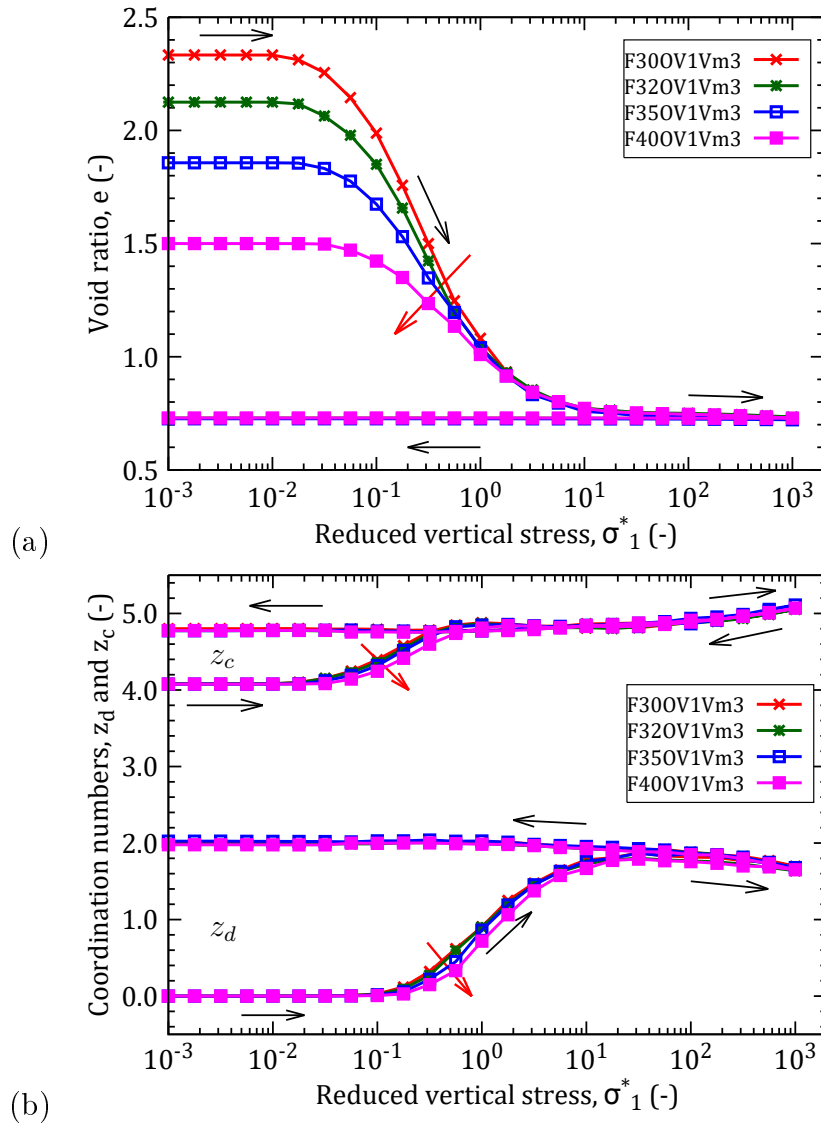


Figure 4.6: (a) Void ratio e , and (b) coordination numbers z_c and z_d versus σ_1^* for different values of initial solid fraction Φ_0 . Red arrow denotes increasing Φ_0 .

The variation of coordination numbers of compressive and tensile contacts for differ-

ent values of initial solid fraction is displayed in Fig. 4.7. Initially, under low vertical stress, the compressive and tensile contacts are approximately balanced. z_- and z_+ fluctuate around 2. Under growing of vertical stress, the population of compressive contacts gradually increases while the population of tensile ones is steadily depleted until the end of loading path. z_- and z_+ vary in opposite directions upon unloading, the former decreasing and the latter increasing. At the end of unloading, both z_- and z_+ remain almost constant, z_+ being larger than z_- . The variations of z_- and z_+ are similar with the ones obtained for the isotropic system (see Fig. 3.22 of Chapter 3).

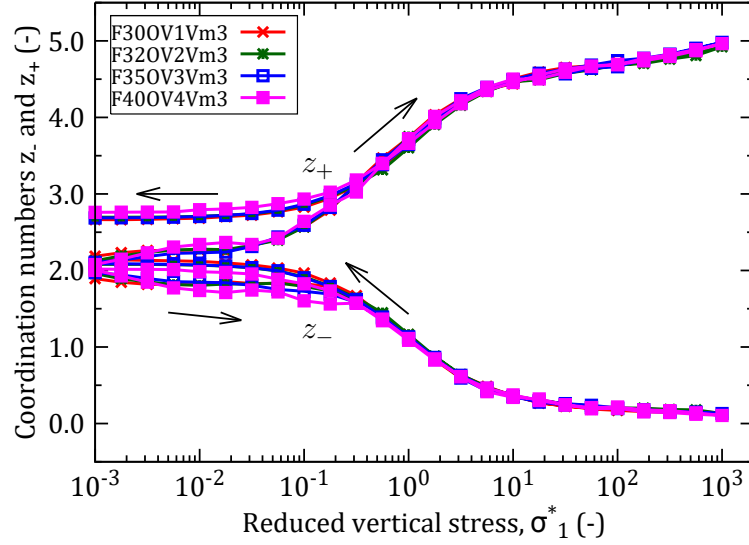


Figure 4.7: Coordination numbers of z_+ and z_- versus reduced vertical stress σ_1^* for different values of Φ_0 . Red arrow denotes increasing Φ_0 .

Concerning the coefficient of lateral pressure K_0 , its variation during the compression and decompression cycles for different values of Φ_0 is illustrated in Fig. 4.8. Initially, K_0 equals 0.4. In other words, the horizontal stress is approximately 40% of the vertical stress in all cases. K_0 is then slightly decreased in Regime I in the stress interval $10^{-3} \leq \sigma_1^* \leq 10^{-2}$ (to 3×10^{-2}). During the collapse of all specimens, K_0 is significantly increased and it approaches to 1 at the end of the collapse (at $\sigma_1^* = 10^1$). Subsequently, in Regime III ($\sigma_1^* \geq 10^1$), K_0 is negligibly decreased. At the end of loading path, the horizontal stress is approximately 80% of the vertical one ($K_0 \approx 0.8$). Upon unloading, K_0 is slightly increased until the vertical stress decreases down to $\sigma_1^* = 10^0$. Since then, K_0 strongly increases when the vertical stress decreases to very low values. In other words, the horizontal stress is higher than vertical one, from sevenfold to thirty-fold. This could be explained by the increase in the number of tensile contacts z_- (see Fig. 4.7). Besides, the volumetric deformation of each specimen also contributes to the difference of K_0 when the vertical stress is very low. In other words, the horizontal stress is directly proportional to the specimen's volume while the vertical one is inversely proportional to it. In our simulation, the denser the systems, the smaller the total volumes. That

demonstrates the remarkable difference of K_0 at the end of the unloading path.

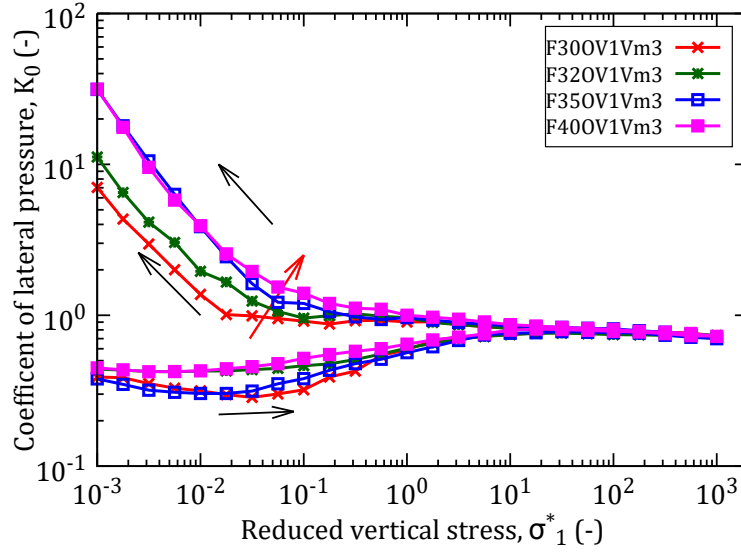


Figure 4.8: Coefficient of lateral pressure K_0 versus reduced axial stress σ_1^* for different values of Φ_0 . Red arrow denotes increasing Φ_0 .

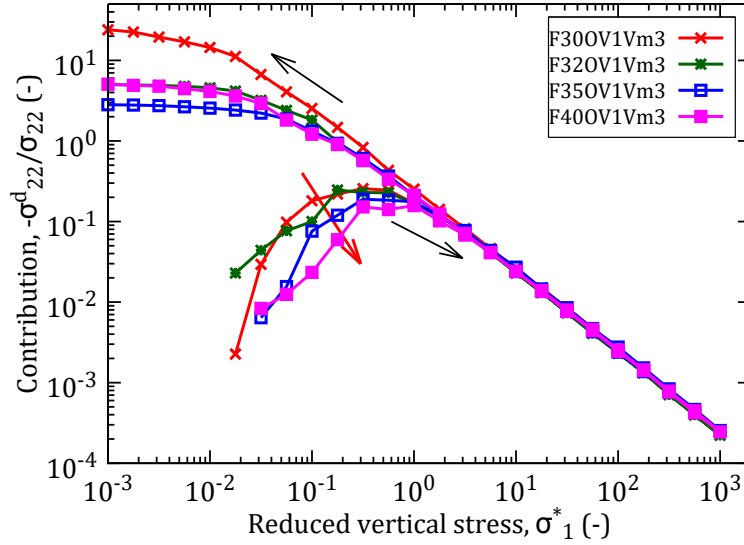


Figure 4.9: Contribution of distant interactions to normal stress σ_{22} for different values of Φ_0 . Red arrow denotes increasing Φ_0 .

The contribution of the distant interacting pairs to the normal stress σ_{22} for different Φ_0 is depicted in Fig. 4.9. As mentioned for Fig. 4.6(b), no distant interacting pairs z_d are created under very low vertical stress with small initial agitations. σ_{22}^d is therefore null in four cases at the beginning of loading path. σ_{22}^d is strongly decreased in the intermediate interval stress, $2 \times 10^{-2} \leq \sigma_1^* \leq 10$ when the number of interacting pairs is increased. It downs to the minimum at $\sigma_1^* = 3 \times 10^{-1}$. Under higher vertical stress, this contribution to the normal stress σ_{22} is gradually increased. This is due to the strong increase in the

total stress σ_{22} while the stress of distant interactions σ_{22}^d is insignificantly decreased. Conversely, the $\sigma_{22}^d/\sigma_{22}$ is steadily decreased until the end of unloading path. When the vertical stress decreases to very low values, $\sigma_1^* \leq 10^{-1}$, the $\sigma_{22}^d/\sigma_{22}$ is remarkably different in four cases. Because in the looser system, the total stress σ_{22} is smaller than in the denser system (as we already mentioned in the discussion on K_0). The $\sigma_{22}^d/\sigma_{22}$ of the F30OV1Vm3 (red curve) is therefore smaller than for the other cases.

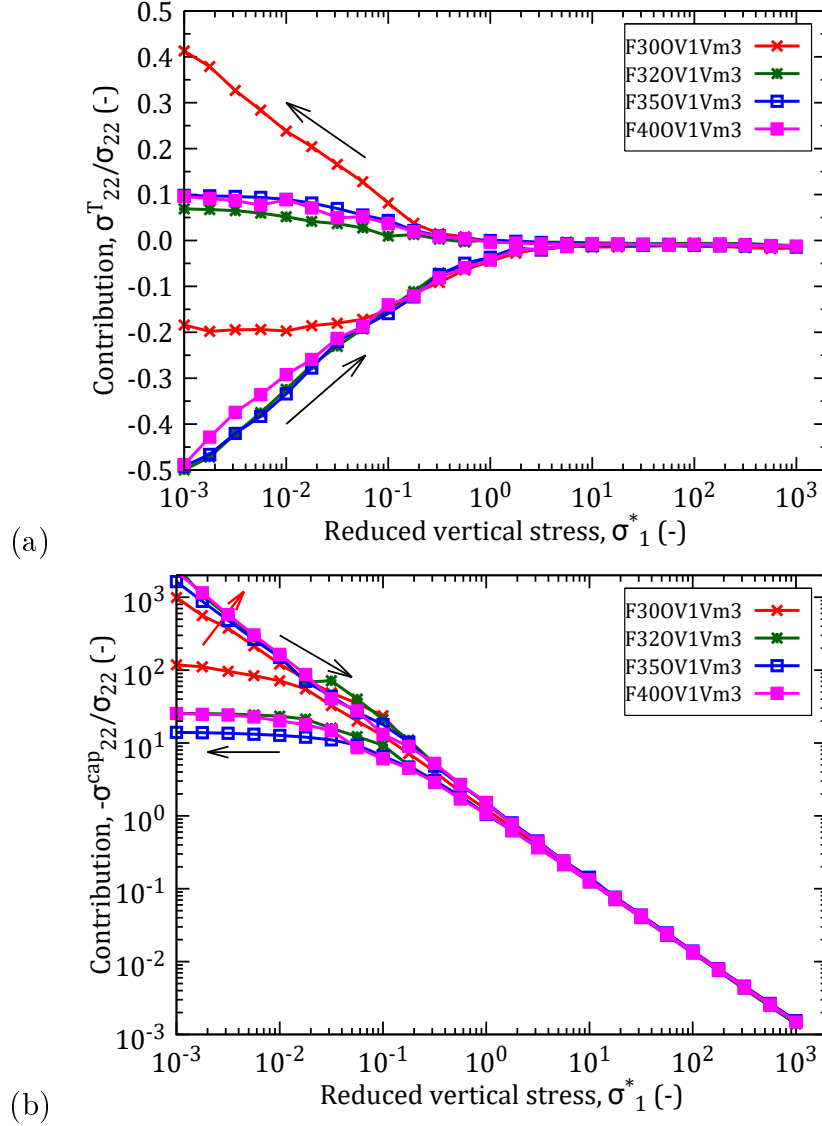


Figure 4.10: (a) Contributions of tangential (a) and capillary (b) interactions to normal stress σ_{22} for different values of Φ_0 . Red arrow denotes increasing Φ_0 .

The contributions of tangential and capillary interactions to the normal stress σ_{22} for different values of Φ_0 are shown in Fig. 4.10. The variation of $\sigma_{22}^{cap}/\sigma_{22}$ is generally similar with the variation shown in Fig. 4.5(b). σ_{22}^{cap} maximally contributes to σ_{22} under low vertical stress. σ_{22}^{cap} then decreases or the ratio $\sigma_{22}^{cap}/\sigma_{22}$ is gradually increased until the end of loading. Upon unloading, $\sigma_{22}^{cap}/\sigma_{22}$ is steadily decreased in all cases. Distinct values appear at the end of decompression when $\sigma_1^* \leq 10^{-1}$. The smallest ratio is obtained

for F30OV1Vm3 (red curve), while the other case have higher ratios (dark-green, blue and magenta curves). Similar observations were discussed above for the smallest case of density.

4.3 Oedometric versus isotropic compression

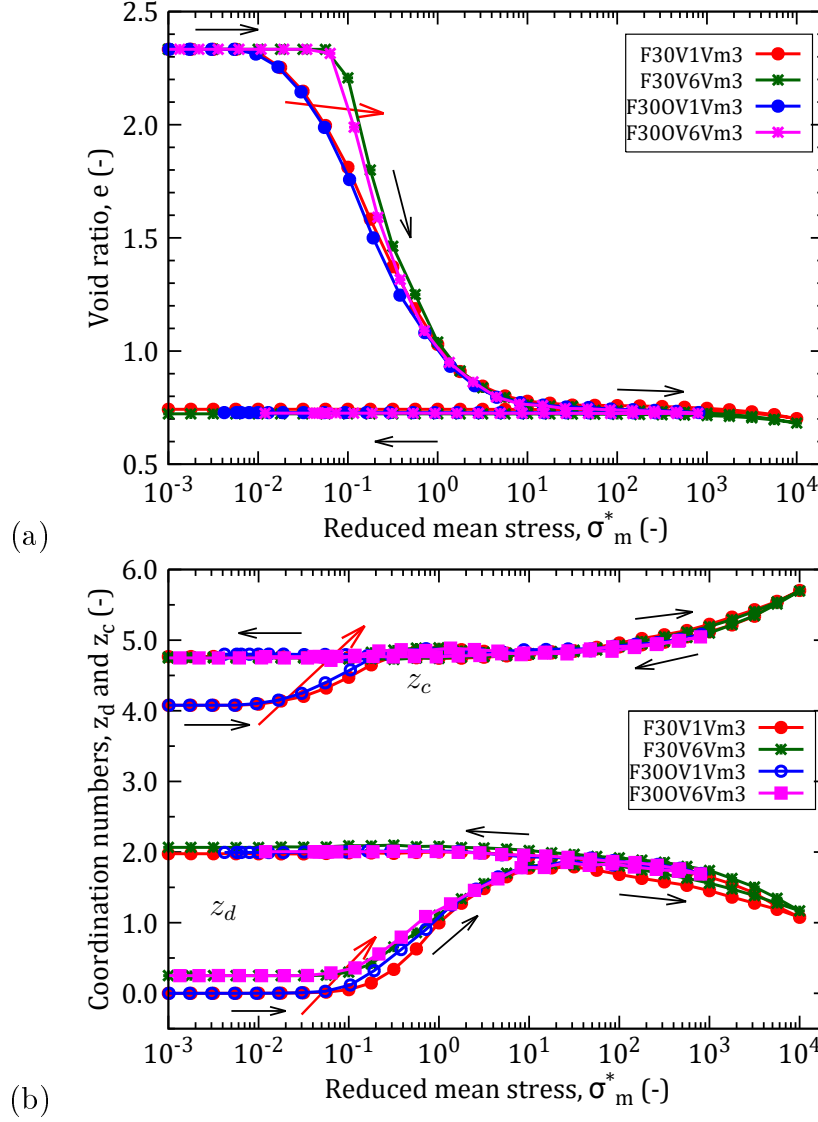


Figure 4.11: (a) Void ratio e , and (b) coordination numbers z_c and z_d versus σ_m^* for the minimum and maximum V_0/V^* in both simulations of oedometric and isotropic tests. Red arrow denotes increasing V_0/V^* .

Many similarities have been pointed out between isotropic and oedometric compression tests. We now turn to more direct and quantitative comparisons. The reference case ($\Phi_0 = 0.30$) is chosen with two values of the minimum and maximum initial agitation intensities V_0/V^* . In this comparison, the mean stress $\sigma_m = (\sigma_1 + \sigma_2 + \sigma_3)/3$ (as well as the reduced mean stress σ_m^*) is used for the two cases. The variations of void ratio e and

coordination numbers z_c and z_d along a compression cycle, for the two cases of V_0/V^* , are illustrated in Fig. 4.11.

In general, plots of e , z_d and z_c versus reduced mean stress σ_m^* , corresponding either to isotropic or to oedometric compressions, are quite similar. Under low mean stress σ_m^* , the plateaus of Regime I in both systems are almost similar in the interval stress, $10^{-3} \leq \sigma_m^* \leq 10^{-1}$ and $10^{-3} \leq \sigma_m^* \leq 7 \times 10^{-1}$ (see Fig. 4.11(a)). Under growing of mean stress in Regime II, the collapse of the two systems is slightly different: the structure of oedometrically compressed systems collapses earlier than in isotropic tests. A deviator stress thus seems somewhat more efficient to create rearrangements. Conversely, in unloading path, when the axial stress decreases, the lateral stresses remain higher than the axial one. That is why the decompression curves of oedometric tests finish at $\sigma_m^* \approx 4 \times 10^{-3}$ for the F30OV1Vm3, and at $\sigma_m^* \approx 10^{-2}$ for the F30OV1Vm3. Numbers z_d and z_c vary almost similarly in both models. More contacts and distant interacting pairs are created for the larger agitations under low vertical mean stress. z_d for both tests only shown a small difference in the interval stress $10^{-1} \leq \sigma_m^* \leq 10^0$. At the end of loading, z_d in the oedometric tests (blue and magenta curves) is higher than the one in the isotropic tests (red and dark-green curves). The opposite stands for z_c (Fig. 4.11(b)).

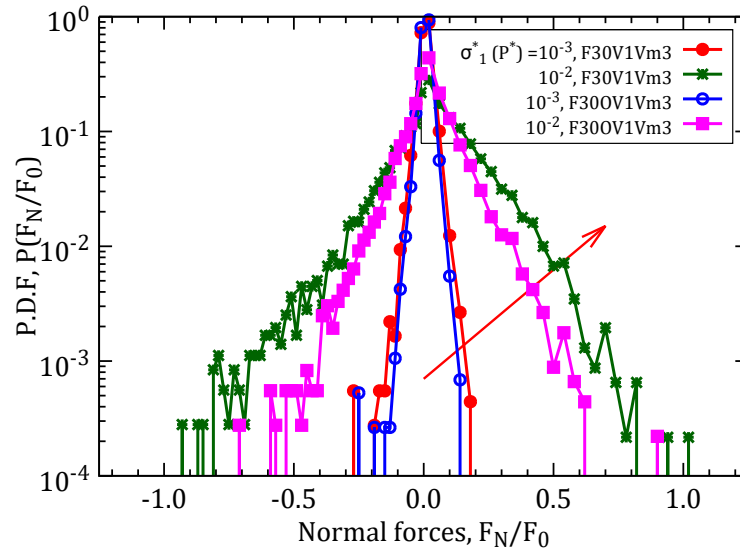


Figure 4.12: Distribution of normal forces for both oedometric and isotropic models at low vertical stress, normalized by the maximal tensile force F_0 . Red arrow denotes the increasing of stress or pressure.

Additional information on the plateau of Regime I in both oedometric and isotropic models is provided in Fig. 4.12. In general, all P.D.Fs are roughly symmetric about 0 and diverge near 0 as a power law (with an exponent between 0.2 and 1.0) in the range of forces between $2 \times 10^{-4}F_0$ and $10^{-3}F_0$. It is clearly apparent that at $\sigma_1^* = 10^{-2}$, the P.D.F of the isotropic case (dark-green curve) is wider than the one of the oedometric case (magenta curve). The P.D.F of the isotropic case vanishes at $-F_0$ and F_0 while

it vanishes at $-0.5F_0$ and $0.5F_0$ for the oedometric test. That F_N reaches $-F_0$ signals the onset of in Regime II collapse (red curve in Fig. 4.11(a)). Meanwhile, a distribution bounded by $|F_N/F_0| \leq 0.5$ in the oedometric case (magenta curve) implies that the initial network may support further stress increments without rearranging. This explains why the plateau of Regime I in the oedometric case is wider than the one in the isotropic case (Fig. 4.11(a)). Under high axial stress, the P.D.Fs of normal forces F_N , normalized by the average normal force $\langle F \rangle_N$, for both models, are quite similar, as shown in Fig. 3.14 in Chapter 3.

4.4 Experiment versus simulation

This section aims to confront the results of the experiments of Chapter 2 and the ones of the simulated oedometric compression test in Sec. 4.2. The comparison is carried out for the macroscopic compression curve and for microstructural changes. All stresses are given here in kPa.

4.4.1 Compaction behavior

A comparison of compression behavior between experiment and simulation of oedometric compression tests for four values of initial solid fraction Φ_0 ($\Phi_0 = 0.30$, $\Phi_0 = 0.32$, $\Phi_0 = 0.35$, and $\Phi_0 = 0.40$) is shown in Fig. 4.13. In general, both experimental and simulated curves have the same S-shape as already mentioned in Chapter 2. Three regimes can be equally identified in the compression curves, depending on the range of vertical stress σ_1 .

Fig. 4.13(a) shows the experimental and simulated compression curves for the initial solid fraction $\Phi_0 = 0.30$ in which the dashed curve (CT01) was obtained with the cell $\phi 20$. The global features of those curves are in agreement. Some differences are notable in the stress corresponding to the onset of plastic collapse, which is larger by a factor of 2 or 3 in the laboratory (whence a lateral shift in comparison to the numerical results); in the compression index (slope of the fastly decreasing part of the curves in Regime II), which is somewhat smaller in experimental results; and final void ratio, which is larger in the numerical case.

It is well recognized that Regime I in experimental curves exists in a very short range of vertical stress. The plateau of Regime I, if it exists, may be at the very low vertical stress ($\sigma_1 < 10^{-2}$ kPa). Under low stress, the initial structure of experiment is slightly collapsed while the one of simulation can sustain the increasing stress without rearrangement, with a void ratio e remaining almost constant. In Regime II, under growing of vertical stress, the collapse in simulation happens earlier in comparison with the experimental curves. This is confirmed by the slope of three curves in Fig. 4.13(a). For instance, Regime II of simulated curve exists in interval $4 \times 10^{-2} \text{ kPa} \leq \sigma_1 \leq$

8×10^0 kPa while its intervals in experimental curves are 7×10^{-2} kPa $\leq \sigma_1 \leq 2 \times 10^1$ kPa (OD01), and 7×10^{-2} kPa $\leq \sigma_1 \leq 3 \times 10^1$ kPa (CT01). However, for CT01, the void ratio at the end of the collapse is higher than the ones of OD01 as well as the F30OV1Vm3. This reflects the effect of the cell's size and the friction between grains and cell. This friction contributes to prevent the settlement of all grains. Therefore, the collapse of experimental specimen is slower than the simulated one. Under higher stress, at the end of loading path, the minimal void ratio of OD01 is lower than the simulated one. With the cell $\phi 20$, the void ratio is still higher than the ones of the cell $\phi 50$ and simulation. This can be explained by the effect of the cell size, already mentioned in Chapter 2. In addition to possible friction on the side walls, experimental test results are likely affected by initial large scale sample heterogeneities evidence in the XRCT-scans of Chapter 2.

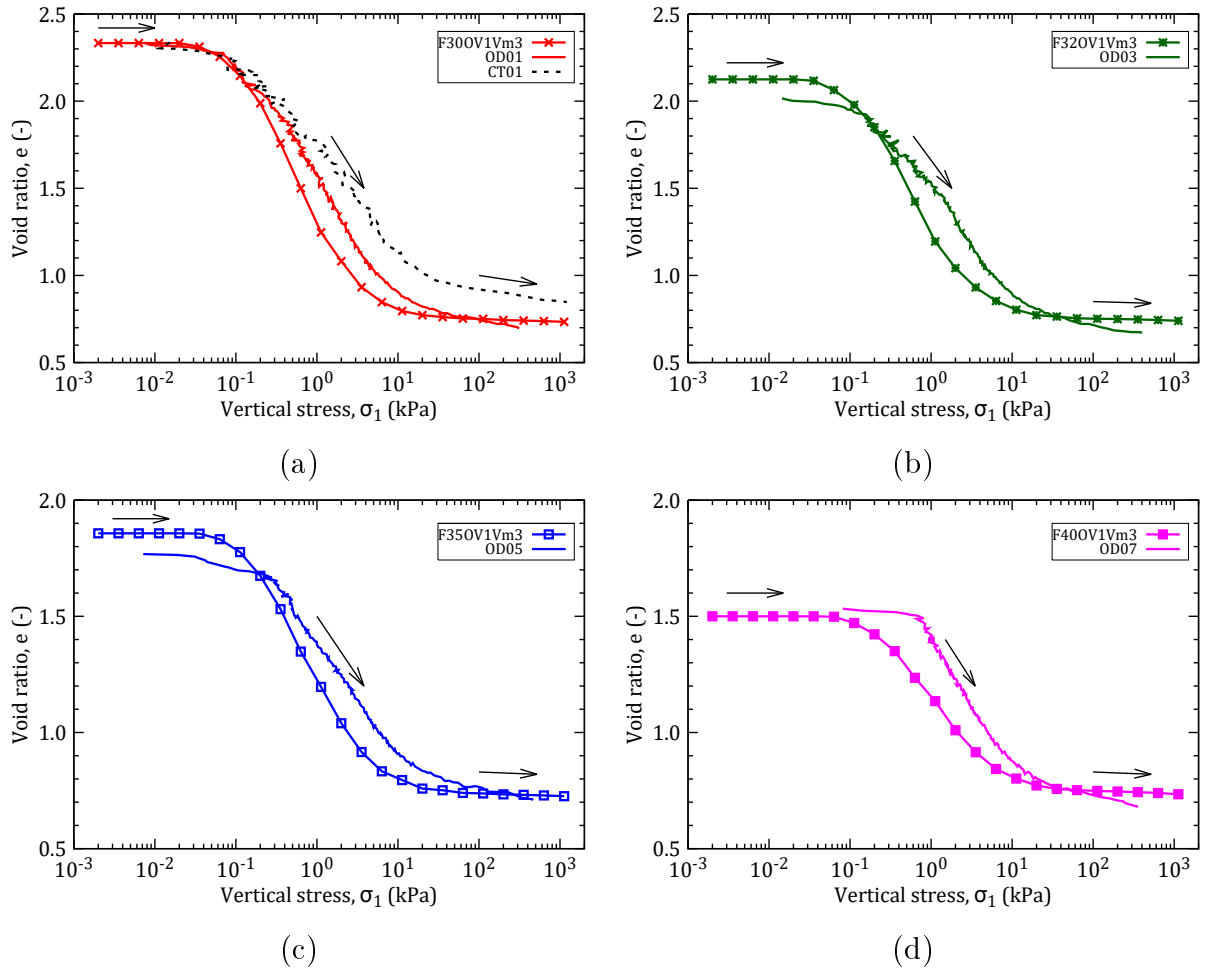


Figure 4.13: Oedometric compression curves in experiments and simulations (no RPR) for different values of Φ_0 . (a) $\Phi_0 = 0.30$, (b) $\Phi_0 = 0.32$, (c) $\Phi_0 = 0.35$, (d) $\Phi_0 = 0.40$.

For the experiments with $\Phi_0 = 0.32$ (Fig. 4.13(b)) and $\Phi_0 = 0.35$ (Fig. 4.13(c)), the plateau of Regime I does not exist. Under low stress, $\sigma_1 \leq 2 \times 10^{-1}$ kPa, the initial structures of experiments are remarkably collapsed and void ratios e are lower than simulated ones. For instance, at $\sigma_1 \approx 1 \times 10^{-2}$, $e = 1.99$ in the OD03 as compared with

$e = 2.15$ in the F32OV1Vm3, $e = 1.76$ in the OD05 in comparison with $e = 1.85$ in the F35OV1Vm3. In Regime II, under growing of high stress, the experimental specimens are collapsed later than the simulated ones. The collapse finishes at $\sigma_1 = 10^1$ kPa for the F32OV1Vm3 and F35OV1Vm3, and at $\sigma_1 = 2 \times 10^1$ kPa for the OD03 and OD05. The void ratio of experimental curves decreases down to lower values than the ones of simulated curves at the end of loading path. For the $\Phi_0 = 0.40$ (Fig. 4.13(d)), the initial structure of experiment (OD074) is stronger than the one of simulation (F40OV1Vm3). This is reflected by the starting of the collapse in Regime II, at $\sigma_1 = 1 \times 10^{-1}$ kPa for the simulated case (F40OV1Vm3) and at $\sigma_1 = 10^0$ kPa for the experimental case (OF07). These two curves nearly merge at the end of the collapse. However, under high stress, the void ratio e of experimental curve also decreases down to lower values than the simulated one. The slight difference in bead diameters between the experimental ($d_{\text{exp}} = 80$ to $104 \mu\text{m}$) and the numerical ($d_{\text{num}} = 115 \mu\text{m}$) is not sufficient to correct the horizontal shift between experimental and numerical curves (the same reduced stress σ_1^* should be obtained on multiplying the numerical value by $d_{\text{num}}/d_{\text{exp}}$). The experimental polydispersity, though, could partly explain the larger final density of experimental systems.

As to the differences in compression index and in the reduced stress corresponding to collapse, the results of the numerical parametric study indicate that it could be reduced with a choice of small RPR parameters and an appropriate initial connectivity, determined by agitation intensity V_0 . However, a more quantitative assessment of size and boundary effects in experiments is needed.

4.4.2 Geometrical structure change

In this section, only the case F30OV1Vm3 (see more details in Table 4.1) of the oedometric compression test is chosen in order to compare with the experimental results (from the local scan observations mentioned in Chapter 2).

Fig. 4.14 plots the coordination numbers of neighbours, $z(h)$, versus axial stress σ_1 , and the total coordination number z in the local scan observations (see Sec. 2.5 of Chapter 2), versus positions of scans along the loading path. The total coordination number including lost contacts z_{exp}^{lc} is also plotted (brown triangle point). The results of the case F30OV1Vm3 is only displayed in the loading path with five values of h , denoted as h_1 to h_5 , with $h_1/d = 0$, $h_2/d = 0.025$, $h_3/d = 0.05$, $h_4/d = 0.075$, and $h_5/d = 0.1$. As mentioned in Chapter 3, when $h/d = 0$, $z(h)$ is equal to z_c , the contact coordination number (see Sec. 3.5.1 in Chapter 3). The positions of scans are directly interpolated from the compression curves of Fig. 2.11 in Chapter 2. In general, the order of magnitude and the general trend of the z_{exp} is well captured by the simulation. At $\sigma_1 \approx 4 \times 10^{-2}$ kPa, $z_{\text{exp}} = 4.75$ is remarkably higher than all of the $z(h)$. This could be explained by the stability of Regime I in the simulated case, where void ratio e is

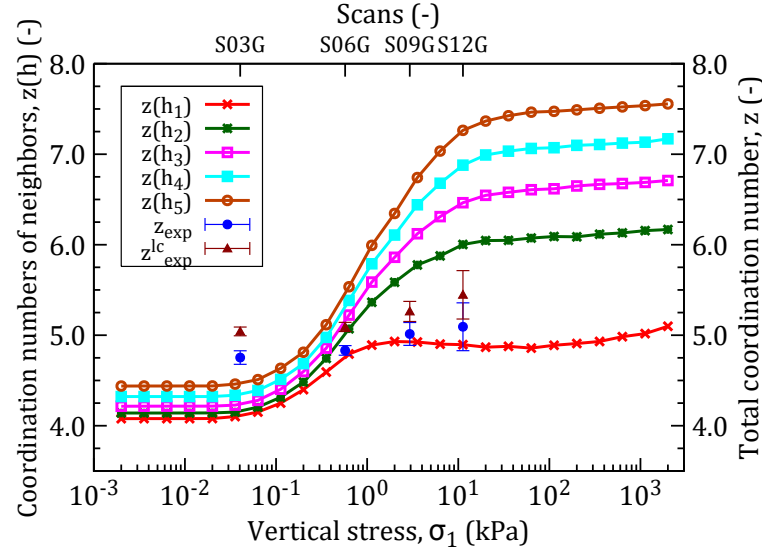


Figure 4.14: Coordination numbers of neighbors $z(h)$ versus vertical stress σ_1 and the total coordination number z versus positions of scans.

almost constant and insignificantly decreases at the starting of the collapse. Meanwhile, in Regime I of the experimental case, the initial structure is slightly collapsed with a very small rearrangement. Moreover, the first local scan was performed at $h_1 = 9.8$ mm, not at the initial height (see Table 2.2 in Chapter 2). z_{exp} is therefore higher than the $z(h)$ at this stage. For the other scans (S06G, S09G, and S12G), z_{exp} is higher than $z(h = 0)$ (red curve) while it is globally lower than the other values of $z(h)$. In experiments, a tolerance of 1 voxel is mainly used in all calculations. This value is equal to $h/\langle d \rangle = 0.07$ which is corresponding to $z(h_4)$ at $h/d = 0.075$ (cyan curve). However, z_{exp} at the S09G and S12G is significantly lower than $z(h_4)$. This is due to the heterogeneity of specimen. There still exists several large pores during the compaction test even at the highest level of compaction (S12G). This phenomenon is already described in Chapter 2 (see Fig. 2.26). Conversely, in simulation, the specimen is definitely homogeneous during the compression cycle, especially at the high pressure.

Nevertheless, when counting the lost contacts, $z_{\text{exp}}^{\text{lc}}$ approaches closely to the $z(h)_4$ at $h/d = 0.075$, especially for the scan S06G. In other words, the total coordination number obtained in experiment is fairly underestimated when compared with the coordination numbers of neighbors in simulation.

4.5 Conclusion

In this Chapter, we have performed the simulation of oedometric compression tests for the monodisperse system without RPR. The results of this system are then compared in turn with the ones of the isotropic compression tests (in Chapter 3) and with the ones of the local scan observations (in Chapter 2).

Several conclusions can be drawn as follows.

The results obtained from the simulation of oedometric compression tests, including the compaction behavior and the microstructural characterizations, are globally similar with the results of isotropic tests, especially if mean stress is regarded as the control parameter for both tests. The stress ratio, K_0 , in oedometric compression, as studied here for initially isotropic states, depends on initial connectivity and goes through a minimum in the course of oedometric compression, in Regime II (from 0.3 in initially well connected systems to about 0.5 in barely rigid ones. As the minimum void ratio is approached, it increases to a common value near 0.8. Strongly overconsolidated states with small σ_m^* may exhibit comparatively very large stresses in some directions, of order $z\Phi F_0/d^2$.

A comparison of compression behavior between the oedometric compression test and the experiments reveals several remarks. Regime I exists in the experimental tests with a very small rearrangement of the initial structure but the plateau of Regime I does not exist. In other words, it is really difficult to maintain the stable-state of initial structure under very low stress in experiment without rearrangement. Furthermore, the difference of the collapse between simulation and experiment obviously confirms the significant effect of the friction between the cell and grains during the test.

For the prediction of z , although the experimental result is underestimated in comparison to the DEM simulation result, we obtained the correct trends for the changes of the microstructure in both oedometric simulation and experimental tests.

Conclusions and Perspectives

General conclusions

The present work is a contribution to the understanding of the mechanical behavior of wet granular materials in very loose states. We have proposed both a numerical tool based on the DEM and experimental procedures to study the 3D plastic response of glass beads subjected to isotropic and oedometric compression tests. Microstructural changes of the specimen induced by increasing applied external force were also characterized in both experiments and DEM simulations. The main conclusions of this work are briefly summarized as follows.

Firstly, we can produce in the laboratory specimens of wet granular soils presenting a very loose –yet stable– state, even using a very small water content. This is one of the main originalities of the present work as compared with past studies which focused on denser states and higher initial water contents (e.g. Bruchon *et al.* [35]). Similar solid fractions are obtained by a suitable numerical aggregation process prior to compression.

Secondly, the compression behavior of wet beads at loose states obtained from experiment and DEM simulations (isotropic and oedometric compression tests) has usually three regimes: (i) at stresses lower than an apparent precompression stress, the initial structure can sustain the load without any rearrangement (in the DEM simulations) or with very small rearrangements (in the experiments); (ii) when the stresses exceed this apparent precompression stress, the loose structures collapse and restructure; and (iii) at higher stresses, only elastic deformation of grains at contact points occurs. This behavior abides by the classical logarithmic law of soil mechanics in the intermediate stage. The compression index is not an intrinsic material property, but depends on its initial density and connectivity. This latter feature of initial loose states depends on the aggregation process, and affecting the subsequent behavior in the earlier stages of plastic compression. The properties of wet granular soils in plastic compression in the later stages of plastic collapse are not too much dependent on the assembling process.

Thirdly, we presented a numerical approach to precisely measure several fundamental microstructure properties of loose systems from 3D tomography images. Although this approach underestimates several microstructure properties in comparison with DEM

simulations and other studies in the literature, it provides an appropriate characterization of the grain-scale behavior of wet granular soils at very loose state during compression.

Fourthly, we emphasized the important differences between cohesive and non-cohesive granular assemblies. The most important differences, which are brought by cohesion in macroscopic behavior, are the existence of stable very loose structures and the response during compression. Moreover, the influence of size polydispersity was investigated only under isotropic compression. Our results show that the size polydispersity negligibly affects the plastic behavior of wet beads.

Finally, our results also emphasize the remarkable influence of the rolling and pivoting resistances at contacts between grains. Even a small RPR is enough to produce strong differences in the plastic behavior, with the collapse under growing confining stress becoming notably more gradual.

Perspectives

The research program developed here can be extended in many potential research directions, as follows.

On the experimental side, in order to increase the accuracy of the microstructural characteristics in experiments, the entire specimen should be used for the detection process. However, this process requires a very large memory for the calculation. So the detection for the REV (mentioned in Sec. 2.4.4 of Chapter 2) is preferably proposed for the detection process. Moreover, the sub-voxel algorithm could be also applied in order to increase the resolution of the tomography images. Furthermore, the algorithm of detection should be improved to obtain the real value of the detected radii instead of the rounded value.

The pore-scale deformation of specimens during compression can be analyzed in details by using the Digital Volume Correlation (DVC or 3D DIC) method. This is one of the most interesting phenomenon of wet granular materials at very loose state. Besides, the pore size distribution can be directly analyzed from the 3D tomography images based on the preliminary analyses in Sec. 2.4.4 of Chapter 2.

On the numerical side, the quasistatic behavior of a 3D model, in pendular state, accounting for the possible effect of rolling and pivoting resistances at contacts under triaxial compression tests where the macroscopic deviatoric stress will play a major role, is a straightforward extension of the present work. Ref. [47] contains a preliminary comparison with the properties of the critical state in quasistatic simple shear flow. The wide range of stress and microstructural states between isotropically or oedometrically compressed states and steadily deformed materials at large strains remains to be explored. In addition, the role played by solid bridges (e.g. cemented granular soils or methane hydrate soils) instead of capillary bonds should also be investigated.

Bibliography

- [1] D. M. Wood. *Soil Behaviour and Critical State Soil Mechanics*. Cambridge University Press, 1990. (Cited on pages [1](#), [10](#), [11](#) and [62](#).)
- [2] J. Biarez and P.-Y. Hicher. *Elementary Mechanics of Soil Behaviour*. A. A. Balkema, Rotterdam, 1993. (Cited on pages [1](#), [10](#) and [11](#).)
- [3] J. H. Atkinson. *An Introduction to Mechanics of Soils and Foundations: Through Critical State Soil Mechanics*. McGraw-Hill, New York, 1993. (Cited on pages [1](#) and [10](#).)
- [4] M.A. Tripodi, V.M. Puri, H.B. Manbeck, and G.L. Messing. Elastoplastic finite element model development and validation for low pressure uniaxial compaction of dry cohesive powders. *Powder Technology*, 85(3):241 – 251, 1995. (Cited on pages [1](#) and [10](#).)
- [5] J. K. Mitchell and K. Soga. *Fundamentals of Soil Behavior*. Wiley, 2005. (Cited on pages [1](#), [10](#), [11](#), [62](#) and [119](#).)
- [6] D. Poquillon, J. Lemaitre, V. Baco-Carles, Ph. Tailhades, and J. Lacaze. Cold compaction of iron powders - relations between powder morphology and mechanical properties: Part i: Powder preparation and compaction. *Powder Technology*, 126(1):65 – 74, 2002. (Cited on pages [1](#), [10](#) and [118](#).)
- [7] A. R. Cooper and L. E. Eaton. Compaction behavior of several ceramic powders. *Journal of the American Ceramic Society*, 45(3):97–101, 1962. (Cited on pages [1](#) and [10](#).)
- [8] J. S. Reed. *Principles of Ceramic Processing*. Wiley, New York, 1995. (Cited on pages [1](#) and [10](#).)
- [9] D. Falgon, E. Vidal-Sallé, J.-C. Boyer, R. Peczalski, and J. Andrieu. Identification procedure of a hardening law for powder compaction. *Powder Technology*, 157:183 – 190, 2005. 4th French Meeting on Powder Science and Technology Papers presented at the 4th French meeting on Powder Science and Technology. (Cited on pages [1](#) and [10](#).)
- [10] P. Pierrat and H. S. Caram. Tensile strength of wet granula materials. *Powder Technology*, 91(2):83 – 93, 1997. (Cited on pages [1](#), [10](#) and [53](#).)
- [11] T. Gröger, U. Tüzün, and D. M. Heyes. Modelling and measuring of cohesion in wet granular materials. *Powder Technology*, 133(3):203 – 215, 2003. (Cited on pages [1](#), [10](#) and [15](#).)
- [12] Z. Fournier, D. Geromichalos, S. Heminghaus, M.M. Kohonen, M. Mugele, F. Scheel, M. Schulz, B. Schulz, Ch. Schier, R. Seemann, and A. Skudelný. Mechanical properties of wet granular materials. *J. Phys.: Condens. Matter*, 17:S477, 2005. (Cited on pages [1](#), [10](#), [19](#), [22](#), [23](#) and [53](#).)
- [13] F. A. Gilabert, J.-N. Roux, and A. Castellanos. Computer simulation of model cohesive powders: Influence of assembling procedure and contact laws on low consolidation states. *Phys. Rev. E*, 75:011303, 2007. (Cited on pages [1](#), [2](#), [11](#), [15](#), [31](#), [37](#), [38](#), [43](#), [99](#), [103](#), [111](#), [125](#), [143](#) and [144](#).)
- [14] F. A. Gilabert, J.-N. Roux, and A. Castellanos. Computer simulation of model cohesive powders: Plastic consolidation, structural changes, and elasticity under isotropic states. *Phys. Rev. E*, 78:031305, 2008. (Cited on pages [1](#), [2](#), [11](#), [15](#), [31](#), [32](#), [38](#), [39](#), [99](#), [105](#), [118](#), [125](#), [143](#), [146](#) and [150](#).)
- [15] K. J. Dong, R. Y. Yang, R. P. Zou, and A. B. Yu. Role of interparticle forces in the formation of random loose packing. *Phys. Rev. Lett.*, 96(14):1–4, 2006. (Cited on pages [1](#) and [31](#).)
- [16] D. Kadau, G. Bartels, L. Brendel, and D.E. Wolf. Contact dynamics simulations of compacting cohesive granular systems. *Computer Physics Communications*, 147:190 – 193, 2002. Proceedings of the Europhysics Conference on Computational Physics Computational Modeling and Simulation of Complex Systems. (Cited on pages [1](#) and [31](#).)
- [17] D. Kadau, G. Bartels, L. Brendel, and D.E. Wolf. Pore stabilization in cohesive granular systems. *Phase Transitions: A Multinational Journal*, 76(4):315–331, 2003. (Cited on pages [1](#), [2](#), [31](#), [32](#) and [143](#).)

- [18] D. E. Wolf, T. Unger, D. Kadau, and L. Brendel. Compaction of cohesive powders. In *Powders and Grains 2005*, pages 525–533, 2005. (Cited on pages 1 and 31.)
- [19] G. Bartels, T. Unger, D. Kadau, D. E. Wolf, and J. Kertész. The effect of contact torques on porosity of cohesive powders. *Granul. Matter*, 7:139–143, 2005. (Cited on pages 1, 31 and 143.)
- [20] J.-Y. Delenne, M. S. El Youssoufi, and J.-C. B  net. Mechanical behaviour and rupture of cohesive granular media. *Comptes Rendus Mecanique*, 330(7):475–482, 2002. (Cited on pages 1 and 32.)
- [21] J.-Y. Delenne, M. S. El Youssoufi, F. Cherblanc, and J.-C. B  net. Mechanical behaviour and failure of cohesive granular materials. *International Journal for Numerical and Analytical Methods in Geomechanics*, 28(15):1577–1594, 2004. (Cited on pages 1 and 32.)
- [22] C. Thornton and L. Liu. How do agglomerates break? *Powder Technology*, 143:110 – 116, 2004. (Cited on pages 1 and 32.)
- [23] R. Y. Yang, R. P. Zou, and A. B. Yu. Numerical study of the packing of wet coarse uniform spheres. *AIChE Journal*, 49(7):1656–1666, 2003. (Cited on pages 1 and 33.)
- [24] V. Richefeu, M. S. El Youssoufi, and F. Radaj  . Shear strength properties of wet granular materials. *Phys. Rev. E*, 73:051304, 2006. (Cited on pages 1, 2, 11, 14, 33 and 110.)
- [25] R. Brewster, G. S. Grest, J. W. Landry, and A. J. Levine. Plug flow and the breakdown of bagnold scaling in cohesive granular flows. *Physical Review E*, 72(6):061301, 2005. (Cited on pages 2 and 33.)
- [26] L. Aarons and S. Sundaresan. Shear flow of assemblies of cohesive and non-cohesive granular materials. *Powder Technology*, 169(1):10 – 21, 2006. (Cited on pages 2 and 33.)
- [27] P. G. Rognon, J.-N. Roux, D. Wolf, M. Naa  m, and F. Chevoir. Rheophysics of cohesive granular materials. *EPL (Europhysics Letters)*, 74(4):644, 2006. (Cited on pages 2 and 33.)
- [28] P. G. Rognon, J.-N. Roul, M. Naa  m, and F. Chevoir. Dense flows of cohesive granular materials. *Journal of Fluid Mechanics*, 596:21–47, 1 2008. (Cited on page 2.)
- [29] S. Khamseh, J.-N. Roux, and F. Chevoir. Flow of wet granular materials: a numerical study. *Phys. Rev. E*, 92:022201–19, 2015. (Cited on pages 2, 11, 99, 101, 111 and 129.)
- [30] J. A. Mu  oz Castelblanco, P. Delage, J.-M. Pereira, and Y.-J. Cui. Some aspects of the compression and collapse behaviour of an unsaturated natural loess. *G  otechnique Letters*, 1:17–22(5), 2011. (Cited on pages 2 and 62.)
- [31] J.A. Mu  oz Castelblanco, J.-M. Pereira, P. Delage, and Y.-J. Cui. The water retention properties of a natural unsaturated loess from northern france. *G  otechnique*, 62:95–106(11), 2012. (Cited on page 2.)
- [32] M.J. Jiang, H. Hu, and F. Liu. Summary of collapsible behaviour of artificially structured loess in oedometer and triaxial wetting tests. *Can. Geotech. J.*, 1157(July 2011):1147–1157, 2012. (Cited on pages 2 and 53.)
- [33] T. G. Mason, A. J. Levine, D. Ertas, and T. C. Halsey. Critical angle of wet sandpiles. *Phys. Rev. E*, 60:R5044–R5047, Nov 1999. (Cited on pages 2, 18, 22 and 53.)
- [34] N. Mitarai and F. Nori. Wet granular materials. *Advances in Physics*, 55(1-2):1–45, 2006. (Cited on pages 2, 10, 13, 53, 101, 110 and 111.)
- [35] J.-F. Bruchon, J.-M. Pereira, M. Vandamme, N. Lenoir, P. Delage, and M. Bornert. Full 3d investigation and characterisation of capillary collapse of a loose unsaturated sand using x-ray ct. *Granul. Matter*, 15(6):783–800, 2013. (Cited on pages 2, 19, 24, 25, 53, 95, 131 and 173.)
- [36] Y.-H. Wang and S.-C. Leung. A particulate-scale investigation of cemented sand behavior. *Can. Geotech. J.*, 45:29–44, 2008. (Cited on pages 2, 10, 11 and 42.)
- [37] Y. H. Wang and S. C. Leung. Characterization of cemented sand by experimental and numerical investigations. *J. Geotech. Geoenvironmental Eng.*, 134(7):992–1004, 2008. (Cited on pages 2, 10, 11 and 42.)
- [38] M.J. Jiang, H.B. Yan, H.H. Zhu, and S. Utili. Modeling shear behavior and strain localization in cemented sands by two-dimensional distinct element method analyses. *Comput. Geotech.*, 38(1):14–29, jan 2011. (Cited on page 2.)
- [39] M. J. Jiang, Y. G. Sun, and Q. J. Yang. A simple distinct element modeling of the mechanical behavior of methane hydrate-bearing sediments in deep seabed. *Granul. Matter*, 15(2):209–220, 2013. (Cited on page 2.)

- [40] J.P. de Bono and G. R. McDowell. Discrete element modelling of one-dimensional compression of cemented sand. *Granular Matter*, 16(1):79–90, 2014. (Cited on pages 2 and 11.)
- [41] J. P. de Bono and G. R. McDowell. Dem of triaxial tests on crushable sand. *Granular Matter*, 16(4):551–562, 2014. (Cited on pages 2 and 11.)
- [42] G. R. McDowell and J. P. de Bono. On the micro mechanics of one-dimensional normal compression. *Géotechnique*, 63:895–908, 2013. (Cited on pages 2 and 11.)
- [43] P.A. Cundall and O.D. Strack. A discrete numerical model for granular assemblies. *Géotechnique*, 29:47–65, 1979. (Cited on pages 2 and 29.)
- [44] J.-Y. Delenne, F. Soulié, M. S. El Youssoufi, and F. Radjai. From liquid to solid bonding in cohesive granular media. *Mech. Mater.*, 43(10):529–537, 2011. (Cited on page 2.)
- [45] J.-Y. Delenne, V. Richefeu, and F. Radjai. Liquid clustering and capillary pressure in granular media. *J. Fluid Mech.*, 762(R5):R5–1–R5–10, dec 2015. (Cited on pages 2 and 15.)
- [46] V. Richefeu, M. S. El Youssoufi, E. Azéma, and F. Radjaï. Force transmission in dry and wet granular media. *Powder Technology*, 190:258–263, 2009. (Cited on pages 2 and 11.)
- [47] V.-D. Than, S. Khamseh, A.-M. Tang, J.-M. Pereira, F. Chevoir, and J.-N. Roux. Basic mechanical properties of wet granular materials: A DEM study. *J. Eng. Mech.*, page C4016001, 2016. (Cited on pages 2, 11, 38, 39, 63, 120, 131 and 174.)
- [48] X. Fu, M. Dutt, A. C. Bentham, B. C. Hancock, R. E. Cameron, and J. A. Elliott. Investigation of particle packing in model pharmaceutical powders using x-ray microtomography and discrete element method. *Powder Technol.*, 167(3):134–140, 2006. (Cited on pages 2, 40, 41, 42 and 47.)
- [49] D. J. Golchert, R. Moreno, M. Ghadiri, J. Litster, and R. Williams. Application of X-ray microtomography to numerical simulations of agglomerate breakage by distinct element method. *Adv. Powder Technol.*, 15(4):447–457, 2004. (Cited on pages 2, 19, 40, 42 and 44.)
- [50] R. Moreno-Atanasio, R. A. Williams, and X. Jia. Combining X-ray microtomography with computer simulation for analysis of granular and porous materials. *Particuology*, 8(2):81–99, 2010. (Cited on pages 2, 40, 43, 44 and 89.)
- [51] K. Iwashita and M. Oda. *Mechanics of Granular Materials: An Introduction*. A.A.Balkema, 1999. (Cited on page 7.)
- [52] J. Lanier. *Mécanique des milieux granulaires*. Hermès Science Publications, 2001. (Cited on page 7.)
- [53] B. Cambou, M. Jean, and F. Radjaï. *Micromechanics of granular materials*. ISTE Ltd and John Wiley & Sons, Inc, 2009. (Cited on pages 7 and 8.)
- [54] S. T. Antony, W. Hoyle, and Y. Ding. *Granular Materials: Fundamentals and Applications*. The Royal Society of Chemistry, Cambridge, 2004. (Cited on page 8.)
- [55] M. Oda. The mechanism of fabric changes during compressional deformation of sand. *Soils and foundations*, 12(2):1–18, 1972. (Cited on page 8.)
- [56] E. Andò, S. A. Hall, G. Viggiani, J. Desrues, and P. Bésuelle. Grain-scale experimental investigation of localised deformation in sand: A discrete particle tracking approach. *Acta Geotech.*, 7(1):1–13, 2012. (Cited on pages 8, 9, 19, 49 and 53.)
- [57] P. Dantu. Contribution à l’étude mécanique et géométrique des milieux pulvérulents. In *Proceedings of 4th international conference on soil mechanics and foundation engineering*, pages 144 – 148. Butterworths Scientific Publications, 1957. (Cited on page 9.)
- [58] H. M. Jaeger, S. R. Nagel, and R. P. Behringer. Granular solids, liquids, and gases. *Reviews of Modern Physics*, 68(4):1259–1273, 1996. (Cited on page 9.)
- [59] F. Radjaï and S. Roux. Friction-induced self-organization of a one-dimensional array of particles. *Phys. Rev. E*, 51:6177–6187, Jun 1995. (Cited on page 9.)
- [60] F. Radjaï, D. E. Wolf, M. Jean, and J.-J. Moreau. Bimodal character of stress transmission in granular packings. *Phys. Rev. Lett.*, 80:61–64, Jan 1998. (Cited on page 9.)
- [61] D. M. Mueth, H. M. Jaeger, and S. R. Nagel. Force distribution in a granular medium. *Phys. Rev. E*, 57:3164–3169, Mar 1998. (Cited on page 10.)
- [62] F. Radjaï, M. Jean, J.-J. Moreau, and S. Roux. Force distributions in dense two-dimensional granular systems. *Phys. Rev. Lett.*, 77:274–277, Jul 1996. (Cited on pages 10 and 124.)
- [63] F.J. Pettijohn, P.E. Potter, and R. Siever. *Sand and sandstone*. Springer-Verlag, New York, second edition edition, 1987. (Cited on page 10.)

- [64] J.C. Santamarina, K.A. Klein, and M.A. Fam. *Soils and Waves: Particulate Materials Behavior, Characterization and Process Monitoring*. John Wiley & Sons, New York, 2001. (Cited on page 10.)
- [65] J.-M. Dupas and A. Pecker. Static and dynamic properties of sand-cement. *J. Geotech. Eng. Div.*, 105:419–436, 1979. (Cited on page 10.)
- [66] Y. B. Acar and E. El-Tahir. Low strain dynamic properties of artificially cemented sand. *J. Geotech. Eng.*, 112(11):1001–1015, 1986. (Cited on page 10.)
- [67] G. W. Clough, N. Sitar, and R. C. Bachus. Cemented sands under static loading. *J. Geotech. Eng. Div.*, 107(6):799–817, 1981. (Cited on page 10.)
- [68] S. K. Saxena, A. S. Avramidis, and K. R. Reddy. Dynamic moduli and damping ratios for cemented sands at low strains. *Can. Geotech. J.*, 25(2):353–368, 1988. (Cited on page 10.)
- [69] J.T. Huang and D.W. Airey. Properties of artificially cemented carbonate sand. *J. Geotech. Geoenvironmental Eng.*, 124(6):492–499, 1998. (Cited on page 10.)
- [70] A. A. Abdulla and P. D. Kioussis. Behavior of Cemented sands - I. Testing. *Int. J. Numer. Anal. Methods Geomech.*, 21:533–547, 1997. (Cited on page 10.)
- [71] F. Schnaid, D.M. Prietto, and N. C. Consoli. Characterization of cemented sand in triaxial compression. *J. Geotech. Geoenvironmental Eng.*, 127(10):857–868, 2001. (Cited on page 10.)
- [72] S. Leroueil and P.R. Vaughan. The general and congruent effects of structure in natural soils and weak rocks. *Géotechnique*, 40, 1990. (Cited on page 10.)
- [73] D. W. Airey. Triaxial testing of naturally cemented carbonate soil. *J. Geotech. Eng.*, 119(9):1379–1398, 1993. (Cited on page 10.)
- [74] M. A. Ismail, H. A. Joer, W. H. Sim, and M. F. Randolph. Effect of cement type on shear behavior of cemented calcareous soil. *J. Geotech. Geoenvironmental Eng.*, 128(6):520–529, 2002. (Cited on page 10.)
- [75] M.J. Jiang, Y.G. Sun, L.Q. Li, and H.H. Zhu. Contact behavior of idealized granules bonded in two different interparticle distances: An experimental investigation. *Mech. Mater.*, 55:1–15, 2012. (Cited on page 10.)
- [76] M.J. Jiang, Y. G. Sun, and Y. Xiao. An experimental investigation on the mechanical behavior between cemented granules. *Geotech. Test. J.*, 35(5):104408, 2012. (Cited on page 10.)
- [77] M.J. Jiang, H. Hu, and F. Liu. Summary of collapsible behaviour of artificially structured loess in oedometer and triaxial wetting tests. *Can. Geotech. J.*, 49:1147–1157, 2012. (Cited on page 10.)
- [78] S. M. Iveson, J. D. Litster, and B. J. Ennis. Fundamental studies of granule consolidation part 1: Effects of binder content and binder viscosity. *Powder Technol.*, 88(1):15–20, 1996. (Cited on page 10.)
- [79] S. M. Iveson, J. D. Litster, K. Hapgood, and B. J. Ennis. Nucleation, growth and breakage phenomena in agitated wet granulation processes: a review. *Powder Technology*, 117(1):3 – 39, 2001. Granulation and Coating of Fine Powders. (Cited on pages 10 and 13.)
- [80] A. Nokhodchi. An overview of the effect of moisture on compaction and compression. *Pharm. Technol.*, 1:46–66, 2005. (Cited on page 10.)
- [81] C Cardell, F. Delalieux, K Roumpopoulos, A. Moropoulou, F. Auger, and R. V. Grieken. Salt-induced decay in calcareous stone monuments and buildings in a marine environment in sw france. *Construction and Building Materials*, 17(3):165 – 179, 2003. (Cited on page 10.)
- [82] B. Lubelli, R. P. J. van Hees, and C. J. W. P. Groot. The role of sea salts in the occurrence of different damage mechanisms and decay patterns on brick masonry. *Construction and Building Materials*, 18(2):119 – 124, 2004. (Cited on page 10.)
- [83] A. R. Lourens, P. Leo, P. H. Henk, and K. Klaas. Salt crystallization as damage mechanism in porous building materials - a nuclear magnetic resonance study. *Magnetic Resonance Imaging*, 23(2):273 – 276, 2005. Proceedings of the Seventh International Conference on Recent Advances in MR Applications to Porous Media Proceedings of the Seventh International Conference on Recent Advances in MR Applications to Porous Media. (Cited on page 10.)
- [84] S. Herminghaus. Dynamics of wet granular matter. *Advances in Physics*, 54(3):221–261, 2005. (Cited on pages 10, 37, 102, 110 and 111.)
- [85] D. Poquillon, V. Baco-Carles, Ph. Tailhades, and E. Andrieu. Cold compaction of iron powders - relations between powder morphology and mechanical properties: Part ii. bending tests: results and analysis. *Powder Technology*, 126(1):75 – 84, 2002. (Cited on page 10.)

- [86] J. P. de Bono, G. R. McDowell, and D. Wanatowski. Investigating the micro mechanics of cemented sand using dem. *Int. J. Numer. Anal. Methods Geomech.*, 39:655–675, 2015. (Cited on pages 11 and 48.)
- [87] M.J. Jiang, W. Zhang, Y. Sun, and S. Utili. An investigation on loose cemented granular materials via dem analyses. *Granul. Matter*, 15(1):65–84, 2013. (Cited on page 11.)
- [88] M.J Jiang, H. Chen, M. Tapias, M. Arroyo, and R. Fang. Study of mechanical behavior and strain localization of methane hydrate bearing sediments with different saturations by a new dem model. *Comput. Geotech.*, 57:122–138, 2014. (Cited on page 11.)
- [89] T. Mikami, H. Kamiya, and M. Horio. Numerical simulation of cohesive powder behavior in a fluidized bed. *Chem. Eng. Sci.*, 53(10):1927–1940, 1998. (Cited on page 11.)
- [90] C. D. Willett, M. J. Adams, S. A. Johnson, and J. P. K. Seville. Capillary bridges between two spherical bodies. *Langmuir*, 16(24):9396–9405, 2000. (Cited on pages 11, 37 and 102.)
- [91] F. Soulié, F. Cherblanc, M. S. El Youssoufi, and C Saix. Influence of liquid bridges on the mechanical behaviour of polydisperse granular materials. *Int. J. Numer. Anal. Geomech.*, 30:213–228, 2006. (Cited on pages 11, 35 and 103.)
- [92] T.-H. Kim and C. Hwang. Modeling of tensile strength on moist granular earth material at low water content. *Eng. Geol.*, 69(3-4):233–244, 2003. (Cited on pages 11 and 15.)
- [93] L. Scholtès, P.-Y. Hicher, F Nicot, B. Chareyre, and F. Darve. On the capillary stress tensor in wet granular materials. *Int. J. Numer. Anal. Methods Geomech.*, 33:1289–1313, 2009. (Cited on pages 11, 14 and 110.)
- [94] L. Scholtès, B. Chareyre, F. Nicot, and F. Darve. Micromechanics of granular materials with capillary effects. *Int. J. Eng. Sci.*, 47(11-12):1460–1471, nov 2009. (Cited on pages 11, 14 and 110.)
- [95] P. Guo. Capillary interaction-induced rolling resistance between elliptical particles and its influence on grain column length at pendular state. *Acta Geotechnica*, pages 1–13, 2015. (Cited on page 11.)
- [96] J. C. Santamarina. Soil Behavior at the Microscale: Particle Forces. In Charles C Ladd, editor, *Soil Behav. Soft Gr. Constr.*, number October, pages 1–32, 2001. (Cited on pages 12, 36, 53 and 90.)
- [97] D. M. Newitt and J. M. Conway-Jones. A contribution to the theory and practice of granulation. *Trans. I. Chem. Eng.*, 36:422–442, 1958. (Cited on page 13.)
- [98] K. Terzaghi. *Principles of soil mechanics: a summary of experimental studies of clay and sand*. McGraw-Hill, New York, 1925. (Cited on page 14.)
- [99] M. Nuth and L. Laloui. Effective stress concept in unsaturated soils: Clarafication and validation of a unified framework. *Int. J. Numer. Anal. Methods Geomech.*, 32:771–801, 2008. (Cited on page 14.)
- [100] A. W. Bishop. The principle of effective stress. *Tecnisk Ukeblad*, 39:859–863, 1959. (Cited on page 14.)
- [101] R. Al-Raoush and C. S. Willson. Extraction of physically realistic pore network properties from three-dimensional synchrotron X-ray microtomography images of unconsolidated porous media systems. *J. Hydrol.*, 300(1–4):44–64, 2005. (Cited on pages 16, 41, 45, 46 and 89.)
- [102] A. M. Petrovic, J. E. Siebert, and P. E. Rieke. Soil Bulk Density Analysis in Three Dimensions by Computed Tomographic Scanning. *Soil Sci. Soc. Am. J.*, 46(6):445–450, 1982. (Cited on page 17.)
- [103] S. Crestana, S. Mascarenhas, and R. S. Pozzi-Mecelli. Static and dynamic three-dimensional studies of water in soil using computed tomographic scanning. *Soil Sci.*, 140(5):326–332, 1985. (Cited on pages 17, 24 and 25.)
- [104] S. Crestana, R. Cesareo, and S. Mascarenhas. Using a computed tomography miniscanner in soil science. *Soil Sci.*, 142(1):56–61, 1986. (Cited on page 17.)
- [105] Harold J. Vinegar and Scott L. Wellington. Tomographic imaging of three-phase flow experiments. *Rev. Sci. Instrum.*, 58(1):96–107, 1987. (Cited on page 17.)
- [106] P. K. Hunt, P. Engler, and C. Bajsarowicz. Computed Tomography as a Core Analysis Tool: Applications, Instrument Evaluation, and Image Improvement Techniques. *J. Pet. Technol.*, 40(09):1203–1210, 1988. (Cited on page 17.)
- [107] G. S. Warner, J. L. Nieber, I. D. Moore, and R. A. Geise. Characterizing Macropores in Soil by Computed Tomography. *Soil Sci. Soc. Am. J.*, 53(3):653–660, 1989. (Cited on page 17.)

- [108] D. K. Cassel, J. M. Brown, and G. A. Johnson. Computer tomographic analysis of water distribution and flow in porous media. *Theor. Appl. Climatol.*, 42(4):223–228, 1990. (Cited on page 17.)
- [109] P. Spanne, J. F. Thovert, C. J. Jacquin, W. B. Lindquist, K. W. Jones, and P. M. Adler. Synchrotron computed microtomography of porous media: Topology and transports. *Phys. Rev. Lett.*, 73(14):2001–2004, 1994. (Cited on page 17.)
- [110] C. D. Montemagno and W. G. Gray. Photoluminescent volumetric imaging: A technique for the exploration of multiphase flow and transport in porous media. *Geophys. Res. Lett.*, 22(4):425–428, 1995. (Cited on page 17.)
- [111] F. M. Auzeais, J. Dunsmuir, B. B. Ferréol, N. Martys, J. Olson, T. S. Ramakrishnan, D. H. Rothman, and L. M. Schwartz. Transport in sandstone: A study based on three dimensional microtomography. *Geophys. Res. Lett.*, 23(7):705–708, 1996. (Cited on page 17.)
- [112] D. A. Coker, S. Torquato, and J. H. Dunsmuir. Morphology and physical properties of Fontainebleu sandstone via a tomographic analysis. *J. Geophys. Res.*, 101:17497–17506, 1996. (Cited on page 17.)
- [113] W. B. Lindquist, S.-M. Lee, D. A. Coker, K. W. Jones, and P. Spanne. Medial axis analysis of void structure in three-dimensional tomographic images of porous media. *J. Geophys. Res.*, 101(B4):8297, 1996. (Cited on page 18.)
- [114] C. A. Baldwin, A. J. Sederman, M. D. Mantle, P. Alexander, and L. F. Gladden. Determination and Characterization of the Structure of a Pore Space from 3D Volume Images. *J. Colloid Interface Sci.*, 181(1):79–92, 1996. (Cited on page 18.)
- [115] J. Pauli, G. Scheying, C. Mügge, A. Zschunke, and P. Lorenz. Determination of the pore widths of highly porous materials with NMR microscopy. *Fresenius J. Anal. Chem.*, 357(5):508–513, 1997. (Cited on page 18.)
- [116] P. Klobes, H. Riesemeier, K. Meyer, J. Goebbels, and K.-H. Hellmuth. Rock porosity determination by combination of X-ray computerized tomography with mercury porosimetry. *Fresenius J. Anal. Chem.*, 357(5):543–547, 1997. (Cited on page 18.)
- [117] A. Khalili, A. J. Basu, and U. Pietrzyk. Flow visualization in porous media via Positron Emission Tomography. *Phys. Fluids*, 10(4):1031–1033, 1998. (Cited on page 18.)
- [118] M.E Coles, R.D Hazlett, P Spanne, W.E Soll, E.L Muegge, and K.W Jones. Pore level imaging of fluid transport using synchrotron X-ray microtomography. *J. Pet. Sci. Eng.*, 19(1-2):55–63, 1998. (Cited on pages 18 and 29.)
- [119] H.-T. Hsieh, G O Brown, and M L Stone. Quantification of porous media using computerized tomography and a statistical segregation threshold. *Am. Soc. Agric. Eng.*, 41(6):1697–1706, 1998. (Cited on page 18.)
- [120] V. Clausnitzer and J. W. Hopmans. Determination of phase-volume fractions from tomographic measurements in two-phase systems. *Adv. Water Resour.*, 22(6):577–584, 1999. (Cited on page 18.)
- [121] W. B. Lindquist and A. Venkatarangan. Investigating 3D geometry of porous media from high resolution images. *Phys. Chem. Earth, Part A Solid Earth Geod.*, 24(7):593–599, 1999. (Cited on page 18.)
- [122] M. Solyman and I. L. Fabricius. Image analysis and estimation of porosity and permeability of Arnager Greensand, Upper Cretaceous, Denmark. *Phys. Chem. Earth, Part A Solid Earth Geod.*, 24(7):587–591, 1999. (Cited on page 18.)
- [123] F. Musso, E. Romero Morales, A. Gens, and E. Castellanos. The role of structure in the chemically induced deformations of febex bentonite. *Appl. Clay Sci.*, 23(1-4):229–237, 2003. (Cited on pages 18 and 22.)
- [124] O. Lame, D. Bellet, M. Di Michiel, and D. Bouvard. In situ microtomography investigation of metal powder compacts during sintering. *Nucl. Instruments Methods Phys. Res. Sect. B Beam Interact. with Mater. Atoms*, 200:287–294, 2003. (Cited on pages 18 and 24.)
- [125] M. M. Kohonen, D. Geromichalos, Scheel. M., C. Schier, and S. Herminghaus. On capillary bridges in wet granular materials. *Physica A: Statistical Mechanics and its Applications*, 339(1):7 – 15, 2004. (Cited on pages 19, 22, 101, 110 and 129.)
- [126] G. Viggiani, N. Lenoir, P. Besuelle, M. Dimichiel, S. Marelli, J. Desrues, and M. Kretzschmer. X-ray microtomography for studying localized deformation in fine-grained geomaterials under triaxial compression. *Comptes Rendus Mec.*, 332(10):819–826, 2004. (Cited on page 19.)

- [127] C. L. Lin and J. D. Miller. 3D characterization and analysis of particle shape using X-ray microtomography (XMT). *Powder Technol.*, 154(1):61–69, 2005. (Cited on pages 19 and 43.)
- [128] T. Aste, M. Saadatfar, and T. Senden. Geometrical structure of disordered sphere packings. *Phys. Rev. E*, 71(6):1–15, 2005. (Cited on pages 19, 53 and 89.)
- [129] S. A. Hall, M. Bornert, J. Desrues, Y. Pannier, N. Lenoir, G. Viggiani, and P. Bésuelle. Discrete and continuum analysis of localised deformation in sand using X-ray μ CT and volumetric digital image correlation. *Géotechnique*, 60(5):315–322, 2010. (Cited on pages 19 and 49.)
- [130] S. D. N. Lourenço, D. Gallipoli, C. E. Augarde, D. G. Toll, P. C. Fisher, and A. Congreve. Formation and evolution of water menisci in unsaturated granular media. *Géotechnique*, 62(3):193–199, 2012. (Cited on pages 19, 22 and 24.)
- [131] R. Alikarami, E. Andò, M. Gkiousas-Kapnis, a. Torabi, and G. Viggiani. Strain localisation and grain breakage in sand under shearing at high mean stress: insights from in situ X-ray tomography. *Acta Geotech.*, 10(1):15–30, 2014. (Cited on page 19.)
- [132] B. Zhao, J. Wang, M. R. Coop, G. Viggiani, and M. Jiang. An investigation of single sand particle fracture using X-ray micro-tomography. *Géotechnique*, 65(8):625–641, 2015. (Cited on page 19.)
- [133] K. W. Lim, R. Kawamoto, E. Andò, G. Viggiani, and J. E. Andrade. Multiscale characterization and modeling of granular materials through a computational mechanics avatar: a case study with experiment. *Acta Geotech.*, 11(2):243–253, 2016. (Cited on page 19.)
- [134] T. Banhart. *Advanced Tomographic Methods in Materials Research and Engineering*. Oxford University Press, New York, 2008. (Cited on page 22.)
- [135] J. Hsieh. *Computed Tomography - Principles, Design, Artifacts, and Recent Advances*. SPIE and John Wiley & Sons, Inc., second edition edition, 2009. (Cited on page 22.)
- [136] G. R. McDowell. On the Yielding and Plastic Compression of Sand. *Soils Found.*, 42(1):139–145, 2002. (Cited on pages 22 and 23.)
- [137] D. J. Stokes and A. M. Donald. In situ mechanical testing of dry and hydrated breadcrumb in the environmental scanning electron microscope (esem). *J. Mater. Sci.*, 35(3):599–607, 2000. (Cited on page 22.)
- [138] N. Maeda, J. N. Israelachvili, and M. M. Kohonen. Evaporation and instabilities of microscopic capillary bridges. *Proceedings of the National Academy of Sciences*, 100(3):803–808, 2003. (Cited on pages 22, 24, 37 and 102.)
- [139] E. Romero and P. H. Simms. Microstructure investigation in unsaturated soils: A review with special attention to contribution of mercury intrusion porosimetry and environmental scanning electron microscopy. *Lab. F. Test. Unsaturated Soils*, 26:705–727, 2008. (Cited on page 22.)
- [140] G. Lian, C. Thornton, and M. J. Adams. A Theoretical Study of the Liquid Brid Forces between Two Rigid Spherical Bodies. *J. Colloid Interface Sci.*, 161:138–147, 1993. (Cited on pages 24, 37 and 111.)
- [141] J. P. K. Seville, C. D. Willett, and P. C. Knight. Interparticle forces in fluidisation: A review. *Powder Technol.*, 113(3):261–268, 2000. (Cited on page 24.)
- [142] R. A. Williams and X. Jia. Tomographic imaging of particulate systems. *Adv. Powder Technol.*, 14(1):1–16, 2003. (Cited on page 24.)
- [143] D. Wildenschild, C. M. P. Vaz, M. L. Rivers, D. Rikard, and B. S. B. Christensen. Using x-ray computed tomography in hydrology: Systems, resolutions, and limitations. *J. Hydrol.*, 267(3-4):285–297, 2002. (Cited on pages 24 and 25.)
- [144] L. Farber, G. Tardos, and J. N. Michaels. Use of x-ray tomography to study the porosity and morphology of granules. *Powder Technology*, 132(1):57–63, 2003. (Cited on pages 24, 26, 45 and 53.)
- [145] F. H. Kim, D. Penumadu, and D. S. Hussey. Water distribution variation in partially saturated granular materials using neutron imaging. *J. Geotech. Geoenvironmental Eng.*, 138(2):147–154, 2012. (Cited on pages 24 and 27.)
- [146] I. Riedel, E. Andò, S. Salager, P. Bésuelle, and G. Viggiani. Water retention behaviour explored by x-ray ct analysis. In C. Mancuso, C. Jommi, and F. D’Onza, editors, *Unsaturated Soils Res. Appl. Vol. 1*, pages 81–88, 2012. (Cited on pages 24 and 27.)
- [147] D. Wildenschild and A. P. Sheppard. X-ray imaging and analysis techniques for quantifying pore-scale structure and processes in subsurface porous medium systems. *Adv. Water Resour.*, 51:217–246, 2013. (Cited on pages 24, 25 and 26.)

- [148] J.-F. Bruchon. *Analyse par microtomographie aux rayons X de l'effondrement capillaire dans les matériaux granulaires*. PhD thesis, Université Paris-Est, 2014. (Cited on pages 25 and 35.)
- [149] M. Menon, X. Jia, G. J. Lair, P. H. Faraj, and A. Blaud. Analysing the impact of compaction of soil aggregates using X-ray microtomography and water flow simulations. *Soil Tillage Res.*, 150:147–157, 2015. (Cited on pages 27 and 28.)
- [150] S. Succi. *The Lattice Boltzmann Equation for Fluid Dynamics and Beyond*. Oxford University Press, USA, 2001. (Cited on page 29.)
- [151] M. C. Sukop and D. T. Thorne. *Lattice Boltzmann Modeling: An Introduction for Geoscientists and Engineers*. Springer Publishing Company, Incorporated, 1st edition, 2010. (Cited on page 29.)
- [152] J. Harting, M. Venturoli, and P. V. Coveney. Large-scale grid-enabled lattice Boltzmann simulations of complex fluid flow in porous media and under shear. *Philos. Trans. A. Math. Phys. Eng. Sci.*, 362(1821):1703–22, 2004. (Cited on pages 29 and 42.)
- [153] C. Selomulya, X. Jia, and R.a. Williams. Direct Prediction of Structure and Permeability of Flocculated Structures and Sediments Using 3D Tomographic Imaging. *Chem. Eng. Res. Des.*, 83(7):844–852, 2005. (Cited on pages 29, 40, 42 and 45.)
- [154] J. Wang, X. Zhang, A. G. Bengough, and J. W. Crawford. Domain-decomposition method for parallel lattice Boltzmann simulation of incompressible flow in porous media. *Phys. Rev. E*, 72(1):1–11, 2005. (Cited on pages 29, 40 and 42.)
- [155] C. Selomulya, T. M. Tran, X. Jia, and R. A. Williams. An integrated methodology to evaluate permeability from measured microstructures. *AIChE J.*, 52:3394–3400, 2006. (Cited on pages 29 and 42.)
- [156] M. C. Sukop, H. Huang, C. L. Lin, M. D. Deo, K. Oh, and J. D. Miller. Distribution of multi-phase fluids in porous media: Comparison between lattice Boltzmann modeling and micro-x-ray tomography. *Phys. Rev. E*, 77(2):1–7, 2008. (Cited on pages 29, 40 and 42.)
- [157] Y. Nakashima and Y. Watanabe. Estimate of transport properties of porous media by microfocus X-ray computed tomography and random walk simulation. *Water Resour. Res.*, 38(12):1271, 2002. (Cited on pages 29, 40 and 42.)
- [158] Y. Nakashima, T. Nakano, K. Nakamura, K. Uesugi, A. Tsuchiyama, and S. Ikeda. Three-dimensional diffusion of non-sorbing species in porous sandstone: Computer simulation based on X-ray microtomography using synchrotron radiation. *J. Contam. Hydrol.*, 74(1-4):253–264, 2004. (Cited on pages 29 and 42.)
- [159] A. V. Potapov, M. L. Hunt, and C. S. Campbell. Liquid-solid flows using smoothed particle hydrodynamics and the discrete element method. *Powder Technol.*, 116(2-3):204–213, 2001. (Cited on pages 29 and 30.)
- [160] P. W. Cleary and M. Prakash. Discrete-element modelling and smoothed particle hydrodynamics: potential in the environmental sciences. *Philos. Trans. A. Math. Phys. Eng. Sci.*, 362(1822):2003–2030, 2004. (Cited on pages 29 and 30.)
- [161] J.J. Monaghan. Smoothed Particle Hydrodynamics. *Reports Prog. Phys.*, 68(8):1703–1759, 2005. (Cited on page 29.)
- [162] J.J. Monaghan. Smoothed Particle Hydrodynamics and Its Diverse Applications. *Annu. Rev. Fluid Mech.*, 44(1):323–346, 2012. (Cited on page 29.)
- [163] W. Chen and T. Qiu. Numerical simulations for large deformation of granular materials using Smoothed Particle Hydrodynamics Method. *Int. J. Geomech.*, 12(4):127–135, 2012. (Cited on page 29.)
- [164] S.G. Bardenhagen, J.U. Brackbill, and D. Sulsky. The material-point method for granular materials. *Comput. Methods Appl. Mech. Eng.*, 187(3):529–541, 2000. (Cited on page 29.)
- [165] S.G. Bardenhagen and E. M. Kober. The generalized interpolation material point method. *Comput. Model. Eng. Sci.*, 5(6):477–495, 2004. (Cited on page 29.)
- [166] J. E. Guilkey and J. A. Weiss. Implicit time integration for the material point method: Quantitative and algorithmic comparisons with the finite element method. *Int. J. Numer. Methods Eng.*, 57(9):1323–1338, 2003. (Cited on pages 29 and 30.)
- [167] Z. Więckowski. The material point method in large strain engineering problems. *Comput. Methods Appl. Mech. Eng.*, 193:4417–4438, 2004. (Cited on page 29.)
- [168] E. Oñate, S. R. Idelsohn, F. Del Pin, and R. Aubry. The Particle Finite Element Method - an Overview. *Int. J. Comput. Methods*, 01(02):267–307, 2004. (Cited on page 29.)

- [169] S. R. Idelsohn, E. Oñate, and F. Del Pin. The particle finite element method: A powerful tool to solve incompressible flows with free-surfaces and breaking waves. *Int. J. Numer. Methods Eng.*, 61(7):964–989, 2004. (Cited on page 29.)
- [170] M. P. Allen and D. J. Tildesley. *Computer Simulation of Liquids*. Oxford University Press, 1987. (Cited on page 29.)
- [171] D. C. Rapaport. *The Art of Molecular Dynamics Simulation*. Cambridge University Press, 2 edition, 2004. (Cited on page 29.)
- [172] F. Radjaï and F. Dubois. *Discrete-element Modeling of Granular Materials*. ISTE Ltd and John Wiley & Sons, Inc, 2011. (Cited on pages 29, 30, 37 and 112.)
- [173] Y. T. Feng, K. Han, and D. R J Owen. Coupled lattice Boltzmann method and discrete element modelling of particle transport in turbulent fluid flows: Computational issues. *Int. J. Numer. Methods Eng.*, 72:1111–1134, 2007. (Cited on page 30.)
- [174] K. Han, Y. T. Feng, and D. R J Owen. Coupled lattice Boltzmann and discrete element modelling of fluid-particle interaction problems. *Comput. Struct.*, 85(11-14):1080–1088, 2007. (Cited on page 30.)
- [175] Y. T. Feng, K. Han, and D. R J Owen. Combined three-dimensional lattice Boltzmann method and discrete element method for modelling fluid-particle interactions with experimental assessment. *Int. J. Numer. Methods Eng.*, 81(2):229–245, 2010. (Cited on pages 30 and 42.)
- [176] F. Lominé, L. Scholtès, L. Sibille, and P. Poullain. Modeling of fluid-solid interaction in granular media with coupled lattice Boltzmann / discrete element methods: application to piping erosion. *Int. J. Numer. Anal. Methods Geomech.*, 37:577–596, 2013. (Cited on page 30.)
- [177] S. A. Galindo-Torres. A coupled Discrete Element Lattice Boltzmann Method for the simulation of fluid-solid interaction with particles of general shapes. *Comput. Methods Appl. Mech. Eng.*, 265:107–119, 2013. (Cited on page 30.)
- [178] M. Aminpour, S.A. Galindo-Torres, A. Scheuermann, and L. Li. Micro-scale characterization of fluid flow in a uniform particle pack using coupled discrete element-lattice Boltzmann method. In Harris, Whitehouse, and Moxon, editors, *Scour Eros.*, pages 77–84, London, UK, 2016. (Cited on page 30.)
- [179] M. Nitka, G. Combe, C. Dascalu, and J. Desrues. Two-scale modeling of granular materials: a DEM-FEM approach. *Granul. Matter*, 13(3):277–281, mar 2011. (Cited on page 30.)
- [180] T.K. Nguyen, G. Combe, D. Caillerie, and J. Desrues. FEM x DEM modelling of cohesive granular materials: numerical homogenisation and multi-scale simulation. *Acta Geophys.*, 62(3):1–18, 2014. (Cited on page 30.)
- [181] Kh. A. Bagherzadeh, A. A. Mirghasemi, and S. Mohammadi. Numerical simulation of particle breakage of angular particles using combined DEM and FEM. *Powder Technol.*, 205(3):15–29, 2011. (Cited on page 30.)
- [182] C. Wellmann and P. Wriggers. A two-scale model of granular materials. *Comput. Methods Appl. Mech. Eng.*, 205-208:46–58, jan 2012. (Cited on page 30.)
- [183] E. Oñate and J. Rojek. Combination of discrete element and finite element methods for dynamic analysis of geomechanics problems. *Comput. Methods Appl. Mech. Eng.*, 193(27-29):3087–3128, 2004. (Cited on page 30.)
- [184] G. Y. Onoda and E. G. Liniger. Random loose packings of uniform spheres and the dilatancy onset. *Phys. Rev. Lett.*, 64(22):2727–2730, 1990. (Cited on pages 30 and 31.)
- [185] S. Luding. Shear flow modeling of cohesive and frictional fine powder. *Powder Technol.*, 158(1-3):45–50, 2005. (Cited on page 33.)
- [186] S. Luding. The effect of friction on wide shear bands. *Part. Sci. Technol.*, 26(1):33–42, 2007. (Cited on page 33.)
- [187] V. Richefeu, F. Radajï, and M. S. El Youssoufi. Stress transmission in wet granular materials. *European Physical Journal E*, 21:359–369, 2006. (Cited on pages 33, 111 and 125.)
- [188] K. Hotta, K. Takeda, and K. Iinoya. The capillary binding force of a liquid bridge. *Powder Technol.*, 10(4-5):231–242, 1974. (Cited on page 34.)
- [189] D. Maugis. *Contact, Adhesion and Rupture of Elastic Solids*. Springer Series in Solid-State Sciences 130. Springer Berlin Heidelberg, 2000. (Cited on pages 36 and 102.)

- [190] O Pitois, P Moucheron, and X Chateau. Liquid Bridge between Two Moving Spheres: An Experimental Study of Viscosity Effects. *J. Colloid Interface Sci.*, 231:26–31, 2000. (Cited on page 37.)
- [191] R. Al-Raoush and M. Alsaleh. Simulation of random packing of polydisperse particles. *Powder Technol.*, 176(1):47–55, 2007. (Cited on pages 41, 42, 46, 53 and 89.)
- [192] R. Al-Raoush. Microstructure characterization of granular materials. *Phys. A Stat. Mech. its Appl.*, 377(2):545–558, 2007. (Cited on pages 42, 43, 46, 48, 53 and 89.)
- [193] X. Fu, J. A. Elliott, A. C. Bentham, B. C. Hancock, and R. E. Cameron. Application of x-ray microtomography and image processing to the investigation of a compacted granular system. *Part. Part. Syst. Charact.*, 23(3-4):229–236, 2006. (Cited on pages 40, 41, 42 and 47.)
- [194] X. Jia, M. Gan, R. A. Williams, and D. Rhodes. Validation of a digital packing algorithm in predicting powder packing densities. *Powder Technol.*, 174(1-2):10–13, 2007. (Cited on pages 41 and 42.)
- [195] X. Jia, R. Caulkin, M. Fairweather, and R. A. Williams. A novel approach to predicting the behavior of arbitrary particulate mixtures under vibration. In V. Plesu and P. S. Agachi, editors, *17th Eur. Symp. Comput. Aided Process Eng. – ESCAPE17*, Bucharest, Romania, 2007. Elsevier B.V. (Cited on pages 41 and 42.)
- [196] D. Golchert, R. Moreno, M. Ghadiri, and J. Litster. Effect of granule morphology on breakage behaviour during compression. *Powder Technol.*, 143-144:84–96, 2004. (Cited on pages 40, 42 and 44.)
- [197] S. R. Stock. Recent advances in X-ray microtomography applied to materials. *Int. Mater. Rev.*, 53(3):129–181, 2008. (Cited on page 40.)
- [198] C. Y. Wu, O. M. Ruddy, A. C. Bentham, B. C. Hancock, S. M. Best, and J. A. Elliott. Modelling the mechanical behaviour of pharmaceutical powders during compaction. *Powder Technol.*, 152(1–3):107–117, 2005. (Cited on page 40.)
- [199] L. Wang, J.-Y. Park, and Y. Fu. Representation of real particles for DEM simulation using X-ray tomography. *Constr. Build. Mater.*, 21:338–346, 2007. (Cited on page 43.)
- [200] E. J. Garboczi. Three-dimensional mathematical analysis of particle shape using X-ray tomography and spherical harmonics: Application to aggregates used in concrete. *Cem. Concr. Res.*, 32(10):1621–1638, 2002. (Cited on page 43.)
- [201] M. A. Taylor, E. J. Garboczi, S. T. Erdogan, and D. W. Fowler. Some properties of irregular 3-D particles. *Powder Technol.*, 162(1):1–15, 2006. (Cited on page 43.)
- [202] M. Suzuki, T. Tsuchitani, K. Limura, and M. Hirota. Measurement of voidage distribution in particle packed bed using X-ray micro computed tomography. In M. Takei, editor, *The 4th world congress on industrial process tomography*, volume 9, pages 930–935, Aizu, Japan, 2005. (Cited on page 45.)
- [203] V.-D. Than, P. Aïmedieu, J.-M. Pereira, J.-N. Roux, M. Bornert, and A.-M. Tang. Macro-microscopic one-dimensional compression of wet granular soils by experimental investigation. In Pierre Delage, Yu-Jun Cui, Siavash Ghabezloo, Jean-Michel Pereira, and Anh-Minh Tang, editors, *The 3rd European Conference on Unsaturated Soils*, volume 9, pages 06001–06006, Paris, France, 2016. EDP Sciences. (Cited on page 45.)
- [204] H. Taud, R. Martinez-Angeles, J. F. Parrot, and L. Hernandez-Escobedo. Porosity estimation method by X-ray computed tomography. *J. Pet. Sci. Eng.*, 47(3-4):209–217, 2005. (Cited on page 45.)
- [205] G. T. Vladislavljević, M. Shimizu, and T. Nakashima. Permeability of hydrophilic and hydrophobic Shirasu-porous-glass (SPG) membranes to pure liquids and its microstructure. *J. Memb. Sci.*, 250(1-2):69–77, 2005. (Cited on page 45.)
- [206] G. T. Seidler, G. Martinez, L. H. Seeley, K. H. Kim, E. a. Behne, S. Zaranek, B. D. Chapman, S. M. Heald, and D. L. Brewster. Granule-by-granule reconstruction of a sandpile from X-ray microtomography data. 62(6B):8175–8181, 2000. (Cited on pages 46 and 47.)
- [207] S. Neethirajan, D. S. Jayas, N. D G White, and H. Zhang. Investigation of 3D geometry of bulk wheat and pea pores using X-ray computed tomography images. *Comput. Electron. Agric.*, 63(2):104–111, 2008. (Cited on page 46.)
- [208] P. Bhattad, C. S. Willson, and K. E. Thompson. Effect of Network Structure on Characterization and Flow Modeling Using X-ray Micro-Tomography Images of Granular and Fibrous Porous Media. *Transp. Porous Media*, 90(2):363–391, 2011. (Cited on page 46.)

- [209] E. Andò, P. Bésuelle, S. a. Hall, G. Viggiani, and J. Desrues. Experimental micromechanics: grain-scale observation of sand deformation. *Géotechnique Lett.*, 2(July-September):107–112, 2012. (Cited on pages 46, 49 and 53.)
- [210] A. Marmottant, L. Salvo, C. L. Martin, and A. Mortensen. Coordination measurements in compacted NaCl irregular powders using X-ray microtomography. *J. Eur. Ceram. Soc.*, 28(13):2441–2449, 2008. (Cited on pages 46, 47 and 89.)
- [211] P. Jouannot-Chesney, J.-P. Jernot, and C. Lantuéjoul. Practical Determination of the Coordination Number in Granular Media. *Image Anal. Stereol.*, 25(1):55–61, 2006. (Cited on page 47.)
- [212] S. Torquato. *Random Heterogeneous Materials: Microstructure and Macroscopic Properties*. Springer-Verlag, New York, 2002. (Cited on pages 47 and 91.)
- [213] P. Richard, P. Philippe, F. Barbe, S. Bourlès, X. Thibault, and D. Bideau. Analysis by x-ray microtomography of a granular packing undergoing compaction. *Phys. Rev. E*, 68:020301–4, 2003. (Cited on page 47.)
- [214] A. Marri, D. Wanatowski, and H.S. Yu. Drained behaviour of cemented sand in high pressure triaxial compression tests. *Geomech. Geoengin.*, 7(3):159–174, 2012. (Cited on page 48.)
- [215] Y. Watanabe, N. Lenoir, J. Otani, and T. Nakai. Displacement in sand under triaxial compression by tracking soil particles on x-ray ct data. *Soils and foundations*, 52(2):312–320, 2012. (Cited on page 49.)
- [216] G. Viggiani, A. Andò, C. Jaquet, and H. Talbot. Identifying and following particle-to-particle contacts in real granular media: An experimental challenge. *AIP Conf. Proc.*, 1542(6):60–65, 2013. (Cited on page 49.)
- [217] T. Aste, M. Saadatfar, A. Sakellariou, and T. J. Senden. Investigating the geometrical structure of disordered sphere packings. *Phys. A Stat. Mech. its Appl.*, 339(1-2):16–23, 2004. (Cited on page 53.)
- [218] T. Aste. Variations around disordered close packing. *J. Phys. Condens. Matter*, 17(24):S2361–S2390, 2005. (Cited on pages 53 and 89.)
- [219] A.-M. Tang, Y.-J. Cui, J. Eslami, and P. Défossez. Analysing the form of the confined uniaxial compression curve of various soils. *Geoderma*, 148(3-4):282–290, 2009. (Cited on pages 62 and 63.)
- [220] T. W. Ridler and S. Calvard. Picture Thresholding Using an Iterative Slection Method. *IEEE Trans. Syst. Man Cybern.*, 8(8):630–632, 1978. (Cited on page 65.)
- [221] R. P. Dougherty and K.-H. Kunzelmann. Computing local thickness of 3D structures with ImageJ. *Microsc. Microanal.*, 13:1678–1679, 2007. (Cited on page 72.)
- [222] T. Hildebrand and P. Rüegsegger. A new method for the model-independent assessment of thickness in three-dimensional images. *J. Microsc.*, 185(1):67–75, 1997. (Cited on page 72.)
- [223] L. Xie, R. E Cianciolo, B. Hulette, H. W. Lee, Y. Qi, G. Cofer, and G. A. Johnson. Magnetic resonance histology of age-related nephropathy in the Sprague Dawley rat. *Toxicol. Pathol.*, 40(5):764–78, 2012. (Cited on page 75.)
- [224] T. Peng, A. Balijepalli, S. K. Gupta, and T. LeBrun. Algorithms for On-Line Monitoring of Micro Spheres in an Optical Tweezers-Based Assembly Cell. *J. Comput. Inf. Sci. Eng.*, 7(4):330, 2007. (Cited on page 75.)
- [225] J. Illingworth and J. Kittler. The Adaptive Hough Transform. *IEEE Trans. Pattern Anal. Mach. Intell.*, 9(5):690–698, 1987. (Cited on page 76.)
- [226] T.-C. Lee, R. L. Kashyap, and C.-N. Chu. Building skeleton models via 3D medial surface/axis thinning algorithms. *Graph. Model. Image Process.*, 56(6):464–478, 1994. (Cited on page 76.)
- [227] M. Doube, M. M. Klosowski, I. Arganda-Carreras, F. P. Cordelières, R. P. Dougherty, J. S. Jackson, B. Schmid, J. R. Hutchinson, and S. J. Shefelbine. BoneJ: Free and extensible bone image analysis in ImageJ. *Bone*, 47(6):1076–1079, 2010. (Cited on page 76.)
- [228] T. Aste, M. Saadatfar, and T. J. Senden. Local and global relations between the number of contacts and density in monodisperse sphere packs. *J. Stat. Mech. Theory Exp.*, 2006(07):P07010, 2006. (Cited on page 89.)
- [229] N. Estrada, E. Azéma, F. Radjaï, and A. Taboada. Identification of rolling resistance as a shape parameter in sheared granular media. *Physical Review E*, 84:011306, 2011. (Cited on page 99.)
- [230] I. Agnolin and J.-N. Roux. Internal states of model isotropic granular packings. i. assembling process, geometry, and contact networks. *Phys. Rev. E*, 76:061302, 2007. (Cited on pages 101, 104, 108, 109, 111, 112, 114, 121, 124 and 128.)

- [231] P.-E. Peyneau and J.-N. Roux. Frictionless bead packs have macroscopic friction, but no dilatancy. *Phys. Rev. E*, 78:011307, Jul 2008. (Cited on pages 101 and 124.)
- [232] P.-E. Peyneau and J.-N. Roux. Solidlike behavior and anisotropy in rigid frictionless bead assemblies. *Physical Review E*, 78:041307, 2008. (Cited on page 101.)
- [233] D. Elata and J. G. Berryman. Contact force-displacement laws and the mechanical behavior of random packs of identical spheres. *Mechanics of Materials*, 24:229–240, 1996. (Cited on page 104.)
- [234] M. R. Kuhn and C. S. Chang. Stability, Bifurcation and Softening in Discrete Systems: A Conceptual Approach for Granular Materials. *International Journal of Solids and Structures*, 43:6026–6051, 2006. (Cited on page 104.)
- [235] J.-N. Roux. Geometric origin of mechanical properties of granular materials. *Phys. Rev. E*, 61:6802–6836, Jun 2000. (Cited on page 109.)
- [236] C. S. O’Hern, L. E. Silbert, A. J. Liu, and S. R. Nagel. Jamming at zero temperature and zero applied stress: The epitome of disorder. *Phys. Rev. E*, 68:011306, 2003. (Cited on page 109.)
- [237] A. Donev, S. Torquato, and F. H. Stillinger. Pair correlation function characteristics of nearly jammed disordered and ordered hard-sphere packings. *Phys. Rev. E*, 71:011105, 2005. (Cited on pages 109 and 124.)
- [238] F. Radjaï and V. Richefeu. Bond anisotropy and cohesion of wet granular materials. *Philos. Trans. A. Math. Phys. Eng. Sci.*, 367(1909):5123–5138, 2009. (Cited on page 110.)
- [239] I. Agnolin and J.-N. Roux. Internal states of model isotropic granular packings. ii. compression and pressure cycles. *Phys. Rev. E*, 76:061303, 2007. (Cited on pages 112 and 119.)
- [240] L. E. Silbert, D. Ertas, G. S. Grest, T. C. Halsey, and D. Levine. Geometry of frictionless and frictional sphere packings. *Phys. Rev. E*, 65:031304, 2002. (Cited on page 124.)